

TOPICS IN GRAVITATIONAL-WAVE ASTROPHYSICS

By
Prayush Kumar

A THESIS SUBMITTED IN
PARTIAL FULFILLMENT OF THE
REQUIREMENTS FOR THE DEGREE OF

DOCTOR OF PHILOSOPHY

IN
PHYSICS

at
Syracuse University
August 2014

TOPICS IN GRAVITATIONAL-WAVE ASTROPHYSICS

By
Prayush Kumar

A THESIS SUBMITTED IN
PARTIAL FULFILLMENT OF THE
REQUIREMENTS FOR THE DEGREE OF

DOCTOR OF PHILOSOPHY

IN
PHYSICS

at
Syracuse University
August 2014

Duncan Brown

Date

Graduate School Approval

Date

TOPICS IN GRAVITATIONAL-WAVE ASTROPHYSICS

By
Prayush Kumar

Syracuse University, 2014

Under the Supervision of Professor Duncan Brown

ABSTRACT

A direct observable consequence of General Relativity is gravitational radiation. A direct detection of gravitational waves would not only be a much awaited discovery, but also open up the possibility of doing astronomy and observing exotic astrophysical phenomena in a different light. There will also be an opportunity to test the theory of General Relativity in a strong field regime, which no past tests have probed. There are concerted efforts in the present era towards this aim. The major ground based observatories include the LIGO detectors in the United States, Virgo detector in Italy, GEO600 in Germany, the planned KAGRA detector in Japan and the LIGO-India project in India. The second generation detectors are expected to begin observation next year, with the hope of reaching design sensitivity in 2019.

Binary systems of compact astrophysical objects such as black holes and neutron stars emit gravitational waves as they move in orbit. With the emitted radiation, they lose energy and momentum resulting in the shrinking of their orbit, leading eventually to a merger. These are also the sources of prime importance for the ground-based detectors operating in the 10 – 2000 Hz frequency band. As the gravitational waves become very weak by the time they reach us, instrumental noise usually overwhelms them in the detector data making it a challenge to search for them. Contemporary and past gravitational wave searches fold in the theoretical knowledge of expected signals by using modeled waveforms to filter the data. This technique is called matched-filtering, and is highly sensitive to the accuracy of pre-known waveform templates.

There has been considerable effort in the recent decades to develop systematic approximations to the Einstein field equations of General Relativity. Most of such schemes use the assumption that the two bodies are moving slowly and are well separated. As the binary shrinks, these waveform *models* become increasingly inaccurate. More recently, numerical relativists have been able to solve the field equations of gravity numerically to high accuracy. With the advent of this field, we have gained detailed knowledge of the last stages of the binary motion before the black holes and/or neutron stars merge. However, due to the pressing computational cost of numerical simulations, these are restricted to the very last stages of binary coalescence. Some theoretical techniques are able to interpolate between the post Newtonian regime and the numerical relativity regime, in an attempt to capture the entire inspiral and merger process.

In this thesis we probe the question of accuracy of waveform models for comparable mass binaries. Computational cost is expected to be a significant for advanced LIGO searches. We determine the domain of applicability of the computationally inexpensive closed form models, and the same for the more expensive calibrated semi-analytic ones. We further explore the option of using *hybrid* waveforms constructed by numerically stitching post Newtonian and numerically simulated ones. Beyond matched-filtering, there is extensive processing of the filter output before a detection candidate can be confirmed. We also utilize recent results from numerical relativity to study the ability of LIGO searches to make detections in (recolored) detector noise. Lastly, we develop two waveform models using the self-force formalism, one that covers the inspiral phase and the other that captures the entire coalescence process. This formalism was developed to model extreme mass-ratio binaries, and we successfully extend it to intermediate mass-ratios.

Duncan Brown

Date

© Copyright 2014

by

Prayush Kumar

*to
my parents and Bithika*

Contents

Preface	xii
Acknowledgments	xiv
Conventions	xv
List of Tables	xviii
List of Figures	xxxii
1 Introduction	1
2 Gravitational waves and Compact binaries in General Relativity	7
2.1 General Relativity	7
2.1.1 Manifolds: Vectors, Forms and Tensors	8
2.1.2 The Metric Tensor	9
2.1.3 Covariant Derivative and Parallel Transport	9
2.1.4 The Christoffel Symbols	12
2.1.5 Field Equations of Gravity	12
2.2 Gravitational Radiation	15
2.3 Effect of Gravitational Waves	18
2.4 Modeling Gravitational Waves	20
2.5 Gravtional Waveforms for Compact Binaries	22
2.5.1 Post-Newtonian Approximations	22
2.5.2 Numerical Relativity	25
2.5.3 Effective One-Body	29

3	Introduction to LIGO	35
3.1	Design of LIGO	35
3.2	Dominant Noise Sources	38
3.3	Calibration of LIGO	40
3.4	Detector response to Gravitational wave polarizations	41
4	Search template banks for low-mass binary black holes in the Advanced gravitational-wave detector era	44
4.1	Waveforms and Template Bank Placement	46
4.1.1	Waveform Approximants	46
4.1.2	Bank Placement metric	47
4.2	Results	49
4.2.1	EOBNRv2 templates placed using TaylorF2 metric	51
4.2.2	Effectualness of TaylorF2 templates	54
4.2.3	Effect of sub-dominant modes	57
4.3	Conclusions	63
5	Binary black hole search template banks with Numerical Relativity waveforms	65
5.1	Waveforms	69
5.1.1	Numerical Relativity simulations	69
5.1.2	Post-Newtonian waveforms	70
5.1.3	PN-NR hybrid waveforms	70
5.1.4	Effective-One-Body model	71
5.2	Quantifying waveform accuracy & bank effectualness	71
5.3	Constructing a template bank for NR waveforms	76
5.4	Constructing a template bank for NR-PN hybrids	81
5.5	Complete NR-PN hybrid bank for non-spinning BBH	88
5.6	Conclusions	95
6	NINJA-2: Detecting gravitational waveforms modelled using numerical binary black hole simulations	100
6.1	PN-NR Hybrid Waveforms	103
6.2	Modified Detector Noise	110

6.3	Injection Parameters	114
6.4	Search Pipelines	115
6.4.1	<i>ihope</i>	116
6.5	Blind Injection Challenge Results	118
6.5.1	<i>ihope</i>	118
6.6	Conclusion	121
7	Modeling of intermediate mass-ratio inspirals: Exploring the form of the self-force in the intermediate mass-ratio regime	123
7.1	Self-force corrections in the intermediate-mass-ratio regime	126
7.1.1	IMRI self-force model	126
7.1.2	Radial evolution prescription	130
7.2	ISCO shift: connecting the extreme, intermediate and comparable-mass ratio regimes	139
7.3	Extension to equal-mass binaries	144
7.4	Conclusions	145
8	Self-forced evolutions of an implicit rotating source: a natural framework to model comparable and intermediate mass-ratio systems from inspiral through ringdown	150
8.1	Introduction	150
8.2	Modeling	155
8.2.1	Nomenclature	155
8.2.2	Inspiral evolution	156
8.2.3	Dissipative dynamics	161
8.2.4	Transition and plunge phases	167
8.2.5	Ringdown Waveform	172
8.2.6	Ringdown waveform construction in the context of an Implicit Rotating Source	175
8.2.7	Summary	177
8.3	Conclusions	180
9	Conclusions	183

A Post-Newtonian Waveforms	184
A.1 Phasing	184
A.1.1 TaylorT1 phasing	188
A.1.2 TaylorT4 phasing	189
A.1.3 TaylorT2 phasing	189
A.1.4 TaylorF2 phasing	190
A.1.5 Waveform amplitudes	190
Bibliography	227

Preface

The work presented in this thesis stems from my participation in the LIGO Scientific Collaboration (LSC) and the NINJA-2 Collaboration. This work does not reflect the scientific opinion of the LSC and it was not reviewed by the collaboration.

Chapter 4 is based on material from

D. A. Brown, P. Kumar and A. H. Nitz, “Template banks to search for low-mass binary black holes with Advanced Gravitational-wave detectors,” *Phys. Rev. D* **87**, 082004 (2013)

Chapter 5 is based on material from

P. Kumar, I. MacDonald, D. A. Brown, H. P. Pfeiffer, K. Cannon, M. Boyle, L. E. Kidder, A. H. Mroue, B. Szilagyi and A. Zeninoglu, “Template banks for binary black hole searches with numerical relativity waveforms,” *Phys. Rev. D* **89**, 042002 (2014)

Chapter 6 is based on material from

The LIGO Scientific Collaboration, the Virgo Collaboration, the NINJA-2 Collaboration, “The NINJA-2 project: Detecting and characterizing gravitational waveforms modelled using numerical binary black hole simulations,” *arXiv:1401.0939* (2014)
Submitted to Classical and Quantum Gravity

Chapter 7 is based on material from

E. A. Huerta, P. Kumar, D. A. Brown, “Accurate modeling of intermediate-mass-ratio inspirals: Exploring the form of the self-force in the intermediate-mass-ratio regime,”

Phys. Rev. D **86**, 024024 (2012)

Chapter 8 is based on material from

E. A. Huerta, P. Kumar, J. R. Gair, S. T. McWilliams, “Self-forced evolutions of an implicit rotating source: a natural framework to model comparable and intermediate mass-ratio systems from inspiral through ringdown,” *arXiv:1403.0561* (2014)

Submitted to Phys. Rev. D

Acknowledgments

I have been fortunate to work with many wonderful people through my membership in the LIGO-Virgo and NINJA collaborations. Sadly space makes it impossible to thank them all individually, and I hope the vast majority I must omit will forgive me.

I would first and foremost like to thank my advisor, Duncan Brown..

Conventions

We adopt the Einstein summation convention where repeated indices are summed over. The signature of spacetime is taken to be $(-1, +1, +1, +1)$.

Except where otherwise noted we work in geometric units where $G = c = 1$. We will often measure masses in multiples of the mass of the sun $1M_{\odot} \approx 1.99 \times 10^{30}$ kg

We define the Fourier transform of a function of time $g(t)$ to be $\tilde{g}(f)$, where

$$\tilde{g}(f) = \int_{-\infty}^{\infty} g(t) e^{-2\pi ift} dt$$

and the inverse Fourier transform is

$$g(t) = \int_{-\infty}^{\infty} \tilde{g}(f) e^{2\pi ift} dt$$

This convention differs from that used in some gravitational-wave literature, but is the adopted convention in the LIGO Scientific Collaboration.

List of Tables

1	SpEC BBH simulations used in this study. Given are symmetric mass-ratio η , mass-ratio $q = m_1/m_2$, and the length in orbits of the simulation. The last column gives the lowest total masses for which the NR simulations cover the entire coalescence process within the sensitive band of aLIGO, starting at 15 Hz.	70
2	List of mass-ratios, a template bank restricted to which will be effectual over the region of the non-spinning BBH mass space where $m_1 + m_2 \gtrsim 12M_\odot$ and $1 \leq q \leq 10$. The fraction of optimal SNR recovered by such a bank, accounting for discreteness losses, remains above 98%. This is shown in Fig. 20.	90
3	Submissions to NINJA-2	108
4	Submissions to NINJA-2	109

5	The details of the blind injections that were added to the NINJA-2 datasets prior to analysis. In this table the Event ID will be used throughout the paper to refer to specific injections. The network SNR of each injection is denoted by ρ_N . This is the sum of the overlaps of the injection with itself in each detector, using 30 Hz as the starting frequency in the overlap integrals. M denotes the total mass and q the mass ratio. χ denotes the spin on <i>each</i> black hole, in all 7 cases both black holes in the binary had the same spin. RA and dec give the right ascension and declination of the signals respectively. Dist. denotes the distance to the source. Detectors online lists the detectors for which data is present at the time of signal. Hybridization range gives the range of frequencies in which the signal is hybridized between the post-Newtonian and numerical components. Waveform label indicates which numerical waveform was used, as shown in Tables 3 and 4.	115
6	The low mass <code>ihope</code> search results. The Event IDs correspond to the Event ID of each blind injection given in Table 5; this association is based on the time of the candidates relative to the time of the injections. The cFARs are calculated from all possible 5 s time shifts over the entire two-month dataset. M and q give the total mass and mass ratio respectively that were recovered in each detector. The recovered SNR (ρ_{rec}) and re-weighted SNR ($\hat{\rho}$) are reported separately for each detector. To calculate the cFARs, the quadrature sum of $\hat{\rho}$ was used. Unless noted, the cFARs were calculated after category 1-3 vetoes were applied.	119
7	Ω_{ansatz} fit coefficients used in Eq. 7.3.	129
8	\dot{L}_z fit coefficients	130
9	$z_{\text{SF}}(x)$ fit coefficients	134

10	The Table shows the value of the angular momentum L_z as a function of the gauge invariant object $x = (M\Omega)^{2/3}$ evaluated at the ISCO radius (see Eq. (7.8)). The SF (self-force) values are computed using the prescription given in Eq. (7.12) to compute the orbital frequency shift, and Eq. (7.8) with the coefficients b_i quoted in [234], i.e., evaluated in the context of extreme-mass-ratio inspirals. Incomplete stands for a prescription in which we use the prescription for the orbital frequency given by Eq. (7.18), and the angular momentum prescription given by Eq. (7.8) with the coefficients b_i quoted in [234]. The b_i values of the IMRI model are obtained using a model that reproduces the dynamical evolution of intermediate-mass-ratio inspirals, as compared with the EOBNRv2 model, and for which we have derived a new prescription for the red-shift observable $z_{\text{SF}}(x)$ which actually reproduces the features of true inspirals.	143
11	The table summarizes the nomenclature we will use throughout our analysis.	156

List of Figures

1	Schematic of interferometric detectors, like LIGO.	36
2	Model for the control loop of the LIGO length sensing and control system.	40
3	The Euler angles $\{\theta, \phi, \psi\}$ to go from the gravitational wave propagation frame to the detector frame.	41
4	This figure shows the effectualness of a bank of EOBNRv2 templates, placed using the 2PN accurate hexagonal template placement of Ref. [87], to search for a population of BBH signals simulated with EOBNRv2 waveforms. The masses of the BBH population are chosen from a uniform distribution of component masses between 3 and $25 M_{\odot}$. For each injection, we plot the component masses of the injection, and the fitting factor (\mathcal{FF}).	52
5	This figure shows a cumulative histogram of the fraction of the BBH signal space (on the y-axis), where the bank of EOBNRv2 waveforms has \mathcal{FF} less than the respective values on the x-axis. The EOBNRv2 bank has a fitting factor \mathcal{FF} below the 0.97 for less than $\sim 1.5\%$ of all simulated signals with component-masses m_1, m_2 between $3 M_{\odot}$ and $25 M_{\odot}$	53
6	The fitting factor \mathcal{FF} of a bank of TaylorF2 waveforms, constructed with MM = 0.97, for a population of BBH systems which are modeled using EOBNRv2 signals.	55

- 7 The (blue) curve shows the upper-bound on total-mass for the sub-region over which the TaylorF2 bank has a minimal-fitting-factor as given on the x-axis. We observe that the TaylorF2 bank has a minimal-fitting-factor of 0.965 (0.947) for the region with total masses below $\sim 11.4M_{\odot}$ ($19M_{\odot}$). The minimal-fitting-factor is the fitting-factor value which is less than the fitting-factors of the TaylorF2 bank for $\geq 99.75\%$ of the points sampled in the sub-region. 56
- 8 (top) The \mathcal{FF} of a bank of EOBNRv2 waveforms, constructed with a minimal match of 0.97 at each point in the stellar-mass BBH component-mass region. While the templates are modeled as the dominant-mode $l = m = 2$ EOBNRv2 waveforms, the signals are modeled including the sub-dominant waveform modes as well (EOBNRv2HM). (bottom) This figure shows the upper-bound on mass-ratio (q) for the region where a bank of EOBNRv2 templates has a minimal-fitting-factor as given on the x-axis. We observe that for the region with $q \leq 1.68$ (4), the minimum-match of the bank is below 0.965 (0.947). From both the figures, we notice a systematic fall in the coverage of the EOBNRv2 template bank with increasing mass-ratio. 58
- 9 (top) The \mathcal{FF} of a bank of EOBNRv2 waveforms, constructed with a minimal match of 0.97 at each point in the stellar-mass BBH $q - \iota$ space. While the templates are modeled as the dominant-mode $l = m = 2$ EOBNRv2 waveforms, the signals are modeled including the sub-dominant waveform modes as well (EOBNRv2HM). We observe a loss in fitting-factors, upto $\sim 8\%$, for systems with high mass-ratios (q) and inclination angle (ι) close to $\pi/2$. (bottom) The \mathcal{FF} for the same population of signals, now shown on the $M - \iota$ plane. We observe the loss in fitting factors to be relatively lesser for more massive binaries. 59

13	The color at each point in the figure gives the value of $\mathcal{FF} \simeq 1 - \Gamma_{\text{bank}}$ of the bank for that binary, for the NR bank restricted to $\mathcal{S}_q = \{1, 2, 3, 4, 6, 8\}$. This is the same as the fraction of the optimal SNR, for the binary, that the template bank recovers. The black dots show the location of the templates in the bank. We note that they all lie along straight lines of constant q passing through the origin. The region shaded light-grey (towards the bottom of the figure) is where the \mathcal{FF} drops sharply below 97%.	79
14	This figure is similar to Fig. 13. The color at each point gives the value of $\mathcal{FF} \simeq 1 - \Gamma_{\text{bank}}$ of the bank for that binary, for the NR bank restricted to $\mathcal{S}_q = \{1, 2, 3, 4, 6, 9.2\}$. The black dots show the location of the templates in the bank. The region shaded light-grey (towards the bottom of the figure) is where the \mathcal{FF} drops below 97%. We note that with an additional NR waveform for mass ratio $q = 9.2$, the coverage of the bank is extended to include binaries with $10 \leq q \leq 11$.	80
15	Bounds on mismatches of PN-NR hybrid waveforms, for the currently existing NR simulations. The PN error is for hybrids matched at $M\omega_m = 0.025$ for $q = 1$, $M\omega_m = 0.038$ for $q = 2$, and $M\omega_m = 0.042$ for $q = 3, 4, 6, 8$. The black circles indicate the lower bound of the template bank in Table 1. The black square show the lower bound with a hybrid error of 1.5%. The inset shows these lower bounds as a function of mass ratio.	82

16 These figures show fitting factors \mathcal{FF} obtained when using a discrete mass-ratio template bank for $q = 1, 2, 3, 4, 6, 8$. For each mass-ratio, the templates are extended down to a total mass where the NR-PN hybridization mismatch becomes 3%. The bank is placed using the stochastic algorithm, similar to Ref. [130, 131, 132]. The black dots show the location of the templates. The fitting factor on the top plot does *not* take into account the hybridization error, and therefore shows the effect of the sparse placement of the templates alone. The bottom plot accounts for the hybridization error and gives the actual fraction of the optimal SNR that would be recovered with this bank of NR-PN hybrid templates. The region bounded by the magenta (solid) line in both plots indicates the lower end of the coverage of the bank of un-hybridized NR waveforms. Lastly, the shaded grey dots show the points where the fitting factor was below 96.5%.

84

17 These figures are similar to Fig. 16. The figures show fitting factors \mathcal{FF} obtained when using a discrete mass-ratio template bank for $q = 1, 2, 3, 4, 6, 8$. For each mass-ratio, the templates are extended down to a total mass where the NR-PN hybridization mismatch becomes 3%. Templates are placed independently for each mass-ratio, and span the full range of total masses. For each mass-ratio, neighboring templates are required to have an overlap of 97%. The union of the six single- q one-dimensional banks is taken as the final bank. The black dots show the location of the templates. The fitting factor on the top plot does *not* take into account the hybridization error, and therefore shows the effect of the sparse placement of the templates alone. The bottom plot accounts for the hybridization error and gives the actual fraction of the optimal SNR that would be recovered with this bank of NR-PN hybrid templates. The region bounded by the magenta (solid) line in both plots indicates the lower end of the coverage of the bank of un-hybridized NR waveforms. Lastly, the shaded grey dots show the points where the fitting factor was below 96.5%.

85

- 18 This figure is similar to Fig. 17. The figures show fitting factors
 \mathcal{FF} obtained when using a discrete mass-ratio template bank for $q =$
1, 2, 3, 4, 6, 8. Templates are placed independently for each mass-ratio,
and span the range of total masses, down to the region where the hy-
brid errors become 3%. For each mass-ratio, neighboring templates
are required to have an overlap of 97%. The union of the six single- q
one-dimensional banks is taken as the final bank. The black dots show
the location of the templates. The GW signals are modeled using the
EOBNRv2 approximant [38], while TaylorT4+NR hybrids are used as
templates. The fitting factor on the left plot shows the combined effect
of the sparse placement of the templates, and the (relatively small) dis-
agreement between the hybrid and EOBNRv2 waveforms. The right
plot explicitly accounts for the hybridization error and gives the (con-
servative) actual fraction of the optimal SNR that would be recovered
with this bank of NR-PN hybrid templates. The region bounded by the
magenta (solid) line in both plots indicates the lower end of the cov-
erage of the bank of un-hybridized NR waveforms. Lastly, the shaded
grey dots show the points where the fitting factor was below 96.5%.
- 19 These figures show the coverage of template banks restricted to single
mass-ratios, i.e. (from top to bottom) $q = 1, 4, 8$. We note that at
higher total masses, the templates are correlated to simulated signals
for considerably different mass-ratios, than at lower total masses. This
agrees with what we expect as with decreasing total mass, the number
of cycles in the sensitive frequency band of Advanced LIGO increases.

86

89

20	This figure shows fitting factors for a hybrid template bank which samples from the 26 mass ratios $q = 1, 1.5, 1.75, 2, \dots, 9.6$, and allows coverage to masses down to $m_1 + m_2 = 12M_\odot$ and $1 \leq q \leq 10$, with a minimal-match of 98% at the lowest masses. The left and right panel show the same on $M - q$ and $m_1 - m_2$ axes, respectively. The magenta lines, in both panels, shows the upper bound in total mass, below which frequency-domain PN waveforms can be used to construct template banks for aLIGO searches [100, 127]. The dash-dotted line in the right panel shows the lower mass limit on the smaller component object, to which a bank of currently available NR-PN hybrids can cover, i.e. $\min(m_1, m_2) = 12M_\odot$ (see Sec. 5.4). The blue (solid) curve in the right panel gives the lower mass limit to which a bank of currently available NR waveforms can cover (see Sec. 5.3). Thus, between the simulations listed in Table 2, and frequency domain PN waveforms, we can search for the entire range of BBH masses.	91
21	The maximum mismatch between different PN approximants for hybrid waveforms plotted against the total mass for at different matching frequencies ($M\omega_m$). The dotted lines indicate a mismatch of 1.5% and a lower total mass limit, $12M_\odot$ for $q = 1$, and $M_2 = 3M_\odot$ for $q = 4, 8$. The thick dashed lines indicate the currently possible matching frequency for hybrids based on the length of NR waveforms. The numbers next to each line indicate the number of orbits before merger where the PN and NR (or EOB) waveforms were stitched together.	93
22	This plot shows the lower mass limit of a template bank constructed with hybrid waveforms in terms of the number of NR orbits (left panel) and initial gravitational wave frequency (right panel) needed to have a PN error below 1.5% (solid curves) or 3% (dashed curves). The dotted line indicates the lower total mass limit when one component mass is $3M_\odot$	94
23	Parameters of the NINJA-2 submissions	104

- 24 Top: predicted sensitivity curves for aLIGO and AdV. Shown are both
the design curves and predicted 2015 – 2016 *early* sensitivity curves.
Also shown is the early AdV noise curve rescaled such that the horizon
distance for a ($10 M_{\odot}$, $10 M_{\odot}$) binary system is equal to that obtained
with the early aLIGO noise curve. Bottom: Horizon distance as a
function of observed total mass for the early aLIGO and rescaled early
AdV sensitivity curves. This plot is made considering only equal mass,
non-spinning systems and calculated using the EOBNRv2 [146] waveform
approximant. Results in this paper are generated from the early aLIGO
noise curve and the rescaled early AdV curve. 111
- 25 Sensitivity curves of the recolored data for the LIGO Hanford detector
(left) and the Virgo detector (right). In both cases the black dashed
line shows the predicted 2015 – 2016 sensitivity curve (with the scaling
factor added for Virgo). The dark colored region indicates the range
between the 10 % and 90 % quantiles of the PSD over time. The
lighter region shows the range between the minimum and maximum of
the PSD over time. 113
- 26 SNR time series in a 20 s window around a known glitch in the original
data (left) and in the recolored data (right). While the SNR time series
clearly change, the primary features of the glitch are preserved across
the recoloring procedure. These SNR time series were obtained by
matched-filtering a short stretch of recolored and original data against
a ($23.7, 1.3$) M_{\odot} template. 113

- 27 The panels show the orbital frequency, as a function of the radial coordinate r , obtained using the fit described in the text (solid red line), and the orbital frequency predicted by the EOB model (solid black line). The systems shown in the panels correspond to binaries of component masses $17M_{\odot} + 100M_{\odot}$ (top-left panel), $10M_{\odot} + 100M_{\odot}$ (top-right) and $1M_{\odot} + 100M_{\odot}$ (bottom-left panel). The bottom-right panel demonstrates the accuracy with which our IMRI model reproduces the orbital frequency predicted by the EOBNRv2 for the systems 17:100 (dashed blue), 10:100 (dashed-dot red) and 1:100 (solid black). Note that the spikes are due to artifacts in the interpolation function used to plot the EOBNRv2 orbital frequency and the numerical fit used to reproduce it. Also notice that the discrepancy between the data and the fit is always smaller than one part in a thousand. 129
- 28 We compare the calibrated flux of angular momentum described in Eq. (7.6) against the prediction of the EOBNRv2 model for binaries of component masses $17M_{\odot} + 100M_{\odot}$ (top left panel), $10M_{\odot} + 100M_{\odot}$ (top right panel), and $1M_{\odot} + 100M_{\odot}$ (bottom-left panel). The bottom-right panel shows the accuracy with which the IMRI model reproduces the EOBNRv2 angular momentum flux, $\dot{L} = dL_z/dt$, for the systems: 17:100 (dashed blue), 10:100 (dashed-dot red) and 1:100 (solid black). The spikes in the bottom-right panel are due to numerical artifacts of the interpolating function used to plot the EOBNRv2 angular momentum flux and the numerical fit to reproduce it. The fit is such that its discrepancy to the EOBNRv2 is always smaller than one part in a thousand. 132
- 29 The top panel shows the angular momentum flux for binaries of mass ratio 1:100 computed using the EOBNRv2 model and the fit to Teukolsky data introduced in [237]. Both formalisms present a remarkable agreement all the way down to the ISCO. Note that the angular momentum flux fit to Teukolsky data is valid only from early inspiral until the ISCO. The bottom panel shows the relative difference between the two prescriptions for the angular momentum flux $\dot{L} = dL_z/dt$ 133

30	The panels show the radial and azimuthal evolution for a $17M_{\odot} + 100M_{\odot}$ system (top panels), $10M_{\odot} + 100M_{\odot}$ system (middle panels), and $1M_{\odot} + 100M_{\odot}$ system (bottom panels), obtained using the IMRI model compared against the EOBNRv2 model.	135
31	The panels show the accuracy with which the IMRI model proposed in the chapter reproduces the radial (top panel) and azimuthal (bottom-panel) time evolution predicted by the EOBNRv2 model for the systems $17M_{\odot} + 100M_{\odot}$ (dashed blue), $10M_{\odot} + 100M_{\odot}$ (dashed-dot red), and $1M_{\odot} + 100M_{\odot}$ (solid black). Notice that our model reproduces the EOBNRv2 orbital and azimuthal evolution point to point with an accuracy better than one part in a thousand.	136
32	The panels show the radial evolution using the EOBNRv2 model, the IMRI model described in the text, and a model (Unfitted) which is the same as the IMRI model described in text except for the fact that the coefficients used in Eq. (7.9) for the function $z_{SF}(x)$ were derived using available self-force data from extreme-mass ratio calculations [234]. The plots correspond to binaries of component masses $17M_{\odot} + 100M_{\odot}$ (top-left panel), $10M_{\odot} + 100M_{\odot}$ (top-right panel) and $1M_{\odot} + 100M_{\odot}$ (bottom-left panel). The bottom-right panel shows that the orbital evolution predicted by a model that incorporates self-force corrections from extreme-mass-ratio inspirals (EMRIs) deviates from the orbital evolution predicted by the EOBNRv2 model at late inspiral. This discrepancy is more noticeable for systems with mass-ratios 17:100 (dashed blue) and 10:100 (dashed-dot red). Furthermore, for smaller mass-ratios, 1:100 (solid black), the discrepancy becomes comparatively smaller, as expected.	138
33	ISCO shift using various approximations as described in the text. The ‘Numerical Data’ has been obtained using calculations in the extreme-mass ratio regime [230] and the EOBNRv2. The prescription that encapsulates results from the extreme, intermediate and comparable mass-ratio regime is labeled as ‘Numerical Fit’ and is given by Eq. (7.18) in the main text.	142

- 34 The panels show the invariant angular momentum $L_z(x)$, with $x = (M\Omega)^{2/3}$, from early inspiral to the ISCO using two different prescriptions. The ‘IMRI’ prescription reproduces accurately the expected inspiral evolution, as compared with results from the EOBNRv2 model —which has been calibrated to NR simulations. The ‘Self-Force’ prescription encapsulates self-force corrections derived in the context of EMRIs [232, 234]. Note that for the three binary systems studied, $17M_\odot + 100M_\odot$ (top-left panel), $10M_\odot + 100M_\odot$ (top-right panel), and $1M_\odot + 100M_\odot$ (bottom-left panel), the ‘Self Force’ prescription for the angular momentum presents a deviation from its expected value that becomes more noticeable near the ISCO. The bottom-right panel shows the fractional accuracy between the two different prescriptions for the angular momentum for the systems 17:100 (dashed blue), 10:100 (dashed-dot red) and 1:100 (solid black). Notice also that, as expected, for binaries with small mass-ratio the ‘Self Force’ and ‘IMRI’ prescriptions are fairly consistent all the way down to the ISCO. As in the previous plots, the spikes in the bottom-right panel are due to numerical artifacts. 148
- 35 The panels show the accuracy with which our model can reproduce the dynamics of an equal mass (EM) binary system with masses ($10M_\odot + 10M_\odot$), as compared with the EOBNRv2 model. The top panels show that our model can reproduce the orbital angular evolution and the flux of angular momentum predicted by the EOBNRv2 model point to point with an accuracy better than one part in a thousand. The middle panels show that our model can reproduce with a similar accuracy the radial and azimuthal evolution of a $10M_\odot + 10M_\odot$ binary system. The bottom panel shows that the expression for the gauge-invariant angular momentum $L_z(x)$ for an EM mass deviates clearly from the EMRI prescription even before nearing the ISCO. 149

- 36 The panel shows the expected sensitivity for two configurations of the Einstein Telescope (ET), namely, ETD (black), ETB (blue) and LIGO’s Zero Detuned High Power (ZDHP) configuration (red). The vertical axis measures $F_{\text{normalized}} = (f/f_{\max})^{-7/6} \sqrt{S_n(f_{\max})/S_n(f)}$, where f_{\max} is the maximum of the corresponding power spectral density, $S_n(f)$ 152
- 37 The phase discrepancy in radians between the PN approximant TaylorT4, and the Effective One Body model, shown as a function of time from $r = 30M$ to the point when the TaylorT4 model reaches the ISCO. The systems have mass-ratio, q , total mass, M_{tot} , and final phase discrepancy, $\Delta\Phi$: $(q, M_{\text{tot}}, \Delta\Phi) = (1/6, 7M_{\odot}, 21.5 \text{ rads})$ (top-left), $(1/8, 9M_{\odot}, 30.2 \text{ rads})$ (top-right), $(1/10, 11M_{\odot}, 70.1 \text{ rads})$ (bottom-left) and $(1/15, 16M_{\odot}, 83.2 \text{ rads})$ (bottom-right) respectively. 155
- 38 The panels show the energy and angular momentum given by Eqs. (8.13)-(8.14), respectively. We show the functional form of these parameters for binary systems with mass-ratio values, from top to bottom, $q \in [0, 1/100, 1/20, 1/10, 1/6, 1/5, 1]$ 159
- 39 The location of the innermost stable circular orbit is determined by the condition $dE/dx = 0$. The panel shows dE/dx as a function of the gauge invariant quantity $x = (M\Omega)^{2/3}$. The various curves represent binary systems with mass-ratios, from top to bottom, $q \in [0, 1/100, 1/20, 1/10, 1/6, 1/5, 1]$. Note that binaries with mass-ratios $q \gtrsim 1/6$ do not have an ISCO in this model. 160
- 40 The (top, bottom) panels show the results of the optimization runs that were used to constrain the values of the b_i coefficients given in Eq. (8.21). The panels show the results for binaries of mass-ratio $q \in [1/6, 1/8]$, and total mass $M_{\text{tot}} = [7M_{\odot}, 9M_{\odot}]$. The ‘optimal’ value for the coefficients has been chosen by ensuring that the flux prescription minimizes the phase discrepancy between the EOB model and our self-force model. The color bar shows the phase difference squared between both models, which is integrated from $r = 20M$ all the way to the light-ring. 165

- 41 The panels show the orbital phase evolution of a self-force model making use of optimized PN energy flux given by Eq. (8.20) and the phase evolution as predicted by the EOB model. The [top/bottom] panels exhibit this evolution for a compact binary with mass–ratio $q = [(1/6, 1/8), (1/10, 1/15)]$, and total mass $M_{\text{tot}} = [(7M_{\odot}, 9M_{\odot}), (11M_{\odot}, 16M_{\odot})]$, respectively. 166
- 42 Left panel: The object sits at the minimum of the effective potential, Eq. (8.32), which corresponds to the case $\xi = L - L_{\text{ISCO}} \gg 0$. Right panel. Blue (top) curve: radial geodesic motion, which corresponds to $\xi = L - L_{\text{ISCO}} \gg 0$; Red (middle) curve: the object nears the ISCO and the orbit shrinks due to radiation reaction. Note that the minimum of the potential has moved inwards ($\xi = 0.35$). Yellow (bottom) curve: body’s inertia prevents it from staying at the minimum of the potential, and adiabatic inspiral breaks down ($\xi = 0$). At this point the transition regime takes over the late inspiral evolution [244]. Note: this plot is based on Figure 1 of [244]. 168
- 43 The left panel shows the effective potential for a Schwarzschild BH without including finite mass–ratio corrections. Note that the minimum of the potential takes place at the ISCO, which can be determined using Eq. (8.18). The right panel exhibits the influence of finite mass–ratio corrections on the effective potential used to modify Ori and Thorne transition regime [244]. The curves represent binaries, from top to bottom, with mass–ratios $q \in [0, 1/100, 1/20, 1/10, 1/6, 1/5, 1]$ 169
- 44 (Top, bottom) panels: the left panel shows the inspiral, transition and plunge radial evolution for a BH binary of mass–ratio $q = (1/6, 1/8)$ — and total mass $M_{\text{tot}} \in (7M_{\odot}, 9M_{\odot})$ — using the coordinate transformation given by Eq. (8.15). The right panel shows the orbital frequency $M\Omega$ from late inspiral all the way to the light ring. The evolution starts from an initial radial value $r = 30M$ 171
- 45 As in Figure 44, but with the (top, bottom) panels showing the radial and orbital frequency evolution for binaries with mass–ratios $q = (1/10, 1/15)$, and total mass $M_{\text{tot}} \in (11M_{\odot}, 16M_{\odot})$, respectively. As before, the evolution starts from an initial radial value $r = 30M$ 172

- 46 The panels show sample waveforms from inspiral to ringdown for systems with mass-ratios $q \in [1/6, 1/8]$ —and total mass $M_{\text{tot}} \in (7M_{\odot}, 9M_{\odot})$ — (top panels—from left to right) and $q \in [1/10, 1/15]$ —and total mass $M_{\text{tot}} \in (11M_{\odot}, 16M_{\odot})$ — (bottom panels —from left to right). The inspiral evolution for the [top, bottom] panels starts from $r = [30M, 25M]$ 175
- 47 The panels show sample the late-time evolution of waveforms whose ringdown phase is modeled using the implicit rotating source (IRS) model and a sum of quasinormal modes (QNMs). The systems shown correspond to binaries with mass-ratios $q \in [1/6, 1/8]$ —and total mass $M_{\text{tot}} \in (7M_{\odot}, 9M_{\odot})$ — (top panels—from left to right) and $q \in [1/10, 1/15]$ —and total mass $M_{\text{tot}} \in (11M_{\odot}, 16M_{\odot})$ — (bottom panels —from left to right). The inspiral evolution for the [top, bottom] panels starts from $r = [30M, 25M]$ 176

Chapter 1

Introduction

Gravitational waves, as predicted by General Relativity, are ripples in the curvature of spacetime that propagate at the speed of light. Like water waves on the ocean, the concept of gravitational wave requires an ideal, i.e. a smooth and unperturbed background on which the waves propagate. Unlike water waves, however, gravitational waves are not the motion of a material medium, but are ripples in the fabric of spacetime itself. The phenomena can be intuitively described with an analogy to electromagnetism. When an electromagnetic wave is incident upon a charged particle, it accelerates the particle in a direction transverse to its own direction of propagation. This acceleration depends on the electric charge and the inertial mass of the particle. Incident gravitational waves, similarly, produce an acceleration that is transverse to their direction of propagation; with the difference that the acceleration produced is independent of the mass of the particle experiencing it and will be the same for any particle at that point. Free falling particles also experience the same acceleration, and an observer sitting in their frame, also known as a local inertial frame, will not be able to measure the local acceleration. It is only through non-local measurements between points that are separated in spacetime that one would be able to discern the effect of a passing gravitational wave.

Gravitational waves carry energy away from their source. They couple minimally with matter, which allows for the preservation of information from distant sources. This will enable us to do precision observation and characterization of astrophysical sources. On the other hand, the relatively weak coupling with matter also makes

them demonstrably quite difficult to detect directly in a laboratory. The first indirect detection of gravitational waves was made by Russell Hulse and Joseph Taylor, when they discovered a binary system with a pulsating neutron star PSR 1913+16 in 1974 [1]. They observed pulses of radio waves emitted by the pulsar, and through precise measurement of their timing, they were able to determine the rate at which the binary orbit was shrinking. Orbital energy is directly co-related with the separation of the objects in the binary, and their measurement allowed them to calculate the rate at which the binary was losing energy. It was soon shown that this rate agreed within a percent with that predicted by General Relativity [2, 3]. Hulse and Taylor were awarded the Nobel prize in Physics in 1993 for this discovery. In the following years, there have been similar pulsar binaries have been discovered, allowing for more precise measurements of the effect of gravitational waves as predicted by General Relativity [4].

Felix Pirani first suggested the use of an interferometer for precise measurement of the distance between two test masses in 1956 [5]. In 1971, Moss, Miller and Forward built and tested the first laser interferometric gravitational wave transducer [6]. The design of the modern interferometric detectors are built on the contributions of Weiss [7] and Drever [8] from 1970s. The core of such detectors is a Michelson interferometer, with two laser cavities oriented perpendicular to each other. The end mirrors of each cavity is held vertically, and are practically freely falling in the transverse direction. Incoming gravitational waves will cause different changes in the length of each cavity, and these instruments measure with great precision the change in the difference in the length of both cavities [9]. There is currently a concerted effort worldwide towards the direct detection of gravitational waves, and several ground based gravitational wave observatories are being planned and built. These include:

1. Laser Interferometer Gravitational-wave Observatory (LIGO): This United States funded project comprises of two independent detectors, one located in Hanford, Washington and the other in Livingston, Louisiana.
2. Virgo observatory: A French-Italian project based in Cascina, Italy.
3. GEO 600, near Sarstedt, Germany.
4. The Kamioka Gravitational Wave Detector (KAGRA), formerly the Large-scale

Cryogenic Gravitational-wave Telescope (LCGT), is a Japanese project, and has begun construction in the tunnels of Kamioka mines in Japan.

5. LIGO-India: This is a tentative project between LIGO and several institutions in India, aimed at having a third LIGO-like instrument in the eastern hemisphere.

The first-generation LIGO and Virgo detectors were constructed in stages, and began observation in 2002 and 2007, respectively. There were 6 observation runs performed with LIGO, called Science run 1 (S1) to Science run 6 (S6). During the fifth Science run (S5) in 2007, the LIGO detectors reached their design sensitivity (Hanford and Livingston), being sensitive to gravitational waves from systems similar to the Hulse-Taylor binary pulsar out to (sky-averaged) ~ 15 Mpc. For comparison, the Virgo supercluster, of which our own galaxy is a part, has a diameter of 33 Mpc. In the sixth Science run, the sensitivity of the instruments was improved by increasing the laser power in its cavities, adding an output-mode cleaner and implementing other technological upgrades. After these upgrades, the LIGO detectors operated from July 2009 to October 2010, being sensitive to fiducial binary pulsar systems out to ~ 20 Mpc. Similarly, the Virgo detector observed in three disjoint periods called Virgo Science Runs (VSR1-3), extending over late 2007 to 2011. While no detection was made, the LIGO-Virgo Scientific Collaboration (LVC) was able to put upper limits on the rate of compact object binary mergers within its range. Results from these observation periods have been published since, e.g. [10, 11, 12, 13, 14, 15, 16, 17, 18, 19, 20, 21, 22, 23, 24].

The second generation Advanced LIGO (aLIGO) and Virgo detectors are currently under construction and commissioning [25, 26]. The two aLIGO detectors are expected to begin operation late next year, and plan to achieve their design sensitivity by 2019 [27]. The Virgo detector is also being upgraded on a similar timeline. These upgrades will increase the sensitivity of both detectors in two important ways, (i) provide a factor of 10 improvement in sensitivity across the entire LIGO frequency band, and (ii) lower the lower frequency bound from 40 Hz down to about 15 Hz [25]. These enhancements would mean a thousandfold increase in the volume of the universe that we would be able to probe for source of gravitational waves. Astrophysical estimates and numerical simulations suggest that the Advanced detectors would detect about

40 mergers a year of Hulse-Taylor type compact binaries [28].

Gravitational wave astronomy can probe regions that the electromagnetic spectrum cannot, like black holes, interiors of neutron stars, supernovae mechanism etc. They also offer the unique avenue of probing gravity in the strong-field regime, providing a valuable test of General Relativity. There are several astrophysical sources of gravitational waves, such as supernovae explosions, cosmic strings, black hole ring-downs, etc. Binaries of stellar-mass compact objects are of special interest for ground based detectors like LIGO and Virgo as they emit gravitational radiation in the operating frequency range of the detectors, which extends from about 15 Hz to a few kHz. As binary stars evolve and undergo supernovae, a significant fraction of them get disrupted. The ones that survive form binaries containing neutron stars and/or black holes. While the mass of neutron stars are observationally constrained between $1 - 3M_{\odot}$, the upper bound on the mass of stellar-collapse black holes is something that can also be better determined with gravitational wave observations.

Searches for gravitational waves from compact binaries operate by matched-filtering the detector data to dig out the weak gravitational wave signatures that are otherwise buried in the instrumental noise. They take advantage of the fact that we can theoretically model the expected form of the gravitational wave signatures, called *waveforms*, and use those as filtering templates. While an exact analytic solution in General Relativity for the dynamics of compact binary systems has not been found, several perturbative formalisms exist that are capable of describing the inspiral dynamics. In the slow-motion large-separation post-Newtonian (PN) approximation [29], various orbital quantities are calculated as Taylor series in the binary velocity parameter v (normalized by the speed of light). There exist careful resummation techniques, e.g. within the Effective-One-Body (EOB) framework [30], that are built on PN theory results and extend them to the strong-field fast-motion regime which the binary enters close to its merger. For binaries where one body is substantially more massive than the other, the recently developed self-force (SF) formalism proves to be accurate [31, 32]. On the other hand, there has been tremendous progress recently in Numerical Relativity, which includes high-accuracy numerical simulations of binary black hole mergers in non-perturbative General Relativity. The field saw the first breakthrough simulations in 2005 by Frans Pretorius [33, 34], the Goddard group [35] and the research group at the University of Texas – Brownville and Florida Atlantic

University [35]. More recently, the Simulating eXtreme Spacetimes (SXS) collaboration [36] between California Institute of Technology, Cornell University, Canadian Institute of Theoretical Astrophysics, and the California State University at Fullerton has made rapid progress in increasing the stability and efficiency of the numerical methods involved in simulating mergers of black holes [37]. Owing to the computational complexity of these simulations, they are available only for a restricted set of binary configurations. The information from these simulations is traditionally used to calibrate semi-analytic waveform models [38], as well as purely phenomenological closed-form models [39]. There has also been concerted progress in including the effect of the internal matter structure of the neutron stars in binaries, e.g. [40], and in simulating other matter systems, e.g. supernovae [41]. In this dissertation, we will restrict ourselves to systems in vacuum, neglecting possible matter effects.

With its increased sensitivity, the Advanced detectors will need more accurate waveform templates as well as better methods for efficiently using those to filter out the noise from true gravitational wave signals. The goal of the research presented in this dissertation is to construct, and improve the techniques of using waveform templates in gravitational wave searches. The rest of the dissertation is organized as follows:

1. In chapter 2, I describe the production of gravitational waves from compact binaries, and its effect on the interferometric detectors.
2. In chapter 3, I discuss the construction of terrestrial interferometers like LIGO, and their response to incident gravitational waves.
3. In chapter 4 I study the importance of the accuracy of the PN theory in the predictive modeling of the late-inspiral of binaries. We estimate the range of binary parameters where the weak-field slow-motion PN theory is accurate and sufficient for aLIGO filter templates.
4. In chapter 5, I study the possibility of using a restricted set of accurate Numerical Relativity simulations as filter template in aLIGO searches.
5. In chapter 6, I describe work done as part of the NINJA-2 project. This involved using accurate NR waveforms as simulated signals embedded in LIGO noise that

is recolored to aLIGO sensitivity, in order to test different search algorithms that are being developed by the LIGO-Virgo collaboration.

6. In chapter 7, I describe a waveform model that we developed using recent calculations in the self-force picture. This model suffices to describe the inspiral dynamics of compact binaries with $m_1/m_2 \gtrsim 6$.
7. In chapter 8, I describe a waveform model that completes the one described in the chapter 7 by extending to and accurately capturing the late-inspiral, plunge and merger phases of compact binary coalescence.
8. Finally, chapter 9 is a summary of the conclusions from the research presented in this work.

Chapter 2

Gravitational waves and Compact binaries in General Relativity

In this chapter we briefly review the treatment of compact object binaries in General Relativity (henceforth GR), with a view at providing a description of the gravitational waves emitted during their coalescence. In Sec. 2.1, we revise the basic concepts of differential geometry and their application in general relativity. Then we go on to describe the generation of gravitational radiation in linearized GR in Sec. 2.2. In Sec. 2.3, we describe the effect of incident gravitational waves on freely-falling particles. This discussion will be carried over in the next chapter where we discuss the concept and design of interferometric gravitational wave detectors. In Sec. 2.5.1 we discuss the generation of gravitational waves by a compact object binary system in quasi-circular orbits, as it evolves through the inspiral phase to its coalescence. Searches performed over detector data use theoretically modeled waveforms for compact binaries as filters. We briefly summarize two of the primary waveform models applicable to LIGO-Virgo sources in Sec. 2.5.1.

2.1 General Relativity

We begin with summarizing basic concepts of differential geometry used and work up to writing down Einstein’s equations. Readers are referred to the books by Misner, Thorne and Wheeler [42], Schutz [43], and Wald [44] for broader treatments of these topics.

2.1.1 Manifolds: Vectors, Forms and Tensors

An manifold is a set that has the local differential structure of \mathcal{R}^n , but not necessarily its global properties. An n-dimensional, infinitely continuously differentiable (i.e. C^∞) real manifold M is a set along with sub-sets S_α , which together obey the following properties:

1. Every element $p \in M$, is a member of at least one S_α . This ensures that $\{S_\alpha\}$ covers M.
2. There exists a one-to-one, onto, map $\Psi_\alpha : S_\alpha \rightarrow U_\alpha$ for each subset S_α to an open subset of \mathcal{R}^n , U_α . This ensures that locally, every *patch* of the manifold M has the properties of a Euclidian space.
3. If any two subsets S_α and S_β overlap, there exists a C_∞ map $\zeta := \Psi_\beta \circ \Psi_\alpha^{-1}$ which maps elements of the open set $U_\alpha \subset \mathcal{R}^n$ to $U_\beta \subset \mathcal{R}^n$ (with notation as above).

Curves are maps from \mathcal{R}^n to the manifold M , and *scalar functions* are reverse maps from $M \rightarrow \mathcal{R}^n$. A composite of a function f with a curve γ gives a map from $\mathcal{R}^n \rightarrow \mathcal{R}^n$. Doing calculus on manifolds invokes the concept of *vectors* in a local sense, or *tangent* vectors. In general, there is no concept of vector operations over vectors at different points in the manifold, as there is in vector spaces. A tangent vector u at a point $p \in M$ is defined as a linear differentiation operator which maps functions defined at p , to \mathcal{R} . By definition, u obeys the Leibnitz rule:

$$u(f(p)g(p)) = u(f(p))g(p) + f(p)u(g(p))$$

where both f and g are functions in the sense mentioned above. The tangent vectors exist in a *distinct* n-dimensional vector space $T_p M$ at each point p in the manifold. They can be identified with local directional derivatives and be decomposed in the local coordinate basis $\partial/\partial x^\mu$, where $\{x^\mu\}$ forms the coordinate system on \mathcal{R}^n . We will denote this special basis as ∂_μ or \vec{e}_μ henceforth. A tangent vector field can be defined over the manifold, associating each point $p \in M$ to a vector defined locally at p .

A *one-form* (or a *dual vector*) is a linear map from vectors to \mathcal{R} , e.g. for a point $p \in M$, $\omega : T_p M \rightarrow \mathcal{R}$. The set of one-forms at the point p form a vector space. A natural basis for the same, $\{\tilde{\omega}^\mu\}$, can be obtained by solving

$$\tilde{\omega}^\nu \vec{e}_\mu = \delta_\mu^\nu$$

The components of an arbitrary form ω in this basis may be found by the application of the form to basis vectors, i.e. $\omega_\mu := \omega(\vec{e}_\mu)$. From vectors and one-forms, we can build up an arbitrary $\binom{m}{n}$ tensor as a linear map from outer products of m vectors and n one-forms to \mathcal{R} . The components of a tensor T in a choice of coordinates can be found by applying it to combinations of the basis vectors and basis one-forms. Finally, a $\binom{m}{n}$ tensor field is a map that associates to each point p in M an element in the space of $\binom{m}{n}$ tensors at p .

2.1.2 The Metric Tensor

Over the 4-dimensional manifold of spacetime, we can define a metric g which is a $\binom{2}{0}$ tensor with the following properties:

- It defines the notion of a distance between infinitesimally separated points ds ,

$$ds^2 := g_{\mu\nu} dx^\mu dx^\nu. \quad (2.1)$$

- It is symmetric in its indices, i.e. $g_{\mu\nu} = g_{\nu\mu}$.
- The determinant $|g_{\mu\nu}|$ is non-zero, making g invertible: $\exists g^{\rho\nu} : g_{\mu\rho} g^{\rho\nu} = \delta_\mu^\nu$.

Given a vector x^μ the object $g_{\mu\nu} x^\mu$ maps another vector to a real number, and is therefore a one-form. The metric therefore maps between the space of vectors and the space of one-forms. In special relativity, in Cartesian coordinates, the metric has components $(-1, 1, 1, 1)$ along the diagonal, and all other components are zero. This *flat* spacetime metric will be denoted $\eta_{\mu\nu}$ henceforth.

2.1.3 Covariant Derivative and Parallel Transport

A (*covariant*) *derivative operator* ∇ on a manifold M is a map which takes each differentiable $\binom{m}{n}$ tensor field to a smooth tensor field of type $\binom{m}{n+1}$, and satisfies the

following properties:

- Linearity: $\nabla_\alpha(kA_{b_1\dots b_n}^{a_1\dots a_m} + lB_{b_1\dots b_n}^{a_1\dots a_m}) = k\nabla_\alpha A_{b_1\dots b_n}^{a_1\dots a_m} + l\nabla_\alpha B_{b_1\dots b_n}^{a_1\dots a_m}$,
- Leibnitz rule: $\nabla_\alpha(A_{b_1\dots b_n}^{a_1\dots a_m} B_{b_1\dots b_n}^{a_1\dots a_m}) = \nabla_\alpha(A_{b_1\dots b_n}^{a_1\dots a_m})B_{b_1\dots b_n}^{a_1\dots a_m} + A_{b_1\dots b_n}^{a_1\dots a_m}\nabla_\alpha(B_{b_1\dots b_n}^{a_1\dots a_m})$,
- Commutativity with contraction of indices: $\nabla_\alpha(A_{b_1\dots c\dots b_n}^{a_1\dots c\dots a_m}) = \nabla_\alpha A_{b_1\dots c\dots b_n}^{a_1\dots c\dots a_m}$, and,
- Agrees with the notion of tangent vectors as directional derivatives on scalar fields.

In GR, it is additionally required that the commutator of the derivative operator $[\nabla_\alpha, \nabla_\beta]f := [\nabla_\alpha \nabla_\beta - \nabla_\beta \nabla_\alpha]f$ be zero when acting on a scalar field $f : M \rightarrow \mathcal{R}$, a condition that has so far been borne by experiments. This commutator is called the *torsion tensor*, and ∇ is called *torsion free* if the above condition is satisfied.

The application of ∇ on a vector field gives

$$\nabla_\mu x^\nu \vec{e}_\nu = \nabla_\mu(x^\nu) \vec{e}_\nu + x^\nu \nabla_\mu \vec{e}_\nu, \quad (2.2)$$

where the second term on the right may not vanish in coordinate systems other than Cartesian in flat spacetime, or in curved spacetime. However, we must be able to write the new vector in the original basis. The components are called *connection coefficients*, and are denoted as $\Gamma_{\mu\nu}^\rho$:

$$\nabla_\mu x^\nu \vec{e}_\nu = \nabla_\mu(x^\nu) \vec{e}_\nu + x^\nu \Gamma_{\nu\mu}^\rho \vec{e}_\rho \quad (2.3)$$

$$= (\partial_\mu x^\nu + x^\rho \Gamma_{\rho\mu}^\nu) \vec{e}_\nu \quad (2.4)$$

In similar notation, the action of ∇ on a one-form ω can be obtained, noting that $\nabla_\mu(v^\nu \omega_\nu) = \partial_\mu(v^\nu \omega_\nu)$, such that

$$\nabla_\mu \omega_\nu = \partial_\mu \omega_\nu + \Gamma_{\mu\nu}^\rho \omega_\rho. \quad (2.5)$$

Extending this to general $\binom{m}{n}$ tensors, we get that

$$\nabla_\mu T_{b_1\dots b_n}^{a_1\dots a_m} = \partial_\mu T_{b_1\dots b_n}^{a_1\dots a_m} + \sum_i \Gamma_{\mu d}^{a_i} T_{b_1\dots b_n}^{a_1\dots a_{i-1}d\dots a_m} - \sum_i \Gamma_{\mu b_i}^d T_{b_1\dots b_{i-1}d\dots b_n}^{a_1\dots a_m}. \quad (2.6)$$

The covariant derivative gives differential structure to the manifold M , allowing for moving a vector *without changing it*, or in other words the “parallel transport” of a vector. Given the operator ∇_α , a vector v is said to be parallel transported along a curve C , with a tangent vector t^α , if

$$t^\alpha \nabla_\alpha v^\beta = 0 \quad (2.7)$$

all along C . An intuitive visualization of parallel transport is of moving a vector that is perpendicular to the Equator of the Earth (at longitude L_0) parallel to itself along the Equator, followed by transporting it along a different longitude L_1 till it reaches the North pole, and further parallel transporting it back along L_0 to its original location. The returned vector would not be parallel to the original vector, even though it was never rotated with respect to itself. This therefore indicates that the surface on which it was moved is itself curved. Eq. 2.7 shows that the parallel transport of v^α depends solely on itself along the curve C . Also, it can be shown that given an initial value of v^α , Eq. 2.7 always has a unique solution [44]. A remarkable result follows, which is that a vector at a point p on the curve C uniquely defines a “parallel transported vector” everywhere else on C . This idea will also help us define curvature in a later section of this chapter.

Of particular interest is the case where a vector is parallel-transported along itself

$$v^\mu \nabla_\mu v^\nu = v^\mu (\partial_\mu v^\nu + \Gamma_{\mu\rho}^\nu v^\rho) = 0.$$

Now consider a curve $x(\lambda)$ such that v is the tangent to this curve, $v^\mu = dx^\mu/d\lambda$, then

$$\begin{aligned} \frac{dx^\mu}{d\lambda} \frac{\partial}{\partial x^\mu} \frac{dx^\nu}{d\lambda} + \Gamma_{\mu\rho}^\nu \frac{dx^\mu}{d\lambda} \frac{dx^\rho}{d\lambda} &= 0 \\ \frac{d^2 x^\nu}{d\lambda^2} + \Gamma_{\mu\rho}^\nu \frac{dx^\mu}{d\lambda} \frac{dx^\rho}{d\lambda} &= 0 \end{aligned} \quad (2.8)$$

Eq. 2.8 is called the the *geodesic equation*. The solution to this equation defines the path along which test masses that are acting solely under the influence of gravity move, in other words it defines the trajectory of freely falling particles.

2.1.4 The Christoffel Symbols

Given just the manifold structure, many distinct derivatives can be defined on it. However, with the availability of a metric $g_{\mu\nu}$, we can require another condition that scalars do not change under parallel transport along an arbitrary vector t^α . For arbitrary vector fields u^α and v^β , we take the scalar $g_{\mu\nu}u^\mu v^\nu$ and require that

$$t^\mu \nabla_\mu (g_{\alpha\beta} u^\alpha v^\beta) = 0 = x^\mu (\nabla_\mu g_{\alpha\beta}) u^\alpha v^\beta + g^{\alpha\beta} (x^\mu \nabla_\mu u^\alpha) v^\beta + g^{\alpha\beta} u^\alpha (x^\mu \nabla_\mu v^\beta). \quad (2.9)$$

As this must hold for arbitrary u and v , it must also hold when both are constant. This sets the last two terms on the right hand side of Eq. 2.9 to zero. We have left

$$\nabla_\mu g_{\alpha\beta} = 0, \quad (2.10)$$

which is also known as the *metric compatibility* condition.

Equation 2.10 and the requirement that ∇ be torsion-free together fix the connection coefficients Γ , which can be written in terms of the metric as:

$$\Gamma_{\mu\nu}^\rho = \frac{1}{2} g^{\rho\sigma} [\partial_\nu g_{\mu\sigma} + \partial_\mu g_{\nu\sigma} - \partial_\sigma g_{\mu\nu}] \quad (2.11)$$

Combining this with Eq. 2.8 in the previous section, we see that the motion of particles are completely specified once we know the metric of the spacetime and their initial positions and velocities.

2.1.5 Field Equations of Gravity

When a vector is parallel transported from a point p to q along C in the manifold M , the final vector at q will, in general, depend on the choice of C . We can generalize the example given in Sec. 2.1.3 and use the path dependence of parallel transport to define an intrinsic notion of curvature of the underlying manifold. We transport a vector u^α along an infinitesimal parallelogram with sides defined by v^β and w^γ . The failure of a vector to return to its original value when parallel transported about a closed loop can be used to define the Riemann tensor $R_{\sigma\mu\nu}^\rho$:

$$[\nabla_\mu \nabla_\nu - \nabla_\nu \nabla_\mu] v^\rho = R_{\sigma\mu\nu}^\rho v^\sigma \quad (2.12)$$

A number of properties follow from this definition (which are either follow trivially or may be proven by substituting the definition of the covariant derivative, Eq. 2.3). First, we note that $R_{\sigma\mu\nu}^\rho$ is (anti-)symmetric in the first and last pair of its indices:

$$R_{\rho\sigma\mu\nu} = -R_{\sigma\rho\mu\nu} = -R_{\rho\sigma\nu\mu} = R_{\mu\nu\rho\sigma} \quad (2.13)$$

which also imply

$$R_{[\sigma\mu\nu]}^\rho = 0, \quad (2.14)$$

where $[\dots]$ denotes the anti-symmetrization over the enclosed indices. Second, we have the Bianchi identities,

$$\nabla_\alpha R_{\rho\sigma\mu\nu} + \nabla_\mu R_{\rho\sigma\nu\alpha} + \nabla_\nu R_{\rho\sigma\alpha\mu} = 0 \quad (2.15)$$

Eq. 2.12 can be straightforwardly generalized to obtain the change in an arbitrary tensor upon being parallel-transported around an infinitesimal loop. It can be shown that [44]

$$[\nabla_\mu \nabla_\nu - \nabla_\nu \nabla_\mu] B^{\rho_1 \rho_2 \dots \rho_n} = -R_{\sigma\mu\nu}^{\rho_1} B^{\sigma\rho_2 \dots \rho_n} - R_{\sigma\mu\nu}^{\rho_2} B^{\rho_1 \sigma \dots \rho_n} - \dots - R_{\sigma\mu\nu}^{\rho_n} B^{\rho_1 \rho_2 \dots \sigma} \quad (2.16)$$

which can be proved by expanding

$$[\nabla_\mu \nabla_\nu - \nabla_\nu \nabla_\mu] (\vec{e}_\rho \otimes \vec{e}_\sigma)$$

and subsequently using the second principle of mathematical induction.

Due to the symmetries of the Riemann tensor, it can be shown that there is exactly one non-trivial contraction, up to a sign, which is between its first and third or second and fourth indices:

$$R_{\mu\nu} = R_{\mu\sigma\nu}^\sigma. \quad (2.17)$$

$R_{\mu\nu}$ is also known as the *Ricci* tensor. Contracting again, we get

$$R = R_\mu^\mu \quad (2.18)$$

which is the unique non-trivial *Ricci* scalar that can be formed from the Riemann tensor.

Contracting the Bianchi identity twice gives

$$\nabla_\alpha R_{\sigma\mu\nu}^\alpha + \nabla_\sigma R_{\mu\nu} - \nabla_\mu R_{\sigma\nu} = 0.$$

Raising the index ν and contracting over μ and ν , we obtain

$$\nabla_\alpha R_\mu^\alpha + \nabla_\sigma R_\mu^\sigma - \nabla_\mu R = 0$$

Relabeling the dummy indices and using metric compatibility gives

$$2\nabla^\mu \left(R_{\mu\nu} - \frac{1}{2}g_{\mu\nu}R \right) = 0,$$

which defines the divergenceless tensor $G_{\mu\nu}$:

$$G_{\mu\nu} = R_{\mu\nu} - \frac{1}{2}g_{\mu\nu}R \quad (2.19)$$

It follows trivially that G is symmetric: $G_{\mu\nu} = G_{\nu\mu}$.

Continuous matter distributions in special relativity are described by a symmetric tensor $T_{\mu\nu}$ called the *stress-energy-momentum* tensor. For an observer with 4-velocity u^μ , the component $T_{\mu\nu}u^\mu u^\nu$ is the energy density as measured by the observer. For non-relativistic matter, the energy density $\simeq T^{00}$ and is the same as the mass density ρ ; while T^{0i} is the momentum in the i -th direction. Conservation of momentum, i.e. $\partial_t \rho = \partial_i p^i$ can therefore be written as

$$-\nabla^0 T_{00} + \nabla^i T_{0i} = \nabla^\nu T_{0\nu} = 0$$

However, as the time direction is not uniquely specified, a change of coordinates will mix space and time components. Therefore, the above equation must generalize to

$$\nabla^\nu T_{\mu\nu} = 0,$$

which says that the stress-energy-momentum tensor T is divergenceless like G , and

like G it is also symmetric. Einstein proposed the ansatz

$$G_{\mu\nu} \propto T_{\mu\nu},$$

where the proportionality constant is fixed by requiring agreement with Newton's law of gravity in the low energy limit, when $T^{00} \gg$ all other components of T , to 8π . Now, we can finally write down the field equations of gravity which Einstein proposed in 1915:

$$G_{\mu\nu} = 8\pi T_{\mu\nu} \quad (2.20)$$

As $G_{\mu\nu}$ is entirely determined by the spacetime metric, and the tensor T is determined by the stresses, energy and momentum distribution and flows of matter in the universe, these equations connect the curvature of spacetime with properties of matter that resides in it.

2.2 Gravitational Radiation

Due to the nonlinear nature of the gravitational field equations, Eq. 2.20, it is difficult to find its solutions, and only a handful of exact solutions are known. However, solving them in the weak field approximation is often useful, mainly because the gravitational fields encountered in many physical systems are indeed weak. A weak gravitational field is characterized by a metric of the form

$$g_{\mu\nu} = \eta_{\mu\nu} + h_{\mu\nu} \quad (2.21)$$

with $|h_{\mu\nu}| \ll 1$. In this approximation, we can think of the spacetime as flat with $h_{\mu\nu}$ representing a $(^2_0)$ tensor field propagating on it. To linear order in $h_{\mu\nu}$ the Riemann tensor can be found to be:

$$R_{\beta\gamma\delta}^\alpha = \frac{1}{2} (\partial_\gamma \partial_\beta h_\delta^\alpha + \partial_\delta \partial^\alpha h_{\beta\gamma} - \partial_\gamma \partial^\alpha h_{\beta\delta} - \partial_\delta \partial_\beta h_\gamma^\alpha). \quad (2.22)$$

Contracting on two of the indices, we can write the Ricci tensor to be:

$$R_{\alpha\beta} = -\frac{1}{2} (\partial_\alpha \partial_\beta h + \square h_{\alpha\beta} - \partial_\beta \partial_\gamma h_\alpha^\gamma - \partial_\gamma \partial_\alpha h_\beta^\gamma). \quad (2.23)$$

With some algebraic manipulation, and substituting $h_{\mu\nu} \rightarrow \bar{h}_{\mu\nu} = h_{\mu\nu} - \frac{1}{2}\eta_{\mu\nu}h$, the field equations reduce to

$$\square\bar{h}_{\mu\nu} + \eta_{\mu\nu}\partial_\alpha\partial_\beta\bar{h}^{\alpha\beta} - \partial_\nu\partial_\alpha\bar{h}_\mu^\alpha - \partial_\mu\partial_\alpha\bar{h}_\nu^\alpha = -16\pi T_{\mu\nu}. \quad (2.24)$$

It can be shown that this equation is invariant under the gauge transformations produced by a vector ζ_α :

$$\bar{h}^{\mu\nu} \rightarrow \bar{h}'^{\mu\nu} = \bar{h}^{\mu\nu} - \partial^\mu\zeta^\nu - \partial^\nu\zeta^\mu + \eta^{\mu\nu}\partial_\alpha\zeta^\alpha. \quad (2.25)$$

Imposing the following gauge conditions

$$\partial_\nu\bar{h}'^{\mu\nu} = 0, \quad (2.26)$$

the field equations reduce to their familiar form which is manifestly similar to a wave equation:

$$\square\bar{h}^{\mu\nu} = -16\pi T^{\mu\nu}. \quad (2.27)$$

Before discussing the final solutions, we describe an alternate perturbative analysis which has the advantage of being completely gauge invariant. The action of the wave operator \square on the Riemann tensor is

$$\begin{aligned} \square R_{\alpha\beta\gamma\delta} &= 8\pi (\nabla_\alpha(\nabla_\beta\bar{T}_{\gamma\delta} - \nabla_\gamma\bar{T}_{\beta\delta}) - \nabla_\beta(\nabla_\alpha\bar{T}_{\gamma\delta} - \nabla_\gamma\bar{T}_{\alpha\delta})) \\ &\quad + \mathcal{O}(R_{\alpha\beta\gamma\delta}T_{\mu\nu}) + \mathcal{O}(R_{\alpha\beta\gamma\delta}^2), \end{aligned}$$

where the higher order terms involving the product of the curvature tensor with itself or with the stress-energy tensor are ignored in the linear approximation. In the absence of matter or momentum sources, the above equation simplifies further to the free wave equation. The solutions of that can be written down as:

$$R_{\alpha\beta\gamma\delta} = C_{\alpha\beta\gamma\delta}e^{ik_\mu x^\mu}. \quad (2.28)$$

Using the Bianchi identities, Eq. 2.15, it can be shown that the only relevant components of the Riemann tensor are those of the form $R_{\alpha 0\beta 0}$. Imposing Einstein's equations further restricts the possible non-zero components of $R_{\alpha 0\beta 0}$ to be of the

form R_{x0x0} or R_{y0y0} or R_{x0y0} , and it can be also shown that $R_{x0x0} = -R_{y0y0}$ from $R_{00} = 0$. This leaves only two independent degrees of freedom for the gravitational wave solution in empty space.

Going back to the description in terms of the metric perturbations $\bar{h}_{\mu\nu}$, we can write the solution to Eq. 2.27 in empty space as

$$\bar{h}_{\mu\nu}(\vec{x}, t) = \int d^3k A_{\mu\nu}(\vec{k}) e^{i(\vec{k}\vec{x} - \omega t)}. \quad (2.29)$$

Having imposed the gauge condition of Eq. 2.26, the total degrees of freedom become $10 - 4 = 6$. Eq. 2.27 are invariant under transformations of the kind similar to Eq. 2.25 if $\square\zeta^\alpha = 0$ and Eq. 2.26 are still satisfied. The four of the remaining spurious degrees of freedom can be removed by fixing the gauge to the *transverse-traceless* gauge, in which

$$h_{00} = h_{0\mu} = 0; \quad h = h_\mu^\mu = 0; \quad \partial_\mu h^{\mu\nu} = 0. \quad (2.30)$$

It can be shown that while the gauge conditions in Eq. 2.26 can be imposed in the context of linear perturbation theory *irrespective of the presence of sources*, the transition to TT gauge is possible *only* in vacuum. The second gauge fixing reveal the $6 - 4 = 2$ physical degrees of freedom, which is what was shown for the Riemann tensor in the discussion above Eq. 2.29. In fact, a one-to-one correspondance between the two can be found by simplifying Eq. 2.22:

$$R_{\mu 0\nu 0} = \frac{1}{2} \partial_0^2 h_{\mu\nu}^{TT} \quad (2.31)$$

Therefore, in the TT gauge, for a wave propagating in the z-direction, we have:

$$h_{xx}^{TT} = -h_{yy}^{TT} \equiv h_+(t - z); \quad h_{xy}^{TT} = -h_{yx}^{TT} \equiv h_\times(t - z), \quad (2.32)$$

and consequently

$$R_{x0x0} = -\frac{1}{2} \partial_0^2 h_{xx}^{TT}; \quad R_{x0y0} = -\frac{1}{2} \partial_0^2 h_{xy}^{TT}. \quad (2.33)$$

Therefore, there are two independent degrees of freedom in a propagating gravitational wave that can be described in terms of the two functions usually denoted by h_+ and h_\times . In the TT gauge they are simply related to the xx , yy and xy components

of the metric perturbation. Defining two polarization tensors e_+ and e_\times that can be obtained from $h_{\mu\nu}$ by alternately setting $h_+ = 1, h_\times = 0$ and $h_+ = 0, h_\times = 1$, we write down that

$$h_{\mu\nu}^{TT} = h_+ e_+ + h_\times e_\times. \quad (2.34)$$

The incident gravitational waves on Earth, from an astrophysical source is likely to be a superposition of these two polarizations.

2.3 Effect of Gravitational Waves

Gravitational waves have a measurable effect, which can be quantified by observing the geodesic motion of nearby freely falling particles. The proper separation between two such particles, say A and B , will oscillate with the incident wave, even if the coordinate distance between the two does not change. Let us choose the proper coordinate system of A , in which A is at the origin, and its world line is fixed at $A^\mu = \{1, 0, 0, 0\}$. The separation between the two particles is given by $\zeta^\mu := A^\mu - B^\mu$.

It can be shown that ζ^μ obeys the *geodesic deviation* equation [44]

$$A^\mu \nabla_\mu \zeta^\alpha = R_{\beta\gamma\delta}^\alpha A^\beta A^\gamma \zeta^\delta. \quad (2.35)$$

In the proper coordinates of A , we only need the $R_{00\delta}^\alpha$ component. Being a gauge invariant quantity, this can be calculated in the TT gauge from Eq. 2.22,

$$R_{\alpha 00\delta} = -\frac{1}{2} (\partial_0 \partial_0 h_{\alpha\delta}^{TT} + \partial_\alpha \partial_\delta h_{00}^{TT} - \partial_\delta \partial_0 h_{\alpha 0}^{TT} - \partial_\alpha \partial_0 h_{\delta 0}^{TT}) = \frac{1}{2} \partial_0^2 h_{\alpha\delta}^{TT}, \quad (2.36)$$

where the last equality holds since $h_{\alpha 0}^{TT}$ vanishes (see Eq. 2.30). As the Christoffel symbols vanish in the proper coordinate system, Eq. 2.35 reduces to

$$\frac{\partial^2}{\partial t^2} \zeta^\mu = \frac{1}{2} \zeta_\nu \frac{\partial^2 h_{TT}^{\mu\nu}}{\partial t^2}. \quad (2.37)$$

From the previous section, we know that the $h_{\alpha\beta}^{TT}$ can be expressed in terms of two functions, h_+ and h_\times . To understand the effect of the two polarizations better, we

first set $h_x = 0$, and re-write Eq. 2.37 as

$$\frac{\partial^2}{\partial t^2}\zeta^x = \frac{1}{2}\zeta_x \frac{\partial^2}{\partial t^2}h_+ e^{ik_\mu x^\mu}; \quad \frac{\partial^2}{\partial t^2}\zeta^y = -\frac{1}{2}\zeta_y \frac{\partial^2}{\partial t^2}h_+ e^{ik_\mu x^\mu}. \quad (2.38)$$

Solving the two to first order, we get the change in the proper separation of A and B , i.e. $\delta\zeta$,

$$\delta\zeta^x = \zeta^x - \zeta^x(0) = \frac{1}{2}\zeta^x(0) h_+ e^{ik_\mu x^\mu}, \quad (2.39a)$$

$$\delta\zeta^y = \zeta^y - \zeta^y(0) = -\frac{1}{2}\zeta^y(0) h_+ e^{ik_\mu x^\mu}. \quad (2.39b)$$

If particle B is initially on the x -axis, i.e. $\zeta^y(0) = 0$, then it remains on the x -axis. For an oscillatory wave the distance between the two particles likewise oscillates. If B is initially on the y axis, $\zeta^x(0) = 0$, and it remains on the y axis and oscillates out of phase with a corresponding particle on the x axis. The net effect is that, after a quarter cycle, a set of masses initially in a circle are moved into an ellipse flattened along one axis and stretched along the other such that the area remains constant. After another quarter cycle they return to a circle. In the next quarter cycle they are in an ellipse with the axes flipped by $\pi/2$, and the process continues. If the incident wave has only the \times polarization instead, it is straightforward to show that the eigendirections are along the lines $y = \pm x$. The effects are the same as for the $+$ polarization, with the axes rotated by $\pi/4$ radians.

Lastly, in the linearized approximation where we treat $h_{\mu\nu}$ as a tensor field propagating on a flat background, it is possible to define its energy-momentum pseudotensor $t_{\mu\nu}$. This can be written in the Lorenz gauge, where $\nabla_\mu \bar{h}_\nu^\mu = 0$, as

$$t_{\mu\nu} = \frac{1}{32\pi} \langle \nabla_\mu \bar{h}_{\alpha\beta} \nabla_\nu \bar{h}^{\alpha\beta} \rangle. \quad (2.40)$$

The $\langle \dots \rangle$ denote an averaging over a finite region of space around a spacetime event, which is several wavelengths in size, but small enough that the background metric does not vary. This is necessary because the energy can not be localized to any one point of the wave, as any point can be placed in a Local Lorentz Frame where there is no wave. The field equations can then be interpreted as having two sources, one being the conventional matter source given by $T_{\mu\nu}$ and the other being the energy-momentum tensor of the gravitational wave perturbations $t_{\mu\nu}$. We refer to [42, 45]

for a detailed treatment.

2.4 Modeling Gravitational Waves

In the previous sections, we demonstrated the existence of gravitational waves and their effect on matter. In this section, we consider their generation from isolated matter systems. In Lorenz gauge, with $\partial_\mu \bar{h}^{\mu\nu} = 0$, the metric perturbation is generated according to Eq. 2.27, and we now focus on the case when $T_{\mu\nu} \neq 0$ everywhere. From analogy with Maxwell equations in the presence of source, we can immediately write down the ansatz

$$h_{ij}^{TT}(t, \mathbf{r}) = 4 \left[\int d^3x \frac{T_{ij}(x, t-r)}{r} \right]^{TT} \quad (2.41)$$

The tacit assumption here being that the source has a characteristic length $L \ll r$, where $r \equiv |\mathbf{r}|$ is the distance to the source. The origin of our coordinates lies at the source. Expanding the stress-energy tensor about the retarded time $(t-r)$, we can write the right hand side of this equation as a summation over the moments of the stress-energy tensor $S^{ij,kl\dots}$,

$$S^{ij,kl\dots}(t) = \int d^3x T^{ij}(x, t) x^k x^l \dots, \quad (2.42)$$

as

$$h_{ij}^{TT}(t, \mathbf{r}) = \frac{2}{r} \left[S^{kl}(t') + n_m \partial_0 S^{kl,m}(t') + \frac{1}{2} n_m n_p \partial_0^2 S^{kl,mp}(t') + \dots \right]^{TT} \Big|_{t'=t-r}. \quad (2.43)$$

The conservation of energy and momentum, written in terms of the stress-energy tensor can be written as

$$\partial_0 T^{00} = -\partial_j T^{0j}; \quad \partial_0 T^{i0} = -\partial_j T^{ij}. \quad (2.44)$$

These relations help relate the moments of $T_{\mu\nu}$ in terms of the moments of the source mass distribution and momentum distribution, $M^{ij\dots}$, $P^{i,jk\dots}$ respectively, where

$$M^{ij\dots} := \int d^3x T^{00}(x, t) x^i x^j \dots; \quad P^{i,jk\dots} := \int d^3x T^{0i}(t, x) x^j x^k \dots, \quad (2.45)$$

yielding

$$S^{ij} = \frac{1}{2} \partial_0^2 M^{ij}. \quad (2.46)$$

Substituting in Eq. 2.43 at leading order, we arrive at the *quadrupolar radiation formula* which gives the metric perturbation in terms of the quadrupole moment of the source mass distribution,

$$h_{jk}^{TT} = \frac{2}{r} [\partial_0^2 \mathcal{Q}_{jk}(t-r)]^{TT} \quad (2.47)$$

where \mathcal{Q}_{ij} is the traceless part of the quadrupole moment, i.e.

$$\mathcal{Q}_{ij}(t) = \int d^3x \rho(\mathbf{x}, t) (x_i x_j - \frac{1}{3} r^2 \delta^{ij}). \quad (2.48)$$

Any massive system with a time-dependant quadrupole moment will emit gravitational radiation. However, restoring physical units to Eqn. 2.47 scales the right-hand side by $G/c^4 \sim 10^{-46}$. Therefore, for the gravitational waves to be detectable, we need very large masses and/or rapid changes in its distribution. There are many such sources of astrophysical and cosmological interest like (i) quantum fluctuations in the early universe that would produce what are called *relic* gravitational waves [46], (ii) supernovae explosions, (iii) non-axisymmetric Neutron stars and (iv) compact object binaries, comprising of Neutron stars and/or Black holes. We will focus on the last of these for the remainder of the dissertation.

It is straightforward to start from the mass distribution of two point masses in orbit around their center:

$$\begin{aligned} \rho(\mathbf{x}, t) = & m_1 \delta(x - r_1 \cos(\Omega t)) \delta(y - r_1 \sin(\Omega t)) \delta(z) \\ & + m_2 \delta(x + r_2 \cos(\Omega t)) \delta(y + r_2 \sin(\Omega t)) \delta(z) \end{aligned}$$

and calculate h^{TT} . By changing coordinates to those centered on a terrestrial gravitational-wave detector, and choosing a basis we can write the gravitational-wave polarizations

as [47]

$$\begin{aligned} h_+(t) &= -\frac{2G}{c^4 r} \mu (\pi G M f)^{\frac{2}{3}} (1 + \cos^2(\iota)) \cos(2\pi f t - 2\phi_0) \\ h_\times(t) &= -\frac{4G}{c^4 r} \mu (\pi G M f)^{\frac{2}{3}} \cos(\iota) \sin(2\pi f t - 2\phi_0) \end{aligned} \quad (2.49)$$

where $M = m_1 + m_2$, $\mu = m_1 m_2 / M$, f is the *gravitational-wave frequency* which is twice the orbital frequency $f = 2\Omega/2\pi$, ϕ_0 is the orbital phase at a specified time, and ι is the *inclination* between the normal to the plane of the binary with respect to the line joining it to the detector.

We noted in the previous section that gravitational waves carry energy. This energy must be balanced by a loss of energy by the system. From Eq. 2.40, we can find the flux of energy carried by propagating gravitational waves by computing t_{00} . Given the assumption that $h_{\mu\nu}$ is a tensor field on a flat background spacetime, the Christoffel symbols vanish, giving

$$t_{00} = \frac{1}{32\pi} \langle \partial_0 h_{\mu\nu}^{TT} \partial_0 h_{\mu\nu}^{\mu\nu} \rangle. \quad (2.50)$$

Substituting Eq. 2.47 here, we get the net rate of energy loss from the system per unit time as given by the *quadrupole formula*

$$\frac{dE}{dt}(t) = \frac{1}{5} \langle \partial_0^3 Q_{ij}(t-r) \partial_0^3 Q^{ij}(t-r) \rangle \quad (2.51)$$

In a binary system, when the separation between the masses, y , is large and the bodies are moving at non-relativistic speeds, the gravitational energy of the binary is approximately given by the Newtonian formula $E = -\frac{1}{2} \frac{Gm_1 m_2}{y}$. Therefore, orbiting bodies will emit gravitational radiation and **in-spiral** until they collide and merge.

2.5 Gravitational Waveforms for Compact Binaries

2.5.1 Post-Newtonian Approximations

A binary system of compact objects would lose energy according to Eq. 2.51 and, as a result, will be moving on continuously shrinking orbits. The approximations we made in the previous section, are not sufficiently accurate when the two objects

are close and moving fast, especially before they are about to merge. On the other hand, the later portion of their coalescence is what would be visible to terrestrial interferometric detectors, owing simply to the sensitive frequency range of the latter. Also, searches for gravitational waves from astrophysical sources involve looking for signals that are typically embedded in instrumental noise that is order(s) of magnitude higher in amplitude. Precise knowledge of the expected signal is therefore crucial to recognize the signal in such a setting. Einstein, Droste, de Sitter, and Lorentz, began the development of the *post-Newtonian* (pN) theory, which is a tool to extend the equations of motion of a system, say a compact object binary, to higher-orders. There has been tremendous effort in computing very high-order equations of motion for binaries of black holes in the recent years. In the pN approximation, one introduces a small parameter v , which is the characteristic velocity of the binary normalized by c . The metric and stress energy tensor are subsequently computed at different orders in v . Plugging these back in Einstein equations, and equating terms of the same order in v allows for the computation of orbital quantities as expansions in the parameter v .

The key to obtaining the trajectory the binary follows and obtaining the emitted gravitational waveform is equating the decline in the orbital energy of the system with the energy flux carried by the outgoing gravitational radiation,

$$\frac{dE}{dt} = -F. \quad (2.52)$$

The energy of a system of a mass m moving in the background of a Schwarzschild black hole with mass M can be written as

$$E = m \frac{1 - 2M/r}{\sqrt{1 - 3M/r}}. \quad (2.53)$$

This can be written in terms of the velocity parameter v mentioned above, noting that $v := (\pi M \Omega)^{1/3}$ as in Newtonian mechanics. Further, we approximate the inspiral motion as moving through successive circular orbits. This is called the *adiabatic* approximation, and the velocity v on each circular geodesic is $v = \sqrt{M/r}$. Substituting

this above, the energy becomes

$$E = m \frac{1 - 2v^2}{\sqrt{1 - 3v^2}}. \quad (2.54)$$

Eq. 2.51 be re-written in terms of v , giving the flux of energy carried by gravitational radiation F as

$$F = \frac{32}{5} \frac{m}{M} v^{10}. \quad (2.55)$$

Going to higher orders requires detailed calculations within pN theory, and is out of the scope of this dissertation. We collect the expressions for E and F in the Appendix A from literature, and refer the reader to the recent review by Blanchett [29] for further details.

Re-writing the energy balance equation, Eq. 2.52 as

$$F = - \frac{dE}{dv} \frac{dv}{d\phi} \frac{d\phi}{dt}, \quad (2.56)$$

we can relate the instantaneous gravitational-wave phase $\phi := \int dt 2\pi f$ to the orbital velocity v ,

$$\phi = \phi_0 + \frac{2}{M} \int_v^{v_0} dv' \frac{v'^3 dE(v')/dv'}{\mathcal{F}}. \quad (2.57)$$

With the flux and dE/dv known as expansions in v , this integral can be done analytically by expanding $1/F$ as polynomial in v .

We can re-write Eq. 2.49 as

$$h(t) = A(t) \cos(\phi(t)) = \frac{1}{2} A(t) (e^{i\phi(t)} + e^{-i\phi(t)}), \quad (2.58)$$

and obtain its Fourier transform as

$$\tilde{h}(f) = \frac{1}{2} \int dt A(t) (e^{2\pi ift+i\phi(t)} + e^{2\pi ift-i\phi(t)}). \quad (2.59)$$

Gravitational wave searches for the LIGO/Virgo detectors involve filtering the data in the frequency domain with the modeled waveforms, as will be described in the next chapter. Therefore it is preferable to work in the frequency domain from a computational perspective. We can use the *stationary phase approximation* [48] to analytically compute the integrals in Eq. 2.59. Oscillatory integrands contribute the

most at the points where their phase is *stationary*, i.e. at the extrema of the derivative of the phase. Therefore we can expand the exponents in Eq. 2.59 as

$$2\pi ift + i\phi(t) \approx 2\pi ift_0 + i\phi(t_0) + i\frac{1}{2}\frac{\partial^2\phi}{\partial t^2}(t_0)(t - t_0)^2, \quad (2.60)$$

which reduces Eq. 2.59 to Gaussian integrals. Completing the last piece, we get the gravitational wave phase as a function of the instantaneous frequency, which can be written as [47]

$$\tilde{h}(f) = \frac{2GM_{\odot}}{c^2r} \left(\frac{5\mu}{96M_{\odot}} \right)^{\frac{1}{2}} \left(\frac{M}{\pi^2 M_{\odot}} \right)^{\frac{1}{3}} \left(\frac{GM_{\odot}}{c^3} \right)^{-\frac{1}{6}} f^{-\frac{7}{6}} \Theta(f - f_c) e^{i\Psi(f; M, mu)} \quad (2.61)$$

where we have re-introduced physical units, and M_{\odot} is the mass of the sun, the unit in which the two masses M and m are taken. The step function Θ ensures the termination at a certain cutoff frequency, which is the formally where we stop trusting the pN approximation. The phase Ψ is obtained from Eq. 2.57, and it depends strongly on the symmetric mass-ratio $\eta := \mu/M$ and the *chirp* mass $\mathcal{M}_c := M\eta^{3/5}$.

This particular way of solving for and expressing the gravitational waveform is known as the *TaylorF2* approximant. However, there are other ways of solving the energy balance equation, either analytically or numerically, especially in time domain. We provide a summary of different resulting *Taylor* approximants in the Appendix A. It turns out that the second generation terrestrial interferometric detectors might be able to resolve the differences between these approximants, and this has been the subject of recent studies [49, 50].

2.5.2 Numerical Relativity

General Relativity plays a major role in describing some of the most exotic astrophysical systems and processes, such as the physics of neutron stars, black holes and accretion disks, supernova explosions, etc. Yet the theory remains largely untested, except in the weak field slow motion regime. The observation of gravitational radiation from merging neutron stars and/or black holes has the potential of probing the dynamics of strong gravitational fields. Due to their multidimensional and nonlinear nature, very few exact analytic solutions have been found for the field equations, and

all of them correspond to systems with a high degree of symmetry. Analytic approximation schemes like the post-Newtonian theory are valid in the weak field regime, and become increasingly inadequate in modeling the last phases of compact binary coalescence. This statement has been qualified in recent papers, e.g. [51].

Many fields of Science and Engineering make use of (super-)computers for high-accuracy numerical solutions of partial differential equations. Einstein’s field equations are in a particularly difficult class of such equations, but it is possible to obtain fully numerical solutions for dynamical scenarios governed by them. This proved to be a remarkably difficult task when the first attempts were made, both due to technical and conceptual difficulties as well as limited computing power. After the breakthrough simulations of merging black holes by Pretorius in 2005 [33], and foundational work by researchers at Goddard [35], University of Texas at Brownville and Florida Atlantic University [35] in the same year, there has been rapid progress in the field. We refer the reader to review articles by Hindler [52] and Pfeiffer [53] for more details that could not be provided within the scope of this dissertation.

Most approaches in Numerical Relativity (NR) proceed by the “3+1” decomposition, where they split spacetime into three-dimensional space on the one hand, and time on the other. This is achieved through foliation of spacetime into non-intersecting spacelike 3-surfaces which can be thought of as level surfaces of a globally defined time function. The situation is qualitatively similar to classical electromagnetism. Maxwell equations can be written in the manifestly covariant form as

$$\begin{aligned}\nabla_\nu F^{\mu\nu} &= j^\mu \\ \nabla_\nu F_*^{\mu\nu} &= 0\end{aligned}$$

where F is the electromagnetic field strength tensor and F_* is its dual. While conceptually simpler, this is not the form that is the most convenient for performing numerical evolutions. Instead, these are re-written in a form that makes explicit the

role of time, disentangling it from other degrees of freedom:

$$\begin{aligned}\nabla \cdot \mathbf{E} &= 4\pi\rho \\ \nabla \cdot \mathbf{B} &= 0 \\ \partial_t \mathbf{E} &= \nabla \times \mathbf{B} - 4\pi j^\mu \\ \partial_t \mathbf{B} &= -\nabla \times \mathbf{E}\end{aligned}\tag{2.62}$$

where ∇ is the 3-dimensional spatial vector gradient operator. Note that out of the set of four equations above, the first two put *constraints* on electromagnetic fields that could exist in a dynamical situation, while the last two govern the time *evolution* of the same.

In general relativity the spacetime metric can be (implicitly) written as

$$ds^2 = -(\alpha^2 - \gamma_{ij}\beta^i\beta^j)dt^2 + 2\gamma_{ij}\beta^j dt dx^i + \gamma_{ij}dx^i dx^j,$$

to make manifest the split into space+time. Here γ_{ij} is the induced metric on the space hypersurfaces defined by a constant time coordinate. The scalar α and the vector β_i relate the coordinate systems on neighbouring hypersurfaces, as well as encode the foliation structure. This decomposition manifestly separates the time coordinate from the spacial ones. When written in this formalism, Einstein field equations decompose into separate constraint and evolution equations, similar to Maxwell equations written as Eq. 2.62. However, this split is not unique and needs to be carefully engineered to ensure that the constraints remain satisfied as the system is numerically evolved. This is because, when the system is discretized, it is possible for numerical instabilities to grow and possibly lead to constraint violating solutions.

In this dissertation, we would concern ourselves with vacuum systems, where we only need to use the field equations of general relativity. More specifically, we will concern ourselves with black hole binaries, for which $T_{\mu\nu} = 0$ everywhere.

Once the decomposition is chosen, it is necessary to find the initial field configuration that satisfies the Einstein constraint equations as well as describe the system of interest. Most approaches construct the initial data by treating the metric on the initial hypersurface as being *conformally* flat. This means that each spacetime point and a finite neighborhood is treated as having a flat spacetime metric. While we can

put ourselves in a frame where the metric and its first derivatives vanish at a point, it is not true for a finite neighborhood in general. This deviation from true physics manifests as a burst of *junk* radiation at the beginning of the simulation. The spacetime singularity of black holes pose another problem for the numerical construction of the initial data. A careful treatment of the singularity is necessary to ensure that none of the physical fields on the numerical grid blow up to infinity. One conceptually simpler approach is to excise the singularity from the computational grid. In this case, it is made sure that the excised region is causally disconnected with the exterior. Another more commonly used approach involves treating the black holes as “wormholes”, and the interior of the hole is taken as asymptotically flat and compactified.

With the initial data specified on a spacelike hypersurface, the Einstein evolution equations can be used to evolve the dynamical system in time. Most codes use the finite-difference technique, where the derivatives of tensor fields are computed discretely and used to evolve the metric at each point on the hypersurface. An alternative is to use *spectral* methods, in which the solution is expanded in terms of a set of basis functions and the coefficients are evolved. In this scheme, differentiation can be performed analytically. For the same computational cost, the latter exhibits exponential convergence while the former has polynomial convergence [52]. There is always a tradeoff between computational cost and accuracy in numerical evolutions of binary black holes. A finer grid gives more accurate results, but increases the cost of the evolution. Most contemporary codes use *adaptive mesh refinement*, a technique which involves laying down a finer grid only in regions close to the holes where the various tensor fields are changing rapidly.

Finally, the extraction of gravitational radiation is done by computing the *Newman-Penrose scalar*, which in vacuum may be written

$$\Psi_4 = R_{\alpha\beta\gamma\delta} n^\alpha \bar{m}^\beta n^\gamma \bar{m}^\delta$$

where m and n are vectors constructed from the basis vectors. In spherical coordinates

these are

$$n = \frac{1}{\sqrt{2}} (\hat{t} - \hat{r}),$$

$$m = \frac{1}{\sqrt{2}} (\hat{\theta} + i\hat{\phi}),$$

and \bar{m} is the complex conjugate of m . The gravitational waveform can be obtained from Ψ_4 by solving the differential equation

$$\Psi_4 = \ddot{h}_+ - i\ddot{h}_\times,$$

usually decomposing both sides into a basis of spin weighted spherical harmonics.

2.5.3 Effective One-Body

Numerical simulation of BBH systems are computationally expensive, and results are only available for a relatively small number of binary systems (see e.g. [54]). The EOB model [30] provides a framework for computing the gravitational waveforms emitted during the inspiral and merger of BBH systems. By attaching a QNM waveform and calibrating the model to numerical relativity (NR) simulations, the EOB framework provides for accurate modeling of complete BBH waveforms (EOBNR). The EOBNR waveforms can be computed at relatively low cost for arbitrary points in the waveform parameter space [55, 56, 57, 58, 59, 60, 61, 38]. In particular the EOB model has recently been tuned against high-accuracy numerical relativity simulations of non-spinning BBHs of mass-ratios $q = \{1, 2, 3, 4, 6\}$, where $q \equiv m_1/m_2$ [38]; we refer to this as the EOBNRv2 model, which we review the major features of below. Throughout, we set $G = c = 1$.

The EOB approach maps the fully general-relativistic dynamics of the two-body system to that of an *effective* mass moving in a deformed Schwarzschild spacetime [30]. The basic idea is familiar from non-relativistic classical mechanics, where it is common to write the Hamiltonian for the Kepler problem in terms of a particle with reduced mass $\mu = m_1 m_2 / (m_1 + m_2)$ moving in a central potential due to a fixed body of mass $M = m_1 + m_2$. The dynamics is determined by the deformed-spacetime's metric coefficients, the EOB Hamiltonian [30], and the radiation-reaction force. In polar

coordinates (r, Φ) , the EOB metric is written as

$$ds_{\text{eff}}^2 = -A(r)dt^2 + \frac{A(r)}{D(r)}dr^2 + r^2(d\Theta^2 + \sin^2\Theta d\Phi^2). \quad (2.63)$$

The geodesic dynamics of the *effective* mass $\mu = m_1m_2/M$ in the background of Eq. (2.63) is described by an effective Hamiltonian H^{eff} [30, 62]. The EOBNRv2 model uses Pade-resummations of the third-order post-Newtonian Taylor expansions of the metric coefficients $A(r)$ and $D(r)$, with additional 4PN and 5PN coefficients that are calibrated [56, 57, 58, 59, 38] to ensure that the dynamics agrees closely with NR simulations of comparable mass binaries.

Gravitational waves carry energy and angular momentum away from the binary, and the resulting radiation-reaction force \hat{F}_Φ causes the orbits to shrink. This is related to the energy flux as

$$\hat{F}_\Phi = -\frac{1}{\eta\hat{\Omega}}\frac{dE}{dt} = -\frac{1}{\eta v^3}\frac{dE}{dt}, \quad (2.64)$$

where, $v = (\hat{\Omega})^{1/3} = (\pi M f)^{1/3}$ and f is the instantaneous gravitational-wave frequency. The energy flux dE/dt is obtained by summing over the contribution from each term in the multipole expansion of the waveform, i.e.

$$\frac{dE}{dt} = \frac{\hat{\Omega}^2}{8\pi} \sum_l \sum_m \left| \frac{\mathcal{R}}{M} h_{lm} \right|^2. \quad (2.65)$$

\mathcal{R} is the physical distance to the binary, and h_{lm} are the multipoles of the waveform when it is decomposed in spin weighted spherical harmonic basis as

$$h_+ - ih_\times = \frac{M}{\mathcal{R}} \sum_{l=2}^{\infty} \sum_{m=-l}^{m=l} Y_{-2}^{lm} h_{lm}, \quad (2.66)$$

where Y_{-2}^{lm} are the spin weighted spherical harmonics, and h_+ and h_\times are the two orthogonal gravitational wave polarizations. These waveform multipoles depend on

the coordinates and their conjugate momenta, and their Taylor expansions were re-summed as products of individually re-summed factors [63],

$$h_{lm} = h_{lm}^F N_{lm}, \quad (2.67a)$$

$$h_{lm}^F = h_{lm}^{(N,\epsilon)} \hat{S}_{\text{eff}}^{(\epsilon)} T_{lm} e^{i\delta_{lm}} (\rho_{lm})^l; \quad (2.67b)$$

where ϵ is 0 if $(l + m)$ is even, and is 1 otherwise. This factorized-re-summation of the waveform multipoles ensures agreement with NR waveform multipoles [56, 57, 55]. The first factor $h_{lm}^{(N,\epsilon)}$ is the re-summation of the Newtonian order contribution and the second factor $\hat{S}_{\text{eff}}^{(\epsilon)}$ is the source term, given by the mass or the current moments of the binary in the EOB formalism [63, 64]. The tail term T_{lm} is the re-summation of the leading order logarithmic terms that enter into the transfer function of the near-zone multipolar waves to the far-zone [64]. The last term N_{lm} attempts to capture the non-circularity of the quasi-circular orbits. While calculating the energy flux in this study we follow exactly the prescription of Ref. [38], which calibrates the coefficients of the flux so that resulting EOB waveform multipoles reproduce their NR counterparts with high accuracy.

We use the EOBNRv2 Hamiltonian and flux in the equations of motion for the binary, given by

$$\frac{dr}{d\hat{t}} \equiv \frac{\partial \hat{H}^{\text{real}}}{\partial p_r} = \frac{A(r)}{\sqrt{D(r)}} \frac{\partial \hat{H}^{\text{real}}}{\partial p_{r*}}(r, p_{r*}, p_\Phi), \quad (2.68a)$$

$$\frac{d\Phi}{d\hat{t}} \equiv \hat{\Omega} = \frac{\partial \hat{H}^{\text{real}}}{\partial p_\Phi}(r, p_{r*}, p_\Phi), \quad (2.68b)$$

$$\frac{dp_{r*}}{d\hat{t}} = -\frac{A(r)}{\sqrt{D(r)}} \frac{\partial \hat{H}^{\text{real}}}{\partial r}(r, p_{r*}, p_\Phi), \quad (2.68c)$$

$$\frac{dp_\Phi}{d\hat{t}} = \hat{F}_\Phi(r, p_{r*}, p_\Phi); \quad (2.68d)$$

where, $\hat{t} (\equiv t/M)$ is time in dimensionless units.

To obtain the initial values of the coordinates $(r, \Phi, p_{r*}, p_\Phi)$ that the system starts out in, we use the conditions for motion on spherical orbits derived in Ref.[65], where they treat the case of a generic precessing binary. We take their non-spinning limit

to define the initial configuration of the binary, requiring

$$\frac{\partial \hat{H}^{\text{real}}}{\partial r} = 0, \quad (2.69\text{a})$$

$$\frac{\partial \hat{H}^{\text{real}}}{\partial p_{r_*}} = \frac{1}{\eta} \frac{dE}{dt} \frac{(\partial^2 \hat{H}^{\text{real}} / \partial r \partial p_\Phi)}{(\partial \hat{H}^{\text{real}} / \partial p_\Phi)(\partial^2 \hat{H}^{\text{real}} / \partial r^2)}, \quad (2.69\text{b})$$

$$\frac{\partial \hat{H}^{\text{real}}}{\partial p_\Phi} = \hat{\Omega}_0, \quad (2.69\text{c})$$

where $\hat{\Omega}_0 = \pi M f_0$, with f_0 being the starting gravitational wave frequency. Simplifying Eq.(2.69a), and ignoring the terms involving p_{r_*} , as $p_{r_*} \ll p_\Phi/r$ in the early inspiral, we get a relation between p_Φ and r :

$$p_\Phi^2 = \frac{r^3 A'(r)}{2A(r) - rA'(r)}, \quad (2.70)$$

where the prime(') denotes $\partial/\partial r$. Substituting this in Eq.(2.69c), we get the relation:

$$\frac{A'(r)}{2r \left(1 + 2\eta \left(\frac{A(r)}{\sqrt{A(r) - \frac{1}{2}r A'(r)}} - 1 \right) \right)} = \hat{\Omega}_0^2. \quad (2.71)$$

Thus, between Eq.(2.71) and Eq.(2.70), we get the initial values of (r, p_Φ) , corresponding to the initial gravitational wave frequency f_0 , and by substituting these into Eq. 2.69b, we obtain the initial value of p_{r_*} . With these values, we integrate the equations of motion to obtain the evolution of the coordinates and momenta $(r(t), \Phi(t), p_r(t), p_\Phi(t))$ over the course of inspiral, until the light-ring is reached. In the EOB model, the light-ring is defined as the local maximum of the orbital frequency $\hat{\Omega}$. From the coordinate evolution, we also calculate $h_{lm}^F(t)$, which is the analytic expression for the waveform multipole without the non-quasi-circular correction factor (defined in Eq. (2.67b)). While generating $h_{lm}^F(t)$ from the dynamics, the values for the free parameters in the expressions for δ_{lm} and ρ_{lm} , are taken from Eqn.[38a-39b] of Ref. [38], where they optimize these parameters to minimize the phase and amplitude discrepancy between the respective EOB waveform multipoles and those extracted from NR simulations.

The EOB ringdown waveform is modeled as a sum of N quasi-normal-modes

(QNMs) [56, 57, 59, 66]

$$h_{lm}^{\text{RD}}(t) = \sum_{n=0}^{N-1} A_{lmn} e^{-i\sigma_{lmn}(t-t_{lm}^{\text{match}})}, \quad (2.72)$$

where $N = 8$ for the model we consider. The matching time t_{lm}^{match} is the time at which the inspiral-plunge and the ringdown waveforms are attached and is chosen to be the time at which the amplitude of the inspiral-plunge part of $h_{lm}(t)$ peaks (i.e. t_{peak}^{lm}) [56, 38]. The complex frequencies of the modes σ_{lmn} depend on the mass M_f and spin a_f of the BH that is formed from the coalescence of the binary. We use the relations of Ref. [38], given by

$$\frac{M_f}{M} = 1 + \left(\sqrt{\frac{8}{9}} - 1 \right) \eta - 0.4333\eta^2 - 0.4392\eta^3, \quad (2.73a)$$

$$\frac{a_f}{M} = \sqrt{12}\eta - 3.871\eta^2 + 4.028\eta^3. \quad (2.73b)$$

Using the mass and spin of the final BH, the complex frequencies of the QNMs can be obtained from Ref. [66], where these were calculated using perturbation theory. The complex amplitudes A_{lmn} are determined by a hybrid-comb numerical matching procedure described in detail in Sec.II C of Ref. [38].

Finally, we combine the inspiral waveform multipole $h_{lm}(t)$ and the ringdown waveform $h^{\text{RD}}(t)$ to obtain the complete inspiral-merger-ringdown EOB waveform $h^{\text{IMR}}(t)$,

$$h_{lm}^{\text{IMR}}(t) = h_{lm}(t)\Theta(t_{lm}^{\text{match}} - t) + h^{\text{RD}}(t)\Theta(t - t_{lm}^{\text{match}}), \quad (2.74)$$

where $\Theta(x) = 1$ for $x \geq 0$, and 0 otherwise. These multipoles are combined to give the two orthogonal polarizations of the gravitational waveform, h_+ and h_\times ,

$$h_+ - i h_\times = \frac{M}{\mathcal{R}} \sum_l \sum_m Y_{-2}^{lm}(\iota, \theta_c) h_{lm}^{\text{IMR}}, \quad (2.75)$$

where ι is the inclination angle that the binary's angular momentum makes with the line of sight, and θ_c is a fiducial phase angle. To ensure the correctness of our results, we wrote independent code to implement the EOBNRv2 waveform based solely on the content of Ref. [38]. We then validated our code against the EOBNRv2

waveform algorithm in the LSC Algorithm Library (LAL) [67]. We find agreement between these two implementations, giving us confidence in both our results and the correctness of the LAL EOBNRv2 code.

Chapter 3

Introduction to LIGO

The previous chapter elucidated how matter and momenta can affect the spacetime to curve around it, and how waves of this curvature propagate outwards from the matter source itself. Although several methods of detection of gravitational waves have been proposed, we focus here on that behind the LIGO detectors as well as the Virgo, GEO and proposed KAGRA and LIGO-India detectors. We provide a brief description of the interferometric detectors here, and refer the reader to the classic treatise by Saulson [9] for a much more comprehensive study.

3.1 Design of LIGO

Interferometric detectors like LIGO comprise of two laser cavities oriented orthogonal to each other. The end mirrors of each cavity are free to move horizontally, i.e. locally parallel to the surface of the Earth. In this restricted direction and for small fluctuations, they are *freely-falling* masses and the distance between them is the length of the cavity, the latter being strongly coupled to the amount of power stored in the cavities. Therefore, the interferometer converts the polarizations of incoming gravitational radiation to change in the difference in length of two laser cavities, which is converted into fluctuations in the laser power stored in them.

Let us consider the schematic in Fig. ???. The laser source is depicted as a rectangle on the most left. The light from it travels through the *power recycling mirror* (PRM) and reaches the *beam splitter* (BS). The power recycling mirror reflects back the light that leaks out of the cavities in the arms, and in this sense *recycles* the lost laser

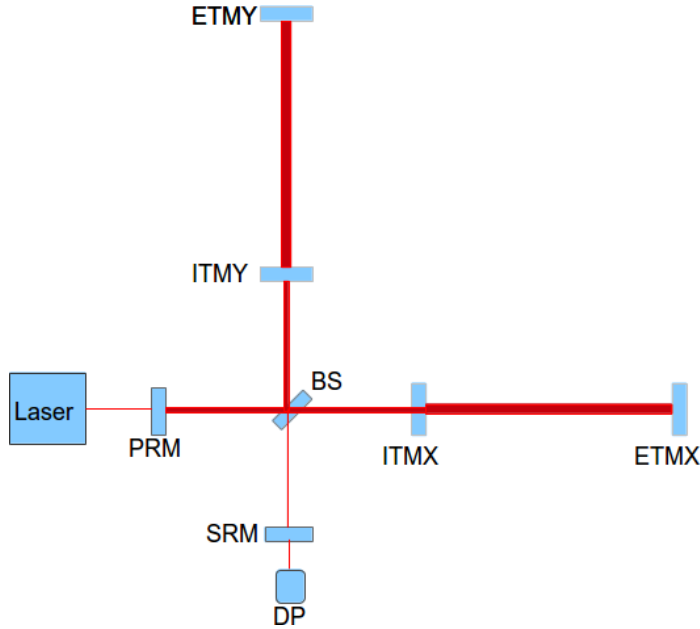


Figure 1: Schematic of interferometric detectors, like LIGO.

power. The beam splitter splits the main beam into two beams, one that travels along the x arm and the other along the y arm. Along the x arm, the *end test-mass mirror* (ETM-X) and the *inner test-mass mirror* (ITM-X) form a resonant laser cavity. Similarly for the y arm. The beams that finally come out of the the two cavities interfere at the beam splitter and the interference pattern is recorded at the *dark port* photodiode. This is called so because the two cavities are aligned in a way which ensures that the beam coming out of the x arm interferes destructively at the BS with that coming out of the y arm, and hence in the absence of gravitational waves the port recording the interference pattern will be dark¹. Finally, a new addition to the Advanced LIGO optics topology is the *signal recycling* (SR) mirror. It sends the signal coming out the dark port back into the arm cavities. The optical system composed of the SR cavity and the arm cavities forms a composite resonant cavity, whose resonances and quality factors can be controlled by the position and reactivity of the SR mirror. Near its resonances, the detector can gain sensitivity. In what follows we discuss the effect of gravitational radiation on interferometric detectors,

¹If the alignment was exactly on a dark fringe then any change in the arm lengths would only increase the light at the dark port, and we would be unable to determine the direction in which the test-mass mirrors were moving. Therefore, the actual alignment is slightly off the dark fringe

and some of the design choices involved.

Let us consider a $+$ -polarized gravitational wave propagating in the z -direction. We can write down the spacetime metric in the TT gauge at the location of the detector, implicitly, as

$$ds^2 = -dt^2 + (1 + h_+)dx^2 + (1 - h_+)dy^2 + dz^2, \quad (3.1)$$

following the discussion in Sec. 2.2. The LIGO cavity length is such that it ensures that the time taken by light to travel back and forth in it is much smaller compared to the time scale of variations in h_+ . Therefore, the time taken by light to make a round-trip between the end test masses in the x cavity

$$t_x \simeq 2L_x(1 - \frac{1}{2}h_+), \quad (3.2)$$

where L_x is the equilibrium length of the x cavity in absence of gravitational waves. Here, we have expanded $\sqrt{1 + h_+}$ as a Taylor series and approximated to by keeping terms up to linear order. It follows that the light travel time for a round trip in the y cavity is

$$t_y \simeq 2L_y(1 - \frac{1}{2}h_+). \quad (3.3)$$

As the two cavities share the laser source, the same light wavefront will return at the beam splitter at different delays in the x than the y cavity. Therefore, the change in the phase of the returning light would manifest as a phase difference $\delta\phi$ given by

$$\begin{aligned} \delta\phi &= \Omega_L(t_x - t_y), \\ &= 2L\Omega_L h_+ = \frac{4\pi L}{\lambda_L} h_+, \end{aligned} \quad (3.4)$$

where Ω_L (λ_L) is the frequency (wavelength) of the laser light, and we have assumed that $L_x = L_y$ and replaced them with L .

The measurable change in phase $\delta\phi$ is directly proportional to the length of the cavities, or the *arms* of the detector. As we are aiming to observe gravitational wave signals from astrophysical sources, which are far enough that the incident signal is expected to be very weak, this motivates that the two arms be made as long as possible before practical considerations become prohibitive. In each arm, the end and

inner test-mass mirrors, $ETM\{X, Y\}$ and $ITM\{X, Y\}$, form a resonant *Fabry-Perot* cavity. The end mirrors are highly polished and stabilized in order to maximize their reflectivity. The laser light forms a standing wave in these cavities, and accumulates power. Therefore, each wavefront bounces back and forth several times before exiting the cavity and interfering at the beam splitter. The net benefit is similar to increasing the effective length of each arm L by a factor of ~ 200 (for LIGO). In addition to the layout in Fig. ??, there are a number of optical, electronic, mechanical, and electromagnetic sub-systems of LIGO detectors that aim to maximize the sensitivity and efficiency of the detectors. A treatment of their details is out of the scope of this dissertation, and we refer the reader to [68, 25] for a more technical overview.

3.2 Dominant Noise Sources

We define the strain signal, s , to be the relative change in the length of the two arms of the interferometer

$$s(t) = \frac{\Delta L_x - \Delta L_y}{L}. \quad (3.5)$$

The signal $s(t)$ can be written as the sum of two components, (i) the actual differential arm length change induced by the incident gravitational wave $h(t)$ (if present), and (ii) the sum of various noises, $n(t)$, that affect the measurement of the difference in the arm lengths ΔL . As the goal of LIGO is to measure remarkably small length changes, several sources of noise that propagate to the measurement of $s(t)$ become consequential. A few intrinsic to the instrument include the brownian motion noise in mechanical systems, lossy optics, cross-talk in electromagnetic systems, noise in control electronics, etc. Additionally, there are noise sources in the environment of the detectors, such as wind and ground motion, fluctuations in the Newtonian gravity due to changes in atmosphere or ground density, electric coupling from nearby power lines etc. It is therefore a challenging task to categorize these sources and reduce the noise to the best extent possible.

Gravitational wave searches in LIGO data are affected by the *power spectral density* of all the noise sources combined. The fundamental noise sources that limit the sensitivity of the interferometer in different frequency ranges are:

1. Seismic noise: The motion of the ground, whether it be due to earthquakes

or due to human activity, couples mechanically to the suspended test masses. This coupling leads to fluctuation in the vertical and horizontal position of the suspended test masses at the end of each arm. The suspension of mirrors as pendula acts as a low pass filter for seismic motion. There are active systems in place as well that sense ground motion and feed the information back to cancel its effect. Seismic noise affects the sensitivity of the detectors at frequencies < 40 Hz.

2. (Suspension) thermal noise: Each degree of freedom has an expected energy that depends on the temperature, leading to thermal noise in the observations related to that degree of freedom. The leading source of thermal noise is the molecular Brownian motion in the mirror suspension wires, and in the surface of the mirror. Thermal noise is a low frequency noise that falls off inversely with frequency. It dominates the detector sensitivity in the range $\sim 40 - 150$ Hz.
3. Photon shot noise: During operation, the interferometer is locked with the optical fields from the two arms interfering destructively at the beam splitter, or in other words at a *dark fringe*. The number of photons that arrive at the readout will be directly proportional to the gravitational wave signal causing the arms to elongate or contract. The arrival times of the photons follows Poissonian statistics. Therefore the counting of the number of photons that arrive in a given interval of time, \mathcal{N} will have an inherent uncertainty proportional to $\sqrt{\mathcal{N}}$. However, the *signal* contained in the laser light increases with \mathcal{N} , allowing for the signal-to-noise ratio to decrease as $1/\sqrt{\mathcal{N}}$. In frequency domain, the shot noise has a flat (or *white*) spectrum. However, the arms of the interferometer act as a filter and amplify the effect of the shot noise on our ability to measure the incident gravitational wave with increasing frequency. As a result, this noise source dominates over all others at $f \gtrsim 1$ kHz.

We refer the reader to the classic book by Saulson [9] for a detailed treatment of these noise sources, which is out of scope of this dissertation.

Apart from these continuous noise sources, there is another class of noise that plagues our ability to systematically extract signals embedded in detector data called *glitches*. Glitches are transient by definition, and have a variety of frequency spectrum and sources. More importantly, if not correctly identified with their cause, they could

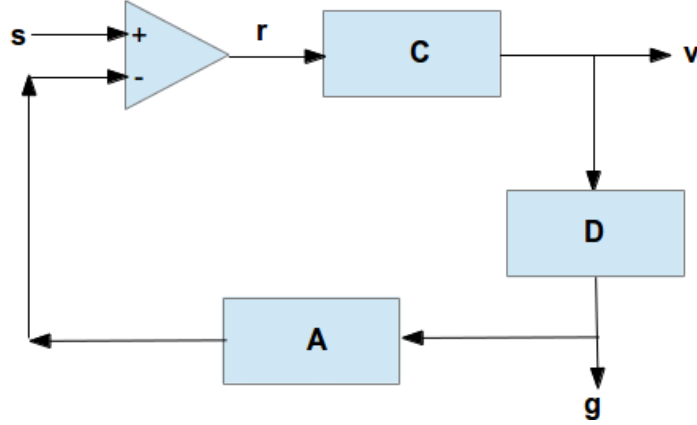


Figure 2: Model for the control loop of the LIGO length sensing and control system.

be unpredictable. For instance, the falling of a heavy object could shake optics and lead to a sharp rise in the noise level in the differential arm length output. There are mechanisms being developed to identify and classify glitches in Advanced LIGO and Virgo, within the Detector characterization group. There are also algorithms in place that allow search methods to differentiate between signals and glitches based on their frequency spectrum and evolution.

3.3 Calibration of LIGO

The signal recorded at the output port $v(t)$ is proportional to the effect of the differential motion of the mirrors in the two arms of the interferometer. This signal is itself used in a control loop to further stabilize the free-falling masses by actuating on them. Therefore the effect of the gravitational waves alone, $s(t)$ has to be decoded from $v(t)$ by understanding this control loop.

Let us model this length sensing control loop as in Fig. ???. All the blocks symbolize the transfer function of a particular logical block, which is the ratio of its output to its input. All quantities hereafter will be in frequency domain, while the transfer functions themselves could be slowly varying in time as well. Block C denotes the length sensing function. It measures the response of the arm cavities to gravitational waves. Block D converts the output of block C , i.e. the fluctuation in the differential arm length into a control signal that is sent to block A . Block A is the *actuation* function that reacts to the control signal and actuates upon the suspended masses in

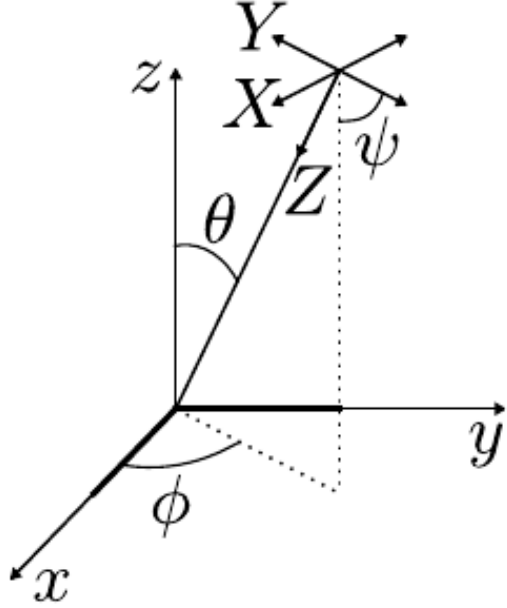


Figure 3: The Euler angles $\{\theta, \phi, \psi\}$ to go from the gravitational wave propagation frame to the detector frame.

a way so as to stabilize them.

We calculate the transfer function G between the readout and the actual gravitational wave signal as

$$\begin{aligned} v &= C r; \quad g = D v = C D r; \quad r = s - A g = s - C D A r, \\ \Rightarrow G &:= \frac{s}{v} = \frac{1 + C D A}{C}. \end{aligned} \tag{3.6}$$

The process of calibrating interferometer data therefore involves measuring the aforementioned transfer functions to high accuracy and using them to obtain the final data channel containing the possible gravitational wave signal.

3.4 Detector response to Gravitational wave polarizations

We start with defining the radiation frame which has its $x - y$ plane in the plane of the sky if one is looking towards the source. The line connecting the source and the detector defines its z -axis. Therefore we can determine the polar angles (θ, ϕ) that point correspond to the z -axis of the radiation frame. Finally, we denote the

angle between the x -axis of the radiation frame and the plane made by joining the x -arm of the detector and the z -axis of the radiation frame. The detector frame is intuitively defined by defining the x and y axes along the two arms with the z -axis coming out of the plane of the detector on Earth.

It can be shown that the polarization amplitudes in the radiation frame depend on the *inclination* angle ι between the orbital (or total) angular momentum of the binary and the line of sight from the detector to the source as [69]

$$h_+ = \frac{1}{2}(1 + \cos^2 \iota) h_0 \cos \Phi(t); \quad h_\times = \cos \iota h_0 \sin \Phi(t). \quad (3.7)$$

h_0 is an overall amplitude that varies slowly in time compared to the instantaneous gravitational wave phase $\Phi(t)$. In the radiation frame the tensorial metric perturbation can be written as (bold fonts indicate tensors or vectors with indices suppressed)

$$\mathbf{h} = h_+ \mathbf{e}_+ + h_\times \mathbf{e}_\times \quad (3.8)$$

where the basis tensors are defined as

$$\mathbf{e}_+ := \mathbf{e}_x^R \otimes \mathbf{e}_x^R - \mathbf{e}_y^R \otimes \mathbf{e}_y^R; \quad \mathbf{e}_\times := \mathbf{e}_x^R \otimes \mathbf{e}_y^R + \mathbf{e}_y^R \otimes \mathbf{e}_x^R, \quad (3.9)$$

with \mathbf{e}_x^R and \mathbf{e}_y^R being unit vectors along the x and y axes of the radiation frame. Next we define the *detector tensor*, which can be thought of as the projection tensor for the detector, as

$$\mathbf{d} := L(\mathbf{e}_x^D \otimes \mathbf{e}_x^D - \mathbf{e}_y^D \otimes \mathbf{e}_y^D), \quad (3.10)$$

where \mathbf{e}_x^D and \mathbf{e}_y^D are unit vectors along the x and y axes of the detector frame, and they point along the direction of the arms from the central beam splitter. L is the length of each arm of the interferometer. The change in length of the arms $\delta L(t)$ can therefore be obtained as the scalar product between the \mathbf{h} tensor and the detector tensor, i.e.

$$\delta L(t) = \mathbf{d} \cdot \mathbf{h} := d_{ij} h^{ij} \quad (3.11)$$

This allows the strain produced in the arms to be written as

$$h(t) := \frac{\delta L}{L} = F_+(\theta, \phi, \psi) h_+ + F_\times(\theta, \phi, \psi) h_\times, \quad (3.12)$$

where the functions F_+ and F_\times can be found using the geometry in Fig. ?? as the scalar product of the basis tensors \mathbf{e}_+ and \mathbf{e}_\times with the detector tensor [69],

$$\begin{aligned} F_+ &= \frac{1}{2}(1 + \cos^2 \theta) \cos(2\phi) \cos(2\psi) - \cos(\theta) \sin(2\phi) \sin(2\psi), \\ F_\times &= \frac{1}{2}(1 + \cos^2(\theta)) \cos(2\phi) \sin(2\psi) + \cos(\theta) \sin(2\phi) \cos(2\psi). \end{aligned} \quad (3.13)$$

These two functions are called the *antenna patterns* of the detector, and they define the response of the detector to incoming gravitational radiation governed purely due to the relative geometry between the source and the detector itself. Finally, collecting Eq. (3.7) and Eq. (3.12) we can write the strain $h(t)$ seen by the detector as

$$h(t) = F_+ h_+ + F_\times h_\times = \mathcal{A} h_0 \cos(\Phi(t) - \Phi_0), \quad (3.14)$$

where $\Phi(t)$ has the same meaning as in Eq. (3.7), and

$$\begin{aligned} \mathcal{A} &:= \left(\left(\frac{1}{2} F_+ (1 + \cos^2 \iota) \right)^2 + (F_\times \cos \iota)^2 \right)^{1/2}, \\ \Phi_0 &:= \tan^{-1} \left(\frac{2F_\times \cos \iota}{F_+ (1 + \cos^2 \iota)} \right), \end{aligned} \quad (3.15)$$

are combinations of the antenna patterns and the inclination angle folded into a constant amplitude and phase change.

Chapter 4

Search template banks for low-mass binary black holes in the Advanced gravitational-wave detector era

Upgrades to the LIGO and Virgo observatories are underway [25, 26], with first observation runs planned for 2015 [27]. The construction of the Japanese detector KAGRA has also begun [70]. The advanced detectors will be sensitive to gravitational waves at frequencies down to $\sim 10\text{Hz}$, with an order of magnitude increase in sensitivity across the band. This is a significant improvement over the lower cutoff of 40Hz for initial LIGO. Estimates for the expected rate of detection have been placed between 0.4 – 1000 stellar-mass binary black hole (BBH) mergers a year [28]. The uncertainty in these estimates comes from the uncertainties in the various factors that govern the physical processes in the BBH formation channels [71, 72]. In sub-solar metallicity environments, stars (in binaries) are expected to lose relatively less mass to stellar winds and form more massive remnants [73, 74, 75]. Population synthesis studies estimate that sub-solar metallicity environments within the horizon of advanced detectors could increase the detection rates to be as high as a few thousand per year [76, 77]. On the other hand, high recoil momenta during core-collapse and merger during the common-envelope phase of the binary star evolution could also decrease the detection rates drastically [75, 76].

Past searches for BBHs [14, 15, 16, 17, 10] used matched-filtering [78, 79] to search for coalescing compact binaries. These searches divided the BBH mass space into a *low-mass* region with $M = m_1 + m_2 \lesssim 25 M_\odot$ and a *high-mass* region with $M \gtrsim 25 M_\odot$. In this chapter, we focus attention on BBH systems with component masses between $3 M_\odot \lesssim m_1, m_2 \lesssim 25 M_\odot$, which encompasses mass distribution of black hole candidates observed in low-mass X-ray binaries [80]. aLIGO will be able to detect coalescing BBH systems with component masses $m_1 = m_2 = 25 M_\odot$ to a maximum distance of up to ~ 3.6 Gpc. Since we do not know *a priori* the masses of BBHs that gravitational-wave detectors will observe, searches use a *bank* of template waveforms which covers the range of BBH component masses of interest [81, 82]. This technique is sensitive to the accuracy of the waveform templates that are used as filters and the algorithm used to place the template waveforms [83]. An accurate template bank is required as input for matched filter searches in the Fourier domain [79], as well as newer search algorithms such as the singular value decomposition [84].

In this chapter, we investigate three items of importance to advanced-detector BBH searches: First, we study the accuracy of template placement algorithms for BBH searches using EOBNRv2 waveforms. Optimal template placement requires a metric for creating a grid of waveforms in the desired region of parameter space [85], however no analytic metric exists for the EOBNRv2 waveform. In the absence of such a metric, we construct a template bank using the post-Newtonian hexagonal placement algorithm [86, 87, 88, 89] accurate to first and half order. This metric is used to place template grid points for the aLIGO zero-detuning high power sensitivity curve [90] and we use EOBNRv2 waveforms at these points as search templates. We find that the existing algorithm works well for BBHs with component masses in the range $3M_\odot \leq m_1, m_2 \leq 25 M_\odot$. For a template bank constructed with a minimal match of 97% less than 1.5% of non-spinning BBH signals have a mismatch greater than 3%. We therefore conclude that the existing bank placement algorithm is sufficiently accurate for non-spinning BBH searches in this mass region. Second, we investigate the mass range in which the (computationally less expensive) third-and-a-half-order TaylorF2 post-Newtonian waveforms [81, 91, 92, 93, 94, 95, 96, 97, 98, 99] can be used without significant loss in event rate, and where full inspiral-merger-ringdown EOBNRv2 waveforms are required. We construct a TaylorF2 template bank designed to lose no more than 3% of the matched filter signal-to-noise ratio and

use the EOBNRv2 model as signal waveforms. We find that for non-spinning BBHs with $M \lesssim 11.4 M_{\odot}$, the TaylorF2 search performs as expected, with a loss of no more than 10% in the event rate. For higher masses larger event rate losses are observed. A similar study was performed in Ref. [100] using an older version of the EOB model and our results are quantitatively similar. We therefore recommend that this limit is used as the boundary between TaylorF2 and EOBNRv2 waveforms in Advanced LIGO searches. Finally, we investigate the effect of modes other than the dominant $l = m = 2$ mode on BBH searches in aLIGO. The horizon distance of aLIGO (and hence the event rate) is computed considering only the dominant mode of the emitted gravitational waves, since current searches only filter for this mode [28]. However, the inclusion of sub-dominant modes in gravitational-wave template could increase the reach of aLIGO [101, 102]. If we assume that BBH signals are accurately modeled by the EOBNRv2 waveform including the five leading modes, we find that for systems with $(m_1/m_2) \leq 1.68$ or inclination angle: $\iota \geq 2.68$ or $\iota \leq 0.31$ radians, there is no significant loss in the total possible signal-to-noise ratio due to neglecting modes other than $l = m = 2$ in the template waveforms, if one uses a 97% minimal-match bank placed using the hexagonal bank placement algorithm [86, 87, 88, 89]. However, for systems with mass-ratio $(q) \geq 4$ and $1.08 \leq \iota \leq 2.02$, including higher order modes could increase the signal-to-noise ratio by as much as 8% in aLIGO. This increase in amplitude may be offset by the increase in false alarm rate from implementing searches which also include sub-dominant waveform modes in templates, so we encourage the investigation of such algorithms in real detector data.

The remainder of this chapter is organized as follows: In Sec. 4.1 we review the gravitational waveform models used in this study. In Sec. 4.2 we present the results of large-scale Monte Carlo signal injections to test the effectualness of the template banks under investigation. Finally in Sec. 4.3 we review our findings and reccomendations for future work.

4.1 Waveforms and Template Bank Placement

4.1.1 Waveform Approximants

Previous searches for stellar-mass BBHs with total mass $M \lesssim 25M_{\odot}$ in LIGO and Virgo used the restricted TaylorF2 PN waveforms [81, 91, 92]. Since this waveform is

analytically generated in the frequency domain, it has two computational advantages over the EOBNRv2 model: First, the TaylorF2 model does not require either the numerical solution of coupled ODEs or a Fourier transform to generate the frequency domain signal required by a matched filter. We compared the speed of generating and Fourier transforming EOBNRv2 waveforms, to the speed of generating Taylor F2 waveforms in the frequency domain, and found that the former can be $\mathcal{O}(10^2)$ times slower than the latter. Second, the TaylorF2 model can be implemented trivially as a kernel on Graphics Processing Units, allowing search pipelines to leverage significant speed increases due to the fast floating-point performance of GPU hardware. We found the generation of TaylorF2 waveforms using GPUs to be $\mathcal{O}(10^4)$ times faster than generating and Fourier transforming EOBNRv2 waveforms on CPUs. However, use of the TaylorF2 waveform may result in a loss in search efficiency due to inaccuracies of the PN approximation for BBHs. To investigate the loss in search efficiency versus computational efficiency, we use restricted TaylorF2 and EOBNRv2 waveform models which are described in Appendix A.1.4 and Sec. 2.5.3, respectively.

4.1.2 Bank Placement metric

The frequency weighted overlap between two waveforms h_1 and h_2 , can be written as

$$(h_1|h_2) \equiv 2 \int_{f_{\min}}^{f_{\text{Ny}}} \frac{\tilde{h}_1^*(f)\tilde{h}_2(f) + \tilde{h}_1(f)\tilde{h}_2^*(f)}{S_n(f)} df, \quad (4.1)$$

where $S_n(f)$ is the one-sided power spectral density (PSD) of the detector noise; f_{\min} is the lower frequency cutoff for filtering; f_{Ny} is the Nyquist frequency corresponding to the waveform sampling rate; and $\tilde{h}(f)$ denotes the Fourier transform of $h(t)$. The normalized overlap between the two waveforms is given by

$$(\hat{h}_1|\hat{h}_2) = \frac{(h_1|h_2)}{\sqrt{(h_1|h_1)(h_2|h_2)}}. \quad (4.2)$$

In addition to the two mass-parameters of the binary, this normalized overlap is also sensitive to the relative phase of coalescence ϕ_c and to the difference in the time of coalescence between the two waveforms h_1 and h_2 , t_c . These two parameters (ϕ_c , t_c)

can be analytically maximized over to get the maximized overlap \mathcal{O}

$$\mathcal{O}(h_1, h_2) = \max_{\phi_c, t_c} \left(\hat{h}_1 | \hat{h}_2 e^{i(2\pi f t_c - \phi_c)} \right), \quad (4.3)$$

which gives a measure of how “close” the two waveforms are in the waveform manifold. The mismatch M between the same two waveforms is written as,

$$M(h_1, h_2) = 1 - \mathcal{O}(h_1, h_2). \quad (4.4)$$

The match (Eq. 5.5) can be regarded as an inner-product on the space of intrinsic template parameters, and thus one can define a *metric* on this space [88, 85] (at the point θ_1) as

$$g_{ij}(\theta_1) = -\frac{1}{2} \left. \frac{\partial^2 \mathcal{O}(h(\theta_1), h(\theta_2))}{\partial \theta_1^i \partial \theta_2^j} \right|_{\theta_1^k = \theta_2^k}, \quad (4.5)$$

where θ_1 is the set of intrinsic parameters (i.e. m_1, m_2 or some combination) of the binary. Thus the mismatch between waveforms produced by systems with nearly equal mass parameters can be given by

$$M(h(\theta), h(\theta + \Delta\theta)) \simeq g_{ij}(\theta) \Delta\theta^i \Delta\theta^j. \quad (4.6)$$

For the TaylorF2 approximant, $h(\theta)$ is given by Eq. (??, ??), and hence using Eq. (4.1, 5.5) we can get $\mathcal{O}(h(\theta_1), h(\theta_2))$ as an analytic function of θ_1 and θ_2 (albeit involving an integral over frequency). This gives a measure of mismatches between neighbouring points in the manifold of the mass-parameters, and hence a hexagonal 2D lattice placement can be used in the manifold of the mass parameters [88] (and references therein), to construct a geometric lattice based template bank [86, 85, 88].

On the other hand, for the EOBNRv2 approximant, $h(\theta)$ is obtained through numerical solutions of the Hamiltonian equations, Eq.(2.68). In this case, the calculation of the metric would involve derivatives of coordinate evolution obtained from numerically integrated equations of motion, which could introduce numerical instabilities in the metric. So the concept of a metric, as in Eq. (4.5)', cannot be used in a convenient (semi-) analytic form for the construction of a bank with the EOBNRv2 approximant.

4.2 Results

To assess the effectualness of the template banks constructed here, we compute the fitting factors [83] of the template bank, defined as follows. If h_a^e is the waveform emitted by a BBH system then the *Fitting Factor* of a bank of template waveforms (modeled using approximant X) for this waveform, is defined as the maximum value of maximized normalized overlaps between h_a^e and all members h_b^X of the bank of template waveforms [83]; i.e.

$$\mathcal{FF}(a, X) = \max_{b \in \text{bank}} \mathcal{O}(h_a^e, h_b^X). \quad (4.7)$$

This quantity simultaneously quantifies the loss in recovered signal-to-noise ratio (SNR) due to the discreteness of the bank, and the inaccuracy of the template model. The similarly defined quantity MM (minimal match) quantifies the loss in SNR due to only the discreteness of the bank as both the *exact* and the template waveform is modeled with the same waveform model, i.e.

$$\text{MM} = \min_a \max_{b \in \text{bank}} \mathcal{O}(h_a^X, h_b^X), \quad (4.8)$$

where a is any point in the space covered by the bank, and X is the waveform approximant. For a detection search that aims at less than 10% (15%) loss in event detection rate due to the discreteness of the bank and the inaccuracy of the waveform model, we require a bank of template waveforms that has \mathcal{FF} above 0.965 (0.947) [103, 104, 100]. Throughout, we use the aLIGO zero-detuning high power noise curve as the PSD for bank placement and overlap calculations, and set $f_{\min} = 15$ Hz. The waveforms are generated at a sample rate of 8192 Hz, and we set $f_{\max} = 4096$ Hz, i.e. the Nyquist frequency.

The expectation value of the SNR for a signal, ρ , from a source located at a distance D is proportional to $1/D$, which comes from the dependence of the amplitude on the distance. In other words, the range to which a souce can be seen by the detector

$$D_{\text{obs}} = \frac{(g, g)}{\rho^*}, \quad (4.9)$$

where g is the GW strain produced by the same source at the detector, when located

at a unit distance from the detector, and ρ^* is the threshold on SNR required for detection (typically taken as $\rho^* = 8$). For non-precessing binaries, for which the sky-location (θ, ϕ) and polarization angles (ψ) do not change over the course of inspiral, the effective volume in which the same source can be detected is $\propto D_{\text{obs}}^3$ [105], i.e.

$$V_{\text{obs}} = k D_{\text{obs}}^3, \quad (4.10)$$

where the proportionality constant k comes from averaging over various possible sky positions of the binary. The use of discrete template banks, and lack of knowledge of the *true* GW signal model, leads to the observed SNR ρ' being lower than the optimal SNR $\rho = (h, h)$, i.e.

$$\rho' = \mathcal{FF} \rho, \quad (4.11)$$

where \mathcal{FF} is the fitting-factor of the template bank employed in the search for the particular system. The observable volume hence goes down as

$$V_{\text{obs}}^{\text{eff}} = k (\mathcal{FF} \times D_{\text{obs}})^3. \quad (4.12)$$

If we assume that the source population is distributed uniformly in spacial volume in the universe, then the ratio $V_{\text{obs}}^{\text{eff}}/V_{\text{obs}}$ also gives the fraction of systems within the detector's reach that will be seen by the matched-filtering search. For a system with given mass-parameters θ_1 , the ratio of the total $V_{\text{obs}}^{\text{eff}}$ available to it for different inclinations and sky-locations, to the total V_{obs} available to it for the same samples of angles, will give an estimate of the fraction of systems with those masses (marginalized over other parameters - they being uniformly distributed) that will be seen by the matched-filter search. This quantity,

$$\begin{aligned} \epsilon_V(\theta_1) &= \frac{\sum_{\theta_2} V_{\text{obs}}^{\text{eff}}(\theta_1, \theta_2)}{\sum_{\theta_2} V_{\text{obs}}(\theta_1, \theta_2)}, \\ &= \frac{\sum_{\theta_2} \mathcal{FF}^3(\theta_1, \theta_2) V_{\text{obs}}(\theta_1, \theta_2)}{\sum_{\theta_2} V_{\text{obs}}(\theta_1, \theta_2)}, \end{aligned} \quad (4.13)$$

where $\theta_2 = \{\iota, \theta, \phi, \psi\}$ are the parameters being averaged over, we will refer to as the *volume-weighted fitting-factor*. It essentially measures the average of the fractional observable volume loss, weighted by the actual available observable volume, and so simultaneously downweights the loss in the observable volume for binary configurations to which the detector is relatively less sensitive to begin with. We can give the parameter sets θ_1 and θ_2 different elements than the ones shown here, i.e. $\theta_1 \neq \{m_1, m_2\}, \theta_2 \neq \{\iota, \theta, \phi, \psi\}, \theta_1 \cup \theta_2 = \{m_1, m_2, \iota, \theta, \phi, \psi\}$, in order to obtain more information about another set of parameters θ'_1 .

4.2.1 EOBNRv2 templates placed using TaylorF2 metric

In this section we measure the effectualness of the first-and-half-order post-Newtonian hexagonal template bank placement metric described in Ref. [87] when used to place EOBNRv2 waveform templates for aLIGO. The same template placement algorithm was used to place a grid of third-and-a-half order post-Newtonian order TaylorF2 waveforms for low-mass BBH detection searches for initial LIGO and Virgo observations [14, 15, 16, 17, 10]. We construct a template bank which has a desired minimal match of 0.97 for waveforms with component masses between $3M_\odot \leq m_1, m_2 \leq 25M_\odot$. This template bank contains 10,753 template grid points in (m_1, m_2) space for the aLIGO noise curve, compared to 373 grid points for the initial LIGO design noise curve. For the template waveforms at each grid point, we use the EOBNRv2 waveforms, rather than TaylorF2 waveforms. Since the metric itself was derived using the TaylorF2 approximant, we do not, *a priori* know if this metric is a good measure to use to place template banks for EOBNRv2 waveforms.

To test the effectualness of this template bank, we perform a Monte-Carlo simulation over the $3M_\odot \leq m_1, m_2 \leq 25M_\odot$ BBH mass space to find regions where the bank placement algorithm leads to under-coverage. We sample 90,000 points uniformly distributed in individual component masses. For each of these points, we generate an EOBNRv2 waveform for the system with component masses given by the coordinates of the point. We record the \mathcal{FF} of the template bank for each of the randomly generated BBH waveforms in the Monte-Carlo simulation. Since we use EOBNRv2 waveforms both to model the true BBH signals and as matched-filter templates, any departure in fitting factor from unity is due to the placement of the template bank grid.

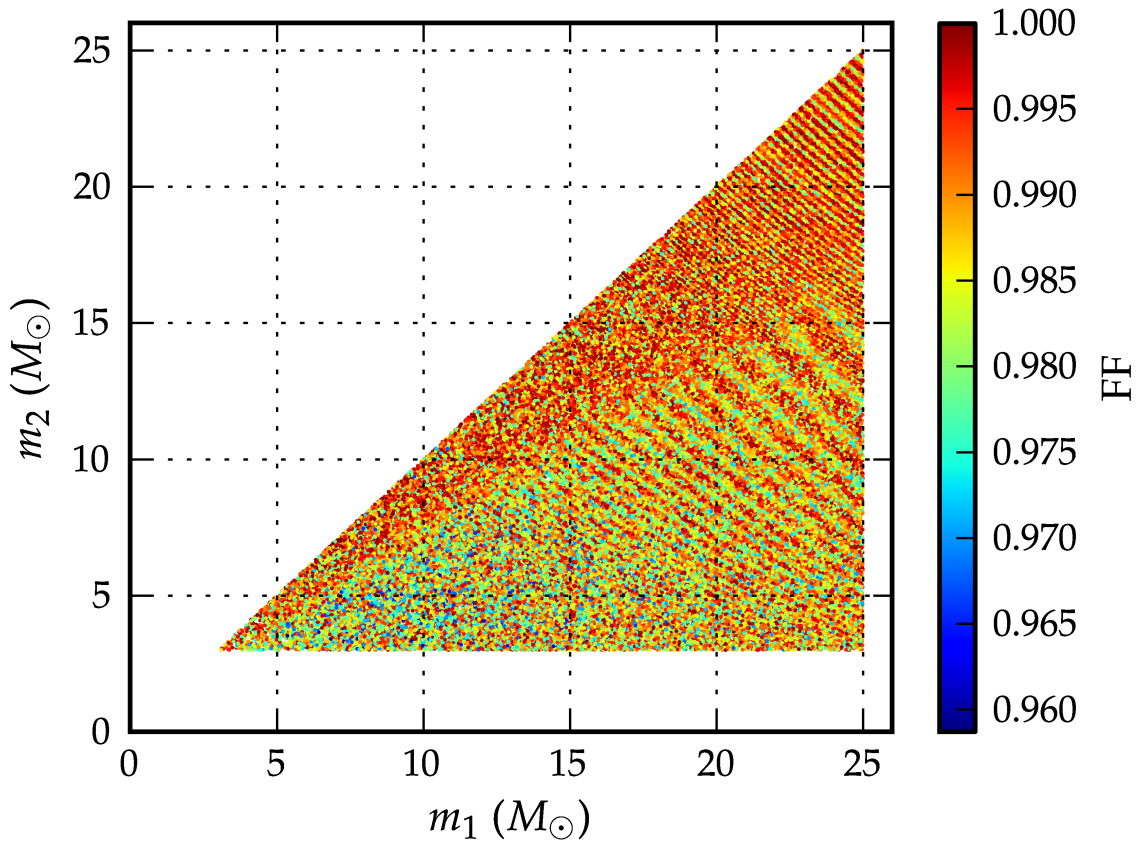


Figure 4: This figure shows the effectualness of a bank of EOBNRv2 templates, placed using the 2PN accurate hexagonal template placement of Ref. [87], to search for a population of BBH signals simulated with EOBNRv2 waveforms. The masses of the BBH population are chosen from a uniform distribution of component masses between 3 and $25 M_{\odot}$. For each injection, we plot the component masses of the injection, and the fitting factor (\mathcal{FF}).

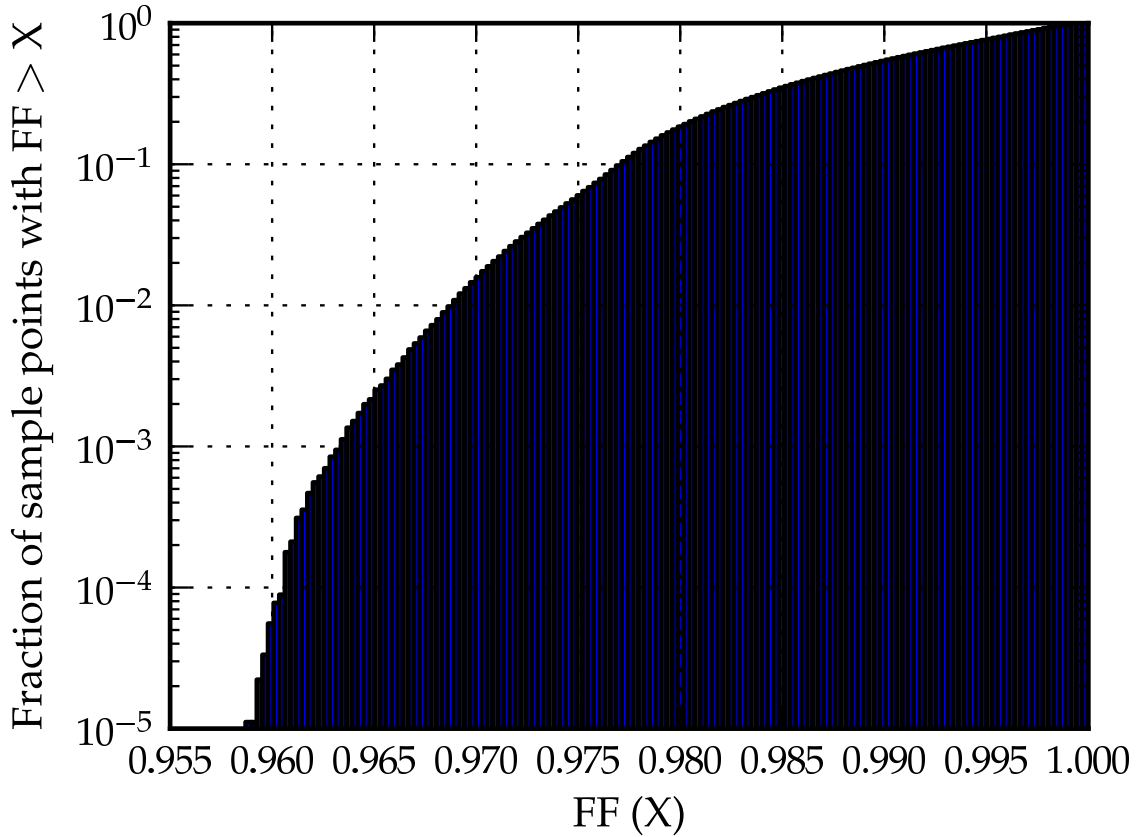


Figure 5: This figure shows a cumulative histogram of the fraction of the BBH signal space (on the y-axis), where the bank of EOBNRv2 waveforms has \mathcal{FF} less than the respective values on the x-axis. The EOBNRv2 bank has a fitting factor \mathcal{FF} below the 0.97 for less than $\sim 1.5\%$ of all simulated signals with component-masses m_1, m_2 between $3 M_\odot$ and $25 M_\odot$.

For a bank of template waveforms constructed with a MM of 0.97, Fig. 4 and Fig. 5 show that the \mathcal{FF} of the bank remains above 0.97 for $\sim 98.5\%$ of all simulated BBH signals. Less than $\sim 1.5\%$ of signals have a minimal match of less than 0.97, with the smallest value over the 90,000 sampled points being ~ 0.96 . The diagonal features observed in Fig. 4 are due to the hexagonal bank placement algorithm and are related to the ellipses of constant chirp mass in Fig. 4 of Ref. [87]. From these results, we conclude that the existing template bank placement metric adequately covers the BBH mass space with EOBNRv2 waveform templates; it is not necessary to construct a metric specific to the EOBNRv2 model. aLIGO detection searches can employ the first-and-half-order post-Newtonian bank placement metric with the hexagonal placement algorithms [88, 86, 87, 85, 89] to place template banks for EOBNRv2 waveforms without a significant drop in the recovered signal-to-noise ratio.

4.2.2 Effectualness of TaylorF2 templates

We next explore the efficiency of using the computationally cheaper TaylorF2 waveforms to search for a population of BBH signals with component masses between $(3\text{--}25)M_{\odot}$. The signals from this population are modeled with the full EOBNRv2 waveforms. We use the same template bank placement as above, however now we use the third-and-a-half PN order TaylorF2 model as the template waveforms. This model does not capture the merger and ringdown of BBH signals, as it is terminated at the Schwarzschild test-particle ISCO. Furthermore, it diverges from the true BBH signal in the late inspiral. It is important to determine when these effects become important.

We sample the $(3\text{--}25)M_{\odot}$ BBH component mass space at 100,000 points by generating an EOBNRv2 waveform to generate the “true” signal waveform. We generate a bank of TaylorF2 template waveforms over the same region, and calculate its \mathcal{FF} for each of the sample points, against the corresponding EOBNRv2 waveform. Fig. 6 shows the distribution of the \mathcal{FF} obtained for the TaylorF2 bank. Clearly the TaylorF2 bank is not effectual for the entire BBH region considered, with mismatches of up to 18% observed. We divide the sampled component mass space into sub-regions which consist of systems with total masses below different thresholds, and compute the minimal-fitting-factor of the bank over those. In Fig. 7, the blue (solid) curve

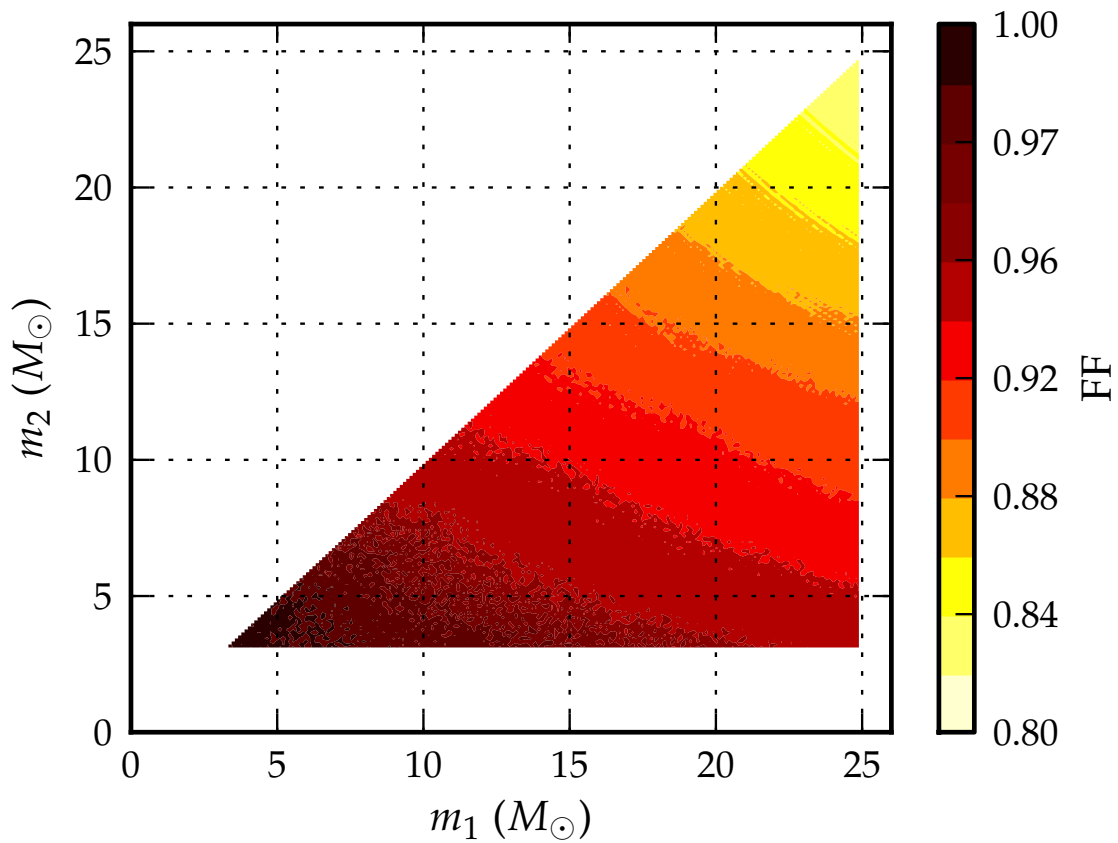


Figure 6: The fitting factor \mathcal{FF} of a bank of TaylorF2 waveforms, constructed with $MM = 0.97$, for a population of BBH systems which are modeled using EOBNRv2 signals.

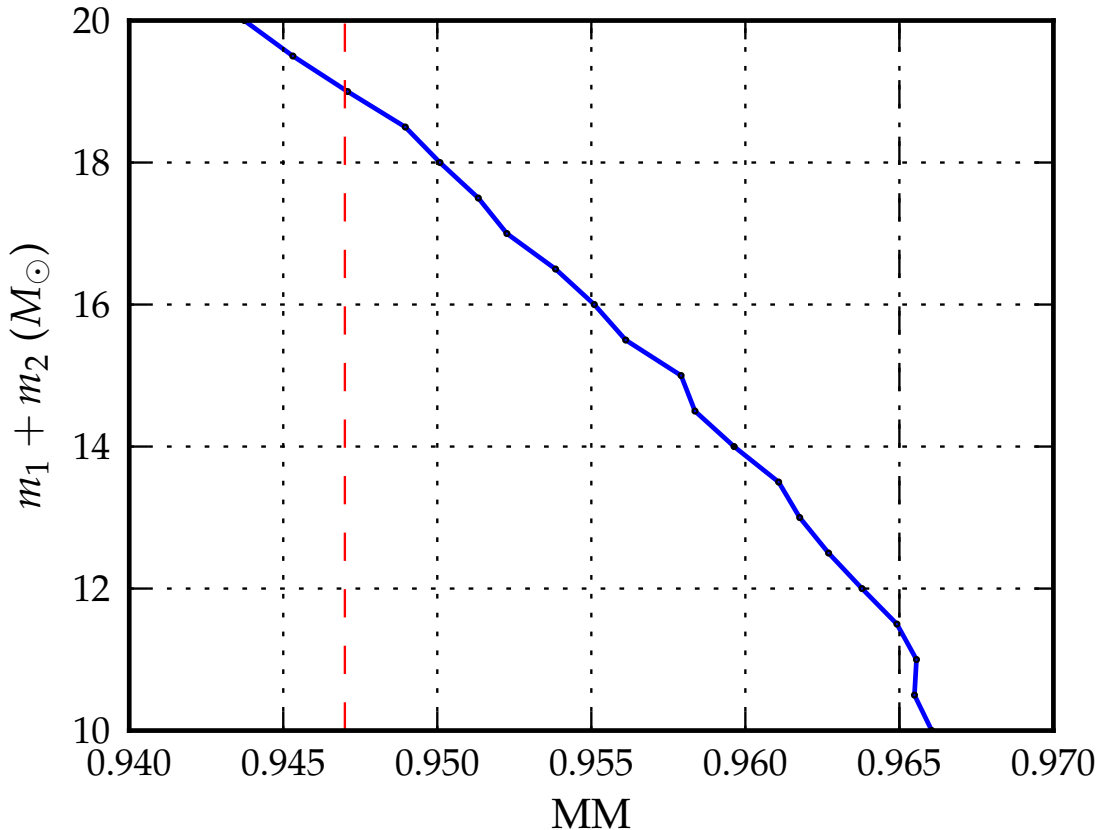


Figure 7: The (blue) curve shows the upper-bound on total-mass for the sub-region over which the TaylorF2 bank has a minimal-fitting-factor as given on the x-axis. We observe that the TaylorF2 bank has a minimal-fitting-factor of 0.965 (0.947) for the region with total masses below $\sim 11.4 M_\odot$ ($19 M_\odot$). The minimal-fitting-factor is the fitting-factor value which is less than the fitting-factors of the TaylorF2 bank for $\geq 99.75\%$ of the points sampled in the sub-region.

shows the upper-limit on total mass for different sub-regions against the minimal-fitting-factor of the TaylorF2 bank over those. The minimal-fitting-factor over a sub-region is taken to be the fitting-factor value which is less than the fitting-factors for $\geq 99.75\%$ of the points sampled in the sub-region. We find that the TaylorF2 template bank has \mathcal{FF} above 0.965 (0.947) for the region with total masses below $11.4M_\odot$ ($19M_\odot$). We conclude that the TaylorF2 bank is effectual for BBH signals below $\sim 11.4M_\odot$.

The value of our limit on total-mass is in agreement with the previous study in Ref. [100], however this analysis used the EOBNRv1 model [106] and an older version of the Advanced LIGO noise curve [100]. This agreement provides confidence that this limit will be robust in aLIGO searches and we propose this limit as the upper cutoff for the computationally cheaper TaylorF2 search. To investigate the loss in the \mathcal{FF} due to the mismatch in the template and signal waveform models, we also performed a Monte-Carlo simulation using a denser TaylorF2 bank with $MM = 0.99$. We found that using this dense bank of third-and-a-half order TaylorF2 waveforms, we can relax the limit on the upper mass to $\sim 16.3M_\odot$ ($21.8M_\odot$) and still achieve a \mathcal{FF} above 0.965 (0.947), for over 99.75% of the signals sampled in the region. However, increasing the minimal match increases the size of the template bank from 10,753 to 29,588 templates. This is a significant increase, compared to the cost of filtering with EOBNRv2 templates.

4.2.3 Effect of sub-dominant modes

Having established that the first-and-half-order post-Newtonian hexagonal template bank is effectual for placing a bank of EOBNRv2 templates, we now investigate the effect of neglecting sub-dominant modes in BBH searches. The sensitivity reach of the aLIGO detectors is normally computed assuming that the search is only sensitive to the dominant $l = m = 2$ mode of the gravitational waveform. For binary black hole signals, sub-dominant modes may contain significant power [102]. A search that includes these modes could, in principle, have an increased reach (and hence event rate) compared to a search that only uses the dominant mode. The EOBNRv2 model of Ref. [38] has been calibrated against higher order modes from numerical relativity simulations. We investigate the effect of ignoring these modes in a search by modeling the BBH signal as an EOBNRv2 signal containing the dominant and sub-dominant

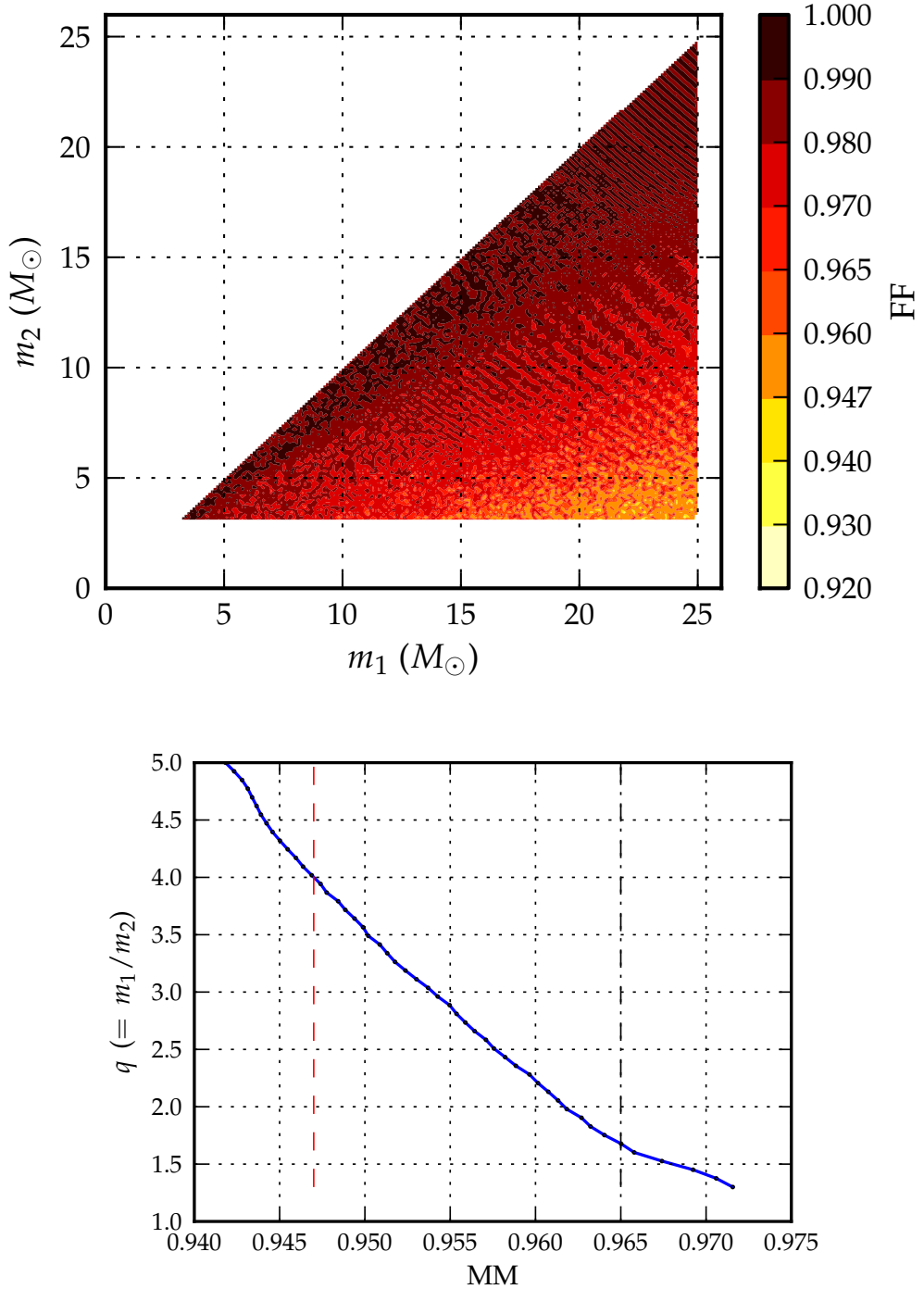


Figure 8: (top) The \mathcal{FF} of a bank of EOBNRv2 waveforms, constructed with a minimal match of 0.97 at each point in the stellar-mass BBH component-mass region. While the templates are modeled as the dominant-mode $l = m = 2$ EOBNRv2 waveforms, the signals are modeled including the sub-dominant waveform modes as well (EOBNRv2HM). (bottom) This figure shows the upper-bound on mass-ratio (q) for the region where a bank of EOBNRv2 templates has a minimal-fitting-factor as given on the x-axis. We observe that for the region with $q \leq 1.68$ (4), the minimum-match of the bank is below 0.965 (0.947). From both the figures, we notice a systematic fall in the coverage of the EOBNRv2 template bank with increasing mass-ratio.

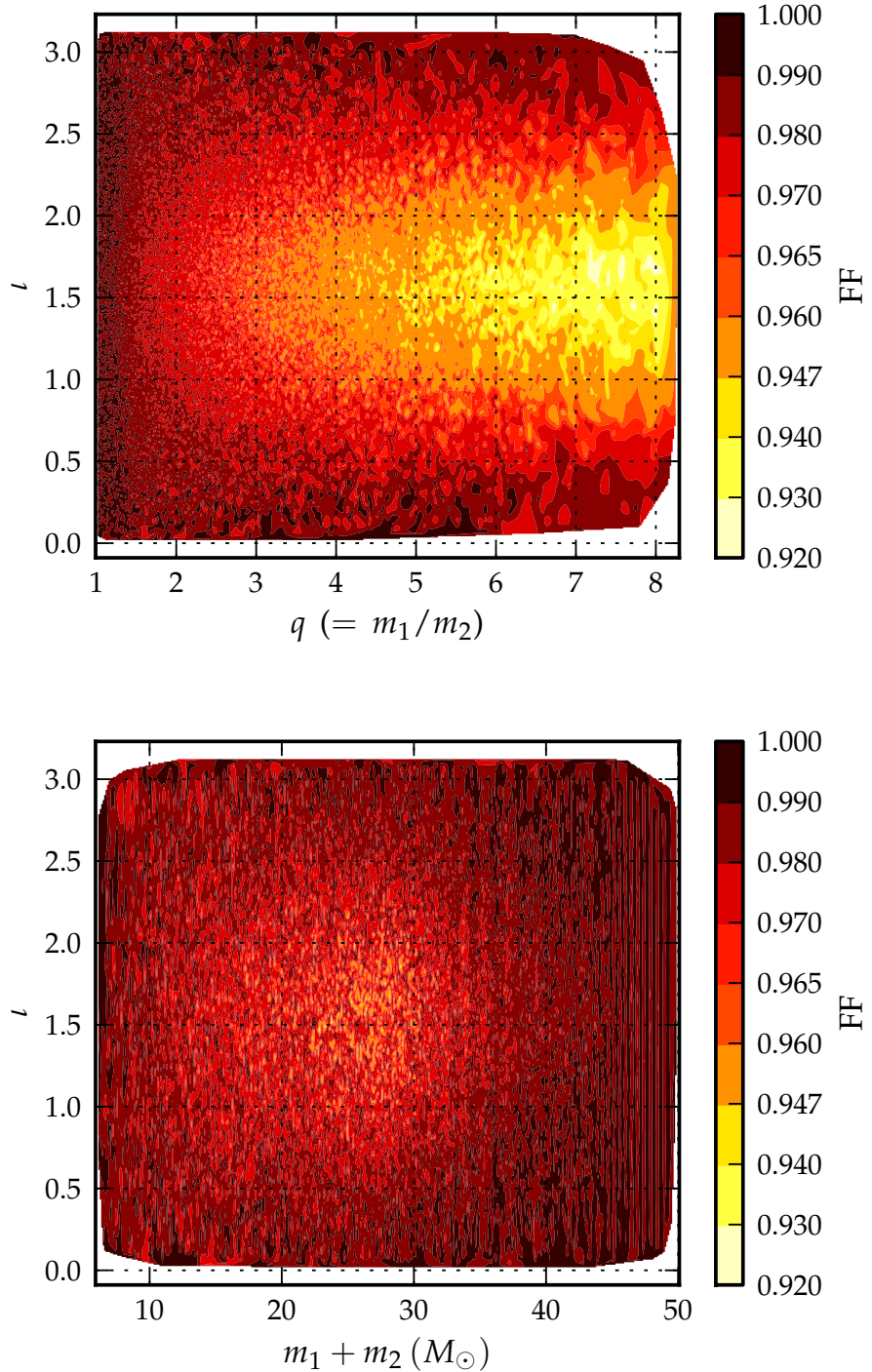


Figure 9: (top) The \mathcal{FF} of a bank of EOBNRv2 waveforms, constructed with a minimal match of 0.97 at each point in the stellar-mass BBH $q - \iota$ space. While the templates are modeled as the dominant-mode $l = m = 2$ EOBNRv2 waveforms, the signals are modeled including the sub-dominant waveform modes as well (EOBNRv2HM). We observe a loss in fitting-factors, upto $\sim 8\%$, for systems with high mass-ratios (q) and inclination angle (ι) close to $\pi/2$. (bottom) The \mathcal{FF} for the same population of signals, now shown on the $M - \iota$ plane. We observe the loss in fitting factors to be relatively lesser for more massive binaries.

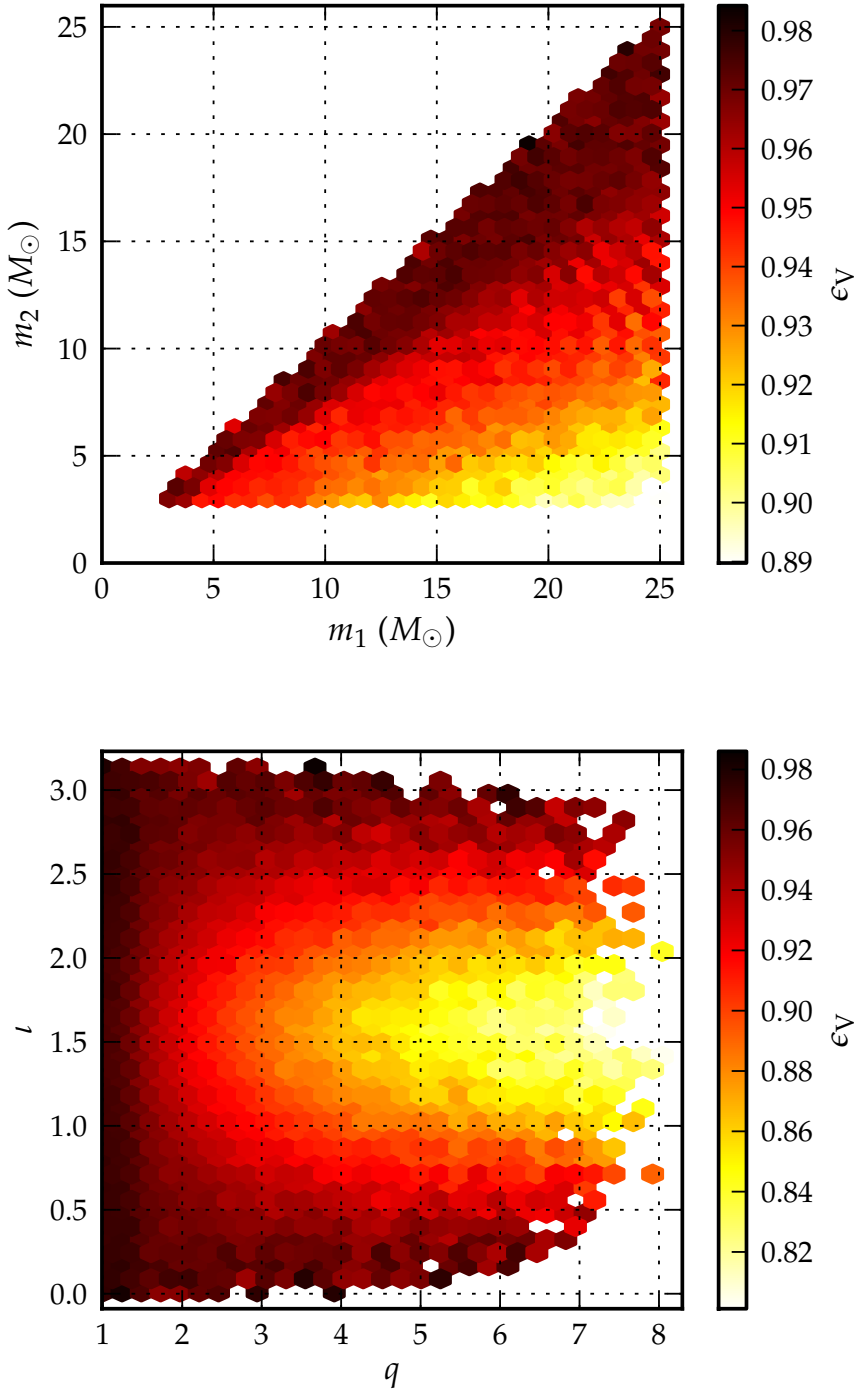


Figure 10: (top) This figure shows $\epsilon_V (\theta_1 = \{m_1, m_2\})$ in the component-mass space (see Eq. 4.13). This gives the fraction of total observable volume that is visible to a search which uses the leading order $l = m = 2$ EOBNRv2 waveform template bank, placed with the 2PN accurate TaylorF2 bank placement metric. For a population of signals, that is distributed uniformly in spacial volume, this is equivalent to the fraction of the maximum possible event observation rate that we get with the use of a discrete bank of matched-filters. We observe that the loss in event observation rate, averaged over all parameters (uniformly distributed) but $\theta_1 = \{m_1, m_2\}$, does not exceed $\sim 11\%$ for any region of the component-mass space. (bottom) This figure shows $\epsilon_V (\theta_1 = \{q, \iota\})$ over the $q - \iota$ plane. We note that the maximum value in the bottom panel is for points with high q and low ι .

multipoles: $h_{lm} = h_{22}, h_{21}, h_{33}, h_{44}, h_{55}$ (which we call EOBNRv2HM) and computing the fitting factor of leading-order EOBNRv2 templates placed using the TaylorF2 metric.

We simulate a population of BBH signals by sampling 100,000 systems uniformly in the $m_1, m_2 \in [3, 25] M_\odot$ component-mass space. These EOBNRv2HM signals are uniformly distributed in sky-location angles and inclination and polarization angles, which appear in the detector's response function to the gravitational-wave signal [107]. The template bank is again placed with a desired minimal match of 0.97 and for each of signal waveforms, we calculate the \mathcal{FF} against the entire bank of EOBNRv2 waveform templates. Fig. 8 (left panel) shows the value of the \mathcal{FF} of the bank of EOBNRv2 waveform templates over the sampled component-mass space. As expected, the highest fitting factors are observed close to the equal mass line, since when the mass ratio is close to unity, the amplitude of the sub-leading waveform modes is several orders of magnitude smaller than the amplitude of the dominant mode. As the mass ratio increases, the relative amplitude of the sub-leading multipoles increases, as illustrated by Fig. 1 of Ref. [38] and the fitting factor decreases. This pattern is brought out further in Fig. 9 (left panel), where we show the \mathcal{FF} values in the mass ratio - inclination angle ($q - \iota$) plane. We observe that when the orbital angular momentum is either parallel or anti-parallel to the line of sight from the detector, the sub-leading multipoles do not contribute significantly to the signal. This is what we would expect from Eq. 2.75, as the spin-weighted harmonics are proportional to $\sin(\frac{\ell}{2})\cos(\frac{\ell}{2})$, except when $l = m = 2$. Similar to Sec. 4.2.2, we divide the sampled component-mass space into sub-regions bounded by $1 \leq q \leq q_{\text{threshold}}$, and compute the minimal-fitting-factor of the EOBNRv2 template bank over those. In Fig. 8 (right panel), the blue (solid) curve shows the value of $q_{\text{threshold}}$ for each restricted sub-region against the minimal-fitting-factor of the bank over the same. For systems with mass-ratio q below 1.68 (4), we find that the \mathcal{FF} of the EOBNRv2 waveform bank is above 0.965 (0.947) over 99.75% of this restricted region. These results demonstrate that the effect of ignoring sub-dominant modes does not cause a significant loss in the total possible signal-to-noise if the mass ratio is less than 1.68. Similar analysis over the range of possible inclination angles shows that the EOBNRv2 waveform bank has fitting factors above 0.965 (0.947) for systems with $2.68 (2.02) \leq \iota \leq \pi$, and $0 \leq \iota \leq 0.31 (1.08)$ (see Fig. 9, left panel).

Fitting factors as low as 0.92 are observed for systems with high mass-ratios *and* inclination angle close to $\pi/2$. As these are also binary configurations to which the detector is relatively less sensitive to [102], fitting-factors alone do not answer the question of where in the parameter space do we lose the most, in terms of detection rate. To address this question, we compute the volume-weighted fitting-factors ϵ_V of the EOBNRv2 template bank, over the sampled BBH parameter space. This gives us an estimate of the expected loss in detection rate, if the source population is distributed uniformly in spacial volume and uniformly in intrinsic and extrinsic source parameters. Fig. 10 (left panel) shows ϵ_V calculated in bins over the component-mass space. In this figure, the color of each bin in the component-mass plane corresponds to, for a population which has all other parameters i.e. the inclination angle and sky/polarization angles uniformly distributed over their possible ranges, the averaged loss in the detection rate incurred due to the use of a bank of leading-order $l = m = 2$ EOBNRv2 templates, placed using the 2PN bank placement metric. We observe that the maximum loss incurred goes up to only $\sim 10\% - 11\%$, which is within our acceptable threshold. Looking at Fig. 9 (left panel), the maximum loss in fitting factor occurs for systems with inclination angles close to $\pi/2$, but (for the same mass-ratio) these gets averaged out with systems with inclinations close to 0 or π , which leads to the low averaged detection-rate losses we observe in Fig. 10 (left panel). The right panel of Fig. 10 shows the same quantity, ϵ_V , calculated over bins in the mass-ratio - inclination angle plane. As expected, we observe that, letting all other parameters be distributed uniformly over their possible ranges, systems with high mass-ratios *and* inclination angles close to $\pi/2$ will incur (averaged) losses in observation volume of up to $\sim 20\%$.

These results suggest that a search that includes higher order modes could achieve a non-trivial increase in sensitivity over leading-order mode templates, only in detecting systems with high q *and* $1.08 \leq \iota \leq 2.02$. However, an algorithm that includes sub-dominant modes could have an increased false-alarm rate (background) over a search that includes only the leading-order mode, and hence the overall gain in search efficiency might not be significant.

4.3 Conclusions

We used the TaylorF2 first-and-half-order post-Newtonian hexagonal placement algorithm from Refs. [88, 87, 89] to construct a template bank of EOBNRv2 waveforms with MM of 0.97. We calculated the fitting factor (\mathcal{FF}) of this bank against $\sim 90,000$ simulated EOBNRv2 signals with component masses uniformly distributed between $3M_{\odot} \leq m_1, m_2 \leq 25M_{\odot}$. We find that the \mathcal{FF} of the template bank is greater than 0.97 for 98.5% of the simulated EOBNRv2 signals, assuming the zero-detuning high power noise spectrum for aLIGO sensitivity [90]. We conclude that the existing placement algorithm is effectual for use in aLIGO BBH searches, assuming that EOBNRv2 is an accurate model of BBH signals in this mass region. We then demonstrated that use of the computationally cheaper third-and-a-half order TaylorF2 waveform results in a loss in search efficiency due to inaccuracies of the post-Newtonian approximation, and neglect of merger-ringdown for BBHs with a total mass $M > 11.4 M_{\odot}$. However, below this limit the TaylorF2 model is an acceptable signal for BBH searches. This was done using a bank with a MM of 0.97. By increasing the density of the bank to 0.99MM, the limit on total-mass can be relaxed to $16.3 M_{\odot}$, with an increase in computational cost due to the number of templates increasing by a factor of ~ 2.7 . Finally, we investigated the loss in the SNR incurred by the using template banks constructed using only the leading order mode of EOBNRv2 waveforms. We found that a leading-order $l = m = 2$ EOBNRv2 template bank constructed with a MM of 0.97 is effectual to search for BBHs for which $1 \leq (m_1/m_2) \leq 1.68$ or $\iota \geq 2.68$ or $\iota \leq 0.31$ radians, and there is no significant loss in potential signal-to-noise ratio for systems with q as high as 4 or $2.02 \leq \iota \leq 2.68$ or $0.31 \leq \iota \leq 1.08$. We also observed that the maximum loss in detection-rate, for a binary with given mass parameters, averaging over other parameters - which are taken to be uniformly distributed over their possible ranges, goes only to a maximum of $\sim 10\% - 11\%$. For any given pair of binary masses, the loss is highest when the binary is inclined at $\simeq \pi/2$, and can go up to $\sim 20\%$, and is lower when its angular momentum is close to being parallel or anti-parallel to the line of sight from the detector. These effects average out, and hence for a population which is expected to have a uniform distribution of inclination angles (and uniform distribution in spacial volume), the average loss in detection rate was estimated to be not higher than $\sim 11\%$. Thus, using EOBNRv2HM templates

is unlikely to give a significant increase in the range to which such a population of sources can be detected. For BBHs with $(m_1/m_2) \geq 4$ and $1.08 \leq \iota \leq 2.02$, detection searches could possibly gain sensitivity by the use of EOBNRv2HM waveforms, if they can be implemented without increasing the false alarm rate.

Our results suggest that a significant portion of the non-spinning stellar-mass BBH parameter space can be searched for using LIGO’s existing search algorithms. For systems with total mass below $\sim 11.4M_\odot$ template banks of TaylorF2 can be used without significant loss in event rate. For higher mass systems, neglecting high-order modes in an EOBNRv2 search does not cause a substantial reduction in the maximum possible reach of BBH searches. Finally, we note that our study does not consider BBH systems with BH masses higher than $M = 25 M_\odot$, or the effect of black hole component spins. Future work will extend this study for systems with spinning and/or precessing black holes and consider the effect of non-Gaussian transients in real detector noise.

Chapter 5

Binary black hole search template banks with Numerical Relativity waveforms

GW searches so far have focused on GW bursts [11, 108, 12]; coalescing compact binaries [14, 15, 16, 17, 10, 18, 19], and ringdowns of perturbed black holes [13], amongst others [20, 21, 22, 23, 24]. For coalescing BBHs, detection searches involve matched-filtering [78, 79] of the instrument data using large banks of theoretically modeled waveform templates as filters [81, 88, 85, 87, 86, 89]. The matched-filter is the optimal linear filter to maximize the signal-to-noise ratio (SNR), in the presence of stochastic noise [109]. It requires an accurate modeling of the gravitational waveform emitted by the source binary. Early LIGO-Virgo searches employed template banks of Post-Newtonian (PN) inspiral waveforms [14, 15, 16, 17, 10], while more recent searches targeting high mass BBHs used complete inspiral-merger-ringdown (IMR) waveform templates [18, 19].

Recent developments in Numerical Relativity (NR) have provided complete simulations of BBH dynamics in the strong-field regime, i.e. during the late-inspiral and merger phases [33, 110, 35, 34, 111]. These simulations have contributed unprecedented physical insights to the understanding of BBH mergers (see, e.g., [112, 113, 52, 53] for recent overviews of the field). Due to their high computational cost, fully numerical simulations currently span a few tens of inspiral orbits before merger. For mass-ratios $q = m_1/m_2 = 1, 2, 3, 4, 6, 8$, the multi-domain Spectral Einstein code

(SpEC) [114] has been used to simulate 15–33 inspiral merger orbits [115, 116, 37]. These simulations have been used to calibrate waveform models, for example, within the effective-one-body (EOB) formalism [30, 56, 38, 117]. Alternately, inspiral waveforms from PN theory can be joined to numerical BBH inspiral and merger waveforms, to construct longer *hybrid* waveforms [118, 119, 120, 121, 122]. NR-PN hybrids have been used to calibrate phenomenological waveform models [123, 39], and within the NINJA project [124, 54] to study the efficacy of various GW search algorithms towards realistic (NR) signals [125, 126].

Constructing template banks for gravitational wave searches has been a long sought goal for NR. Traditionally, intermediary waveform models are calibrated against numerical simulations and then used in template banks for LIGO searches [18, 19]. In this chapter we explore an alternative to this traditional approach, proposing the use of NR waveforms themselves and hybrids constructed out of them as search templates. For a proof of principle, we focus on the non-spinning BBH space, with the aim of extending to spinning binaries in future work. We investigate exactly where in the mass space can the existing NR waveforms/hybrids be used as templates, finding that only six simulations are sufficient to cover binaries with $m_{1,2} \gtrsim 12M_\odot$ upto mass-ratio 10. This method can also be used as a guide for the placement of parameters for future NR simulations. Recent work has shown that existing PN waveforms are sufficient for aLIGO searches for $M = m_1 + m_2 \lesssim 12M_\odot$ [100, 127]. To extend the NR/hybrid bank coverage down to $M \simeq 12M_\odot$, we demonstrate that a total of 26 simulations would be sufficient. The template banks are constructed with the requirement that the net SNR recovered for any BBH signal should remain above 96.5% of its optimal value. Enforcing this tells that these 26 simulations would be required to be ~ 50 orbits long. This goal is achievable, given the recent progress in simulation technology [120, 37, 128]. Our template banks are viable for GW searches with aLIGO, and the framework for using hybrids within the LIGO-Virgo software framework has been demonstrated in the NINJA-2 collaboration [129]. In this chapter, we also derive waveform modeling error bounds which are independent of analytical models. These can be extended straightforwardly to assess the accuracy of such models.

First, we construct a bank for purely-NR templates, restricting to currently available simulations [120, 116, 115, 37, 116]. We use a stochastic algorithm similar to Ref. [130, 131, 132], and place a template bank grid constrained to $q = m_1/m_2 =$

$\{1, 2, 3, 4, 6, 8\}$. The bank placement algorithm uses the EOB model from Ref. [38] (EOBNRv2). As this model was calibrated against NR for most of these mass-ratios, we expect the manifold of EOBNRv2 to be a reasonable approximation for the NR manifold. In Sec. 5.4, we demonstrate that this approximation holds well for NR-PN hybrids as well. To demonstrate the efficacy of the bank, we measure its fitting-factors (FFs) [83] over the BBH mass space. We simulate a population of 100,000 BBH waveforms with masses sampled uniformly over $3M_{\odot} \leq m_{1,2} \leq 200M_{\odot}$ and $M = m_1 + m_2 \leq 200M_{\odot}$, and filter them through the template bank to characterize its SNR recovery. For a bank of NR templates, any SNR loss accrued will be due to the coarseness of the bank grid. We measure this requiring both signals and templates to be in the same manifold, using the EOBNRv2 model for both. We find that for systems with chirp mass $\mathcal{M}_c \equiv (m_1 + m_2)^{-1/5}(m_1 m_2)^{3/5}$ above $\sim 27M_{\odot}$ and $1 \leq q \leq 10$, this bank has FFs $\geq 97\%$ and is sufficiently accurate to be used in GW searches. We also show that the coverage of the purely-NR bank can be extended to include $10 \leq q \leq 11$, if we instead constrain it to templates with mass-ratios $q = \{1, 2, 3, 4, 6, 9.2\}$.

Second, we demonstrate that currently available PN-NR hybrid waveforms can be used as templates to search for BBHs with much lower masses. The hybrids used correspond to mass-ratios $q = \{1, 2, 3, 4, 6, 8\}$. We use two distinct methods of bank placement to construct a bank with these mass-ratios, and compare the two. The first method is the stochastic algorithm we use for purely-NR templates. The second is a deterministic algorithm, that constructs the two-dimensional bank (in M and q) through a union of six one-dimensional banks, placed separately for each allowed value of mass-ratio. Templates are placed over the total mass dimension by requiring that all pairs of neighboring templates have the same noise weighted overlap. As before, we measure the SNR loss from both banks, due to the discrete placement of the templates, by simulating a population of 100,000 BBH signals, to find the SNR recovered. We measure the intrinsic hybrid errors using the method of Ref. [119, 120], and subsequently account for them in the SNR recovery fraction. We find that the NR-PN hybrid bank is effectual for detecting BBHs with $m_{1,2} \geq 12M_{\odot}$, with FFs $\geq 96.5\%$. The number of templates required was found to be close to that of a bank constructed using the second-order TaylorF2 hexagonal bank placement algorithm [81, 88, 85, 87, 86, 89]. We note that by pre-generating the template for

the least massive binary for each of the mass-ratios that contribute to the bank, we can re-scale it on-the-fly to different total masses in the frequency domain [133]. Used in detection searches, such a bank would be computationally inexpensive to generate relative to a bank of time-domain modeled waveforms.

Finally, we determine the minimal set of NR simulations that we would need to extend the bank down to $M \simeq 12M_{\odot}$. We find that a bank that samples from the set of 26 mass-ratios listed in Table 2 would be sufficiently dense, even at the lowest masses, for binaries with mass-ratios $1 \leq q \leq 10$. We show that this bank recovers more than 98% of the optimal SNR, not accounting for hybrid errors. To restrict the loss in event detection rate below 10%, we restrict the total SNR loss below 3.5%. This implies the hybrid error mismatches stay below 1.5%, which constrains the length of the NR part for each hybrid. We find that NR simulations spanning about 50 orbits of late-inspiral, merger and ringdown would suffice to reduce the PN truncation error to the desired level. With such a bank of NR-PN hybrids and purely-PN templates for lower masses, we can construct GW searches for stellar-mass BBHs with mass-ratios $q \leq 10$.

The chapter is organized as follows, in Sec. 5.1.1, we discuss the NR waveforms used in this study, in Sec. 5.1.2 we describe the PN models used to construct the NR-PN hybrids, and in Sec. 5.1.3 we describe the construction of hybrid waveforms. In Sec. 5.1.4 we describe the EOB model that we use to place and test the template banks. In Sec. 5.2 we describe the accuracy measures used in quantifying the loss in signal-to-noise ratio in a matched-filtering search when using a discrete bank of templates and in the construction of hybrid waveforms. In Sec. 5.3 we describe the construction and efficacy of the NR-only banks, while in Sec. 5.4 we discuss the same for the NR-PN hybrid template banks constructed with currently available NR waveforms. In Sec. 5.5, we investigate the parameter and length requirements for future NR simulations in order to cover the entire non-spinning parameter space with $12M_{\odot} \leq M \leq 200M_{\odot}$, $m_{1,2} \geq 3M_{\odot}$, and $1 \leq q \leq 10$. Finally, in Sec. 5.6 we summarize the results.

5.1 Waveforms

In the sections that follow, we will describe the construction of template banks for NR or NR-PN hybrid waveform templates. The NR waveforms that we use correspond to mass ratios $q = \{1, 2, 3, 4, 6, 8\}$, and were simulated using the SpEC code [114]. The construction of hybrid waveforms involves joining a long inspiral portion, modeled using PN theory, to the merger-ringdown waveform from NR. In this section we describe both, the NR waveforms and the PN models used in our study. Measuring the effectualness of these banks involves simulating a population of BBH signals. We use the recently published EOBNRv2 model [38] to obtain waveforms for BBHs with arbitrary masses. This model was calibrated against five out of the six NR simulations we use to construct our banks, and is expected to be faithful at comparable mass ratios [38]. In this section, we briefly summarize the construction of EOBNRv2 waveforms as well.

5.1.1 Numerical Relativity simulations

The numerical relativity waveforms used in this chapter were produced with the SpEC code [114], a multi-domain pseudospectral code to solve Einstein's equations. SpEC uses Generalized Harmonic coordinates, spectral methods, and a flexible domain decomposition, all of which contribute to it being one of the most accurate and efficient codes for computing the gravitational waves from binary black hole systems. High accuracy numerical simulations of the late-inspiral, merger and ring-down of coalescing binary black-holes have been recently performed for mass-ratios $q \equiv m_1/m_2 \in \{1, 2, 3, 4, 6, 8\}$ [115, 134, 50, 116].

The equal-mass, non-spinning waveform covers 33 inspiral orbits and was first discussed in [120, 116]. This waveform was obtained with numerical techniques similar to those of [115]. The unequal-mass waveforms of mass ratios 2, 3, 4, and 6 were presented in detail in Ref. [115]. The simulation with mass ratio 6 covers about 20 orbits and the simulations with mass ratios 2, 3, and 4 are somewhat shorter and cover about 15 orbits. The unequal mass waveform with mass ratio 8 was presented as part of the large waveform catalog in [37, 116]. It is approximately 25 orbits in length. We summarize the NR simulations used in this study in Table 1. In the table, we also give the lowest total masses for which the NR waveforms span the aLIGO

η	q	Length (in orbits)	Minimum total mass (M_\odot)
0.25	1	33	49
0.2222	2	15	76
0.1875	3	18	82
0.1600	4	15	87
0.1224	6	20	83
0.0988	8	25	83

Table 1: SpEC BBH simulations used in this study. Given are symmetric mass-ratio η , mass-ratio $q = m_1/m_2$, and the length in orbits of the simulation. The last column gives the lowest total masses for which the NR simulations cover the entire coalescence process within the sensitive band of aLIGO, starting at 15 Hz.

band, starting at 15 Hz.

5.1.2 Post-Newtonian waveforms

We make use of the Taylor{T1,T2,T3,T4} flavors of the post-Newtonian approximant family to construct hybrid waveforms. The construction of these models is described in Sec. 2.5.1 and explicit expressions for the phasing and amplitudes are detailed in Appendix A. Construction of hybrid waveforms is described in the following section.

5.1.3 PN-NR hybrid waveforms

The hybridization procedure used for this investigation is described in Sec. 3.3 of Ref. [119]: The PN waveform, $h_{\text{PN}}(t)$, is time and phase shifted to match the NR waveform, $h_{\text{NR}}(t)$, and they are smoothly joined together in a GW frequency interval centered at ω_m with width $\delta\omega$:

$$\omega_m - \frac{\delta\omega}{2} \leq \omega \leq \omega_m + \frac{\delta\omega}{2}. \quad (5.1)$$

This translates into a matching interval $t_{\min} < t < t_{\max}$ because the GW frequency continuously increases during the inspiral of the binary. As argued in Ref. [119], we choose $\delta\omega = 0.1\omega_m$ because it offers a good compromise of suppressing residual oscillations in the matching time, while still allowing $h_{\text{PN}}(t)$ to be matched as closely as possible to the beginning of $h_{\text{NR}}(t)$.

The PN waveform depends on a (formal) coalescence time, t_c , and phase, Φ_c . These two parameters are determined by minimizing the GW phase difference in the

matching interval $[t_{\min}, t_{\max}]$ as follows:

$$t'_c, \Phi'_c = \underset{t_c, \Phi_c}{\operatorname{argmin}} \int_{t_{\min}}^{t_{\max}} (\phi_{\text{PN}}(t; t_c, \Phi_c) - \phi_{\text{NR}}(t))^2 dt, \quad (5.2)$$

where t'_c and Φ'_c are the time and phase parameters for the best matching between $h_{\text{PN}}(t)$ and $h_{\text{NR}}(t)$, and $\phi(t)$ is the phase of the (2,2) mode of the gravitational radiation. Since we consider only the (2,2) mode, this procedure is identical to time and phase shifting the PN waveform until it has best agreement with NR as measured by the integral in Eq. (5.2). The hybrid waveform is then constructed in the form

$$h_{\text{H}}(t) \equiv \mathcal{F}(t)h_{\text{PN}}(t; t'_c, \Phi'_c) + [1 - \mathcal{F}(t)]h_{\text{NR}}(t), \quad (5.3)$$

where $\mathcal{F}(t)$ is a blending function defined as

$$\mathcal{F}(t) \equiv \begin{cases} 1, & t < t_{\min} \\ \cos^2 \frac{\pi(t-t_{\min})}{2(t_{\max}-t_{\min})}, & t_{\min} \leq t < t_{\max} \\ 0, & t \geq t_{\max}. \end{cases} \quad (5.4)$$

In this work, we construct all hybrids using the same procedure, Eqs. (5.1)–(5.4), and vary only the PN approximant and the matching frequency ω_m .

5.1.4 Effective-One-Body model

We use the recently published Effective-One-Body model [38] to study the robustness of our template banks. The construction of the model is described in detail in Sec. 2.5.3.

5.2 Quantifying waveform accuracy & bank effectualness

To assess the recovery of SNR from template banks with NR waveforms or NR-PN hybrids as templates, we use the measures proposed in Ref. [83, 81, 82]. The gravitational waveform emitted during and driving a BBH coalescence is denoted as $h(t)$, or simply h . The inner product between two waveforms h_1 and h_2 is defined in Eq. 4.1. In this chapter, we take $S_n(f)$ in Eq. 4.1 to be the *zero-detuning high power* noise curve for aLIGO, for both bank placement and overlap calculations [90]; and

set the lower frequency cutoff $f_{\min} = 15$ Hz. The peak GW frequency for the lowest binary masses that we consider, i.e. for $m_1 + m_2 \simeq 12M_\odot$, is ~ 2.1 kHz during the ringdown phase. We sample the waveforms at 8192 Hz, preserving the information content up to the Nyquist frequency $f_{\text{Ny}} = 4096$ Hz. A waveform, h , is normalized (made to be a unit vector) by $\hat{h} = h/\sqrt{h|h|}$. In addition to being sensitive to their intrinsic mass parameters, the inner product of two normalized waveforms is sensitive to phase and time shift differences between the two, ϕ_c and t_c . These two parameters (ϕ_c and t_c) can be analytically maximized over to obtain the maximized overlap \mathcal{O} ,

$$\mathcal{O}(h_1, h_2) = \max_{\phi_c, t_c} \left(\hat{h}_1 | \hat{h}_2(\phi_c, t_c) \right), \quad (5.5)$$

which gives a measure of how “close” the two waveforms are in the waveform manifold, disregarding differences in overall amplitude. The *mismatch* \mathcal{M} between the two waveforms is then

$$\mathcal{M}(h_1, h_2) = 1 - \mathcal{O}(h_1, h_2). \quad (5.6)$$

Matched-filtering detection searches employ a discrete bank of modeled waveforms as filters. The optimal signal-to-noise ratio (SNR) is obtained when the detector strain $s(t) \equiv h^{\text{tr}}(t) + n(t)$ is filtered with the *true* waveform h^{tr} itself, i.e.

$$\rho_{\text{opt}} = \max_{\phi_c, t_c} \left(h^{\text{tr}} | \hat{h}^{\text{tr}}(\phi_c, t_c) \right) = \|h^{\text{tr}}\|, \quad (5.7)$$

where $\|h^{\text{tr}}\| \equiv \sqrt{(h^{\text{tr}}, h^{\text{tr}})}$ is the noise weighted norm of the waveform. With a discrete bank of filter templates, the SNR we recover

$$\rho \simeq \mathcal{O}(h^{\text{tr}}, h_b) \|h^{\text{tr}}\| = \mathcal{O}(h^{\text{tr}}, h_b) \rho_{\text{opt}}, \quad (5.8)$$

where h_b is the filter template in the *bank* (subscript b) that has the highest overlap with the signal h^{tr} . The furthest distance to which GW signals can be detected is proportional to the matched-filter SNR that the search algorithm finds the signal with. Note that $0 \leq \mathcal{O}(h^{\text{tr}}, h_b) \leq 1$, so the recovered SNR $\rho \leq \rho_{\text{opt}}$ (c.f. Eq. (5.8)). For a BBH population uniformly distributed in spacial volume, the detection rate would decrease as $\mathcal{O}(h^{\text{tr}}, h_b)^3$. Searches that aim at restricting the loss in the detection rate strictly below 10% (or 15%), would require a bank of template waveforms that have

\mathcal{O} above 0.965 (or 0.947) with *any* incoming signal [103, 104].

Any template bank has two sources for loss in SNR: (i) the discreteness of the bank grid in the physical parameter space of the BBHs, and, (ii) the disagreement between the actual GW signal h^{tr} and the modeled template waveforms used as filters. We de-coupled these to estimate the SNR loss. Signal waveforms are denoted as h_x^{tr} in what follows, where the superscript tr indicates a *true* signal, and the subscript x indicates the mass parameters of the corresponding binary. Template waveforms are denoted as h_b^M , where M denotes the waveform *model*, and b indicates that it is a member of the discrete *bank*. Fig. 11 shows the signal h_x^{tr} in its manifold, and the bank of templates h_b^M residing in the model waveform manifold, both being embedded in the same space of all possible waveforms. The point h_{\perp}^M is the waveform which has the smallest mismatch in the entire (continuous) model manifold with h_x^{tr} , i.e. $h_{\perp}^M : \mathcal{M}(h_x^{\text{tr}}, h_{\perp}^M) = \min_y \mathcal{M}(h_x^{\text{tr}}, h_y^M)$. The fraction of the optimal SNR recovered at different points x in the binary mass space can be quantified by measuring the fitting factor \mathcal{FF} of the bank [83],

$$\mathcal{FF}(x) = 1 - \min_b \mathcal{M}(h_x^{\text{tr}}, h_b^M). \quad (5.9)$$

For two waveforms h_1 and h_2 close to each other in the waveform manifold: $\|h_1\| \simeq \|h_2\|$, and mutually aligned in phase and time such that the overlap between them is maximized,

$$\|h_1 - h_2\|^2 \simeq 2(h_1|h_1) \left(1 - \frac{(h_1|h_2)}{\sqrt{(h_1|h_1)}\sqrt{(h_1|h_1)}} \right). \quad (5.10)$$

The mismatch can, hence, be written as (c.f. Eq. (5.6))

$$\mathcal{M}(h_1, h_2) = \frac{1}{2\|h_1\|^2} \|h_1 - h_2\|^2. \quad (5.11)$$

We note that this equation is an upper bound for Eq. (25) of Ref. [135]. From this relation, and treating the space embedding the true and model waveform manifolds as Euclidean at the scale of template separation, we can separate out the effects of

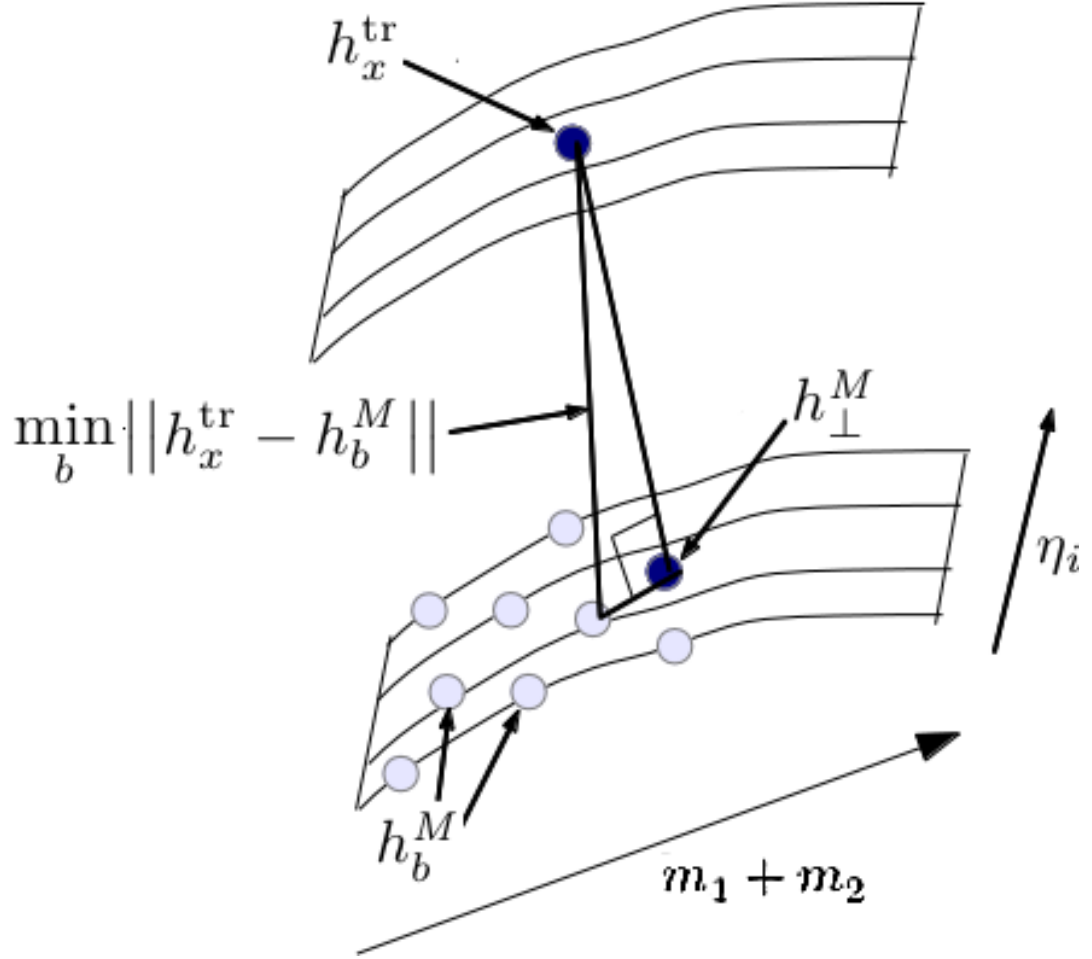


Figure 11: We show the *true* (upper) and the *hybrid* (lower) waveform manifolds here, with the signal residing in the former, and a discrete bank of templates placed along lines of constant mass-ratio in the latter. Both manifolds are embedded in the same space of all possible waveforms. The true signal waveform is denoted as h_x^{tr} , while the templates in the bank are labelled h_b^M . The hybrid waveform that matches the signal H_x^{tr} best is shown as h_{\perp}^M . Also shown is the “distance” between the signal and the hybrid template that has the highest overlap with it. This figure is qualitatively similar to Fig. 3 of Ref. [103].

bank coarseness and template inaccuracies as

$$\mathcal{FF}(x) = 1 - \min_b \frac{1}{2 \|h_x^{\text{tr}}\|^2} \|h_x^{\text{tr}} - h_b^M\|^2, \quad (5.12a)$$

$$= 1 - \Gamma_{\text{Hyb}}(x) - \Gamma_{\text{bank}}(x); \quad (5.12b)$$

where

$$\Gamma_{\text{Hyb}}(x) \equiv \frac{1}{2 \|h_x^{\text{tr}}\|^2} \|h_x^{\text{tr}} - h_{\perp}^M\|^2 = \mathcal{M}(h_x^{\text{tr}}, h_{\perp}^M) \quad (5.13)$$

is the SNR loss from model waveform errors out of the manifold of true signals; and

$$\Gamma_{\text{bank}}(x) \equiv \min_b \frac{1}{2 \|h_x^{\text{tr}}\|^2} \|h_{\perp}^M - h_b^M\|^2 = \min_b \mathcal{M}(h_{\perp}^M, h_b^M) \quad (5.14)$$

is the loss in SNR from the distant spacing of templates in the bank. The decomposition in Eq. (5.12b) allows for the measurement of the two effects separately. NR-PN hybrids have the inspiral portion of the waveform, from PN theory, joined to the available late-inspiral and merger portion from NR (as described in Sec. 5.1.3). Towards the late inspiral, the PN waveforms accumulate phase errors, contaminating the hybrids [119, 120]. For each hybrid, we constrain this effect using mismatches between hybrids constructed from the same NR simulation and different PN models, i.e.

$$\Gamma_{\text{Hyb}}(x) \leq \mathcal{M}(h_x^{\text{tr}}, h_x^{\text{Hyb}}) \lesssim \max_{(i,j)} \mathcal{M}(h_x^{M_i}, h_x^{M_j}), \quad (5.15)$$

where $M_i = \text{TaylorT}[1,2,3,4]+\text{NR}$. However, this is only possible for a few values of mass-ratio for which NR simulations are available. We assume Γ_{Hyb} to be a slowly and smoothly varying quantity over the component-mass space at the scale of template grid separation. At any arbitrary point x in the mass space we approximate Γ_{Hyb} with its value for the “closest” template, i.e.

$$\Gamma_{\text{Hyb}}(x) \leq \max_{(i,j)} \mathcal{M}(h_x^{M_i}, h_x^{M_j}) \simeq \max_{(i,j)} \mathcal{M}(h_b^{M_i}, h_b^{M_j}), \quad (5.16)$$

where h_b^M is the hybrid template in the bank with the highest overlap with the signal at x .

The other contribution to SNR loss comes from the discrete placement of templates in the mass space. In Fig. 11, this is shown in the manifold of the template model. As

NR waveforms (or hybrids) are available for a few values of mass-ratio, we measure this in the manifold of EOBNRv2 waveforms. The EOBNRv2 model reproduces most of the NR simulations that were considered here well [38], allowing for this approximation to hold. For the same reason, we expect h_x^{EOBNRv2} to be close to $h_{\perp}^{\text{EOBNRv2}}$, with an injective mapping between the two. This allows us to approximate (c.f. Eq. (5.14))

$$\Gamma_{\text{bank}}(x) \simeq \min_b \mathcal{M}(h_x^{\text{EOBNRv2}}, h_b^{\text{EOBNRv2}}). \quad (5.17)$$

In Sec. 5.3, we construct template banks that use purely-NR templates, which have negligible waveform errors. The SNR recovery from such banks is characterized with

$$\mathcal{FF}(x) = 1 - \Gamma_{\text{bank}}(x), \quad (5.18)$$

where the SNR loss from bank coarseness is obtained using Eq. (5.17). In Sec. 5.4, 5.5, we construct template banks aimed at using NR-PN hybrid templates. Their SNR recovery is characterized using Eq. (5.12b), where the additional contribution from the hybrid waveform errors are obtained using Eq. (5.16).

5.3 Constructing a template bank for NR waveforms

In this section we demonstrate the effectiveness of a template bank viable for using NR waveforms as templates. The gravitational-wave phase of the dominant waveform multipole extracted from runs at different resolutions was found to converge within ~ 0.3 rad for $q = 3, 4, 6$, and within ~ 0.06 rad for $q = 1, 2$ at merger (see Fig. (6) of Ref. [115], and Fig. (6,7) of Ref. [38] for a compilation). Most of this phase disagreement accumulates over a relatively short duration of $\sim 50M - 100M$ before merger, and is significantly lower over the preceding inspiral and plunge. As the matched-filter SNR accumulates secularly over the entire waveform, these numerical phase errors are negligible in terms of mismatches. We set $\Gamma_{\text{Hyb}} = 0$ while computing the fitting factors, so one is left with considering Γ_{bank} to determine the fidelity of the bank (c.f. Eq. (5.12b)).

With NR simulations as templates, the region that the bank can cover is restricted to binaries that have approximately the same number of waveform cycles within the sensitive frequency band of the detectors as the simulations themselves. We take their

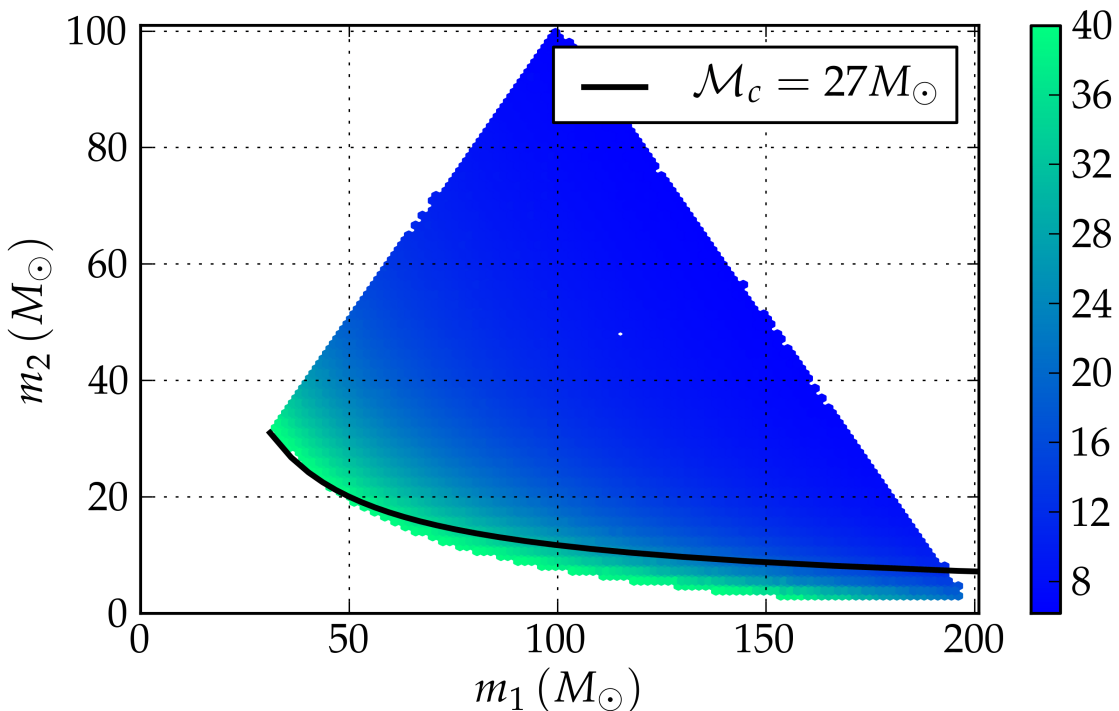


Figure 12: The color at each point gives the number of waveform cycles N_{cyc} , for that particular binary, which contain 99% of the signal power in the aLIGO sensitivity band. The figure is truncated to exclude the region where $N_{\text{cyc}} > 40$. The solid curve shows the lower bounding edge of the region with $\mathcal{M}_c = 27 M_\odot$.

fiducial length to be ~ 40 GW cycles [136]. For BBHs with $3M_{\odot} \leq m_1, m_2 \leq 200M_{\odot}$ and $m_1 + m_2 \leq 200M_{\odot}$ we map out the region with 99% of the signal power within 40 cycles as the target region of the purely-NR bank. For samples taken over the mass space, we determine the frequency interval $[f_1, f_2]$ for which

$$\int_{f_1}^{f_2} df \frac{|\tilde{h}(f)|^2}{S_n(|f|)} = 0.99 \times \int_{f_{\min}}^{f_{\text{Ny}}} df \frac{|\tilde{h}(f)|^2}{S_n(|f|)}. \quad (5.19)$$

This is done by finding the peak of the integrand in Eq. (5.19) and integrating symmetrically outwards from there, in time, till the interval $[f_1, f_2]$ is found. The number of waveform cycles in this interval is

$$N_{\text{cyc}} = \frac{\Phi(t(f_2)) - \Phi(t(f_1))}{2\pi}, \quad (5.20)$$

where $\Phi(t)$ is the instantaneous phase of the waveform, $h_+(t) - i h_{\times}(t) = A(t) e^{-i\Phi(t)}$, un-wrapped to be a monotonic function of time. We find that for a significant portion of the mass-region, the signal power is contained within 40 waveform cycles. This is shown in Fig. 12, where the color at each point gives N_{cyc} for that system, and the region with $N_{\text{cyc}} > 40$ is excluded. Conservatively, this region is bounded by $\mathcal{M}_c = 27M_{\odot}$, as shown by the solid curve in the figure.

We place a bank over this region, using a stochastic method similar to Ref. [130, 131, 132]. The algorithm begins by taking an empty bank, corresponding to step 0. At step i , a proposal point (q, M) is picked by first choosing a value for q from the restricted set $\mathcal{S}_q = \{1, 2, 3, 4, 6, 8\}$. The total mass M is subsequently sampled from the restricted interval corresponding to the pre-drawn q . The proposal is accepted if the waveform at this point has overlaps $\mathcal{O} < 0.97$ with all the templates in the bank from step $i-1$. This gives the bank at step i . The process is repeated till the fraction of proposals being accepted falls below $\sim 10^{-4}$, and $\gtrsim 99\%$ of the parameter space is covered effectually. To complete the coverage, 100,000 points are sampled over the region of mass space depicted in Fig. 12, and \mathcal{FF} of the bank is computed at each point. With the islands of undercoverage isolated, the points sampled in these regions are added to the bank, pushing their mass-ratios to the two neighboring mass-ratios in \mathcal{S}_q along lines of constant chirp mass. This helps accelerate the convergence of the bank, albeit at the cost of over-populating it, as the algorithm for computing the \mathcal{FF}

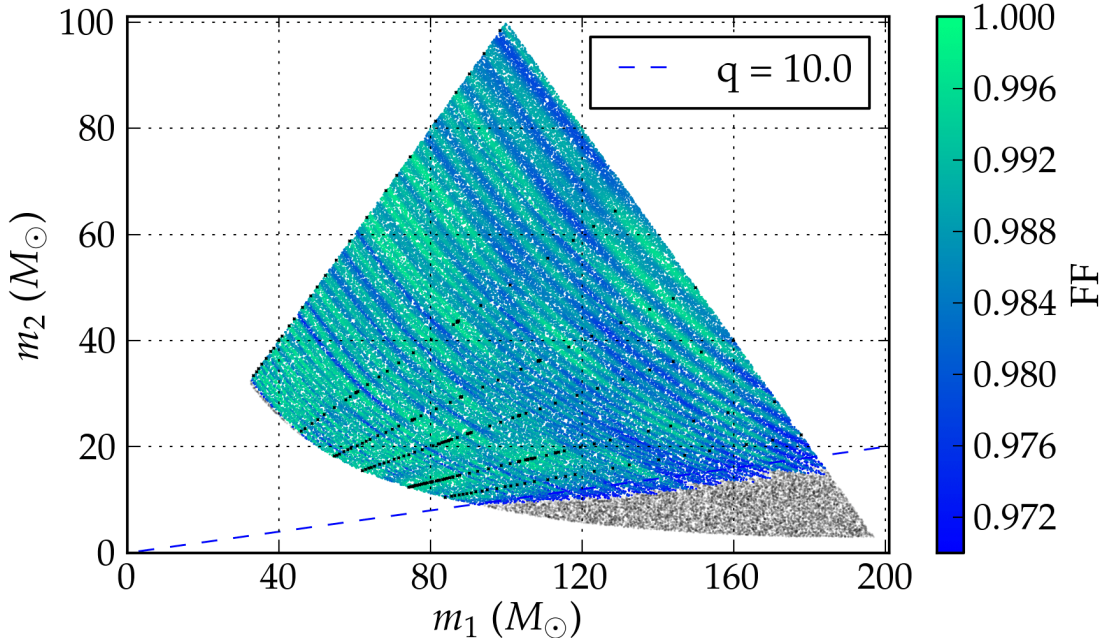


Figure 13: The color at each point in the figure gives the value of $\mathcal{FF} \simeq 1 - \Gamma_{\text{bank}}$ of the bank for that binary, for the NR bank restricted to $\mathcal{S}_q = \{1, 2, 3, 4, 6, 8\}$. This is the same as the fraction of the optimal SNR, for the binary, that the template bank recovers. The black dots show the location of the templates in the bank. We note that they all lie along straight lines of constant q passing through the origin. The region shaded light-grey (towards the bottom of the figure) is where the \mathcal{FF} drops sharply below 97%.

for the sampled points is parallelizable.

We assess the effectiveness of the bank, as discussed in Sec. 5.2, using Eq. (5.18). We draw a population of 100,000 BBH signals, uniformly from the binary mass space, and filter them through the bank. Fig. 13 shows the \mathcal{FF} , or the fraction of the optimal SNR recovered by the bank. The region shown is restricted to binaries with $N_{\text{cyc}} \leq 40$. The black dots in the figure show the position of templates in the bank. The bank recovers $\geq 97\%$ of the optimal SNR over the entire region of interest for $q \leq 10$. We propose an additional simulation for $q = 9.2$, to increase the coverage to higher mass-ratios. Substituting this for $q = 8$ in the set of allowed mass-ratios \mathcal{S}_q , we place another bank as before, with $\mathcal{S}_q = \{1, 2, 3, 4, 6, 9.2\}$. The SNR loss from this bank is shown in Fig. 14. This bank recovers $\geq 97\%$ of the SNR for systems with $q \leq 11$ and $N_{\text{cyc}} \leq 40$. The choice of the additional simulation at $q = 9.2$ was made by choosing a value *close-to* the highest possible value of q that does not lead to under-coverage

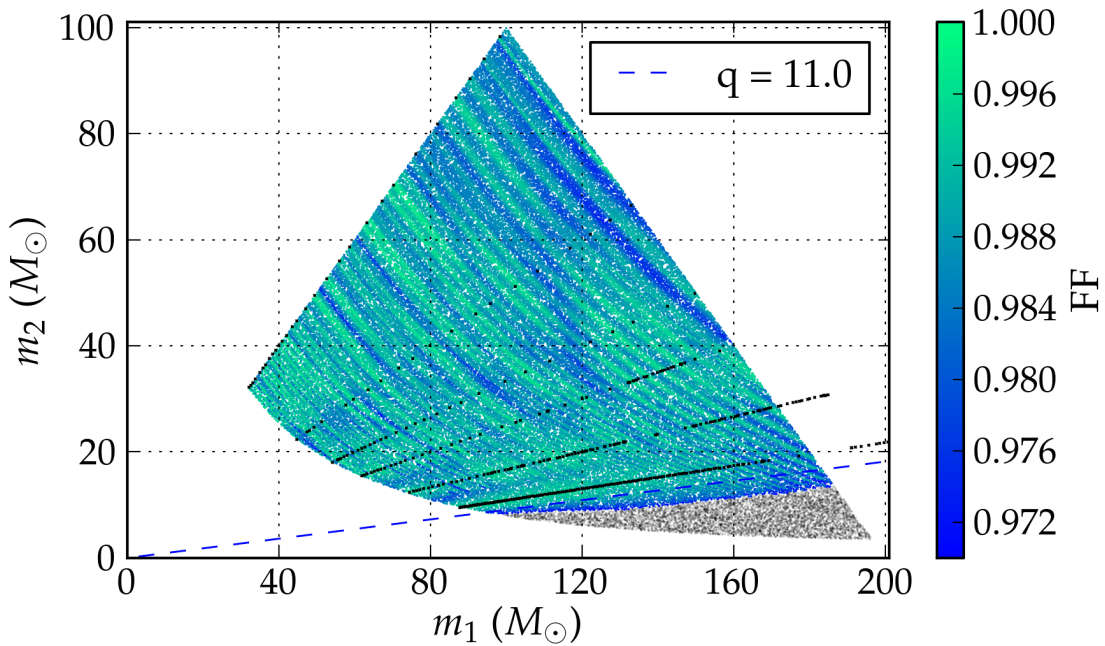


Figure 14: This figure is similar to Fig. 13. The color at each point gives the value of $\mathcal{FF} \simeq 1 - \Gamma_{\text{bank}}$ of the bank for that binary, for the NR bank restricted to $\mathcal{S}_q = \{1, 2, 3, 4, 6, 9.2\}$. The black dots show the location of the templates in the bank. The region shaded light-grey (towards the bottom of the figure) is where the \mathcal{FF} drops below 97%. We note that with an additional NR waveform for mass ratio $q = 9.2$, the coverage of the bank is extended to include binaries with $10 \leq q \leq 11$.

in the region between $q = 6$ and that value. The *exact* highest allowed value was not chosen to reduce the sensitivity of the coverage of the bank to fluctuations in detector sensitivity.

We conclude that with only six NR waveforms for non-spinning BBHs, that are ~ 20 orbits (or 40 GW cycles) in length, a template bank can be constructed that is effectual for detecting binaries with chirp mass above $27M_{\odot}$ and $1 \leq q \leq 10$. With an additional simulation for $q = 9.2$, this bank can be extended to higher mass-ratios, i.e. to $1 \leq q \leq 11$.

5.4 Constructing a template bank for NR-PN hybrids

The template bank contructed in Sec. 5.3 is effectual for GW detection searches focussed at relatively massive binaries with $\mathcal{M}_c \gtrsim 27M_{\odot}$. As the NR waveforms are restricted to a small number of orbits, it is useful to consider NR-PN hybrids to bring the lower mass limit down on the template bank. PN waveforms can be generated for an arbitrarily large number of inspiral orbits, reasonably accurately and relatively cheaply. Thus, a hybrid waveform comprised of a long PN early-inspiral and an NR late-inspiral, merger, and ringdown could also be arbitrarily long. There are, however, uncertainties in the PN waveforms, due to the unknown higher-order terms. During the late-inspiral and merger phase, these terms become more important and the PN description becomes less accurate. In addition, when more of the late-inspiral is in the detector's sensitivity frequency range, hybrid waveform mismatches due to the PN errors become increasingly large, and reduce the recovered SNR. Thus, when hybridizing PN and NR waveforms, there must be enough NR orbits that the PN error is sufficiently low for the considered detector noise-curve. In this section, we construct an NR + PN hybrid template bank, for currently available NR waveforms, and determine the lowest value of binary masses to which it covers.

The hybrids we use are constructed by joining the PN and NR portions, as described in Sec. 5.1.3. The number of orbits before merger at which they are joined depends on the length of the available NR waveforms. We estimate the PN waveform errors using hybridization mismatches Γ_{Hyb} , as discussed in Sec. 5.2. Fig. 15 shows the same for all the hybrids, as a function of total mass. In terms of orbital frequency, these are matched at $M\omega_m = 0.025$ for $q = 1$, $M\omega_m = 0.038$ for $q = 2$, and

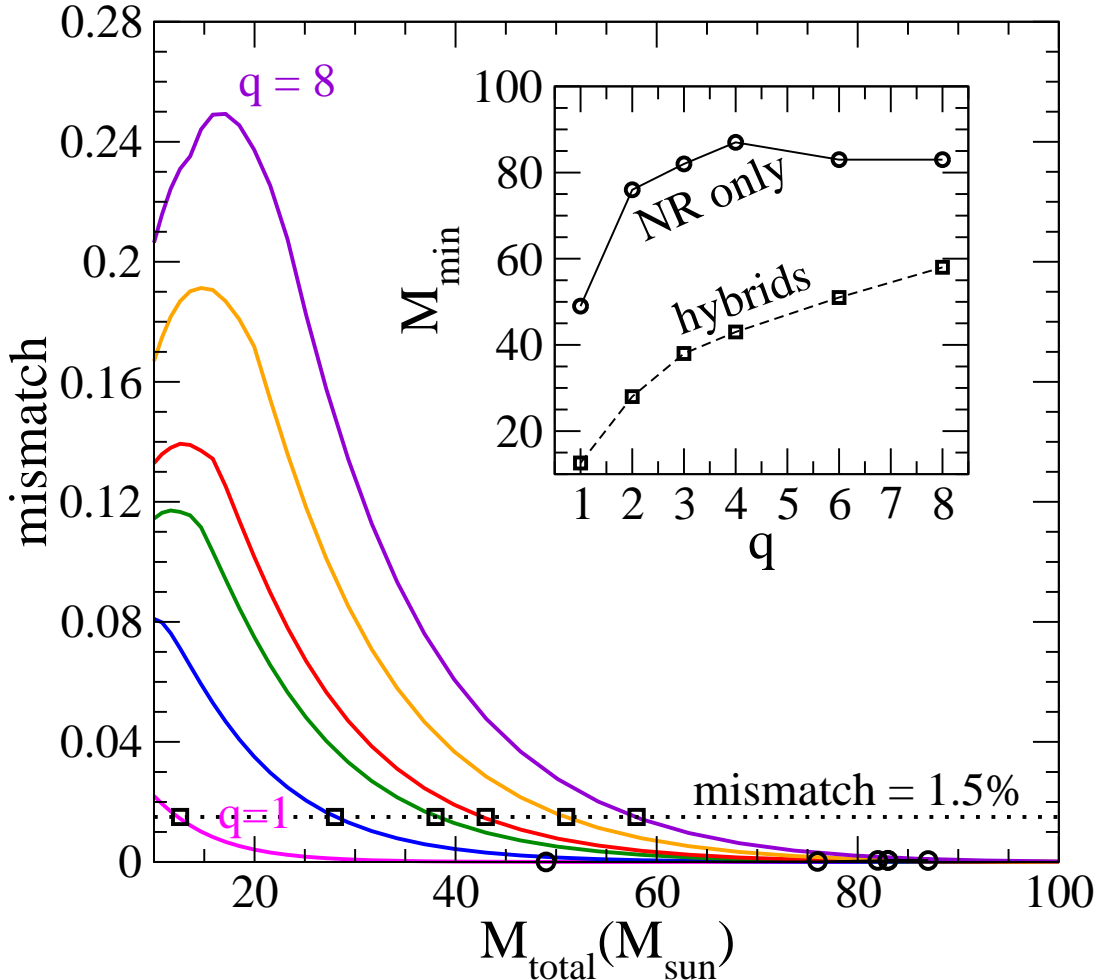


Figure 15: Bounds on mismatches of PN-NR hybrid waveforms, for the currently existing NR simulations. The PN error is for hybrids matched at $M\omega_m = 0.025$ for $q = 1$, $M\omega_m = 0.038$ for $q = 2$, and $M\omega_m = 0.042$ for $q = 3, 4, 6, 8$. The black circles indicate the lower bound of the template bank in Table 1. The black square show the lower bound with a hybrid error of 1.5%. The inset shows these lower bounds as a function of mass ratio.

$M\omega_m = 0.042$ for $q = 3, 4, 6, 8$. In terms of number of orbits before merger, this is 26.9 orbits for $q = 1$, 13.6 orbits for $q = 2$, 12.6 orbits for $q = 3$, 14.3 orbits for $q = 4$, 17.8 orbits for $q = 6$, and 21.4 orbits for $q = 8$. The dotted line indicates a mismatch of 1.5%, a comparatively tight bound that leaves flexibility to accommodate errors due to template bank discreteness. The black circles show the hybrid mismatches at the lower mass bound of the NR-only template bank in Table 1, which are negligible. The inset shows this minimum mass as a function of mass ratio, as well as the minimum attainable mass if we accept a hybrid error of 1.5%. At lower masses, the mismatches increase sharply with more of the PN part moving into the Advanced LIGO sensitivity band. This is due to the nature of the frequency dependence of the detector sensitivity. The detectors will be most sensitive in a comparatively narrow frequency band. As the hybridization frequency sweeps through this band, the hybrid errors rise sharply. They fall again at the lowest masses, for which mostly the PN portion stays within the sensitive band.

We now consider template banks viable for hybrids constructed from currently available NR waveforms at mass ratios $q = 1, 2, 3, 4, 6, 8$. The lower mass limit, in this case, is extended down to masses where the hybridization error exceeds 3%. We demonstrate two independent methods of laying down the bank grid. First, we use the stochastic placement method that proceeds as described in Sec. 5.3. The templates are sampled over the total mass - mass-ratio (M, q) coordinates, sampling q from the restricted set. The total mass M is sampled from the continuous interval between the lower mass limit, which is different for each q , and the upper limit of $200M_\odot$. To assess the SNR loss from the sparse placement of the templates, we simulate a population of 100,000 BBH signal waveforms, with masses sampled with $3M_\odot \leq m_{1,2} \leq 200M_\odot$ and $M \leq 200M_\odot$, and filter them through the bank. This portion of the SNR loss needs to be measured with both signals and templates in the same waveform manifold. We use the EOBNRv2 approximant [38] to model both, as it has been calibrated to most of the NR waveforms we consider here, and it allows us to model waveforms for arbitrary systems. The left panel of Fig. 16 shows the fraction of the optimal SNR that the bank recovers, accounting for its discreteness alone. We observe that, with just six mass-ratios, the bank can be extended to much lower masses before it is limited by the restricted sampling of mass-ratios for the templates. For binaries with both black-holes more massive than $\sim 12M_\odot$, the spacing between mass-ratios

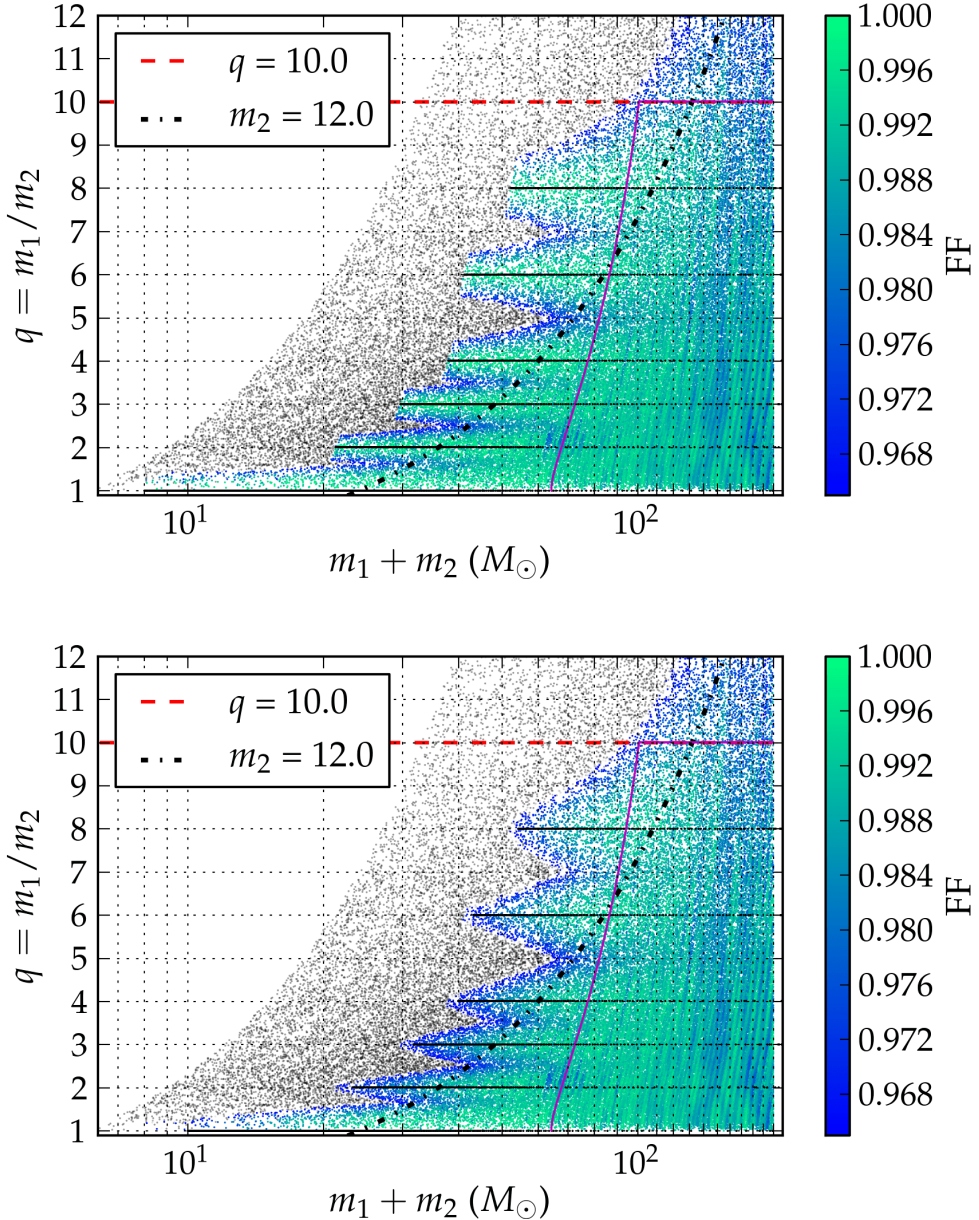


Figure 16: These figures show fitting factors \mathcal{FF} obtained when using a discrete mass-ratio template bank for $q = 1, 2, 3, 4, 6, 8$. For each mass-ratio, the templates are extended down to a total mass where the NR-PN hybridization mismatch becomes 3%. The bank is placed using the stochastic algorithm, similar to Ref. [130, 131, 132]. The black dots show the location of the templates. The fitting factor on the top plot does *not* take into account the hybridization error, and therefore shows the effect of the sparse placement of the templates alone. The bottom plot accounts for the hybridization error and gives the actual fraction of the optimal SNR that would be recovered with this bank of NR-PN hybrid templates. The region bounded by the magenta (solid) line in both plots indicates the lower end of the coverage of the bank of un-hybridized NR waveforms. Lastly, the shaded grey dots show the points where the fitting factor was below 96.5%.

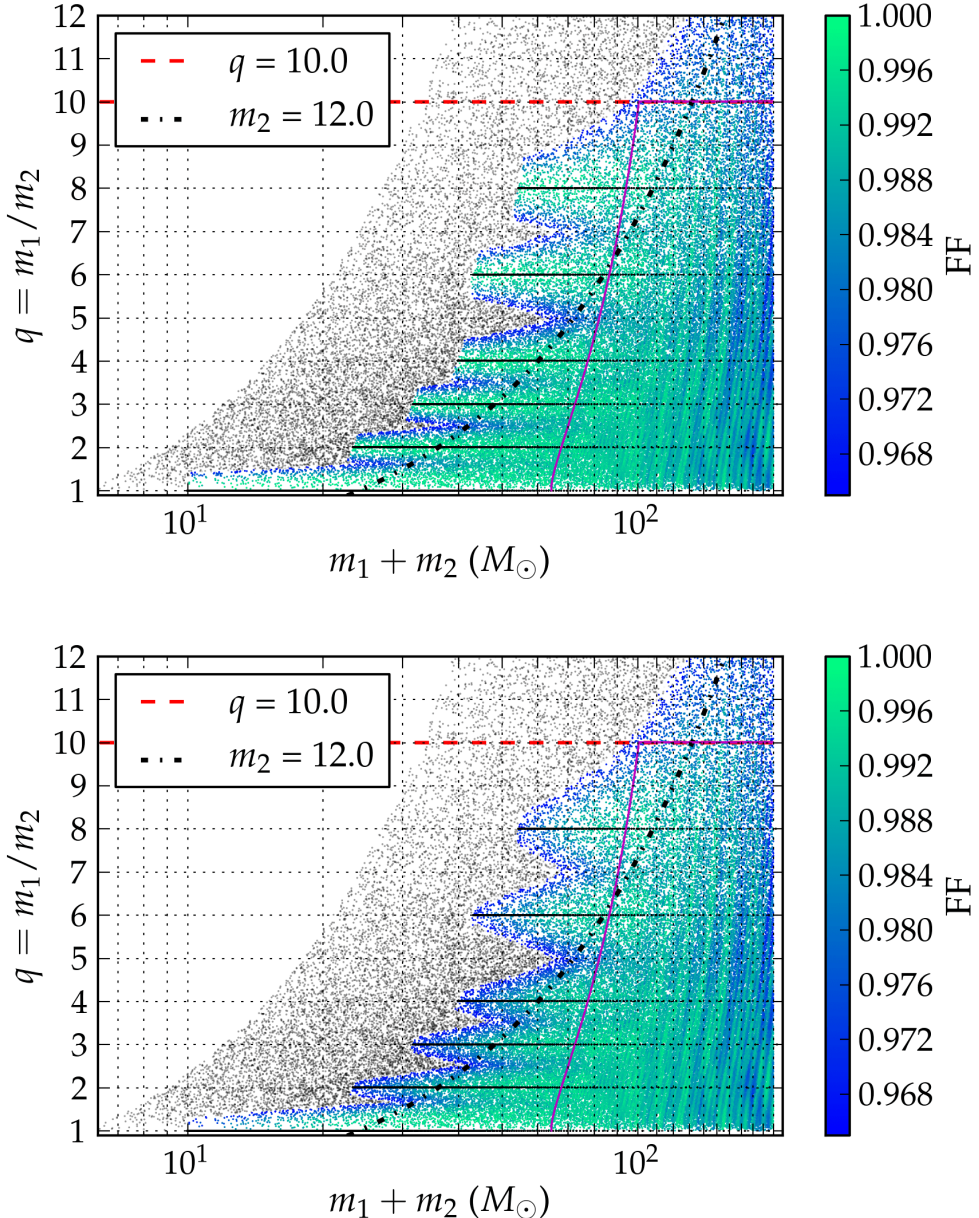


Figure 17: These figures are similar to Fig. 16. The figures show fitting factors \mathcal{FF} obtained when using a discrete mass-ratio template bank for $q = 1, 2, 3, 4, 6, 8$. For each mass-ratio, the templates are extended down to a total mass where the NR-PN hybridization mismatch becomes 3%. Templates are placed independently for each mass-ratio, and span the full range of total masses. For each mass-ratio, neighboring templates are required to have an overlap of 97%. The union of the six single- q one-dimensional banks is taken as the final bank. The black dots show the location of the templates. The fitting factor on the top plot does *not* take into account the hybridization error, and therefore shows the effect of the sparse placement of the templates alone. The bottom plot accounts for the hybridization error and gives the actual fraction of the optimal SNR that would be recovered with this bank of NR-PN hybrid templates. The region bounded by the magenta (solid) line in both plots indicates the lower end of the coverage of the bank of un-hybridized NR waveforms. Lastly, the shaded grey dots show the points where the fitting factor was below 96.5%.

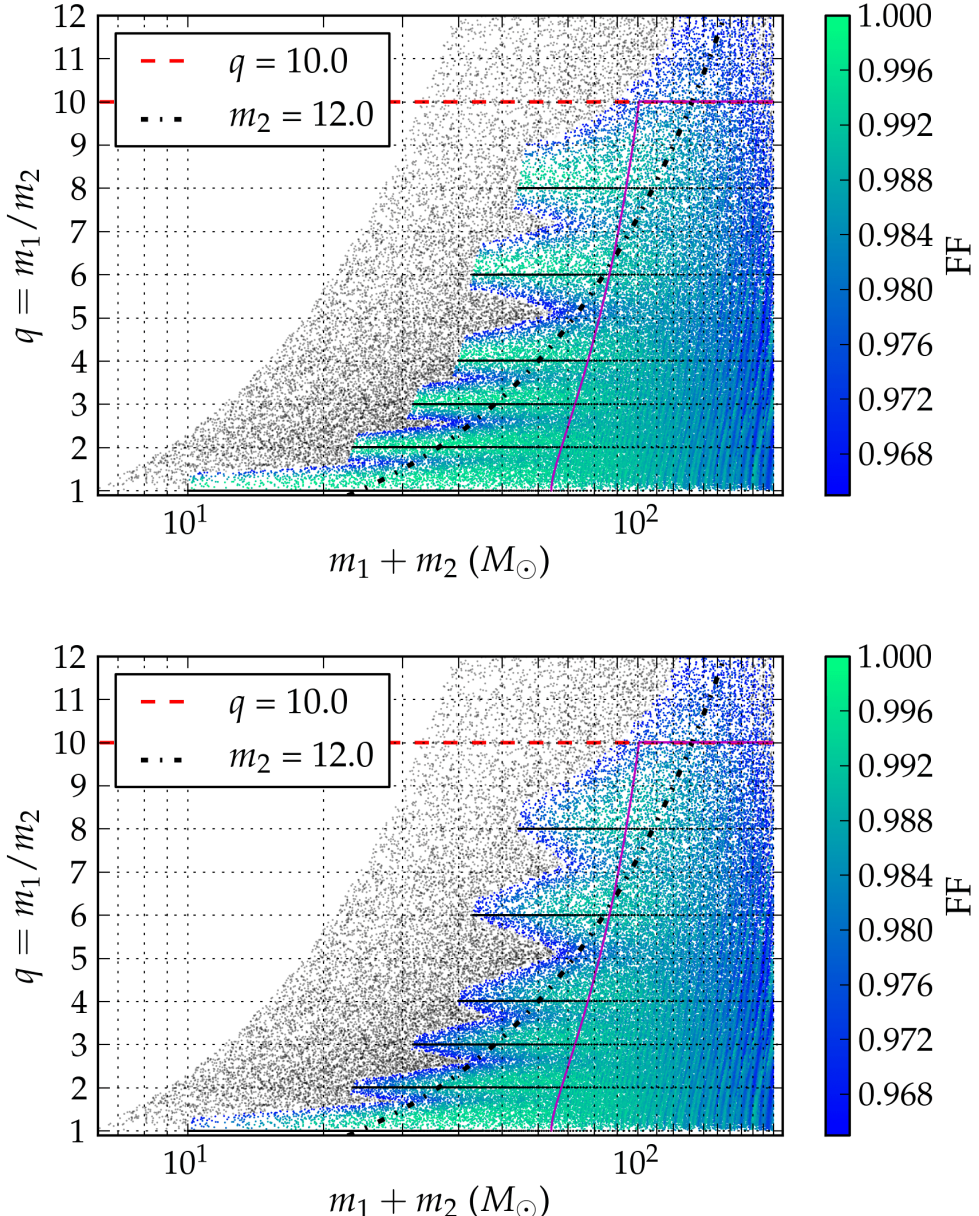


Figure 18: This figure is similar to Fig. 17. The figures show fitting factors \mathcal{FF} obtained when using a discrete mass-ratio template bank for $q = 1, 2, 3, 4, 6, 8$. Templates are placed independently for each mass-ratio, and span the range of total masses, down to the region where the hybrid errors become 3%. For each mass-ratio, neighboring templates are required to have an overlap of 97%. The union of the six single- q one-dimensional banks is taken as the final bank. The black dots show the location of the templates. The GW signals are modeled using the EOBNRv2 approximant [38], while TaylorT4+NR hybrids are used as templates. The fitting factor on the left plot shows the combined effect of the sparse placement of the templates, and the (relatively small) disagreement between the hybrid and EOBNRv2 waveforms. The right plot explicitly accounts for the hybridization error and gives the (conservative) actual fraction of the optimal SNR that would be recovered with this bank of NR-PN hybrid templates. The region bounded by the magenta (solid) line in both plots indicates the lower end of the coverage of the bank of un-hybridized NR waveforms. Lastly, the shaded grey dots show the points where the fitting factor was below 96.5%.

was found to be sufficiently dense. The total SNR loss, after subtracting out the hybrid mismatches from Fig. 15, are shown in the right panel of Fig. 16. At the lowest masses, the coverage shrinks between the lines of constant q over which the templates are placed, due to the hybrid errors increasing sharply. We conclude that this bank is viable for hybrid templates for GW searches for BBHs with $m_{1,2} \geq 12M_\odot$, $1 \leq q \leq 10$, and $M \leq 200M_\odot$. Over this region the bank will recover more than 96.5% of the optimal SNR. This is a significant increase over the coverage allowed for with the purely-NR bank, the region of coverage of which is shown in the right panel of Fig. 17, bounded at lowest masses by the magenta (solid) curve.

Second, we demonstrate a non-stochastic algorithm of bank placement, with comparable results. We first construct six independent bank grids, each restricted to one of the mass-ratios $q = 1, 2, 3, 4, 6, 8$, and spanning the full range of total masses. The template with the lowest total mass is chosen by requiring the hybrid mismatch to be 3% at that point. The spacing between neighboring templates is given by requiring that the overlap between them be 97%. We take the union of these banks as the final two-dimensional bank. As before, we measure the SNR loss due to discreteness of the bank and the waveform errors in the templates separately. To estimate the former, we simulate a population of 100,000 BBH systems, and filter them through the bank. The signals and the templates are both modeled with the EOBNRv2 model. The left panel of Fig. 17 reveals the fraction of SNR recovered over the mass space, accounting for the sparsity of the bank alone, i.e. $1 - \Gamma_{\text{bank}}$. At lower masses, we again start to see gaps between the lines of constant mass ratio which become significant at $m_{1,2} \leq 12M_\odot$. The right panel of Fig. 17 shows the final fraction of the optimal SNR recovered, i.e. the \mathcal{FF} as defined in Eq. (5.12b). As before, these are computed by subtracting out the hybrid mismatches Γ_{Hyb} in addition to the discrete mismatches, as described in Sec. 5.2.

The efficacy of both methods of template bank construction can be compared from Fig. 16 and Fig. 17. We observe that the final banks from either of the algorithms have very similar SNR recovery, and are both effectual over the range of masses we consider here. Both were also found to give a very similar number of templates. The uniform-in-overlap method yields a grid with 2,325 templates. The stochastic bank, on the other hand, was placed with a requirement of 98% minimal mismatch, and had 2,457 templates. This however includes templates with $m_{1,2} < 12M_\odot$. Restricted to

provide coverage over the region with $m_{1,2} \geq 12M_\odot$, $1 \leq q \leq 10$, and $M \leq 200M_\odot$, the two methods yield banks with 627 and 667 templates respectively. The size of these banks is comparable to one constructed using the second-order post-Newtonian TaylorF2 hexagonal template placement method [86, 87, 88, 89], which yields a grid of 522 and 736 templates, for a minimal match of 97% and 98%, respectively.

Finally, we test the robustness of these results using TaylorT4+NR hybrids as templates. As before, we simulate a population of 100,000 BBH signal waveforms. As we do not have hybrids for arbitrary binary masses, we model the signals as EOBNRv2 waveforms. This population is filtered against a bank of hybrid templates. The SNR recovered is shown in the left panel of Fig. 18. Comparing with the left panels of Fig. 16, 17, we find that the EOBNRv2 manifold is a reasonable approximation for the hybrid manifold; and that, at lower masses, there is a small systematic bias in the hybrids towards EOBNRv2 signals with slightly higher mass-ratios. The right panel of Fig. 18 shows the fraction of optimal SNR recovered after subtracting out the hybrid mismatches from the left panel. The similarity of the \mathcal{FF} distribution between the right panels of Fig. 18 and Fig. 16, 17 is remarkable. This gives us confidence that the EOBNRv2 model is a good approximation for testing NR/hybrid template banks, as we do in this chapter; and that a template bank of NR+PN hybrids is indeed effectual for binaries with $m_{1,2} \geq 12M_\odot$, $M \leq 200M_\odot$ and $q \leq 10$.

5.5 Complete NR-PN hybrid bank for non-spinning BBH

The last sections outlined properties of template banks of NR waveforms (and their hybrids) which are available today. We also investigate the parameter and length requirements for future NR simulations, that would let us construct detection template banks all the way to $M = m_1 + m_2 = 12M_\odot$. This lower limit was chosen following Ref. [127, 100] which showed that the region with $M \lesssim 12M_\odot$ can be covered with banks of post-Newtonian inspiral-only waveforms.

Constructing such a bank is a two-step process. First, we pick mass-ratios that allow construction of such a bank given long enough waveforms for these mass-ratios. Second, one needs to determine the necessary length of the NR portion of the waveforms, such that the PN-hybridization error is sufficiently low for all masses of interest.

To motivate the first step, Fig. 19 shows the coverage of banks that sample from a

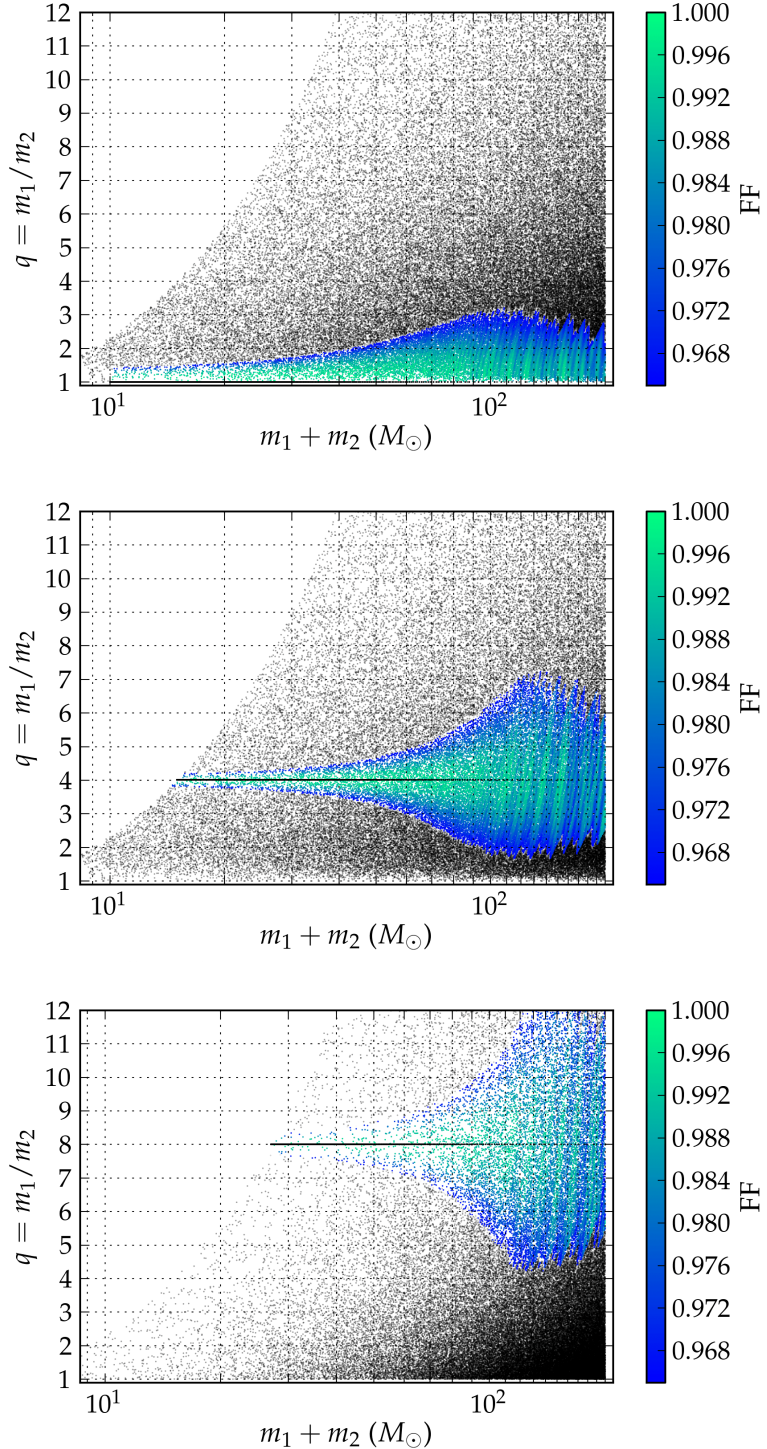


Figure 19: These figures show the coverage of template banks restricted to single mass-ratios, i.e. (from top to bottom) $q = 1, 4, 8$. We note that at higher total masses, the templates are correlated to simulated signals for considerably different mass-ratios, than at lower total masses. This agrees with what we expect as with decreasing total mass, the number of cycles in the sensitive frequency band of Advanced LIGO increases.

$q (\equiv m_1/m_2)$
1, 1.5, 1.75,
2, 2.25, 2.5, 2.75,
3, 3.25, 3.5, 3.8,
4.05, 4.35, 4.65, 4.95,
5.25, 5.55, 5.85,
6.2, 6.55,
7, 7.5,
8, 8.5,
9, 9.6

Table 2: List of mass-ratios, a template bank restricted to which will be effectual over the region of the non-spinning BBH mass space where $m_1 + m_2 \gtrsim 12M_\odot$ and $1 \leq q \leq 10$. The fraction of optimal SNR recovered by such a bank, accounting for discreteness losses, remains above 98%. This is shown in Fig. 20.

single mass-ratio each (from left to right: $q = 1, 4, 8$). We see that the resolution in q required at lower values of M increases sharply below $M \sim 60M_\odot$. This follows from the increase in the number of waveform cycles in aLIGO frequency band as the total mass decreases, which, in turn, increases the discriminatory resolution of the matched-filter along the q axis. To determine the least set of mass-ratios which would sample the q axis sufficiently densely at lower masses, we iteratively add mass-ratios to the allowed set and test banks restricted to sample from it. We find that, constrained to the set \mathcal{S}_q given in Table 2, a template bank can be constructed that has a minimal match of 98% at the lowest masses. The left panel of Fig. 20 shows the loss in SNR due to bank grid coarseness, i.e. $1 - \Gamma_{\text{bank}}$. This loss remains below 2% for mass-ratios $1 \leq q \leq 10$, even at $M = 12M_\odot$. This leaves a margin of 1.5% for the hybrid mismatches that would incur due to the hybridization of the NR merger waveforms with long PN inspirals. The right panel of Fig. 20 shows the same data in the m_1 - m_2 plane. In this figure, the region covered by the NR-only bank is above the blue (solid) curve, while that covered by a bank of the currently available NR-PN hybrids is above the line of $m_2 = 12M_\odot$ (with $m_2 \leq m_1$). The region from Ref. [127, 100] that can be covered by PN templates is in the bottom left corner, bounded by the magenta (solid) line. Our bank restricted to the set of 26 mass-ratios, as above, provides additional coverage for binaries with $M \geq 12M_\odot$, $m_2 \leq 12M_\odot$ and $1 \leq q \leq 10$. Thus between purely-PN and NR/NR-PN hybrid templates, we can construct effectual searches for

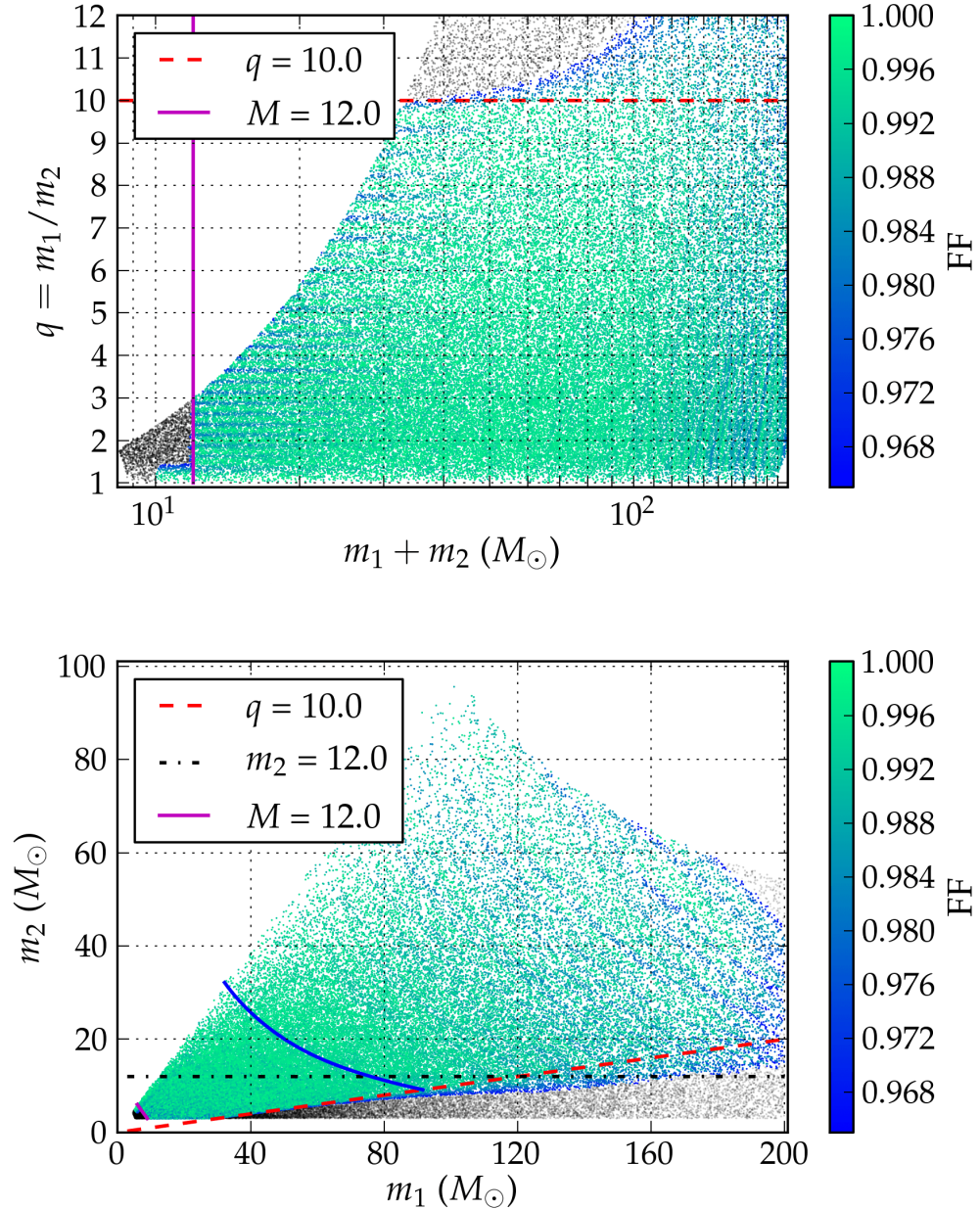


Figure 20: This figure shows fitting factors for a hybrid template bank which samples from the 26 mass ratios $q = 1, 1.5, 1.75, 2, \dots, 9.6$, and allows coverage to masses down to $m_1 + m_2 = 12M_\odot$ and $1 \leq q \leq 10$, with a minimal-match of 98% at the lowest masses. The left and right panel show the same on $M - q$ and $m_1 - m_2$ axes, respectively. The magenta lines, in both panels, shows the upper bound in total mass, below which frequency-domain PN waveforms can be used to construct template banks for aLIGO searches [100, 127]. The dash-dotted line in the right panel shows the lower mass limit on the smaller component object, to which a bank of currently available NR-PN hybrids can cover, i.e. $\min(m_1, m_2) = 12M_\odot$ (see Sec. 5.4). The blue (solid) curve in the right panel gives the lower mass limit to which a bank of currently available NR waveforms can cover (see Sec. 5.3). Thus, between the simulations listed in Table 2, and frequency domain PN waveforms, we can search for the entire range of BBH masses.

non-spinning BBHs with $q \leq 10$.

Having the set of required mass-ratios \mathcal{S}_q determined, we need to decide on the length requirements for the NR simulations, in order to control the PN hybridization error. For a series of matching frequencies, we construct NR-PN hybrids with Taylor{T1,T2,T3,T4} inspirals, and compute their pairwise mismatch as a function of total mass. The maximum of these mismatches serves a conservative bound on the PN-hybridization error for that hybrid (c.f. Eq. (5.16)). Fig. 21 shows the results of this calculation. Each panel of Fig. 21 focuses on one mass-ratio. Within each panel, each line represents one matching-frequency, with lines moving down toward earlier hybridization with smaller mismatches. Because the hybridization frequency is not particularly intuitive, the lines are labeled by the number of orbits of the NR portion of the hybrid-waveform. For a short number of orbits this calculation is indeed done with NR waveforms, whereas for large number of orbits, we substitute EOBNRv2 waveforms. The dashed lines represent the earliest one can match a NR+PN hybrid given the currently available NR waveforms, and are the same as the $q = 1, 4$, and 8 lines in Fig 15. The solid curves show the results using EOB hybrids, while the dotted curves (just barely visible) show the results with NR hybrids. They are virtually identical, which is a confirmation that EOB hybrids can act as a good proxy for NR hybrids in this case. The horizontal dotted line indicates a mismatch of 1.5%, while the vertical dotted line shows a lower mass limit for each mass ratio: $12M_\odot$ for $q = 1$, which is the point at which one can construct a template bank with only PN inspirals, $15M_\odot$ for $q = 4$, and $27M_\odot$ for $q = 8$, which are the lower mass limits if both component masses are $\geq 3M_\odot$.

Fig. 22 presents the information obtained in the previous paragraph in a different way. Given NR-PN hybrids with N orbits of NR, the shaded areas in the left panel of Fig. 22 indicate the region of parameter space for which such hybrids have hybridization errors smaller than 1.5%. As before, we see that for high masses, comparatively few NR orbits are sufficient (e.g. the purple $N = 15$ region), whereas lower total masses require increasingly more NR orbits. The dashed lines indicate the region of parameter space with hybrid error below 3%. The black dotted line designates the point where one component mass is greater than $3M_\odot$, which is a reasonable lower mass limit for a physical black hole. The right panel shows this same analysis instead with initial GW frequency indicated by the solid and dashed lines. Thus, for the

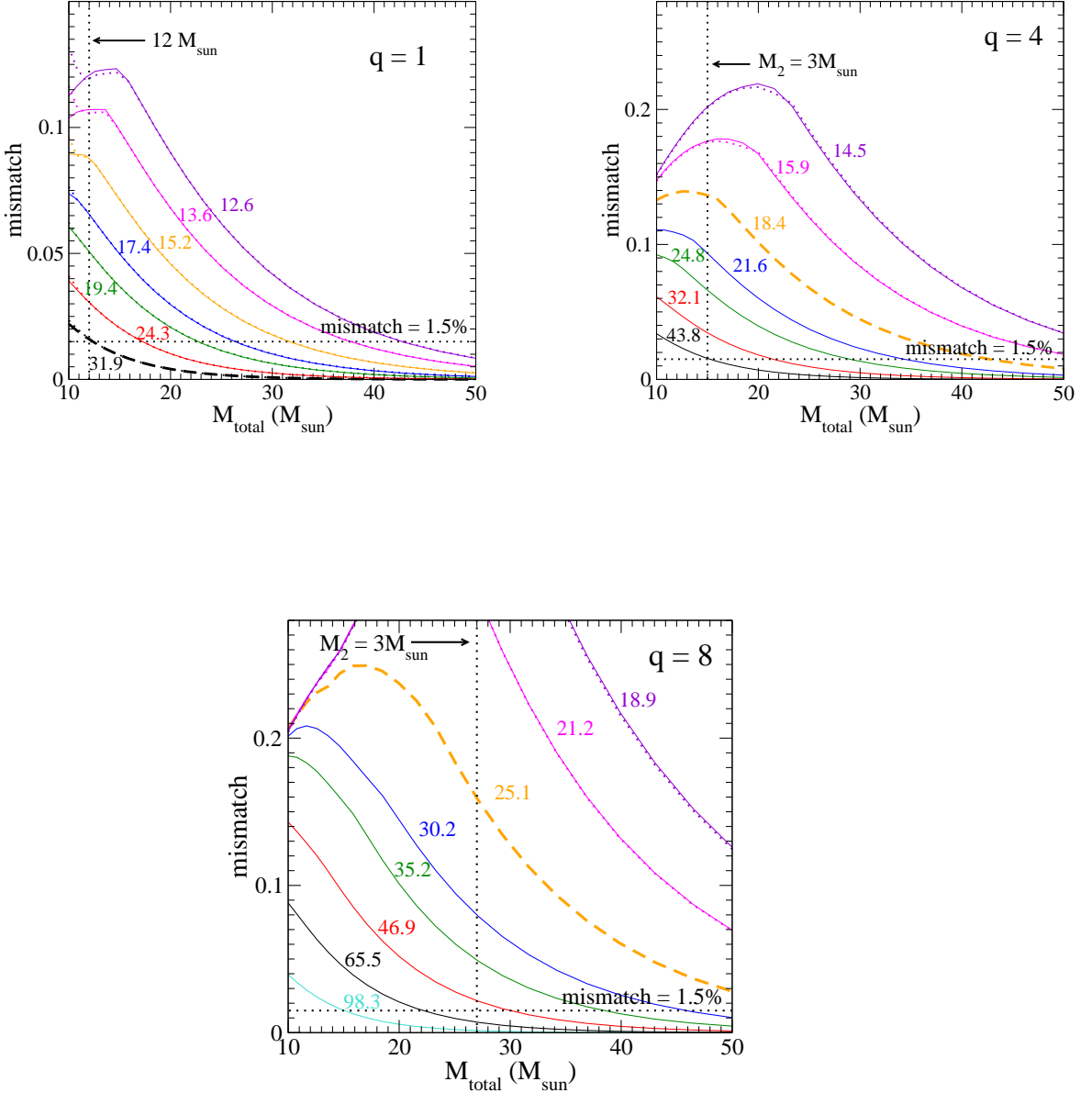


Figure 21: The maximum mismatch between different PN approximants for hybrid waveforms plotted against the total mass for at different matching frequencies ($M\omega_m$). The dotted lines indicate a mismatch of 1.5% and a lower total mass limit, $12M_\odot$ for $q = 1$, and $M_2 = 3M_\odot$ for $q = 4, 8$. The thick dashed lines indicate the currently possible matching frequency for hybrids based on the length of NR waveforms. The numbers next to each line indicate the number of orbits before merger where the PN and NR (or EOB) waveforms were stitched together.

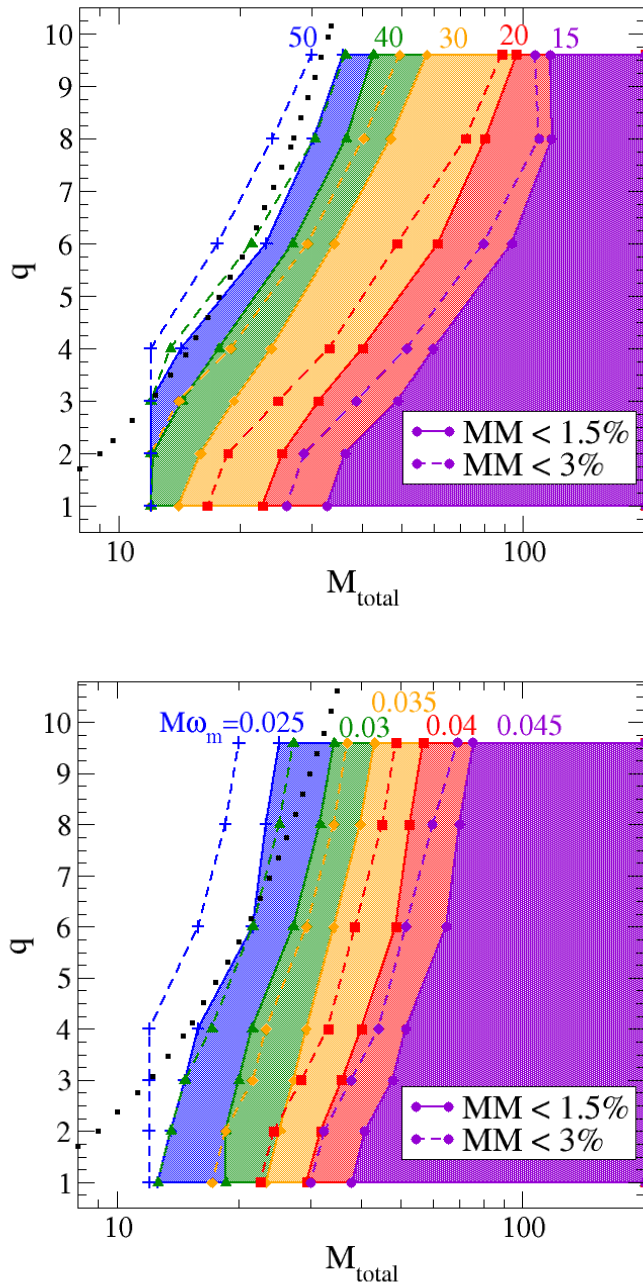


Figure 22: This plot shows the lower mass limit of a template bank constructed with hybrid waveforms in terms of the number of NR orbits (left panel) and initial gravitational wave frequency (right panel) needed to have a PN error below 1.5% (solid curves) or 3% (dashed curves). The dotted line indicates the lower total mass limit when one component mass is $3M_\odot$.

region of parameter space we're interested in, no more than ~ 50 NR orbits, or an initial GW frequency of $M\omega = 0.025$ would be necessary to construct a detection bank with hybrid mismatches below 1.5%.

5.6 Conclusions

The upgrades currently being installed to increase the sensitivity of the ground based interferometric gravitational-wave detectors LIGO and Virgo [25, 26] are scheduled to complete within the next two years. The second generation detectors will have a factor of 10 better sensitivity across the sensitive frequency band, with the lower frequency limit being pushed from 40Hz down to ~ 10 Hz. They will be able to detect GWs from stellar-mass BBHs up to distances of a few Gpc, with the expected frequency of detection between $0.4 - 1000 \text{ yr}^{-1}$ [28].

Gravitational-wave detection searches for BBHs operate by matched-filtering the detector data against a bank of modeled waveform templates [137, 81, 88, 85, 87, 86, 89]. Early LIGO-Virgo searches employed PN waveform template banks that spanned only the inspiral phase of the coalescence [14, 15, 16, 17, 10]. Recent work has shown that a similar bank of PN templates would be effectual for the advanced detectors, to detect non-spinning BBHs with $m_1 + m_2 \lesssim 12M_\odot$ [127, 100]. Searches from the observation period between 2005 – 07 and 2009 – 10 employed templates that also included the late-inspiral, merger and ringdown phases of binary coalescence [18, 19].

Recent advancements in Numerical Relativity have led to high-accuracy simulations of the late-inspiral and mergers of BBHs. The multi-domain SpEC code [114] has been used to perform simulations for non-spinning binaries with mass-ratios $q = 1, 2, 3, 4, 6, 8$ [115, 116, 37]. Owing to their high computational complexity, the length of these simulations varies between 15 – 33 orbits. Accurate modeling of the late-inspiral and merger phases is important for stellar mass BBHs, as they merge at frequencies that the advanced detectors would be sensitive to [127]. Analytic models, like those within the Effective-One-Body formalism, have been calibrated to the NR simulations to increase their accuracy during these phases [30, 56, 38, 117]. Other independent models have also been developed using information from NR simulations and their hybrids [138, 123, 39, 139]. An alternate derived prescription is that of NR+PN hybrid waveforms, that are constructed by joining long PN early-inspirals

and late-inspiral-merger simulations from NR [118, 119, 120, 121, 122].

NR has long sought to contribute template banks for gravitational-wave searches. Due to the restrictions on the length and number of NR waveforms, this has been conventionally pursued by calibrating intermediary waveform models, and using those for search templates. In this chapter, we explore the alternative of using NR waveforms and their hybrids directly in template banks. We demonstrate the feasibility of this idea for non-spinning binaries, and extending it to spinning binaries would be the subject of a future work. We find that with only six non-spinning NR simulations, we can cover down to $m_{1,2} \gtrsim 12M_\odot$. We show that with 26 additional NR simulations, we can complete the non-spinning template banks down to $M \simeq 12M_\odot$, below which existing PN waveforms have been shown to suffice for aLIGO. From template bank accuracy requirements, we are able to put a bound on the required length and initial GW frequencies for the new simulations. This method can therefore be used to lay down the parameters for future simulations.

First, we construct a bank for using pure-NR waveforms as templates, using a stochastic algorithm similar to Ref. [130, 131, 132]. The filter templates are constrained to mass-ratios for which we have NR simulations available, i.e. $q = 1, 2, 3, 4, 6, 8$. We assume that the simulations available to us are ≥ 20 orbits in length. To test the bank, we simulate a population of 100,000 BBH signals and filter them through the bank. The signals and templates are both modeled with the EOBNRv2 model [38]. We demonstrate that this bank is indeed effectual and recovers $\geq 97\%$ of the optimal SNR for GWs from BBHs with mass-ratios $1 \leq q \leq 10$ and chirp-mass $\mathcal{M}_c \equiv (m_1 + m_2)^{-1/5}(m_1 m_2)^{3/5}$ above $27M_\odot$. Fig. 13 shows this fraction at different simulated points over the binary mass space. With an additional simulation for $q = 9.2$, we are able to extend the coverage to higher mass-ratios. We show that a bank viable for NR waveform templates for $q = 1, 2, 3, 4, 6, 9.2$, would recover $\geq 97\%$ of the optimal SNR for BBHs with $10 \leq q \leq 11$. The SNR recovery fraction from such a bank is shown in Fig. 14.

Second, we construct effectual banks for currently available NR-PN hybrid waveform templates. We derive a bound on waveform model errors, which is independent of analytical models and can be used to independently assess the errors of such models (see Sec. 5.2 for details). This allows us to estimate the hybrid waveform mismatches due to PN error, which are negligible at high masses, and become significant at

lower binary masses. We take their contribution to the SNR loss into account while characterizing template banks. For hybrid banks, we demonstrate and compare two independent algorithms of template bank construction. First, we stochastically place a bank grid, as for the purely-NR template bank. Second, we lay down independent sub-banks for each mass-ratio, with a fixed overlap between neighboring templates, and take their union as the final bank. To test these banks, we simulate a population of 100,000 BBH signals and filter them through each. We simulate the GW signals and the templates using the recently developed EOBNRv2 model [38]. The fraction of the optimal SNR recovered by the two banks, before and after accounting for the hybrid errors, are shown in the left and right panels of Fig. 16 and Fig. 17 (respectively). We observe that for BBHs with $m_{1,2} \geq 12M_\odot$ hybrid template banks will recover $\geq 96.5\%$ of the optimal SNR. For testing the robustness of our conclusions, we also test the banks using TaylorT4+NR hybrid templates. The SNR recovery from a bank of these is shown in Fig. 18. We conclude that, the currently available NR+PN hybrid waveforms can be used as templates in a matched-filtering search for GWs from BBHs with $m_{1,2} \geq 12M_\odot$ and $1 \leq q \leq 10$. The number of templates required to provide coverage over this region was found to be comparable to a bank constructed using the second-order post-Newtonian TaylorF2 hexagonal template placement method [86, 87, 88, 89]. The two algorithms we demonstrate yield grids of 667 and 627 templates, respectively; while the metric based placement method yields a grid of 522 and 736 templates, for 97% and 98% minimal match, respectively.

At lower mass, the length of the waveform in the sensitive frequency band of the detectors increases, increasing the resolution of the matched-filter. We therefore see regions of undercoverage between mass ratios for which we have NR/hybrid templates (see, e.g. Fig. 17 at the left edge). For $M \lesssim 12M_\odot$, existing PN waveforms were shown to be sufficient for aLIGO searches. We find the additional simulations that would be needed to extend the hybrid tempalte bank down to $12M_\odot$. We show that a bank of hybrids restricted to the 26 mass-ratios listed in Table 2 would be sufficiently dense at $12M_\odot$. This demonstrates that the method proposed here can be used to decide which NR simulations should be prioritized for the purpose of the GW detection problem. By filtering a population of 100,000 BBH signals through this bank, we show that the SNR loss due to its discreteness stays below 2% over the entire relevant range

of masses. The fraction of optimal SNR recovered is shown in Fig. 20. Constraining the detection rate loss below 10% requires that detection template banks recover more than 96.5% of the optimal SNR. Therefore our bank would need hybrids with hybridization mismatches below 1.5%. From this accuracy requirement, we obtain the length requirement for all the 26 simulations. This is depicted in the left panel of Fig. 22, where we show the region of the mass space that can be covered with hybrids, as the length of their NR portion varies. We find that for $1 \leq q \leq 10$ the new simulations should be about 50 orbits in length. In the right panel of Fig. 22 we show the corresponding initial GW frequencies. The requirement of ~ 50 orbit long NR simulations is ambitious, but certainly feasible with the current BBH simulation technology [128].

In summary, we refer to the right panel of Fig. 20. The region above the dashed (red) line and above the solid (blue) line can be covered with a bank of purely-NR waveforms currently available. The region above the dashed (red) and the dash-dotted (black) line can be covered with the same simulations hybridized to long PN inspirals. With an additional set of NR simulations summarized in Table 2, the coverage of the bank can be extended down to the magenta (solid) line in the lower left corner of the figure. Thus between hybrids and PN waveforms, we can cover the entire non-spinning BBH space. The ability to use hybrid waveforms within the software infrastructure of the LIGO-Virgo collaboration has been demonstrated in the NINJA-2 collaboration [129]. The template banks we present here can be directly used in aLIGO searches. This work will be most useful when extended to aligned spin and precessing binaries [140, 141], which is the subject of a future work.

The detector noise power is modeled using the zero-detuning high-power noise curve for Advanced LIGO [90]. The construction of our template banks is sensitive to the breadth of the frequency range that the detector would be sensitive to. The noise curve we use is the broad-band final design sensitivity estimate. For lower sensitivities at the low/high frequencies, our results would become more conservative, i.e. the template banks would over-cover (and not under-cover).

We finally note that in this chapter we have only considered the dominant (2, 2) mode of the spherical decomposition of the gravitational waveform. For high mass-ratios and high binary masses, other modes would also become important, both for spinning as well as non-spinning black hole binaries [102, 127, 142]. Thus, in future

work, it would be relevant to examine the sub-dominant modes of the gravitational waves. Lastly, though we have looked at the feasibility of using this template bank for Advanced LIGO as a single detector, this instrument will be part of a network of detectors, which comes with increased sensitivity and sky localization. For this reason, in subsequent studies it would be useful to consider a network of detectors.

Chapter 6

NINJA-2: Detecting gravitational waveforms modelled using numerical binary black hole simulations

Of the stellar mass black hole angular momenta (spin) measurements made to date, half are found to have a magnitude $a \gtrsim 0.8$ [143]. With BBH observations, aLIGO and AdV will be able to provide independent measurements of the black hole spin magnitudes. Therefore, it will be interesting to evaluate how well aLIGO and AdV will be able to constrain the magnitude of the black holes' component spins. The direction of the compact objects' angular momenta is also of interest, with particular implications for formation mechanisms [144]. Measuring systems with component spins misaligned with the orbital angular momentum is outside of the scope of this project. However, this study does include systems with component spins that are both aligned and anti-aligned with the orbital angular momenta, and we will evaluate the ability of aLIGO and AdV to distinguish such systems from one another. Since 2007, NR waveforms have been used to calibrate analytical waveform models [106, 145, 146, 117, 147, 39, 148, 149]. Some of the analytical waveforms have been already employed in search pipelines [19]. However, there exists another useful and valuable avenue of communication between numerical relativists and gravitational-wave astronomers. As NR pushes into new regions of parameter space the waveforms can be used directly

to test searches employing previously-calibrated templates, and the degree to which these searches prove to be insufficient can motivate both new template models and additional simulations.

The Numerical INjection Analysis (NINJA) project was created in 2008. The project uses recent advances in numerical relativity ([150] and references therein) to test analysis pipelines by adding numerically-modelled, physically-realistic signals to detector noise and attempting to recover these signals with search pipelines. The first NINJA project (NINJA-1) [126] utilized a total of 23 numerical waveforms, which were injected into Gaussian noise colored with the frequency sensitivity of initial LIGO and Virgo. These data were analyzed by nine data-analysis groups using both search and parameter-estimation algorithms [126].

However, there were four limitations to the NINJA-1 analysis. First, due to the computational cost of NR simulations, most waveforms included only ~ 10 orbits before merger. Therefore the waveforms were too short to inject over an astrophysically interesting mass range without introducing artifacts into the data. The lowest mass binary considered in NINJA-1 had a total mass of $35M_{\odot}$, whereas the mass of black holes could extend below $5M_{\odot}$ [151, 80]. Second, the waveforms were only inspected for obvious, pathological errors and no cross-checks were performed between the submitted waveforms. It was therefore difficult to assess the physical fidelity of the results. Third, the NINJA-1 data set contained stationary noise with the simulated signals already injected into the data. Since the data set lacked the non-Gaussian noise transients present in real detector data, it was not possible to fully explore the response of the algorithms in a real search scenario. Finally, the data set contained only 126 simulated signals, this precluded detailed statistical studies of the effectiveness of search and parameter estimation algorithms. Despite these limitations, the NINJA-1 project lead to a framework within which to perform injection studies using waveforms as calculated by the full nonlinear general theory of relativity, established guidelines for such studies (in particular a well-defined format for the exchange of NR waveforms [152]), and clarified where further work was needed.

This lead to the initiation of the second NINJA project (NINJA-2), whose goals were to build and improve upon NINJA-1 and perform a systematic test of the efficiency of data-analysis pipelines in preparation for the Advanced detector era. A set of 60 NR waveforms were submitted by 8 numerical relativity groups for the NINJA-2

project [153]. These waveforms conform to a set of length and accuracy requirements, and are attached to PN inspiral signals to produce hybrid PN-NR waveforms that can be injected over the full range of physically relevant total binary masses. The construction and verification of these waveforms is described in [153], and summarized here in section 6.1. In the Numerical-Relativity and Analytical-Relativity collaboration, a project complementary to the NINJA collaboration, 22 new NR waveforms were produced and rigorously analysed. These newly produced NR waveforms were compared to the most recent calibrated analytical models, finding that the loss of event rates due to modeling is below 3% [154].

In this chapter we study the ability of a search algorithm (called “*ihope*”) that was used in the last of the Initial LIGO and Virgo science runs to observe numerically-modelled BBH waveforms from the set of 60 waveforms submitted to the NINJA-2 project. The *ihope* search pipeline is under constant development and re-tuning. For both practical reasons, and to mark a clear point in the development and refinement of the methods, we employed *only* the search methods that were approved and used in the last initial-LIGO and Virgo science runs, *without any additional tuning or modifications* [137, 19, 12]. By doing this we aim to provide a benchmark against which future algorithms can be compared. The data set used was obtained by recoloring actual detector data taken during LIGO’s sixth and Virgo’s second science runs to the sensitivity expected during the early science runs of Advanced LIGO and Virgo.

A set of 7 numerical relativity waveforms, with masses ranging from $14.4M_{\odot}$ to $124M_{\odot}$ were added into the recolored data as an unbiased test of the process through which candidate events are identified for BBH waveforms. This data was distributed to analysts who knew that such “blind injections” were present but had no information about the number, parameters or temporal location of these waveforms. Two independent *ihope* analysis were performed over the data. One focused on *low-mass* binaries with $2M_{\odot} \leq m_1 + m_2 \leq 25M_{\odot}$, and the other on *high-mass* binaries with $25 < M_{\odot} \leq m_1 + m_2 \leq 100M_{\odot}$. Between the two analyses, 6 of the injected signals were recovered with more significance than all background events. This allowed upper limits on the false alarm rate ranging between 1 every 5800 years and 1 every 31000 years to be placed on each blind injection. The remaining signal was not recovered due to having a low network signal-to-noise ratio and possessing a large anti-aligned spin, which was not modelled in the bank of waveforms used in the search.

In this chapter we describe the *low-mass ihope* analysis, a modelled search for the 7 blind injections using frequency domain TaylorF2 waveforms for templates with total mass $< 25M_{\odot}$. Also, as in most of this dissertation, we have not scaled observed masses and distances to account for cosmological effects, which will be important especially for high-mass binary black hole collisions. Therefore any masses and distances quoted should be interpreted as *observed* masses and *luminosity* distances.

The remainder of the chapter is organized as follows: In section 6.1 we briefly summarize the waveform catalogue described more fully in [153]. Section 6.2 describes the LIGO/Virgo data used and the processing that was done to make it resemble anticipated advanced-detector noise. Section 6.3 describes how the parameters for the blind injections were chosen and reports the values that were selected. Section 6.4 describes the detection algorithms used in our analysis. Section 6.5 reports the results of the modelled search for the 7 blind injections. We conclude in section 6.6 with a discussion of how well the search algorithm performed, and implications for the Advanced detector era.

6.1 PN-NR Hybrid Waveforms

The NINJA-2 waveform catalog contains 60 PN-NR hybrid waveforms that were contributed by eight numerical relativity groups. This catalog and the procedures used to validate it are described in detail in [153]. We briefly summarize the NINJA-2 catalog here.

Each waveform in the NINJA-2 waveform catalog consists of a PN portion modelling the early inspiral, stitched to a numerical portion modelling the late inspiral, merger and ringdown. This ensures accurate modelling of the late portions of the waveform while simultaneously ensuring that waveforms are long enough to be scaled to masses as low as $10M_{\odot}$ without starting abruptly within the sensitive frequency band of the detectors. We require that for the NR portion of the waveform the amplitude be accurate to within 5% and the phase (as a function of gravitational-wave frequency) have an accumulated uncertainty over the inspiral, merger and ringdown of no more than 0.5 rad. Since we do not have access to exact waveforms we define “accuracy” by convergence of the numerical waveforms as resolution and waveform-extraction radius are increased. We also require at least five orbits of numerical data

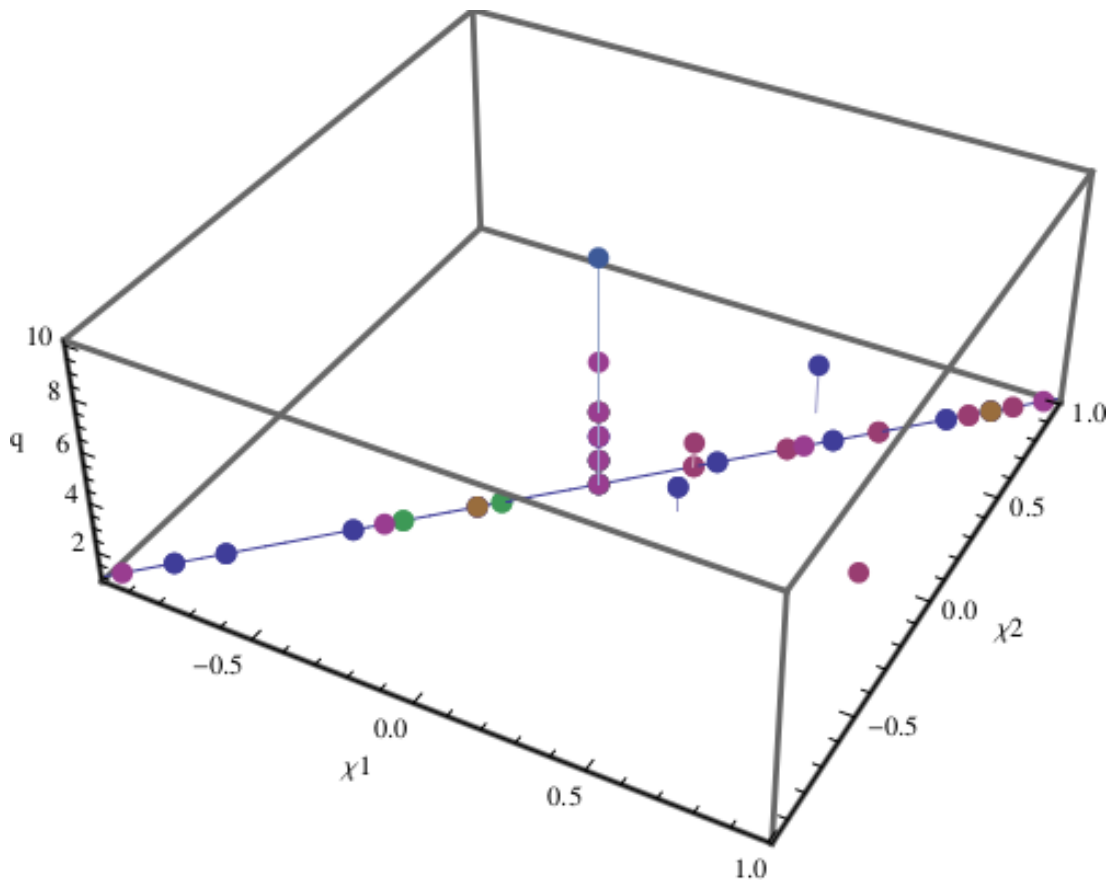


Figure 23: Mass ratio q and dimensionless spins χ_i of the NINJA-2 hybrid waveform submissions. Reproduced from [153].

in order to ensure robust blending with the PN portion. No requirements were placed on the hybridization itself, although it is known that hybridization can introduce significant errors [119, 39, 155]. It was decided to limit NINJA-2 to systems without eccentricity, and with black-hole spins parallel or anti-parallel to the orbital angular momentum. This last condition avoids precession, which we do for two reasons; (i) precession greatly complicates waveform phenomenology and we prefer to first tackle a simpler subset which still maintains the main features of binary evolution and merger; and (ii) at the start of NINJA-2 the precessing-binary parameter space had been sampled by only a handful of numerical simulations. Waveforms were submitted in the format described in [152], and data was provided as strain decomposed into spherical harmonics of weight -2 . Groups were encouraged to submit modes beyond $(l, m) = (2, \pm 2)$ and many did so. However the techniques to validate these higher modes are a current research topic. In order not to delay the NINJA-2 project it was decided to validate only the $(2, \pm 2)$ modes in [153] and employ only these modes for the first NINJA-2 analysis. Different groups employed different codes, as well as different methods for solving initial conditions, dealing with singularities, evolving Einstein’s equations, and extracting gravitational-wave information. In addition different PN approximants and different hybridization methods were used by different groups in constructing the full hybrid waveforms. It was found that the dominant source of disagreement between submissions was in the PN portion, and in particular overlaps between submissions were greater than 0.97 over the range of masses, including regions sensitive to differences in hybridization techniques. See [153] for details.

The parameter space for aligned-spin BBH systems is four dimensional; the masses and spin magnitudes of each of the two holes. However, in the absence of matter Einstein’s equations possess a mass invariance, and a solution obtained by numerical relativity or other method may be trivially rescaled to any total mass. We therefore eliminate total mass from the parameter space of submissions leaving the ratio of the two masses, denoted q , and the dimensionless spins denoted $\chi_{1,2}$ which must lie between $-1 < \chi_{1,2} < 1$.

Tables 3 and 4 give a summary of the submissions for systems where the masses of the two black holes are equal and unequal, respectively. The first column of Tables 3 and 4 gives a label for each waveform, to ease referring to them in later sections.

These labels of the form “G2+20+20_T4” are constructed as follows: The first letter represents the group submitting the numerical simulation:

- F:** The numerical relativity group at Florida Atlantic University, also using the BAM code [156, 157, 158, 159].
- G:** The Georgia Tech group using MayaKrac [160, 161, 162, 163, 164, 165, 166]
- J:** The BAM (Jena) code, as used by the Cardiff-Jena-Palma-Vienna collaboration [167, 168, 147, 169, 157, 170]
- L:** The Lean Code, developed by Ulrich Sperhake [171, 172].
- Li:** The Llama code, used by the AEI group and the Palma-Caltech groups [173, 174, 175]
- R:** The group from Rochester Institute of Technology, using the LazEv code [35, 176, 177, 178].
- S:** The SXS collaboration using the SpEC code [179, 180, 181, 182, 183, 134, 184, 185, 111, 186].
- U:** The group from The University of Illinois [187].

Immediately after this letter follows the mass-ratio $q = m_1/m_2$, where the black holes are labeled such that $q \geq 1$. Subsequently are the components of the initial dimensionless spin along the orbital angular momentum, multiplied by 100 (e.g. ‘+20’ corresponds to $\hat{L} \cdot \vec{S}_1/m_1^2 = 0.2$) of the more massive and the less massive black hole. The label closes with the Taylor-approximant being used for the PN portion of the waveform, with “T1” and “T4” representing TaylorT1 and TaylorT4, respectively. The Georgia Tech group submitted four pairs of simulations where each pair simulates systems with identical physical parameters, stitched to the same PN approximant. These waveforms are not identical however as each simulation within a pair has a different number of NR cycles and was generated at a different resolution. These are distinguished by appending “_1” and “_2” to the label.

Each NR group verified that their waveforms met the minimum NINJA-2 requirements as described above. The minimum-five-orbits requirement was easily verified

by inspection, and the amplitude and phase uncertainties were estimated by convergence tests with respect to numerical resolution and waveform-extraction radius. The full catalog was then verified by the NINJA-2 collaboration. Submissions were inspected in the time and frequency domains to identify any obvious problems caused by hybridization or integration from the Newman-Penrose curvature scalar ψ_4 to strain. Where multiple simulations were available for the same physical parameters these simulations were compared using the matched-filter *overlap*. The inner product $(s_1 | s_2)$ between two real waveforms $s_1(t)$ and $s_2(t)$ is defined in Eq. 4.1, where $S_n(f)$ is the power spectral density, which was taken to be the target sensitivity for the first advanced-detector runs, referred to as the “early aLIGO” PSD. This is described in more detail in section 6.2.

The overlap is then obtained by normalization and maximization over relative time and phase shifts, Δt and $\Delta\phi$.

$$\mathcal{O}(s_1, s_2) := \max_{\Delta t, \Delta\phi} \frac{(s_1 | s_2)}{\sqrt{(s_1 | s_1)(s_2 | s_2)}}, \quad (6.1)$$

which is the same as Eq. 5.5. The investigations in [153] demonstrated that the submitted waveforms met the requirements as outlined above and in addition were consistent with each other to the extent expected. We therefore conclude that these submissions model real gravitational waves with sufficient accuracy to quantitatively determine how data-analysis pipelines will respond to signals in next-generation gravitational-wave observatories.

The NINJA-2 waveforms cover the 3-dimensional aligned-spin parameter space rather unevenly, as indicated in figure 23. The configurations available fall predominantly into two 1-dimensional subspaces: (i) Binaries of varying mass-ratio, but with non-spinning black holes. (ii) Binaries of black holes with equal-mass and equal-spin, and with varying spin-magnitude. Future studies, with additional waveforms covering the gaps that are clearly evident in figure 23 and waveforms including precession [188, 37, 154], would be useful to more fully understand the response of search codes across the parameter space, and would help to better tune analytical waveform models including inspiral, merger and ringdown phases.

Table 3: Summary of the contributions to the NINJA-2 waveform catalog with $m_1 = m_2$. Given are an identifying label, described in section 6.1, mass-ratio $q = m_1/m_2$ which is always 1 for these simulations, magnitude of the dimensionless spins $\chi_i = S_i/m_i^2$, orbital eccentricity e , frequency range of hybridization in $M\omega$, the number of numerical cycles from the middle of the hybridization region through the peak amplitude, and the post-Newtonian Taylor-approximant(s) used for hybridization.

Label	q	χ_1	χ_2	$1000e$	$100 M\omega$ hyb.range	# NR cycles	pN Approx
S1-95-95_T1	1.0	-0.95	-0.95	1.00	3.3 – 4.1	18.42	T1
J1-85-85_T1	1.0	-0.85	-0.85	2.50	4.1 – 4.7	12.09	T1
J1-85-85_T4							T4
J1-75-75_T1	1.0	-0.75	-0.75	1.60	4.1 – 4.7	13.42	T1
J1-75-75_T4							T4
J1-50-50_T1	1.0	-0.50	-0.50	2.90	4.3 – 4.7	15.12	T1
J1-50-50_T4							T4
S1-44-44_T4	1.0	-0.44	-0.44	0.04	4.3 – 5.3	13.47	T4
Ll1-40-40_T1	1.0	-0.40	-0.40		6.1 – 8.0	6.42	T1
Ll1-40-40_T4							T4
J1-25-25_T1	1.0	-0.25	-0.25	2.50	4.5 – 5.0	15.15	T1
J1-25-25_T4							T4
Ll1-20-20_T1	1.0	-0.20	-0.20		5.7 – 7.8	8.16	T1
Ll1-20-20_T4							T4
J1+00+00_T1	1.0	0.00	0.00	1.80	4.6 – 5.1	15.72	T1
J1+00+00_T4							T4
G1+00+00_T4				3.00	5.5 – 7.5	9.77	T4
Ll1+00+00_F2					5.7 – 9.4	8.30	F2
S1+00+00_T4				0.05	3.6 – 4.5	22.98	T4
G1+20+20_T4_1	1.0	0.20	0.20	10.00	6.0 – 7.5	6.77	T4
G1+20+20_T4_2				6.00	5.5 – 7.5	10.96	T4
J1+25+25_T1	1.0	0.25	0.25	6.10	4.6 – 5.0	18.00	T1
J1+25+25_T4							T4
G1+40+40_T4_1	1.0	0.40	0.40	10.00	5.9 – 7.5	7.70	T4
G1+40+40_T4_2				6.00	5.5 – 7.5	12.02	T4
Ll1+40+40_T1					7.8 – 8.6	6.54	T1
Ll1+40+40_T4							T4
S1+44+44_T4	1.0	0.44	0.44	0.02	4.1 – 5.0	22.39	T4
J1+50+50_T1	1.0	0.50	0.50	6.10	5.2 – 5.9	15.71	T1
J1+50+50_T4							T4
G1+60+60_T4_1	1.0	0.60	0.60	12.00	6.0 – 7.5	8.56	T4
G1+60+60_T4_2				5.00	5.5 – 7.5	13.21	T4
J1+75+75_T1	1.0	0.75	0.75	6.00	6.0 – 7.0	14.03	T1
J1+75+75_T4							T4
G1+80+00_T4	1.0	0.80	0.00	13.00	5.5 – 7.5	12.26	T4
G1+80+80_T4_1	1.0	0.80	0.80	14.00	5.9 – 7.5	9.57	T4
G1+80+80_T4_2				6.70	5.5 – 7.5	14.25	T4
J1+85+85_T1	1.0	0.85	0.85	5.00	5.9 – 6.9	15.36	T1
J1+85+85_T4							T4
U1+85+85_T1				20.00	5.9 – 7.0	15.02	T1

Table 4: Summary of the contributions to the NINJA-2 waveform catalog with $m_1 > m_2$. Given are an identifying label, described in section 6.1, mass-ratio $q = m_1/m_2$ magnitude of the dimensionless spins $\chi_i = S_i/m_i^2$, orbital eccentricity e , frequency range of hybridization in $M\omega$, the number of numerical cycles from the middle of the hybridization region through the peak amplitude, and the post-Newtonian Taylor-approximant(s) used for hybridization.

Label	q	χ_1	χ_2	$1000e$	$100 M\omega$ hyb.range	# NR cycles	pN Approx
J2+00+00_T1	2.0	0.00	0.00	2.30	6.3 – 7.8	8.31	T1
J2+00+00_T4							T4
G2+00+00_T4				2.50	5.5 – 7.5	10.42	T4
Ll2+00+00_F2					6.3 – 9.4	7.47	F2
S2+00+00_T2				0.03	3.8 – 4.7	22.34	T2
G2+20+20_T4	2.0	0.20	0.20	10.00	5.6 – 7.5	11.50	T4
J2+25+00_T1	2.0	0.25	0.00	2.00	5.0 – 5.6	15.93	T1
J2+25+00_T4							T4
J3+00+00_T1	3.0	0.00	0.00	1.60	6.0 – 7.1	10.61	T1
J3+00+00_T4							T4
S3+00+00_T2				0.02	4.1 – 5.2	21.80	T2
F3+60+40_T4	3.0	0.60	0.40	1.00	5.0 – 5.6	18.89	T4
J4+00+00_T1	4.0	0.00	0.00	2.60	5.9 – 6.8	12.38	T1
J4+00+00_T4							T4
L4+00+00_T1				5.00	5.1 – 5.5	17.33	T1
S4+00+00_T2				0.03	4.4 – 5.5	21.67	T2
S6+00+00_T1	6.0	0.00	0.00	0.04	4.1 – 4.6	33.77	T1
R10+00+00_T4	10.0	0.00	0.00	0.40	7.3 – 7.4	14.44	T4

6.2 Modified Detector Noise

We stress here that the production of the final noise data set, which emulated data that will be taken by second generation gravitational wave observatories, was performed by members of the NINJA-2 collaboration who are not the authors of this dissertation. However, we find it useful to present a brief description of the same here. The noise emulation was accomplished by recoloring data taken from the initial LIGO and Virgo instruments to predicted 2015 – 2016 sensitivities. Recoloring initial LIGO and Virgo data allows the non-Gaussianity and non-stationarity of that data to be maintained.

The predicted sensitivity curves of the advanced detectors as a function of time can be found in the living document [27]. For this work we are interested in the sensitivity of the advanced detectors in 2015 – 2016 and used a previous prediction of the sensitivity curves for this time period as given in [189] and shown in the left panel of figure 24. These curves were used as the updated predictions given in [27] were not available when we began this study. We refer to the 2015 – 2016 predicted noise curves as the *early* sensitivity curves. It is clear from the figure that the predicted sensitivity of early AdV is significantly greater than that of the early aLIGO curve, when using the predictions given in [189]. In the right panel of figure 24 we show the distance at which optimally oriented, optimally located, non-spinning, equal mass binaries would be detected with a signal-to-noise ratio (SNR) of 8 using both noise curves. This is commonly referred to as the *horizon distance*. The early AdV noise curve was rescaled by a factor of 1.61 so that the sensitive distance for a ($10 M_{\odot}$, $10 M_{\odot}$) binary merger would be equal to the early aLIGO noise curve. This rescaling was found to better reflect the updated predicted sensitivities presented in [27]. The results in this chapter were generated using the early aLIGO and rescaled early AdV sensitivity curves.

As with the initial science runs, we expect data taken from these detectors, in the absence of gravitational-wave signals, to be neither Gaussian nor stationary. It is important that search pipelines demonstrate an ability to deal with these features. To simulate data with advanced detector sensitivities and with realistic non-Gaussian and non-stationary features, we chose to use data recorded by initial LIGO and Virgo and recolor that data to the predicted early sensitivity curves of aLIGO and AdV.

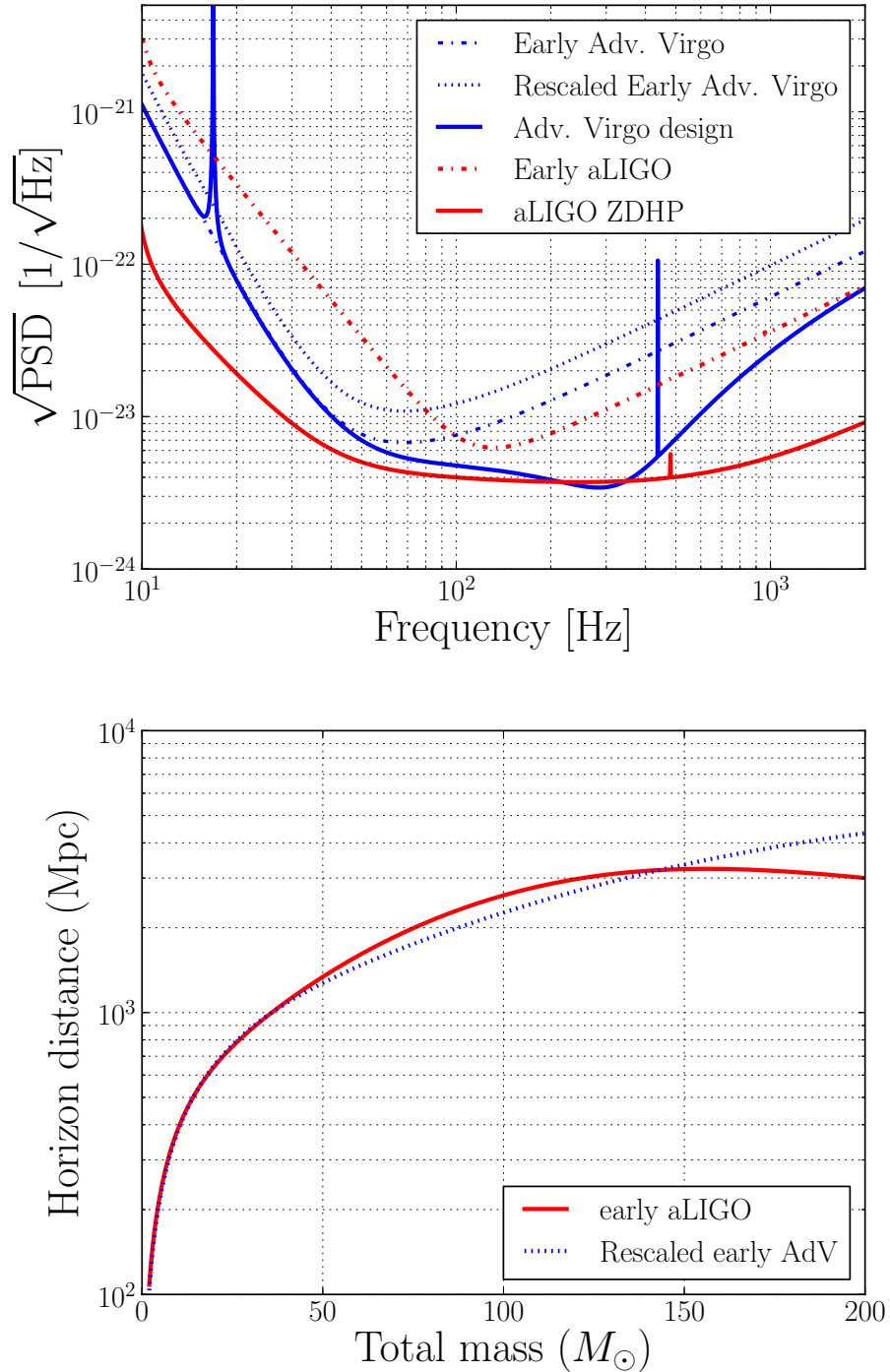


Figure 24: Top: predicted sensitivity curves for aLIGO and AdV. Shown are both the design curves and predicted 2015 – 2016 *early* sensitivity curves. Also shown is the early Adv noise curve rescaled such that the horizon distance for a ($10 M_\odot$, $10 M_\odot$) binary system is equal to that obtained with the early aLIGO noise curve. Bottom: Horizon distance as a function of observed total mass for the early aLIGO and rescaled early AdV sensitivity curves. This plot is made considering only equal mass, non-spinning systems and calculated using the EOBNRv2 [146] waveform approximant. Results in this paper are generated from the early aLIGO noise curve and the rescaled early AdV curve.

The data we chose to recolor was data taken during LIGO’s sixth science run and Virgo’s second science run.

The procedure for producing such *recolored data* was accomplished in the following steps, which were conducted separately for the two LIGO detectors and Virgo.

- Identify a two-month duration of initial detector data to be recolored
- Measure the power spectral density (PSD) for each distinct section of science mode data using the PSD estimation routines in the `lal` software package [67].
- Calculate an *average PSD* over the two month period by taking, for every discrete value of frequency recorded in the PSDs, the median value over each of the PSDs in the set.
- Remove any sharp (*line-like*) features from the resulting PSD and from the predicted early noise curves. This is done because it is difficult to remove or introduce line features from the data without introducing unwanted artifacts. Therefore it is simpler to remove line features in the PSDs, which will have the effect of preserving the line features of the original data into the recolored data.
- For each frequency bin, record the median value of the PSD over each section of science mode
- Take the ratio of the median PSD and the predicted early advanced detector noise curve. This is the reweighting to be used when recoloring.
- Using the time domain filtering abilities of the `gstlal` software package [190], recolor the data using this reweighting factor.

In figure 25 we show some examples of the PSDs obtained from recoloring the data and compare with the predicted sensitivity curves. As there are some small stretches of data in the original science runs where the sensitivity was significantly different from the average, we show the 10 % and 90 % quantiles as well as the maximum and minimum values for the PSD of the recolored data. We notice that the sensitivity of the detector still varies with time, as in the initial data, and that the lines in the initial spectra are still present.

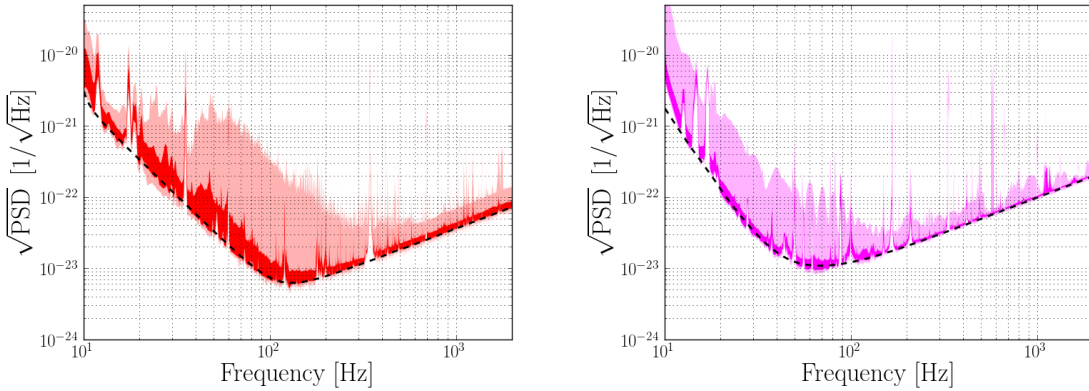


Figure 25: Sensitivity curves of the recolored data for the LIGO Hanford detector (left) and the Virgo detector (right). In both cases the black dashed line shows the predicted 2015 – 2016 sensitivity curve (with the scaling factor added for Virgo). The dark colored region indicates the range between the 10 % and 90 % quantiles of the PSD over time. The lighter region shows the range between the minimum and maximum of the PSD over time.

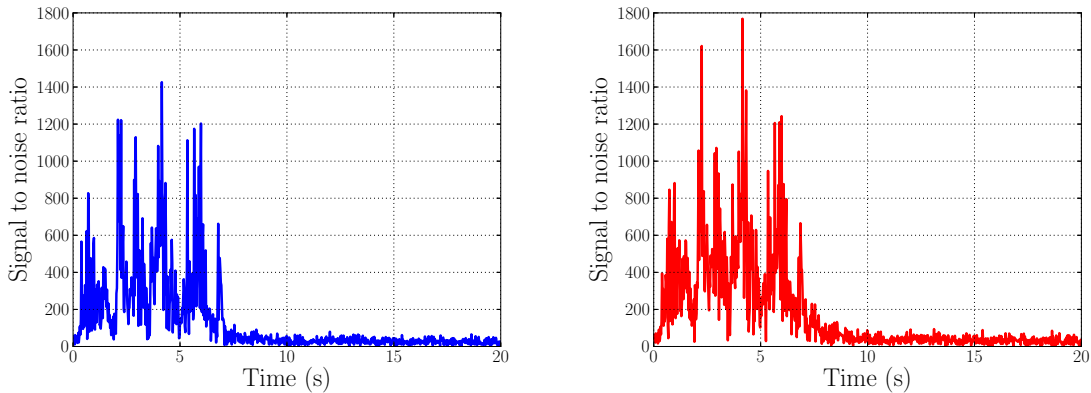


Figure 26: SNR time series in a 20 s window around a known glitch in the original data (left) and in the recolored data (right). While the SNR time series clearly change, the primary features of the glitch are preserved across the recoloring procedure. These SNR time series were obtained by matched-filtering a short stretch of recolored and original data against a (23.7,1.3) M_{\odot} template.

Non-Gaussian features present in the original data will still be present in the recolored data, albeit distorted by the recoloring process. An example of this is shown in figure 26 where we show the SNR time-series around a known glitch in both the original and recolored data. While the recoloring does have some effect on the glitch, the two SNR time series are very comparable. As in searches on the original data, we attempt to mitigate the effect of such features. A set of *data quality flags* were created for the initial detector data [191, 192]. These attempt to flag times where a known instrumental or environmental factor, which is known to produce non-Gaussian artifacts in the resulting strain data, was present. To simulate these data quality flags in our recolored data we simply used the same flags that were present in the original data and apply them to the recolored data.

6.3 Injection Parameters

As an unbiased test of the process through which candidate events are identified for BBH waveforms, 7 BBH waveforms were added to the recolored data. This was performed by one member of the collaboration, who is not the author of this dissertation. We were aware that “blind injections” had been added, however the number and parameters of these simulated signals were not disclosed until the analysis was completed. This was similar to blind injection tests conducted by the LIGO and Virgo collaborations in their latest science runs [193]. These injections are self-blinded to ensure that no bias from knowing the parameters of the signal, or indeed whether a candidate event is a signal or a noise artifact, affects the analysis process.

The 7 waveforms added to the data were taken from the numerical relativity simulations discussed in section 6.1. The parameters of the blind injections are given in Table 5. The distribution of physical parameters used in these blind injections was not intended to represent any physical distribution. Instead, the injections were chosen to test the ability to recover BBH systems across a wide range of parameter space.

Table 5: The details of the blind injections that were added to the NINJA-2 datasets prior to analysis. In this table the Event ID will be used throughout the paper to refer to specific injections. The network SNR of each injection is denoted by ρ_N . This is the sum of the overlaps of the injection with itself in each detector, using 30 Hz as the starting frequency in the overlap integrals. M denotes the total mass and q the mass ratio. χ denotes the spin on *each* black hole, in all 7 cases both black holes in the binary had the same spin. RA and dec give the right ascension and declination of the signals respectively. Dist. denotes the distance to the source. Detectors online lists the detectors for which data is present at the time of signal. Hybridization range gives the range of frequencies in which the signal is hybridized between the post-Newtonian and numerical components. Waveform label indicates which numerical waveform was used, as shown in Tables 3 and 4.

Event ID	Waveform label	ρ_N	q	M (M_\odot)	χ	RA (rad)	Dec. (rad)	Dist. (Mpc)	Detectors Online	Hybrid Range (Hz)
1	J4+00+00_T4	23.9	4	124	0.00	1.26	-0.76	569	HLV	15 – 18
2	Ll1-20-20_T4	14.1	1	35.5	-0.20	1.70	-0.03	244	HLV	52 – 71
3	Ll1+40+40_T4	16.2	1	14.4	0.40	4.18	0.07	170	HLV	175 – 193
4	G2+20+20_T4	15.1	2	26.8	0.20	2.19	-0.36	247	LV	68 – 90
5	L4+00+00_T1	19.2	4	19.1	0.00	1.68	0.14	83	HV	86 – 93
6	J1+25+25_T4	16.9	1	75.7	0.25	4.68	0.49	854	HV	20 – 21
7	J1-75-75_T1	9.8	1	19.3	-0.75	0.81	-0.07	292	HLV	69 – 79

6.4 Search Pipelines

The goal of this work was to evaluate the detection sensitivity to binary black hole systems, modelled from the latest numerical simulations, using the search pipelines that were used to search for gravitational-wave transient signals in data taken during the final initial LIGO and Virgo joint observing run. The two pipelines that were used to do this were the dedicated compact binary coalescence (CBC) search pipeline “`ihope`” [17, 16, 18, 193, 19, 137] and the unmodelled burst pipeline “Coherent Wave-Burst” (cWB) [194, 11, 12, 195]. In this dissertation, we will focus on the modeled `ihope` pipeline. The `ihope` pipeline was developed as a search pipeline for detecting compact binary mergers. It employs a matched-filtering algorithm against a bank of template waveforms [137]. It was used to search for CBC systems (not just binary black holes) with component masses $\in [1, 99] M_\odot$.

In addition to the `ihope` and cWB detection pipelines parameter estimation algorithms were used to provide estimates of the parameters of compact binary systems observed with the detection algorithms. However, we will not focus on those here. In

this section we provide a brief overview of the detection pipeline `ihope`. The results of running the `ihope` searches on the data containing the NINJA-2 blind injections are presented in section 6.5.

6.4.1 `ihope`

The `ihope` pipeline is designed to search for gravitational waves emitted by coalescing compact binaries [137]. It has been optimized for and used in LIGO and Virgo GW searches over the past decade [196, 17, 16, 15, 193, 19], and also in the mock Laser Interferometer Space Antenna (LISA) data challenges [197]. The NINJA-2 `ihope` analysis uses the same pipeline-tuning that was used in the searches performed during the final initial LIGO and Virgo joint observing run [193].

The pipeline matched-filters the detector data against a bank of analytically modelled compact binary merger waveforms [79, 137]. Only nonspinning compact binary merger signals are used as filters and the bank is created so as to densely sample the range of possible binary masses [198]. For each detector, the filtering stage produces a sequence of *triggers* which are plausible events with a high signal to noise ratio SNR ρ . The algorithm proposed in [199] is used to keep only those that are found coincident in more than one detector across the network, which helps remove triggers due to noise. Knowledge of the instrument and its environment is used to further exclude triggers that are likely due to non-Gaussian noise transients, or *glitches*. Periods of heightened glitch rate are removed (*vetoed*) from the analysis. The time periods where the rate of glitches is elevated are divided into 3 *veto categories*. Periods of time flagged by category 1 and 2 vetoes are not included in the analysis as known couplings exist between instrumental problems and the gravitational-wave channel during these periods. Periods of time vetoed at category 3 are *likely* to have instrumental problems. A strong gravitational-wave signal can still be detected during category 3 times, but including these periods in the background estimate can compromise our ability to detect weaker signals in less glitchy periods of time. For this reason the search is performed both before and after category 3 vetoes are applied. The significance of events that survived category 1-3 vetoes were calculated using the background that also survived categories 1-3. The significance of events that survived category 2 but were vetoed at category 3 were calculated using background that survived categories 1-2.

Signal based consistency measures further help distinguish real signals from background noise triggers in those that are not vetoed and pass the coincidence test. The χ^2 statistic proposed in [200] quantifies the disagreement in the frequency evolution of the trigger and the waveform template that accumulated the highest SNR for it, cf. Eq. (4.14) of [200]. We weight the SNR with this statistic to obtain the *reweighted* SNRs for all coincident triggers. The exact weighting depends on the mass range the search is focused on, cf. Eq. (17,18) of [137]. The reweighted SNR is used as the ranking statistic to evaluate the significance, and thus the false alarm rate (FAR), of all triggers.

Following the division of the mass-parameter space used in [193, 19], we performed both *low mass* and *high mass* `ihope` searches on the NINJA-2 data. The low-mass search focused on binaries with $2M_\odot \leq m_1 + m_2 < 25M_\odot$, and used frequency domain 3.5PN waveforms as templates [201, 202, 93]. The high-mass search instead focused on the mass-range $25M_\odot \leq m_1 + m_2 < 100M_\odot$, and used the effective-one-body inspiral-merger-ringdown model calibrated to numerical relativity, as described in [106]. The exact χ^2 -weighting used to define the re-weighted SNR varied between the two analyses [137]. The significance of the triggers found by both was estimated as follows. All coincident triggers are divided into 4 categories, i.e. HL, LV, HV and HLV, based on the detector combination they are found to be coincident in [193]. They are further divided into 3 *mass*-categories based on their chirp mass $\mathcal{M}_c = (m_1 m_2)^{3/5} (m_1 + m_2)^{-1/5}$ for the low-mass search, and 2 categories based on their template duration for the high-mass search [193]. The rate of background noise triggers, or *false alarms*, has been found to be significantly higher for shorter signals from more massive binaries, and also to be different depending on the detector combination, and these categorizations help segregate these effects for estimation of the background [193, 137].

For all the triggers the combined re-weighted SNR $\hat{\rho}$ is computed, which is the quadrature sum of re-weighted SNRs across the network of detectors. All triggers are then ranked according to their $\hat{\rho}$ in each of the mass/duration and coincidence sub-categories independently, allowing us to estimate the trigger false alarm rate (FAR) at a given threshold $\hat{\rho} = \hat{\rho}_0$. This is described by

$$\text{FAR } (\hat{\rho}_0) \simeq \frac{N(\hat{\rho} \geq \hat{\rho}_0)}{T_c}, \quad (6.2)$$

i.e. the number of background noise triggers in a given coincidence sub-category at least as loud as the threshold, $N(\hat{\rho} \geq \hat{\rho}_0)$, divided by the total time analyzed for that sub-category, T_c . The limiting precision on this quantity is of order $1/T_c$; thus, in the limit where *no* background events are louder than $\hat{\rho}$, we quote a FAR of less than $1/T_c$. The calculation of trigger FARs is described in more detail in [203, 17]. As the smallest FAR we can estimate is $1/T_c$, to get a more precise estimate for our detection candidates we simulate additional background time. We shift the time-stamps on the time-series of single detector triggers by Δt relative to the other detector(s), and treat the shifted time-series as independent coincident background time. All coincident triggers found in the shifted times would be purely due to background noise. We repeat this process setting $\Delta t = \pm 5s, \pm 10s, \pm 15s, \dots$, recording all the time-shifted coincidences, until Δt is larger than the duration of the dataset itself. With the additional coincident background time T_c accumulated in this way, we can get a more precise estimate of the low FARs we expect for detection candidates.

The FARs computed this way are further multiplied by a trials factor that accounts for the fact that we rank events in their own template-mass and coincidence sub-categories independently, while each of the sub-categories corresponds to an (independent) analysis of the same stretch of interferometric data. This factor is discussed in detail in section IV of [193]. Taking the trials factor into account, the final combined FAR (cFAR) is reported in Table 6, and the results are described in detail in section 6.5.1.

6.5 Blind Injection Challenge Results

In this section we present the results of using the `ihope` pipeline described in section 6.4 to search for the blind injections listed in Table 5.

6.5.1 `ihope`

The results of the low-mass `ihope` search are presented in Table 6. The Event IDs correspond to the Event IDs of the blind injections in Table 5. The mapping between the `ihope` candidates and the blind injections is based on the event times of each. Between the two `ihope` searches, all injections except for injection 7 were found with high significance. We will focus, however, on the results of the low mass search.

Table 6: The low mass `ihope` search results. The Event IDs correspond to the Event ID of each blind injection given in Table 5; this association is based on the time of the candidates relative to the time of the injections. The cFARs are calculated from all possible 5 s time shifts over the entire two-month dataset. M and q give the total mass and mass ratio respectively that were recovered in each detector. The recovered SNR (ρ_{rec}) and re-weighted SNR ($\hat{\rho}$) are reported separately for each detector. To calculate the cFARs, the quadrature sum of $\hat{\rho}$ was used. Unless noted, the cFARs were calculated after category 1-3 vetoes were applied.

Event ID	1/cFAR (yr)	Detectors	M	q	ρ_{rec}	$\hat{\rho}$	Search
3	≥ 23000	L	13.8	1.15	12.4	11.6	Low mass
		V	14.2	1.41	5.9	5.2	Cat. 3
	$\geq 5800^{\dagger}$	H	13.7	1.15	7.9	7.5	Low mass
		L	13.8	1.15	12.4	11.6	Cat. 2
4	≥ 31000	V	14.2	1.41	5.9	5.2	
		L	25.0	1.80	8.5	8.5	Low mass
5	≥ 21000	V	25.0	1.43	10.9	9.2	
		H	19.5	4.27	16.2	15.6	Low mass
7			<i>Not found</i>				

[†] Only used HL triggers for computing significance of this event; see section 6.5.1.

Event 7 was missed because the injection’s SNR was too small to be detected by the pipeline. The optimal SNR of this injection — obtained by finding the overlap of the injection with itself — was 5.7 in H, 6.0 in L, and 5.3 in V, giving a network SNR of 9.8. However, the injected SNR in Virgo was below the SNR threshold used by the `ihope` pipeline ($= 5.5$). This means that, at best, the event could only surpass threshold in H and L, giving a maximum recoverable network SNR of 8.2; the false alarm rate at this network SNR is order 10^3 per year.

For this analysis we used the same vetoes as were used in [193] and [19] applied to the corresponding times in the recolored data. After veto categories 1-3 were applied, the total analyzed time consisted of 0.6 days of coincident HL data, 5.4 days of coincident LV data, 6.5 days of coincident HV data and 8.9 days of coincident HLV data. FARs were calculated in each bin using the time-shift method described in section 6.4.1, then combined over all bins.

Table 6 also gives the total masses and mass ratios that were recovered by the `ihope` pipeline in each detector for each candidates. We see that the values reported by `ihope` can vary substantially from the injected parameters. This is not surprising as many of the injections had spin. In general, templates are placed in `ihope` so as to maximize detection probability across the parameter space while minimizing computational cost. `ihope` therefore only provides a rough estimate of candidate parameters. For more precise estimates, sophisticated parameter estimation methods were also applied by other members of the collaboration.

Initially we used 100 time shifts to identify candidate events. All of the coincident events associated with the blind injections were louder than all background in the 100 time shifts. These were the only events to be louder than all background. Using 100 time shifts we could only bound the cFAR of the events to $\lesssim 10 \text{ yr}^{-1}$, which is not small enough to claim a detection. To improve our estimate, we performed as many 5 s time shifts as possible in the NINJA-2 dataset. This is the same method that was used for the blind injection described in [193].

Event 3 was found by the low-mass search in all three detectors (before category 3 vetoes were applied). Estimating background using the extended slide method with three detectors adds computational complexity, and has not previously been performed (the blind injection in [193] was only coincident in two detectors). However, in Events 3 one of the three detectors (V) had significantly less $\hat{\rho}$ than the other two (H

and L). We therefore did not include the detector with the smallest $\hat{\rho}$ when estimating the extended background for these two events.

For Event 3 the trigger in the H detector was vetoed at category 3, leaving only L and V. Since the H trigger contributed a substantial amount of the combined re-weighted SNR, we might expect the resulting FAR to be *higher* for this event after category 3. A method to deal with partially vetoed events like this has not been proposed. We therefore simply report both results here.

Event 4 was found with high significance by both the high-mass and low-mass searches. This is not surprising as the injected total mass was $26.8 M_{\odot}$, which is close to the boundary between the two searches. Currently no method has been established on how to combine the results from the low-mass and high-mass searches. We however show only the low mass both results here.

6.6 Conclusion

This chapter presents a systematic study to assess the ability to detect numerically modelled binary black hole data in real data taken from Initial LIGO and Virgo and recolored to predicted sensitivity curves of Advanced LIGO and Advanced Virgo in early observing runs. Building upon the work of the first NINJA project, this work, the culmination of the second NINJA project, studies the ability to do gravitational wave astronomy on a set of 60 binary black hole hybrid waveforms submitted by 8 numerical relativity groups.

In this work, a set of 7 numerically modelled binary black hole waveforms were added into the recolored data. This data was distributed to analysts with no knowledge of the parameters of the systems. The matched-filtered compact binary merger search pipeline, `ihope`, was able to recover 6 of the waveforms with false alarm rate upper limits ranging between 1 every 5800 years and 1 every 31000 years.

These results (completed by those in the published form [204]) represent the next step for the NINJA collaboration; they address shortcomings in NINJA-1 while paving the way for future work. In a sense this work represents a baseline, as it measures the ability of current gravitational-wave analyses to detect and recover the parameters of an important subset of possible BBH signals in non-Gaussian noise in the advanced detector era. From this baseline there are multiple directions in which NINJA can

expand. On the NR front, groups are continuing to fill in the parameter space [37]. As shown in figure 23, even within the subspace of systems with (anti-)aligned spins there are large regions left to explore. Although NINJA-2 chose not to consider precessing signals many groups already have or are working on such simulations [188, 205, 206, 207, 208, 116, 209, 210, 154, 149]. Similarly, although the analyses used only the $\ell = m = 2$ mode in this work, it is expected that higher modes will be important for detection and parameter recovery [102, 211, 212, 127, 146]. Additional modes have been provided for many of the waveforms in the NR catalog, although they have not yet been validated. In all cases, as additional waveforms and modes become available they can be injected into the noise allowing for systematic tests of both detection and parameter estimation analyses.

In parallel the detection and parameter estimation analyses continue to evolve and improve. There is much development work ongoing to improve the analytical waveform models that are used in analysis pipelines, particularly for inspiral-merger-ringdown waveforms. It seems likely that before the first aLIGO and AdV observation runs generic fast IMR precessing analytic models will be available [39, 117, 213, 214, 149]. Improvements in how detection pipelines deal with non-Gaussianities are being explored to attempt to achieve the maximum possible sensitivity to BBH signals across the parameter space. A number of efforts are ongoing to implement aligned-spin waveform models into search algorithms. This will increase sensitivity to BBH systems with aLIGO and AdV [215, 131, 216]. Work is also underway to develop more realistic models of detector noise for parameter estimation pipelines, which account for the non-stationarity and non-Gaussianity present in real noise [217]. Accounting for such features is expected to greatly reduce systematic biases in the recovered masses and spins. The results presented here can provide a measure against which these next-generation analyses can be compared, in a way that measures not only their response to signals but also to realistic noise.

Chapter 7

Modeling of intermediate mass-ratio inspirals: Exploring the form of the self-force in the intermediate mass-ratio regime

Testing Einstein’s theory of general relativity in the strong-field regime by directly detecting the gravitational waves (GWs) emitted by black hole (BH) binaries of extreme mass-ratio has revived interest in a fundamental problem in general relativity: that of the gravitational self-force acting on a mass particle that moves in the background of a more massive BH. The gravitational self-force arises as a result of the back reaction between the small compact object and its own gravitational field, which, at linear order in mass-ratio, corresponds to a linear perturbation of the central BH geometry. Theoretical work in this field has been making steady progress since the seminal contributions of Dirac on the electromagnetic self-force in flat spacetime [218], and the extension of this analysis to curved spacetime by DeWitt and Brehme [219]. The generalization of these early studies to the case of the gravitational self-force was accomplished independently by Quinn and Wald [220] and Mino, Sasaki and Tanaka [221]. More recent developments have introduced mathematical rigor in the theoretical derivation of the gravitational self-force, and have relaxed previous assumptions with regard to the internal structure of the small compact object, i.e, it can now be a small Kerr BH or a small compact object made up of ordinary matter [31, 32].

Likewise, the actual computation of the gravitational self-force has evolved from simplified scalar-field models [222], to more sophisticated solutions that involve electromagnetic and gravitational problems in the context of Schwarzschild circular orbits. At present, the self-force program has succeeded in developing numerical codes to compute the gravitational self-force along generic orbits around a Schwarzschild BH, and actually implementing these computations to develop an accurate waveform model that describes the inspiral evolution of non-spinning stellar mass BHs onto supermassive non-spinning BHs [223]. The development of numerical algorithms to compute the self-force on a scalar charge moving along an eccentric-equatorial orbit of a Kerr BH has also been accomplished [224]. The extension of this algorithm to compute the gravitational self-force for Kerr inspirals is under development [224, 225].

The fact that the self-force program has focused on the computation of the self-force for spinless particles that inspiral into more massive BHs has a physical rationale. It is not just that such a problem would be more difficult to solve. It has also been shown that in the context of extreme-mass ratio inspirals (EMRIs), with typical mass-ratios $1:10^6$, the inclusion of small-body spin corrections in search templates will not allow us to measure the small body spin parameter with good accuracy [226]. Hence, from a data analysis perspective, the inclusion of small body spin effects is not necessary. Additionally, before attempting to compute the self-force for spinning particles, one may need to address a more pressing modeling issue for spinless particles: it has been shown that including conservative self-force corrections in the orbital phase of EMRIs may not be necessary for source detection, but they may still be necessary for accurate parameter reconstruction. Additionally, second order radiative corrections may contribute to the phase evolution at the same level as first-order conservative corrections. This then suggests that a waveform model that aims to provide an accurate description of the inspiral evolution of EMRIs may have to include both first-order conservative corrections, and second-order radiative corrections, as pointed out in [223].

In sharp contrast, modeling BH binaries with intermediate mass ratio, i.e., $1:10\text{-}1:1000$, (IMRIs) presents new challenges that can be neglected in the EMRI limit. In the absence of fully general relativistic gravitational self-force corrections in this mass-ratio regime, some studies have assessed the importance of including post-Newtonian self-force corrections in search templates for spinning BHs of intermediate-mass that

inspiral into supermassive Kerr BHs. These studies have shown that the implementation of first-order post-Newtonian self-force corrections for spin-spin and spin-orbit couplings is essential to ensure the reliability of parameter estimation [227]. They suggest that the computation and implementation of gravitational self-force corrections for spinning binaries is a pressing, important problem both from a theoretical and data analysis perspective.

In this chapter we shed light on the importance of including gravitational self-force corrections in search templates for non-spinning stellar mass BHs that inspiral into Schwarzschild BHs of intermediate-mass. As, at present, we have no access to accurate self-force calculations in this mass-ratio regime, we explore the range of applicability of the information we have at hand to develop accurate waveform templates, and shed light on the regime in which current self-force corrections do not render an accurate dynamical evolution of GW sources. Once advanced LIGO (aLIGO) begins observations, it will be possible to target the inspirals of neutron stars (NSs) and stellar-mass BHs into intermediate-mass BHs with masses $\sim 50M_{\odot} - 350M_{\odot}$ [228]—events which may take place in core-collapsed globular clusters [229]. To perform this study we will make use of the recently developed effective-one-body (EOB) model that has been calibrated using numerical relativity (NR) simulations for non-spinning BH binaries of mass-ratio $q = m_1/m_2 = 1, 2, 3, 4$ and 6 [38]. It is worth pointing out that the calibrated EOBNRv2 (EOBNR version two) model reproduces with great accuracy the features of true inspirals, and hence we will use it as a benchmark to explore the form of the self-force in the intermediate-mass ratio regime. For details of the model, we refer the reader to Sec. 2.5.3. By construction, the EOBNRv2 model reproduces orbital dynamics in the test-mass particle limit, and also encodes self-force corrections that have been derived for small mass-ratios.

Finally, we will make use of the EOBNRv2 model and perturbative results to present a new prescription for the orbital frequency shift at the innermost stable circular orbit (ISCO), originally derived in [230] in the context of EMRIs. Our prescription reproduces exactly the self-force prediction for extreme-mass ratios and provides an accurate prediction in the intermediate and comparable-mass ratio regimes.

The remainder of the chapter is organized as follows. In Section 7.1 we derive an IMRI waveform model that accurately captures the features of true inspirals, as compared with the EOBNRv2 model. The derivation of this model will enable us to

explore what the form of the self-force should be in the intermediate-mass-ratio regime so as to accurately reproduce the orbital dynamics obtained through NR simulations. In Section 7.2 we derive a new prescription for the gravitational self-force correction to the orbital frequency at the ISCO that encodes results from the extreme, intermediate and comparable-mass ratio regimes. Finally, we summarize our results in Section 7.4.

7.1 Self-force corrections in the intermediate-mass-ratio regime

In Sec. 2.5.3, we described the EOB model we will now use to build a waveform model for intermediate-mass-ratio inspirals (IMRIs). Using this IMRI model we will explore whether the inclusion of available self-force corrections, which have been computed in the extreme-mass-ratio regime [231, 232, 230], are able to reproduce the inspiral evolution of intermediate-mass-ratio binary black holes.

7.1.1 IMRI self-force model

In this Section we introduce the key elements we need to build our IMRI model which is simple and flexible enough to explore the form of the self-force in the intermediate-mass-ratio regime, and that, at the same time is able to reproduce with great accuracy the binary's dynamical evolution as predicted by EOBNRv2. In the following we assume that EOBNRv2 dynamics provides a good description of the actual binary black hole dynamical evolution. This is a reasonable assumption because, at present, EOBNRv2 has been calibrated to NR simulations with mass-ratios up to 1:6, and is the best interface to translate NR simulations into a waveform model that uses coordinates which can be related to physical units [233]. The approach we use to build our IMRI model is as follows:

1. We start with an ansatz for the orbital frequency evolution of our IMRI model which is inspired by recent studies on the inclusion of linear order self-force corrections in the EOB approach [234]. We develop this prescription so as to faithfully reproduce the EOBNRv2 orbital frequency evolution (See Figure 27). An accurate modeling of the orbital frequency is necessary to build the gauge-invariant object $x = M\Omega^{2/3}$, which is a crucial element in our model.

2. We propose an ansatz to model the IMRI gravitational wave angular momentum flux which we calibrate so as to faithfully reproduce its EOBNRv2 counterpart (see Figures 28 and 29). Note that the EOBNRv2 angular momentum flux used for this calibration is obtained by summing over 35 leading and subleading waveform multipoles $h_{\ell m}$, with $2 \leq \ell \leq 8$, $1 \leq m \leq \ell$. We include all these modes so as to model the radiative part of the self-force in our IMRI model as accurately as possible.
3. Having derived an accurate prescription for the orbital frequency and the angular momentum flux, we make use of a prescription for the angular momentum $\hat{L}_z(x)$ that goes beyond the test-mass particle limit and includes conservative self-force corrections. The encoded conservative self-force corrections in the redshift observable z_{SF} (see Eq. (7.9)).
4. Because the prescriptions for the orbital frequency and the flux of angular momentum of our IMRI model reproduce their EOBNRv2 counterparts with great accuracy (see Figures 27 and 28), we can now use these objects to constrain the form of the gauge-invariant expression of the angular momentum $\hat{L}_z(x)$ in Eq. (7.7) below by demanding internal consistency in our model, i.e., by reproducing faithfully the dynamical evolution of the binary black hole as predicted by EOBNRv2. This is equivalent to exploring the form of the red-shift observable z_{SF} which encodes the binary's dynamical evolution. The calibration of z_{SF} enable us to reproduce the expected inspiral evolution point to point to better than one part in a thousand, as shown in Figures 30 and 31.
5. Having calibrated z_{SF} to reproduce the dynamical evolution of the systems considered in this analysis, we compare the gauge-invariant expression of $\hat{L}_z(x)$ using our results and self-force corrections obtained in the context of EMRIs. We show that available self-force corrections do not reproduce the late inspiral evolution for systems with mass-ratio 1:6 and 1:10, but that they provide a fair description for systems with mass-ratio 1:100. This result is to be expected because these available self-force corrections were derived in the small mass-ratio limit.

To model the orbital frequency, we follow [235] and [236], and use the prescription

$$\Omega = \frac{A}{\hat{H}} \frac{p_\phi}{r^2}, \quad (7.1)$$

where A is the EOB metric defined implicitly in Eq. 2.63. Assuming circular orbits, we can simplify Eq. (7.1) using the following relations for the conservative Hamiltonian \hat{H}

$$\hat{H} = \sqrt{A(u)(1 + j_0^2 u^2)}, \quad \text{with } p_\phi = j_0, \quad \text{and } j_0^2 = -\frac{A'(u)}{(u^2 A(u))'}, \quad (7.2)$$

where $u = 1/r$ and $'$ denotes d/du . Using a prescription similar to that introduced in [234], we shall use the following ansatz for the potential $A(u)$

$$A_{\text{ansatz}}(u) = 1 - 2u + \eta \left(\sqrt{1 - 3u} k_{\text{fit}} - u \left(1 + \frac{1 - 4u}{\sqrt{1 - 3u}} \right) \right), \quad (7.3)$$

with $k_{\text{fit}} = 2u \frac{1 + a_1 u + a_2 u^2}{1 + a_3 u + a_4 u^2 + a_5 u^3}$.

The prescription for the orbital frequency then simplifies to

$$\Omega(u)_{\text{ansatz}} = u^{3/2} \sqrt{-\frac{A'_{\text{ansatz}}(u)}{2}}. \quad (7.4)$$

The calibrated values of the a_i parameters in the function k_{fit} are given in Table 7. It is worth pointing out that this prescription captures accurately the orbital phase evolution of the sources described above all the way down to ISCO and slightly beyond with much less computational complexity than EOBNRv2. The comparison between this scheme and the EONBRv2 model is shown in Figure 27. Notice that our IMRI model does pretty well from large r to the fast-motion strong-field regime in all three cases shown. Notice that we are modeling the potential $A_{\text{ansatz}}(u)$ using the coordinate u and not M/x as done in [234]. The rationale for using such a prescription, instead of a PN series,a Padé resummed expression, etc, is to simplify the prescription for the orbital frequency without sacrificing its accuracy.

η	a_1	a_2	a_3	a_4	a_5
$\frac{1700}{13689}$	-7.458	15.0179	-7.208	12.152	6.103
$\frac{10}{121}$	-8.037	17.059	-7.826	14.589	5.393
$\frac{100}{10201}$	-9.535	22.984	-9.456	21.862	3.085

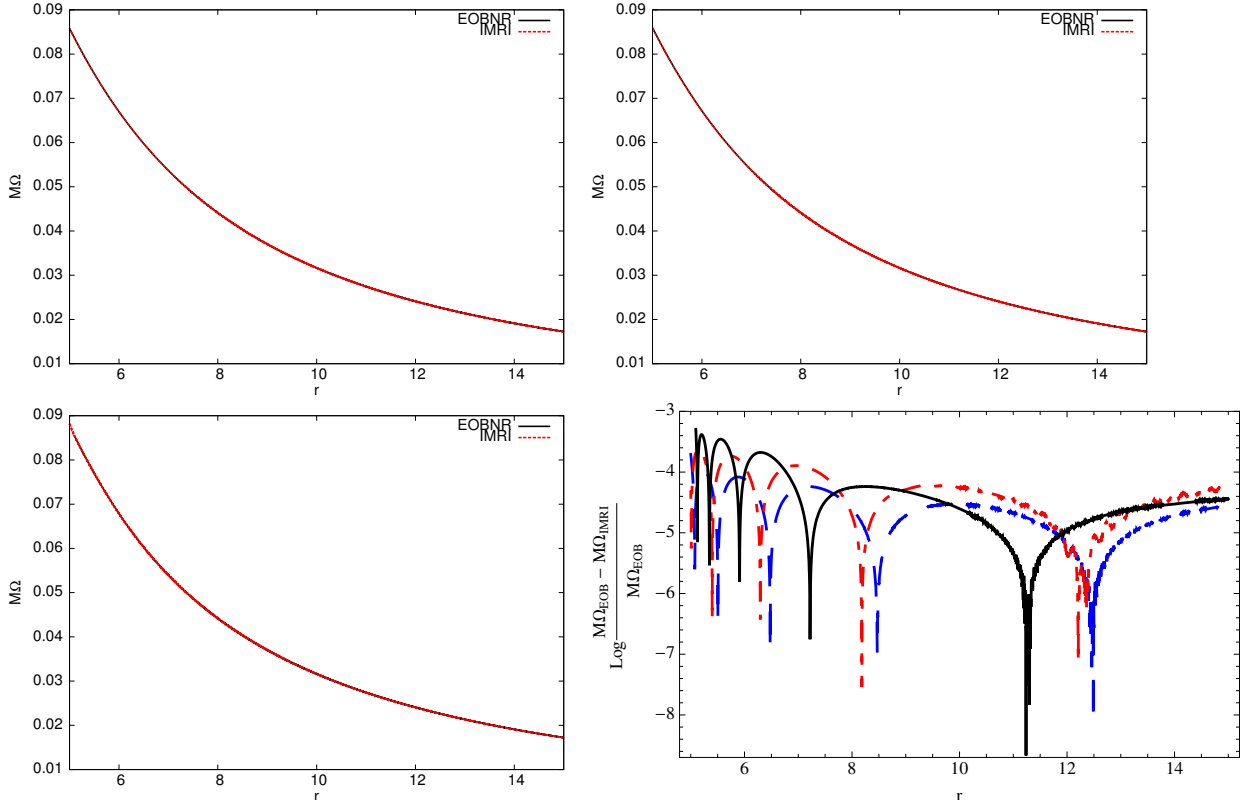
Table 7: Ω_{ansatz} fit coefficients used in Eq. 7.3.

Figure 27: The panels show the orbital frequency, as a function of the radial coordinate r , obtained using the fit described in the text (solid red line), and the orbital frequency predicted by the EOB model (solid black line). The systems shown in the panels correspond to binaries of component masses $17M_\odot + 100M_\odot$ (top-left panel), $10M_\odot + 100M_\odot$ (top-right) and $1M_\odot + 100M_\odot$ (bottom-left panel).

The bottom-right panel demonstrates the accuracy with which our IMRI model reproduces the orbital frequency predicted by the EOBNRv2 for the systems 17:100 (dashed blue), 10:100 (dashed-dot red) and 1:100 (solid black). Note that the spikes are due to artifacts in the interpolation function used to plot the EOBNRv2 orbital frequency and the numerical fit used to reproduce it. Also notice that the discrepancy between the data and the fit is always smaller than one part in a thousand.

We next require a prescription to generate the inspiralling trajectory of the stellar mass compact object. The first step to achieve this consists of deriving a consistent model for the flux of angular momentum, which is discussed in the following section.

7.1.2 Radial evolution prescription

An important component of the IMRI waveform model is the prescription used for the fluxes of energy and angular momentum. Deriving an accurate expression for these quantities is essential to capture the main features of true inspirals, as shown in [237] in the context of EMRIs.

As discussed in Section 2.5.3, in the EOBNRv2 model the flux of energy is constructed using the prescription given by Eq. (2.65), which is obtained by summing over the modes ($h_{\ell m}$) with $2 \leq \ell \leq 8$, $1 \leq m \leq \ell$. Using this prescription as input data and the fact that in the EOB formalism the following relation is fulfilled [234]

$$\dot{E} = \Omega \dot{L}_z, \quad (7.5)$$

we derive a prescription for the gravitational-wave angular momentum flux which is valid from early inspiral all the way to the ISCO and slightly beyond. This prescription, which encapsulates the contribution from 35 dominant and subdominant modes, is inspired by the modeling of accurate EMRI waveform models introduced in [237], i.e.,

$$(\dot{L}_z)_{\text{fit}} = -\frac{32}{5} \frac{\mu^2}{M} \frac{1}{r^{7/2}} \left[1 - \frac{1247}{336} \frac{1}{r} + 4\pi \frac{1}{r^{3/2}} - \frac{44711}{9072} \frac{1}{r^2} + \frac{1}{r^{5/2}} \left(c_{2.5}^1 + c_3^2 \frac{1}{r^{1/2}} + c_{3.5}^3 \frac{1}{r} \right) \right], \quad (7.6)$$

and the coefficients in Eq. (7.6) are given in Table 8.

η	$c_{2.5}^1$	c_3^2	$c_{3.5}^3$
$\frac{1700}{13689}$	-121.903	551.141	-694.699
$\frac{10}{121}$	-110.657	360.261	-156.016
$\frac{100}{10201}$	-75.255	333.449	-363.505

Table 8: \dot{L}_z fit coefficients

Figure 28 provides a comparison between the EOBNRv2 flux and the calibrated angular momentum flux (\dot{L}_z). Notice that our modeling scheme does pretty well from large r all the way to the ISCO and slightly beyond. Hence, this approach will enable us to capture the main features of the inspiral evolution of the systems under consideration in the regime of interest with good accuracy. Modelling the prescription of the flux of angular momentum in our IMRI waveform using all the dominant and subdominant modes in the EOBNRv2 model is equivalent to modeling the radiative part of the self-force with the best information currently available in the literature.

In Figure 29 we present a comparison between the flux of angular momentum predicted by the EOBNRv2 model and the fit to Teukolsky data proposed in [237] for extreme-mass-ratio inspirals. Note the remarkable agreement between both formalisms all the way down to the ISCO. This comparison also confirms that the construction of the EOBNRv2 captures the main features of inspirals with small mass-ratios which are modeled using black hole perturbation theory. This comparison also shows that the EOBNRv2 model encodes fairly well the radiative part of the self-force for systems with small mass-ratio.

Having found a prescription for the angular momentum that captures the dynamics of IMRIs, we can now use it to generate the inspiral trajectory of the stellar mass compact object that inspirals into an IMBH using the relation

$$\frac{dr}{dt} = \frac{dL_z}{dt} \frac{dr}{dL_z}. \quad (7.7)$$

The first term on the right hand side of Eq. (7.7) can be obtained from Eq. (7.6). With regard to the derivative of the angular momentum with respect to the radial coordinate, we need to use a prescription for the angular momentum that goes beyond the test-mass particle limit, as conservative self-force corrections play a more significant role in this regime. Hence, we use the relation derived by Barausse et al in [234] which includes conservative self-force corrections, i.e.,

$$\hat{L}_z(x) = \frac{L_z}{\mu M} = \frac{1}{\sqrt{x(1-3x)}} + \eta \left(-\frac{1}{3\sqrt{x}} z'_{\text{SF}}(x) + \frac{1}{6\sqrt{x}} \frac{4-15x}{(1-3x)^{3/2}} \right) + \mathcal{O}(\eta^2), \quad (7.8)$$

where $x = (M\Omega)^{2/3}$ and $'$ stands for d/dx . Furthermore,

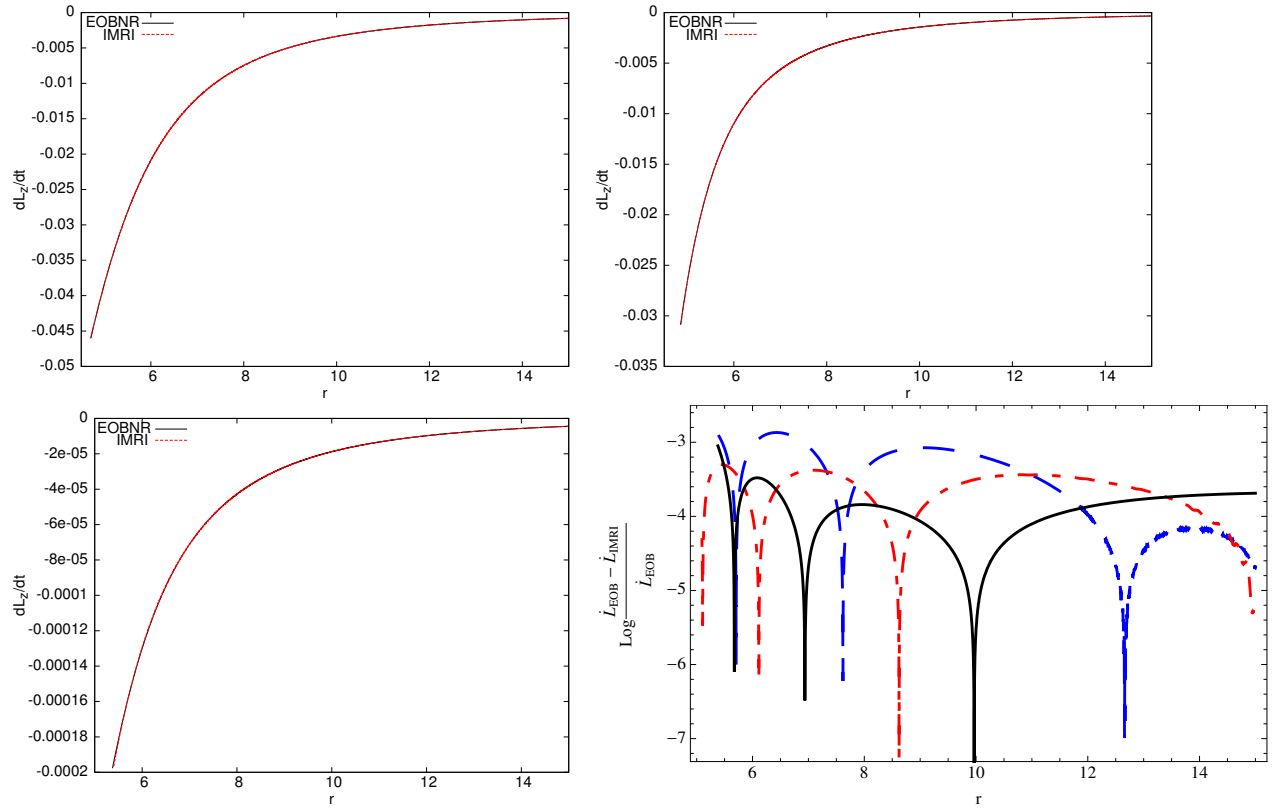


Figure 28: We compare the calibrated flux of angular momentum described in Eq. (7.6) against the prediction of the EOBNRv2 model for binaries of component masses $17M_\odot + 100M_\odot$ (top left panel), $10M_\odot + 100M_\odot$ (top right panel), and $1M_\odot + 100M_\odot$ (bottom-left panel). The bottom-right panel shows the accuracy with which the IMRI model reproduces the EOBNRv2 angular momentum flux, $\dot{L} = dL_z/dt$, for the systems: 17:100 (dashed blue), 10:100 (dashed-dot red) and 1:100 (solid black). The spikes in the bottom-right panel are due to numerical artifacts of the interpolating function used to plot the EOBNRv2 angular momentum flux and the numerical fit to reproduce it. The fit is such that its discrepancy to the EOBNRv2 is always smaller than one part in a thousand.

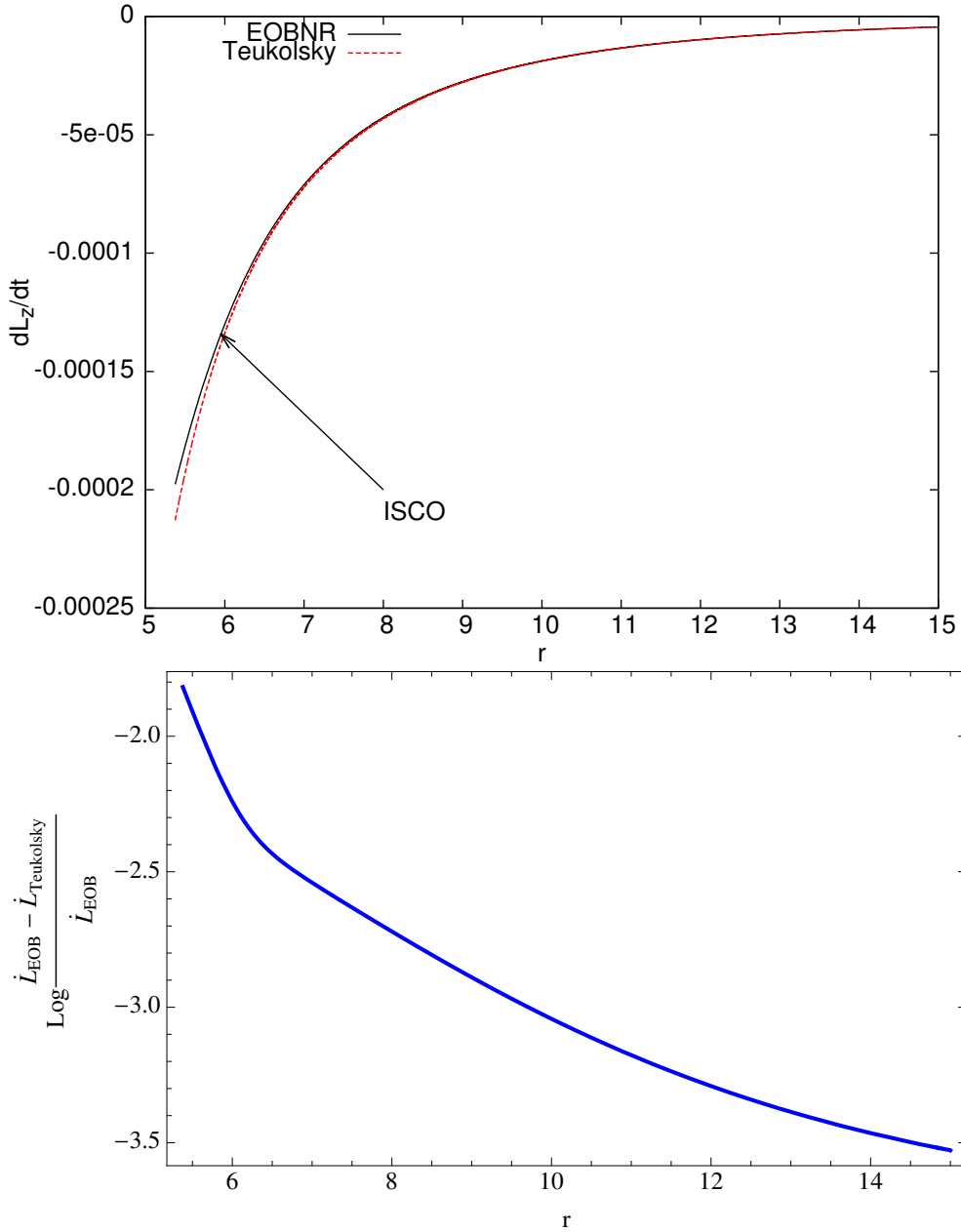


Figure 29: The top panel shows the angular momentum flux for binaries of mass ratio 1:100 computed using the EOBNRv2 model and the fit to Teukolsky data introduced in [237]. Both formalisms present a remarkable agreement all the way down to the ISCO. Note that the angular momentum flux fit to Teukolsky data is valid only from early inspiral until the ISCO. The bottom panel shows the relative difference between the two prescriptions for the angular momentum flux $\dot{L} = dL_z/dt$.

$$z_{\text{SF}}(x) = 2x \frac{1 + b_1x + b_2x^2}{1 + b_3x + b_4x^2 + b_5x^3}, \quad (7.9)$$

and the various coefficients b_i were derived in [234] using available self-force data. In this section we derive the coefficients in Eq. (7.9) that reproduce the actual inspiral evolution all the way down to the ISCO. Note that in Eq. (7.7) we have in place a prescription for the angular momentum flux which faithfully reproduces the expected loss of angular momentum even beyond the ISCO, as compared to the EOBNRv2 model. Hence, the only ingredient that needs to be tuned to reproduce the expected inspiral evolution is contained in Eq. (7.8). We have followed this approach to explore the form that $\hat{L}_z(x)$ should have. Put in different words, the form that the self-force redshift observable $z_{\text{SF}}(x)$ should have to reproduce an inspiral trajectory consistent with EOBNRv2 all the way down to the ISCO. The various coefficients of Eq. (7.9) that generate such an inspiral orbit are given in Table 9.

η	b_1	b_2	b_3	b_4	b_5
$\frac{1700}{13689}$	-3.062	0.760	-3.261	0.550	-6.000
$\frac{10}{121}$	-3.260	0.892	-3.475	0.600	-6.829
$\frac{100}{10201}$	-3.370	1.570	-3.730	0.970	-7.280

Table 9: $z_{\text{SF}}(x)$ fit coefficients

In Figure 30 we show that this prescription captures with great accuracy the features of EOBNRv2 inspirals. To recap, the IMRI model incorporates both first-order conservative corrections –through the construction of the gauge invariant expression of the angular momentum in Eq. (7.8)— and first-order radiative-corrections through the construction of the flux of angular momentum in Eq. (7.6).

In order to show the importance of increasing our knowledge of the self-force in the intermediate-mass-ratio regime, we present in Figure 32 three different curves which describe the time evolution of three binary systems during late inspiral. These plots show that if we use a waveform model (unfitted) that includes: a) an accurate prescription for the orbital frequency $\hat{\Omega}$; b) a prescription for the flux of angular momentum that incorporates the contribution from all dominant and subdominant (ℓ, m) modes; c) an invariant expression for the angular momentum using the object $x = \hat{\Omega}^{2/3}$ (see Eq. (7.8)), and; d) available self-force corrections to constrain the

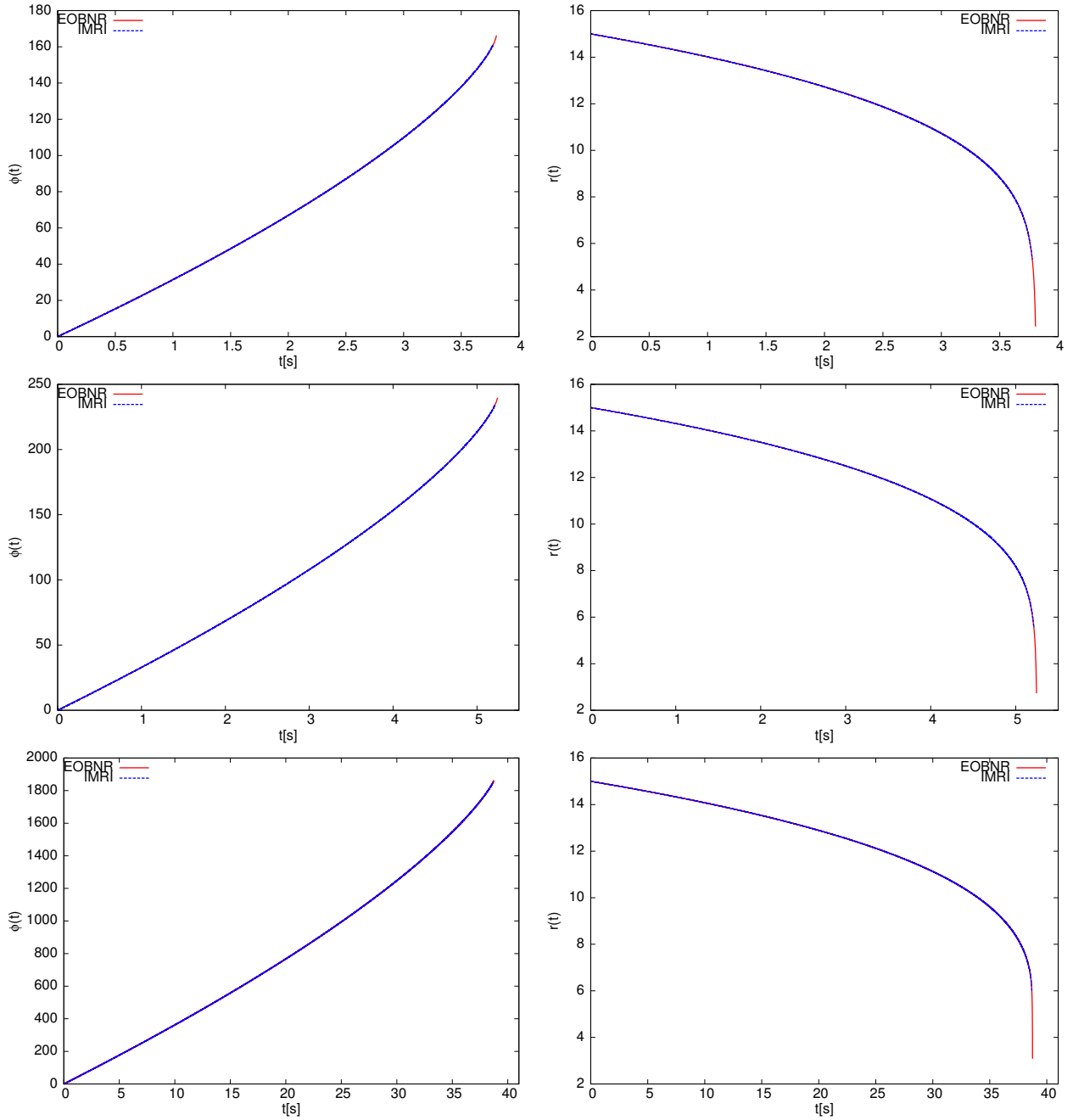


Figure 30: The panels show the radial and azimuthal evolution for a $17M_{\odot} + 100M_{\odot}$ system (top panels), $10M_{\odot} + 100M_{\odot}$ system (middle panels), and $1M_{\odot} + 100M_{\odot}$ system (bottom panels), obtained using the IMRI model compared against the EOBNRv2 model.

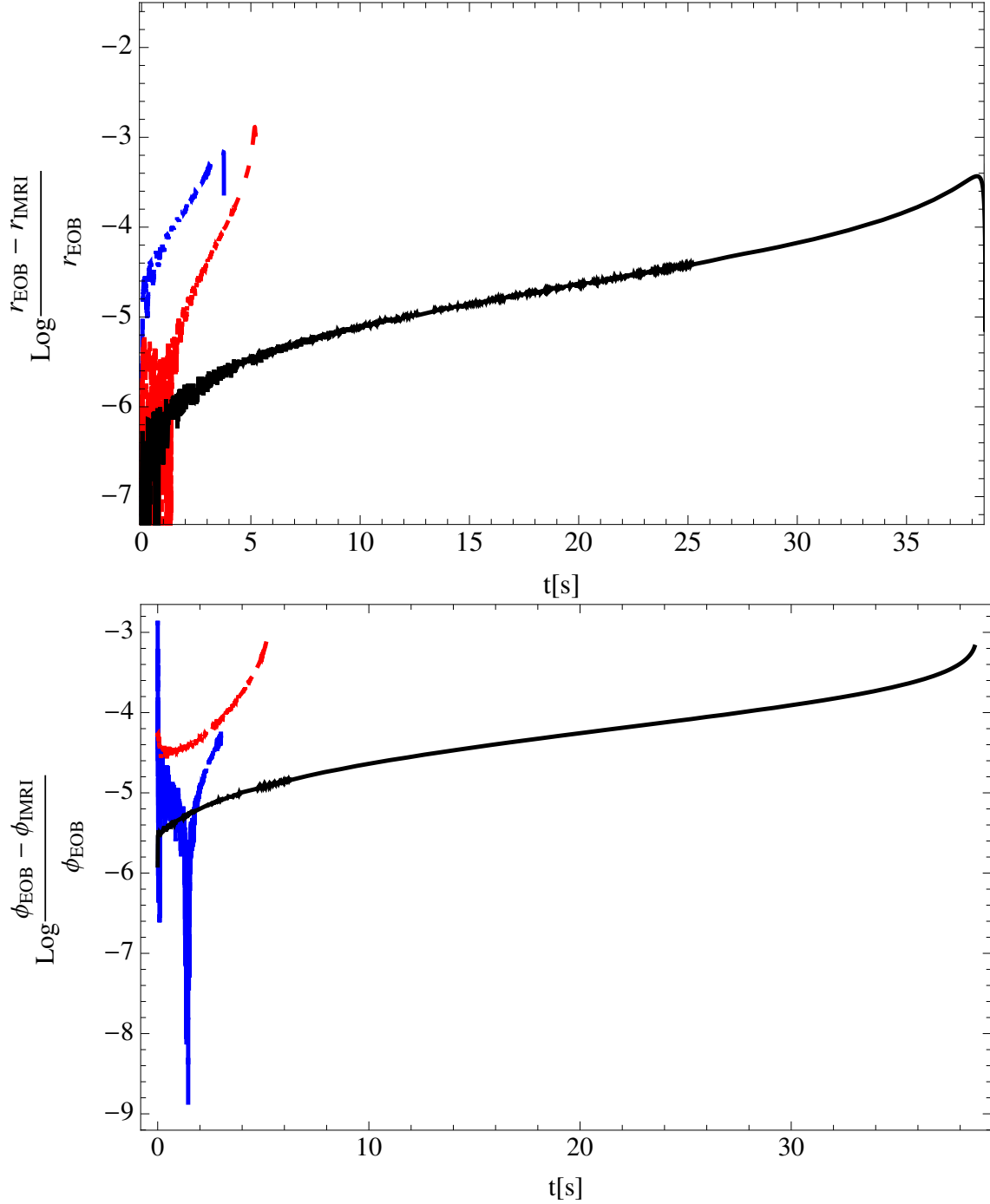


Figure 31: The panels show the accuracy with which the IMRI model proposed in the chapter reproduces the radial (top panel) and azimuthal (bottom-panel) time evolution predicted by the EOBNRv2 model for the systems $17M_\odot + 100M_\odot$ (dashed blue), $10M_\odot + 100M_\odot$ (dashed-dot red), and $1M_\odot + 100M_\odot$ (solid black). Notice that our model reproduces the EOBNRv2 orbital and azimuthal evolution point to point with an accuracy better than one part in a thousand.

coefficients b_i [234], then such a model would generate an inspiral trajectory that deviates from the expected orbital evolution, in particular near the ISCO.

Figure 32 also shows that our model actually predicts the expected orbital evolution all the way down to the ISCO, in agreement with the EOBNRv2 model, and requires a different set of coefficients b_i in the redshift observable $z_{\text{SF}}(x)$, as compared with results in the extreme-mass-ratio limit quoted in [234]. Notice that this is not only a modeling issue. It is an indication that implementing available self-force data into IMRI waveform models will not render the correct inspiral evolution, at the very least for the cases we have considered. This is an important result of this chapter. In order to substantiate this statement, in the following Section we will compute the value of the gauge invariant angular momentum $L_z(x)$ at the ISCO within both the self-force formalism and our IMRI model. We will also show that the evolution of $L_z(x)$ is consistent between both formalisms during early inspiral, but that the form of this object differs as we near the ISCO.

One may also expect that for binaries with small mass-ratios, available self-force corrections may provide a fairly good description of the inspiral evolution. This is what we actually see in the bottom panel of Figure 32. We will also show in the following Section that the evolution of $L_z(x)$ for binaries with mass-ratio 1:100 is consistent from early inspiral to the ISCO with EOBNRv2. This may not be surprising, since current self-force data have been obtained in the context of EMRIs and the EOBNRv2 has been calibrated so as to reproduce the dynamical evolution of binary black holes of small mass-ratio [238, 239, 240, 241]. This exercise then suggests that it may be necessary to go beyond first-order conservative corrections to reproduce accurately the expected dynamical evolution of intermediate-mass ratio systems with $\eta \sim 10^{-2} - 10^{-1}$.

To carry out the analysis described above in the following Section, we will start by using the EOBNRv2 model to compute the orbital frequency ISCO shift for binaries of mass ratio 1:1, 1:2, 1:3, 1:4, 1:5, 1:6, 1:10 and 1:100, along with perturbative results in the context of extreme-mass-ratio inspirals. We will use this expression for the orbital frequency ISCO shift to evaluate the gauge-invariant object x and then compute the value of the angular momentum at the ISCO using Eq. (7.8). We should also acknowledge the fact that EOB has not yet been calibrated using NR simulations of systems with mass-ratio 1:100. It is expected that EOBNRv2 provides a fair

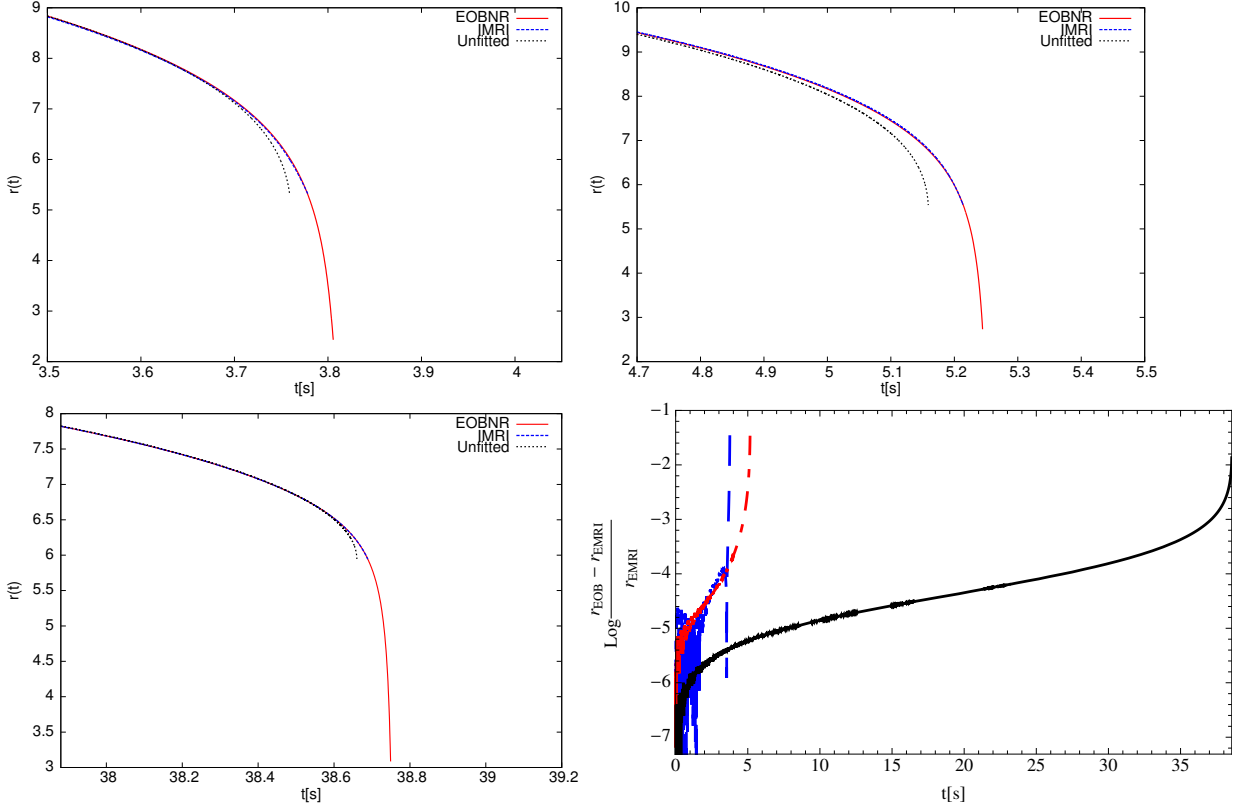


Figure 32: The panels show the radial evolution using the EOBNRv2 model, the IMRI model described in the text, and a model (Unfitted) which is the same as the IMRI model described in text except for the fact that the coefficients used in Eq. (7.9) for the function $z_{\text{SF}}(x)$ were derived using available self-force data from extreme-mass ratio calculations [234]. The plots correspond to binaries of component masses $17M_{\odot} + 100M_{\odot}$ (top-left panel), $10M_{\odot} + 100M_{\odot}$ (top-right panel) and $1M_{\odot} + 100M_{\odot}$ (bottom-left panel). The bottom-right panel shows that the orbital evolution predicted by a model that incorporates self-force corrections from extreme-mass-ratio inspirals (EMRIs) deviates from the orbital evolution predicted by the EOBNRv2 model at late inspiral. This discrepancy is more noticeable for systems with mass-ratios 17:100 (dashed blue) and 10:100 (dashed-dot red). Furthermore, for smaller mass-ratios, 1:100 (solid black), the discrepancy becomes comparatively smaller, as expected.

description of the dynamical evolution of such sources, and we show in the following section that both EOBNRv2 and perturbative calculations provide a consistent modeling of the gauge-invariant angular momentum \hat{L}_z from early inspiral to the ISCO for binaries with mass-ratio 1:100. However, this study should be compared to accurate NR simulations of mass-ratio 1:100 [242] when available in sufficient length.

7.2 ISCO shift: connecting the extreme, intermediate and comparable-mass ratio regimes

In the previous Sections we have mentioned that during the inspiral of a stellar mass compact object of mass m_2 into a supermassive BH of mass m_1 , the radiative part of the self-force drives the inspiral evolution of the small object, whereas its conservative part has a cumulative effect on the orbital phase evolution [243]. These two effects have been considered in the development of EMRI waveform templates [244, 245, 246, 247, 237, 248, 249].

We shall now consider a novel effect that was explored by Barack & Sago [230]. They have shown that the self-force also introduces shifts in the innermost stable circular orbit radius and frequency. For a test-mass particle, these two quantities are given by

$$r_{\text{ISCO}} = 6m_1, \quad m_1\Omega_{\text{ISCO}} = \frac{1}{6\sqrt{6}}, \quad (7.10)$$

whereas, for finite η , in the Lorenz gauge, these two quantities take the form [230]

$$\Delta r_{\text{ISCO}} = -3.269(\pm 3 \times 10^{-3})m_2, \quad \frac{\Delta\Omega_{\text{ISCO}}}{\Omega_{\text{ISCO}}} = 0.4870(\pm 6 \times 10^{-4})\frac{m_2}{m_1}. \quad (7.11)$$

Since Barack & Sago carried out these calculations in Lorenz gauge, it was necessary to translate these results into coordinates that are commonly used for GW observations, i.e., asymptotically flat coordinates. This exercise has been done for the orbital frequency, which is a gauge invariant object, and hence can be compared to results obtained in alternative formalisms, such as PN theory or the EOB approach. In [231] and [233], the authors derive the ‘renormalization’ factor that translates results of Lorenz-gauge calculations into physical units. Applying this renormalization

technique, one finds that the ISCO frequency is given by

$$M\Omega_{\text{ISCO}} = \frac{1}{6\sqrt{6}} (1 + 1.2512\eta + \mathcal{O}(\eta^2)), \quad (7.12)$$

with $M = m_1 + m_2$. This prediction can be compared with PN-based ISCO calculations at different orders of accuracy [250]

$$\begin{aligned} M\Omega_{\text{ISCO}}^{\text{2PN}} &= \frac{1}{6\sqrt{6}} \left(1 + \frac{7}{12}\eta + \mathcal{O}(\eta^2) \right), \\ M\Omega_{\text{ISCO}}^{\text{3PN}} &= \frac{1}{6\sqrt{6}} \left(1 + \left(\frac{565}{288} - \frac{41}{768}\pi^2 \right)\eta + \mathcal{O}(\eta^2) \right). \end{aligned} \quad (7.13)$$

The EOB approach has also been used to describe the orbital frequency shift at ISCO. Damour suggested in [233] that a fit for the ISCO orbital frequency shift that incorporates results from the gravitational self-force and NR simulations may be a quadratic polynomial in η of the form [233]

$$M\Omega_{\text{ISCO}}^{\text{Damour}} = \frac{1}{6\sqrt{6}} (1 + 1.25\eta + 1.87\eta^2). \quad (7.14)$$

In this chapter we build up on this analysis and update this estimate using results from the self-force program, and making use of the EOBNRv2 model, which has been calibrated to NR simulations [38]. The prescription for the orbital frequency ISCO shift that we propose below reproduces accurately the results predicted by the self-force program for EMRIs, and also reproduces the best data currently available for intermediate and comparable-mass systems. To compute the ISCO orbital frequency shift, we use the equation derived in [233], namely,

$$2A(u)A'(u) + 4u(A'(u))^2 - 2uA(u)A''(u) = 0, \quad (7.15)$$

where $u = 1/r$ and $'$ stands for d/du , as before. This ISCO condition can be rewritten in terms of the radial coordinate as [250]

$$rA(r)A''(r) - 2r(A'(r))^2 + 3A(r)A'(r) = 0, \quad (7.16)$$

where $' = d/dr$. We shall use the metric coefficient $A(r)$ quoted in [38], which includes the Padé expression for $A(r)$ at 5PN order. Having obtained the value for r_{isco} using Eq. (7.16), we evaluate the angular orbital frequency $M\Omega_{\text{ISCO}}$ at this fiducial value using Eq. (10b) of [38] with $p_r = 0$.

Using a variety of events, including extreme, $\eta \sim 10^{-5}$, and intermediate, $\eta \sim 10^{-2} - 10^{-1}$, mass ratio inspirals, we derive a quadratic polynomial fit in η for the ISCO orbital frequency shift for these types of events, namely

$$M\Omega_{\text{ISCO}}^{\text{fit}} = \frac{1}{6\sqrt{6}} (1 + 1.05786\eta + 2.12991\eta^2). \quad (7.17)$$

We found that at second order in η , this numerical fit does not reproduce accurately the orbital frequency ISCO shift for small-mass ratios [230]. We can fix these problems using a prescription of the form

$$M\Omega_{\text{ISCO}}^{\text{fit}} = \frac{1}{6\sqrt{6}} (1 + 1.2512\eta - 0.0553751\eta^2 + 5.78557\eta^3). \quad (7.18)$$

At this level of accuracy we exactly reproduce the prediction for EMRIs for small η , as well as the most-up-to-date results for binaries modeled using the EOBNRv2 scheme. We compare the range of applicability of this numerical expression, along the other various approximations mentioned above, in Figure 33.

With our prescription for $M\Omega_{\text{ISCO}}$, we can evaluate the value of the gauge-invariant angular momentum at the ISCO. To do so, we first use Eq. (7.12) to compute the shift in the orbital frequency at the ISCO, and then use Eq. (7.8) in conjunction with the values for the b_i coefficients of Eq. (7.9) calculated in the EMRI limit [234]. We also present results for an ‘incomplete model’, in which we use Eq. (7.18) to evaluate the value of the orbital frequency at the ISCO, and then use Eq. (7.8) with the set of b_i coefficients quoted in [234]. Finally, we use the prescription for the shift of the orbital frequency at the ISCO in Eq. (7.18), and the prescription for the angular momentum (Eq. (7.8)) using the corrections quoted in Table 9. Table 10 shows that, in accord with Figure 32, for binaries with symmetric mass-ratio $\eta \sim 0.01$, the value of the angular momentum evaluated at ISCO is fairly consistent between the two models. However, the predicted value of the angular momentum at ISCO becomes more discrepant for binaries with $\eta \sim 0.1$. This further affirms that the

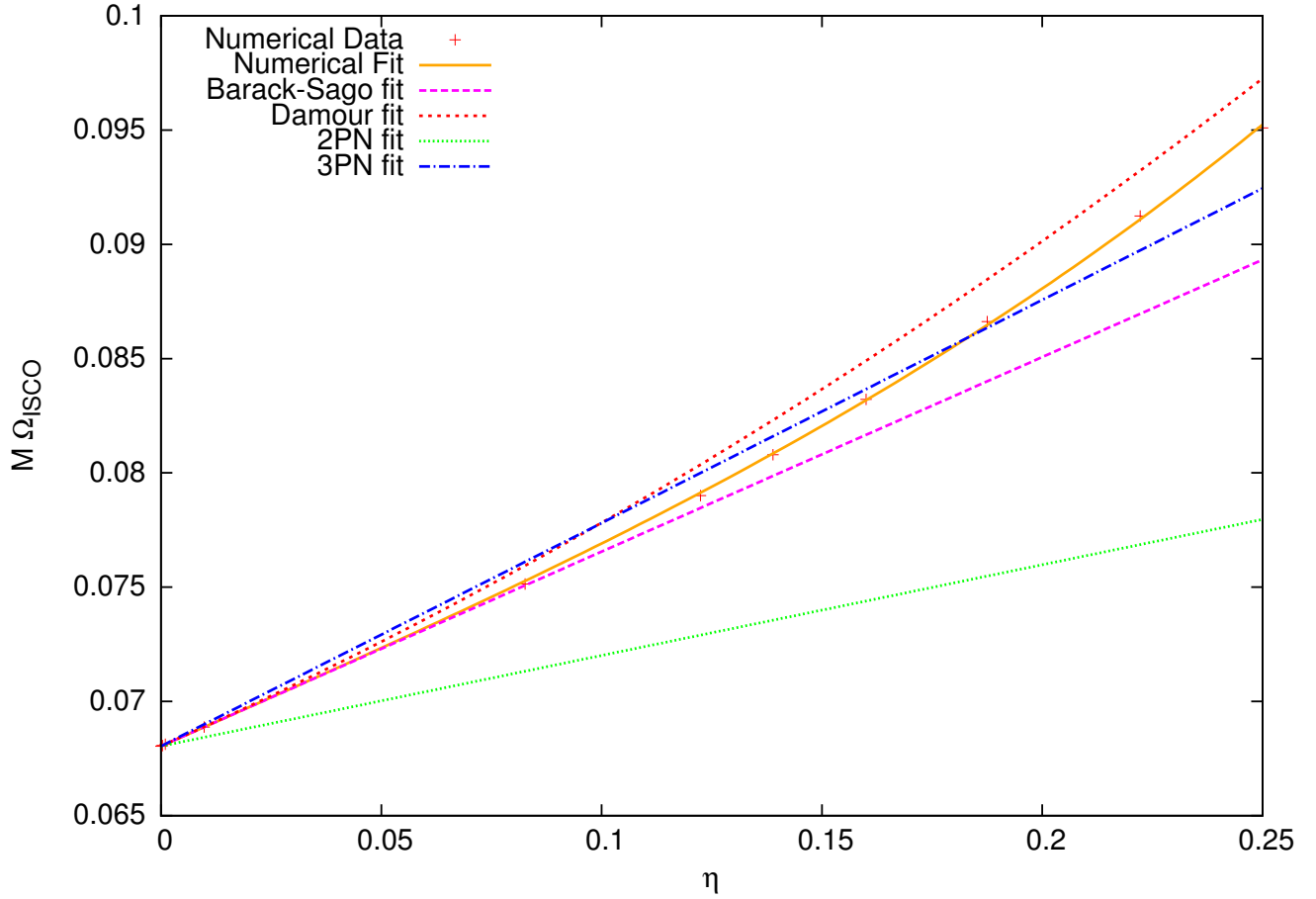


Figure 33: ISCO shift using various approximations as described in the text. The ‘Numerical Data’ has been obtained using calculations in the extreme-mass ratio regime [230] and the EOBNRv2. The prescription that encapsulates results from the extreme, intermediate and comparable mass-ratio regime is labeled as ‘Numerical Fit’ and is given by Eq. (7.18) in the main text.

η	$L_z(x_{\text{ISCO}})$		
	SF Fit	Incomplete	IMRI
$\frac{1700}{13689}$	3.3389	3.3522	3.2918
$\frac{10}{121}$	3.3876	3.3878	3.3254
$\frac{100}{10201}$	3.4561	3.4561	3.4429

Table 10: The Table shows the value of the angular momentum L_z as a function of the gauge invariant object $x = (M\Omega)^{2/3}$ evaluated at the ISCO radius (see Eq. (7.8)). The SF (self-force) values are computed using the prescription given in Eq. (7.12) to compute the orbital frequency shift, and Eq. (7.8) with the coefficients b_i quoted in [234], i.e., evaluated in the context of extreme-mass-ratio inspirals. Incomplete stands for a prescription in which we use the prescription for the orbital frequency given by Eq. (7.18), and the angular momentum prescription given by Eq. (7.8) with the coefficients b_i quoted in [234]. The b_i values of the IMRI model are obtained using a model that reproduces the dynamical evolution of intermediate-mass-ratio inspirals, as compared with the EOBNRv2 model, and for which we have derived a new prescription for the red-shift observable $z_{\text{SF}}(x)$ which actually reproduces the features of true inspirals.

evolution of intermediate-mass ratio inspirals cannot be fully captured by using self-force calculations from extreme-mass ratio inspirals. This can be better visualized in Figure 34 where we show the angular momentum during inspiral all the way down to the ISCO using two formalism, namely, our IMRI prescription and a model that includes only available self-force corrections (labeled as ‘Self Force’).

Table 10 and Figures 32, 34 show that as the mass-ratio increases, the discrepancy between a model that incorporates available self-force corrections [232] and one that has been calibrated to NR simulations becomes more pronounced. For events with mass-ratio 1:10 this difference looks slightly larger than for those of mass-ratio 17:100. Part of the reason for this behavior may be the fact that the model we have used to perform this analysis, EOBNRv2, provides the best prescription currently available for the inspiral evolution of sources with mass-ratios 1:1-1:6. It is expected that the model provides a good description of the inspiral evolution of sources with mass-ratio 1:10, and hence we have extended its realm of applicability to shed light on the form that the self-force is expected to have so as to reproduce the inspiral evolution of these type of sources. Thus, a conservative conclusion we can draw at this stage is that, using the best waveform model currently available in the literature, we have shown

that one may not be able to accurately model the dynamics of sources with mass-ratio 1:10 using available self-force calculations. This trend is also present in the case of events with mass-ratio 17:100 and the results in this case are more conclusive. We have shown that a waveform model that includes available self-force corrections will not be able to capture faithfully the inspiral evolution of these GW sources. These results suggest that one may need to include higher-order corrections in the self-force to capture the behavior of true inspirals in the intermediate-mass-ratio regime.

7.3 Extension to equal-mass binaries

In this Section we show that the approach outlined in the main body of the chapter can still be used to model equal-mass (EM) binaries with great accuracy at an inexpensive computational cost. To do so we consider a system with total mass $20M_{\odot}$. Following the method described in Section 7.1, we start by deriving accurate prescriptions for the orbital frequency Ω_{ansatz} and angular momentum flux \dot{L}_z . Thereafter we derive the corrections that should be implemented in the gauge-invariant expression for the angular momentum (see Eq. (7.8)) to accurately reproduce the inspiral evolution predicted by the EOBNRv2 model.

The prescriptions for the orbital frequency, angular momentum flux and angular momentum which reproduce the inspiral evolution for the $10M_{\odot}+10M_{\odot}$ binary system shown in Figure 35 require the following set of coefficients (compare Tables 7, 8, 9)

$$\begin{aligned} \Omega(u)_{\text{ansatz}} : & a_1 = -5.644, \quad a_2 = 11.003, \quad a_3 = -5.390, \quad a_4 = 8.794, \quad a_5 = 0.458 \\ \dot{L}_z : & c_{2.5}^1 = -90.566, \quad c_3^2 = 304.941, \quad c_{3.5}^3 = -339.500 \\ z_{\text{SF}} : & b_1 = -5.803, \quad b_2 = 14.171, \quad b_3 = -7.074, \quad b_4 = 22.810, \quad b_5 = -25.580 \end{aligned} \tag{7.19}$$

Having shown that the approach outlined in the chapter is still effective to model EM binaries, we consider worthwhile developing a model that encapsulates the physics of binaries of comparable and intermediate-mass-ratio. In order to extend our IMRI model into the comparable mass-ratio regime, we will require some changes in the model. First and foremost, we require expressions for the orbital frequency evolution

(see Eq. (7.4)) and angular momentum (see Eq. (7.8)) which incorporate conservative corrections at second-order in mass ratio η . We can draw this conclusion by comparing the bottom-right panel of Figure 34 with the bottom panel of Figure 35. The former plot shows that for IMRIs the prescription for the angular momentum deviates from the self-force prediction near the ISCO. However, the latter plot shows that in the EM case the prescription for the angular momentum deviates considerably from the self-force prediction even during the inspiral evolution, far away from the ISCO. Because the prescription we have used for the angular momentum in both cases includes corrections at liner order in mass-ratio, this suggest that to derive a model that unifies both regimes we require an expression for the angular momentum which includes second-order conservative corrections. We can follow a similar strategy to encapsulate in a single prescription the radiative piece of the self-force for comparable and intermediate mass-ratio systems by deriving second-order radiative corrections in the prescription for the angular momentum flux.

Once suitable expressions for Ω_{ansatz} , \dot{L}_z and $L_z(x)$ have been derived, we will be able to tune the coefficients of these objects and derive numerical fits for the coefficients in terms of the mass-ratio η of the system. This approach will provide a unified description for the inspiral evolution of IMRIs and comparable-mass systems. This will be the subject of future study.

7.4 Conclusions

In this chapter we have developed a code to reproduce the analysis presented in [38]. Using this code we generated the inspiral evolution of three different systems to perform an exploratory study of the importance of including accurate self-force corrections in search templates that aim to detect non-spinning intermediate-mass ratio inspirals. The choice of the systems to perform this study reflects the knowledge we have at present on the dynamical evolution of non-spinning BH binaries ($17M_\odot + 100M_\odot$), what we want to know ($10M_\odot + 100M_\odot$), and a special system that provides reassurance that the dynamics of intermediate-mass-ratio inspirals with typical mass-ratios $\eta \sim 0.01$ can be captured using perturbative theory, as shown in [242, 251].

The EOBNRv2 model we have used as a benchmark to carry out this study has the advantage of encoding the best information currently available of non-spinning

BH binaries, is capable of reproducing the expected dynamics in the test-mass particle limit, and also includes corrections taken from self-force corrections in the extreme-mass-ratio limit. We have confirmed these statements for systems with $\eta \sim 0.01$ by showing that the EOBNRv2 does predict the expected form of the angular momentum flux, as compared to Teukolsky data, as well as the evolution of the gauge-invariant angular momentum, as compared to self-force data.

In order to explore the form of the self-force in the intermediate-mass-ratio regime, we developed an IMRI model that reproduces the inspiral evolution predicted by the EOBNRv2 model, and which enable us to explore the form that the self-force should have in this mass-ratio regime so as to reproduce the binary's dynamical evolution as predicted by the best available interface to NR simulations. We have found that for systems with component masses $17M_{\odot} + 100M_{\odot}$, available self-force corrections do not accurately reproduce the inspiral evolution. We have shown that there is a clear deviation from the true inspiral trajectory near the ISCO. We have also explored this issue in greater detail by showing that the gauge-invariant angular momentum does deviate from the current self-force prediction near the ISCO. When we extend the realm of applicability of the EOBNRv2 to binaries of mass-ratio 1:10, we observe a similar behaviour. This exploratory study then suggests that it may be necessary to extend conservative corrections beyond the linear order to accurately capture the true inspiral evolution for sources with intermediate-mass-ratio. Furthermore, once NR simulations of systems with mass-ratios 1:10, 1:15 and 1:100 have reached enough resolution near merger, we will be in a good position to calibrate the EOB model so as to reproduce the true dynamical evolution for these type of sources [242, 252, 253]. Such a model will enable us to further probe the parameter space to develop IMRI models, as the one proposed in this chapter, that capture the features of true inspirals at a very inexpensive computational cost.

We have also used our EOBNRv2 code to derive a prescription for the orbital frequency ISCO shift that encapsulates results from the extreme, intermediate and comparable-mass ratio regimes. Our prescription is the first in the literature that reproduces the self-force result in the appropriate limit. We have made use of this new prescription to estimate the value of the angular momentum at the ISCO using our IMRI prescription and available self-force data. We have found a clear discrepancy for systems with mass-ratios $\eta \sim 0.1$, but have confirmed that for systems with small

mass ratios $\eta \sim 0.01$ both predictions are fairly consistent.

This study has also shed light on a pressing issue that needs to be addressed before aLIGO begins observations, namely, at present we use templates in searches for GW sources whose actual dynamics are currently unknown. For instance, searches for BH binaries with total mass $25M_{\odot} - 200M_{\odot}$, and individual masses from $3M_{\odot}$ to $99M_{\odot}$ have been carried out, but not a single model has been calibrated using high-resolution NR simulations for mass-ratios smaller than 1:6. Hence, it is important that numerical relativists and search template developers interact more closely so as to run NR simulations which cover regions in parameter space where future GW detectors may detect GW sources. This meaningful interaction will be important from a theoretical perspective, as we will be able to further our knowledge of the self-force, and from a data analysis perspective, as we will be in a stronger position to develop accurate search templates for use in data analysis.

The approach we have outlined in this chapter is the initial step to construct inspiral-merger-ringdown IMRI waveforms. Having derived a consistent prescription for the inspiral evolution, we can use a similar approach to that described in [254] to include merger and ring-down in a physically consistent way. Developing complete IMRI waveforms may be useful for aLIGO data analysis, as they will provide the accuracy of more complex waveform models at an inexpensive computational cost.

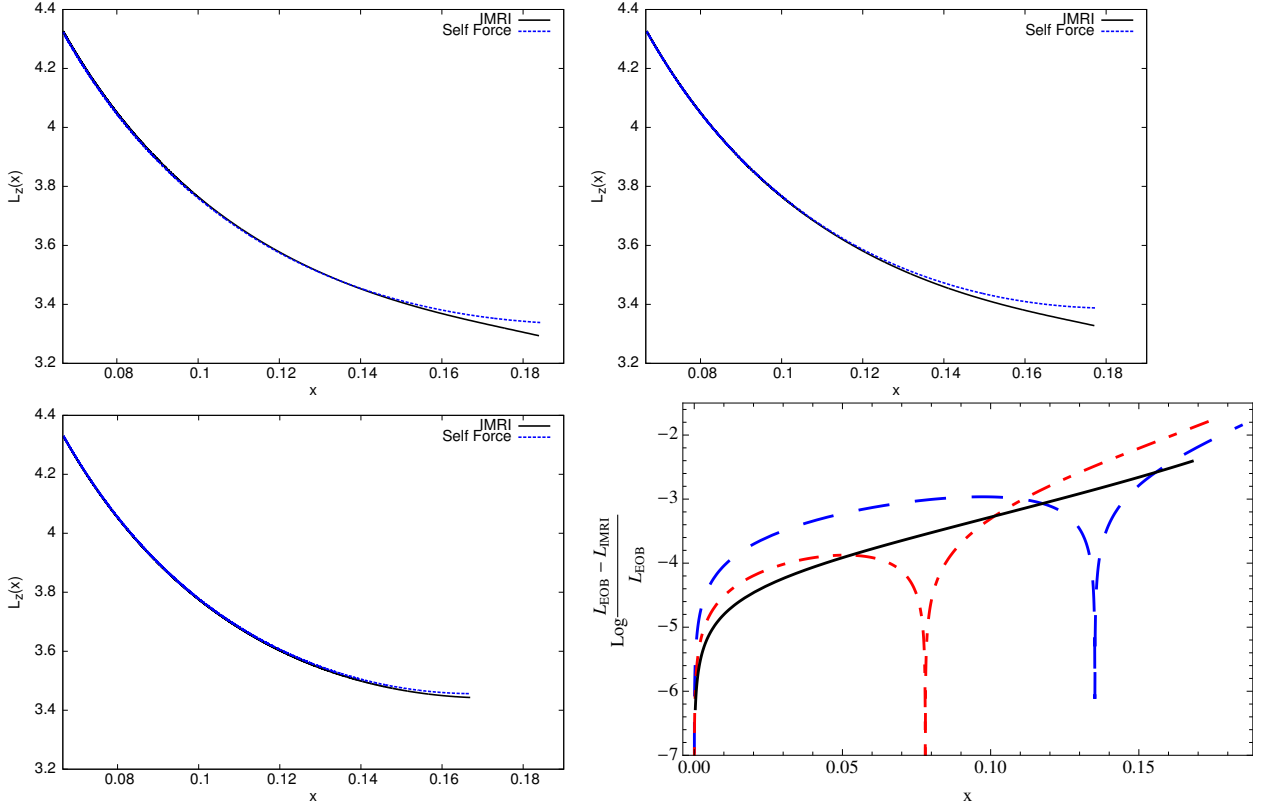


Figure 34: The panels show the invariant angular momentum $L_z(x)$, with $x = (M\Omega)^{2/3}$, from early inspiral to the ISCO using two different prescriptions. The ‘IMRI’ prescription reproduces accurately the expected inspiral evolution, as compared with results from the EOBNRv2 model —which has been calibrated to NR simulations. The ‘Self Force’ prescription encapsulates self-force corrections derived in the context of EMRIs [232, 234]. Note that for the three binary systems studied, $17M_\odot + 100M_\odot$ (top-left panel), $10M_\odot + 100M_\odot$ (top-right panel), and $1M_\odot + 100M_\odot$ (bottom-left panel), the ‘Self Force’ prescription for the angular momentum presents a deviation from its expected value that becomes more noticeable near the ISCO. The bottom-right panel shows the fractional accuracy between the two different prescriptions for the angular momentum for the systems 17:100 (dashed blue), 10:100 (dashed-dot red) and 1:100 (solid black). Notice also that, as expected, for binaries with small mass-ratio the ‘Self Force’ and ‘IMRI’ prescriptions are fairly consistent all the way down to the ISCO. As in the previous plots, the spikes in the bottom-right panel are due to numerical artifacts.

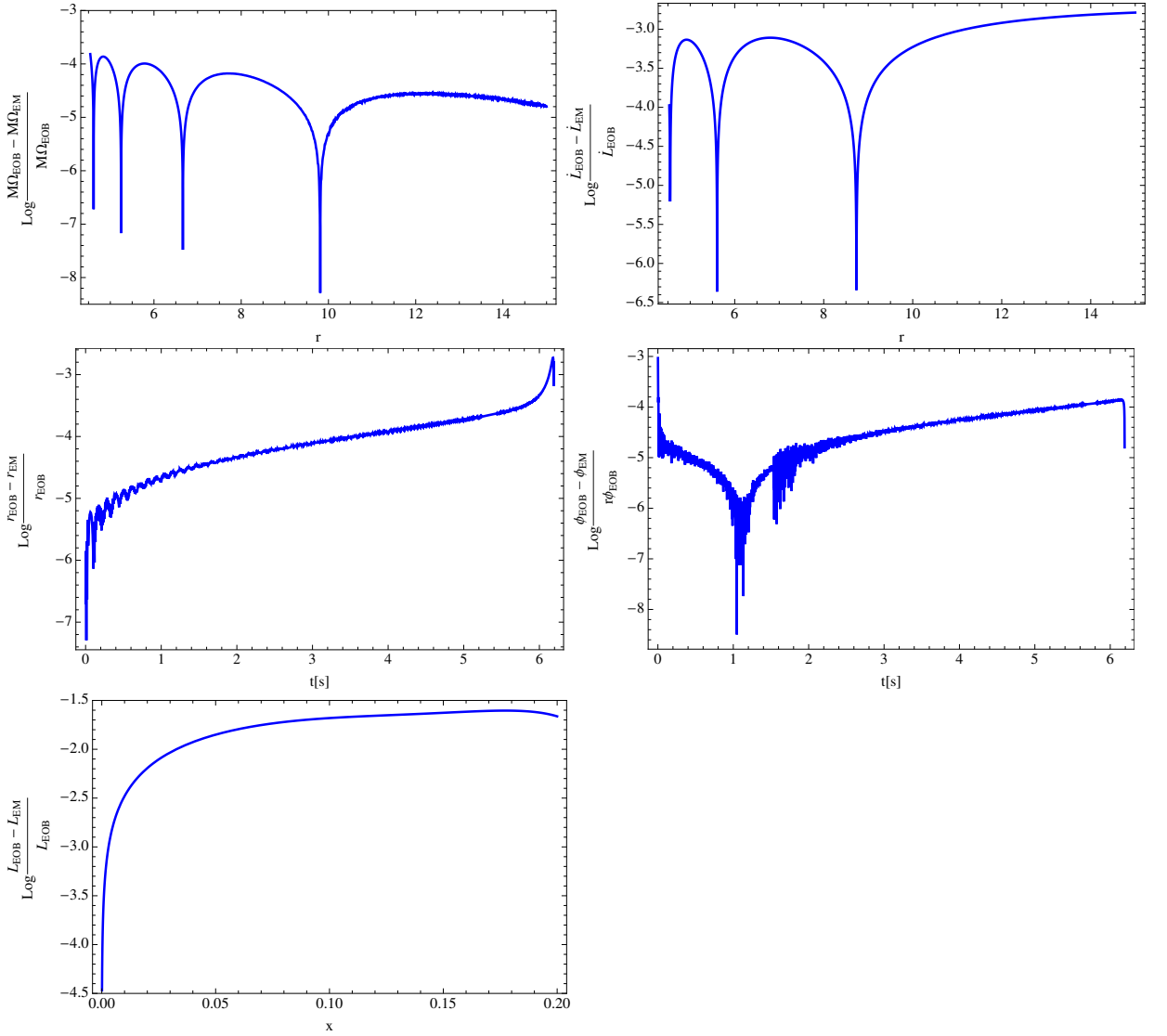


Figure 35: The panels show the accuracy with which our model can reproduce the dynamics of an equal mass (EM) binary system with masses ($10M_\odot + 10M_\odot$), as compared with the EOBNRv2 model. The top panels show that our model can reproduce the orbital angular evolution and the flux of angular momentum predicted by the EOBNRv2 model point to point with an accuracy better than one part in a thousand. The middle panels show that our model can reproduce with a similar accuracy the radial and azimuthal evolution of a $10M_\odot + 10M_\odot$ binary system. The bottom panel shows that the expression for the gauge-invariant angular momentum $L_z(x)$ for an EM mass deviates clearly from the EMRI prescription even before nearing the ISCO.

Chapter 8

Self-forced evolutions of an implicit rotating source: a natural framework to model comparable and intermediate mass-ratio systems from inspiral through ringdown

8.1 Introduction

The black hole (BH) mass function in the local Universe is a strongly bi-modal distribution that identifies two main families: stellar-mass BHs with typical masses $\sim 10M_{\odot}$ observed in Galactic X-ray binaries [255] and, more recently, in globular clusters [256], and supermassive BHs with masses $\gtrsim 10^5M_{\odot}$ observed to be present in most galactic nuclei [257, 258]. However, a population of X-ray sources with luminosities in excess of $10^{39}\text{ erg s}^{-1}$ has recently been observed, and *Chandra* and *XMM-Newton* spectral observations of these ultra-luminous X-ray sources (ULXs) revealed cool disc signatures that were consistent with the presence of intermediate mass BHs (IMBHs) with masses $10^{2-4}M_{\odot}$ [259, 260, 261]. Subsequent observations have shown that these ULXs have spectral and temporal signatures that are not

consistent with the sub-Eddington accretion regime that is expected for IMBHs at typical ULX luminosities. Rather, these later studies suggest that many ULXs are powered by super-Eddington accretion onto $\lesssim 100M_{\odot}$ BH remnants. Nevertheless, recent work by Swartz et al. [262] has demonstrated that as well as the high mass X-ray binaries that characterise most ULXs, there is a subpopulation of ULXs that seem to be powered by a separate physical mechanism. These objects have typical luminosities $L \gtrsim 10^{41} \text{ erg s}^{-1}$, which cannot be explained by close to maximal radiation from super-Eddington accretion onto massive BHs formed in low metallicity regions [263, 264, 265]. Several hyper-luminous X-ray sources, including M82 X-1, ESO 243-49 HLX-1, Cartwheel N10 and CXO J122518.6+144545, present the best indirect evidence for the existence of IMBHs [266, 267, 268, 269]. In particular, the colocation of M82 X-1 with a massive, young stellar cluster, the features of its power spectrum, and some reported transitions between a hard state and a thermal dominant state, make this object a strong IMBH candidate [270, 271, 272, 273]. Recent searches of archival *Chandra* and *XMM-Newton* data sets have also uncovered two new hyper-luminous X-ray sources with luminosities in excess of $10^{39} \text{ erg s}^{-1}$. These sources are the most promising IMBH candidates currently known, although the highest possible super-Eddington accretion rate onto the largest permitted BH remnant cannot yet be ruled out [274]. This increasing body of observational evidence [275, 276], and the fact that the existence of IMBHs provides a compelling explanation for the initial seeding of supermassive BHs present in most galactic nuclei [277, 278, 279] has revived the quest for these elusive objects.

Since hyper-luminous X-ray sources are rare, and our knowledge about their astrophysical properties is still limited, we may have to use a different means to search for IMBHs in order to improve our knowledge about the channels that lead to the formation of these objects, and to shed light on their astrophysical properties, such as mass and spin distributions [280]. In this chapter we explore the use of observations in the gravitational wave (GW) spectrum to gain insight into the properties of IMBHs.

The current upgrade of the Laser Interferometer Gravitational Wave Observatory (LIGO) and its international partners Virgo and Kagra [281, 282, 283], will enable the detection of GWs from coalescences involving IMBHs with masses $50M_{\odot} \lesssim M \lesssim 500M_{\odot}$, if these instruments achieve their target sensitivity down to the low-frequency

cutoff at 10Hz (See Figure 36) [284]. Advanced LIGO (aLIGO) and Advanced Virgo are expected to have greatest sensitivity in the 60Hz - 500Hz range, with a peak at ~ 60 Hz (see Figure 36). Proposed third generation detectors, such as the Einstein Telescope [285], which aim to extend the frequency range of ground-based detectors down to 1Hz, while also maintaining high frequency sensitivity up to 10kHz, will enhance our ability to search for GWs emitted by sources that involve BHs with masses between $10^{2-4} M_{\odot}$ [286, 287, 288].

A promising channel for detection of IMBHs is through the emission of gravitational radiation during the coalescence of stellar-mass compact remnants — neutron stars (NSs) or BHs — with IMBHs in core-collapsed globular clusters. This expectation is backed up by numerical simulations of globular clusters [289, 290, 291, 292, 293, 294, 295, 296] which suggest that IMBHs could undergo several collisions with stellar-mass compact remnants during the lifetime of the cluster through a variety of mechanisms, including gravitational radiation, Kozai resonances and binary exchange processes. As discussed in [297], the most likely mechanism for the formation of binaries involving a stellar-mass compact remnant and an IMBH is hardening via three body interactions, with an expected detection rate of $\sim 1 - 10 \text{ yr}^{-1}$ with ground-based observatories [297, 298].

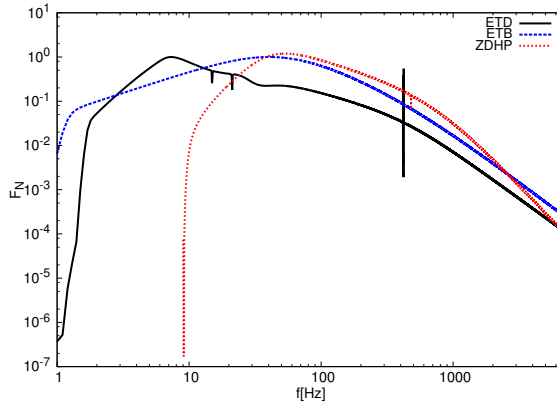


Figure 36: The panel shows the expected sensitivity for two configurations of the Einstein Telescope (ET), namely, ETD (black), ETB (blue) and LIGO’s Zero Detuned High Power (ZDHP) configuration (red). The vertical axis measures $F_{\text{normalized}} = (f/f_{\max})^{-7/6} \sqrt{S_n(f_{\max})/S_n(f)}$, where f_{\max} is the maximum of the corresponding power spectral density, $S_n(f)$.

The frequency of the dominant quadrupolar harmonic in the GWs emitted at the

innermost stable circular orbit (ISCO) for a binary of non-spinning objects is

$$f_{\text{ISCO}} = 4.4 \text{kHz} \left(\frac{M_\odot}{M} \right), \quad (8.1)$$

so for a typical intermediate mass–ratio coalescence (IMRC) with total mass $M \gtrsim 100M_\odot$, advanced detectors will observe the late inspiral, merger and ringdown. However, the heaviest IMRCs, with masses $\gtrsim 500M_\odot$, will coalesce out of band or at the low frequency limit of the bandwidth. Hence, merger and ringdown — which intrinsically generate a signal-to-noise ratio (SNR) suppressed by a factor of symmetric mass-ratio — see Table 11 below — relative to the SNR generated during the inspiral phase— will significantly contribute to the SNR of IMRCs over a considerable portion of the detectable mass-range [299]. In order to get the most information from GW observations of IMRCs, it is therefore necessary to develop waveform models that incorporate the inspiral, merger and ringdown in a physically consistent way. In order to make progress in this direction, we previously developed a waveform model that combined results from Black Hole Perturbation Theory (BHPT) and post-Newtonian (PN) theory to explore the information that could be obtained from observations of IMRCs with the EinsteinTelescope [287, 288]. Although this model provided an important step in exploring the science that could be done with IMRC observations, the model was limited.

In [300, 301, 302, 303] we explored using the self-force formalism [243, 304] to develop a waveform model with a robust description of the dynamical evolution of IMRCs during the inspiral phase. These were found to be effective when used to carry out matched-filter based searches for inspiral-only IMRCs [299], but searches for IMRCs in the advanced detector era will require waveform models that include not only the inspiral but also the merger and ringdown [299]. The model described in [287] included merger and ring down but without the self-force driven inspiral. It would be ideal to develop a consistent inspiral, merger, ringdown waveform model by comparison to numerical relativity simulations, as described in [38, 305]. However, numerical relativity simulations for systems with mass-ratios $q = m_1/m_2 \lesssim 1/10$ are very computationally expensive at present [37]. We can circumvent this problem by making use of recent breakthroughs in the self-force program that have shown that the conservative part of the self-force can reproduce, with good accuracy, results

from numerical relativity simulations of comparable-mass binary systems [306]. Furthermore, the recent computation of the self-force inside the ISCO equips us to now develop models that better reproduce the true dynamics of black hole binaries in the strong field regime [307].

In addition to IMRCs, which may be detected by second generation detectors, and with more likelihood by third generation detectors, we have explored the suitability of using self-forced evolutions to model the mergers of systems involving NSs and stellar mass BHs [308]. Since NSBH mergers are promising GW sources for second generation detectors, we need to develop accurate and computationally inexpensive templates appropriate for these events. Current efforts to model NSBH systems have generally used PN approximants, evaluated to the highest post-Newtonian order available, but these approximates are not sufficiently reliable to model these events [309, 51]. In Figure 37, we show the phase difference between the PN approximant TaylorT4 [310] and the EOB model introduced in [38, 305]. This exhibits a substantial discrepancy near the ISCO. These considerations have impelled us to develop a different approach to model events with the typical mass- ratios expected for NSBH binaries.

In this chapter we combine recent developments in the self-force program, in PN theory and in numerical relativity to develop a model that describes the inspiral, merger and ringdown of IMRCs and comparable mass-ratio systems that could be detected by second and third generation ground-based GW detectors. In Section 8.2 we discuss the modelling of the conservative part of the self-force. We show that using the linear in mass-ratio self force results for binaries with mass-ratios $q \gtrsim 1/6$ gives a system without an ISCO. We then discuss the implications of this result for the modelling of comparable and intermediate mass-ratio binaries. Thereafter, we describe the approach we use to model the radiative part of the self-force for the inspiral evolution. Having constructed the inspiral part of the self-forced waveform model, we extend the transition scheme of Ori and Thorne [254] by including finite mass-ratio corrections, and modelling the orbital phase evolution using the implicit rotating source (IRS) model. We adopt this description for the late-time radiation in order to provide a smooth progression from late inspiral to ringdown. We show that this approach provides the correct orbital frequency evolution in the vicinity of the light-ring. Finally, we construct the ringdown waveform using both a sum of quasinormal modes and the late-time radiation waveform evolution predicted by

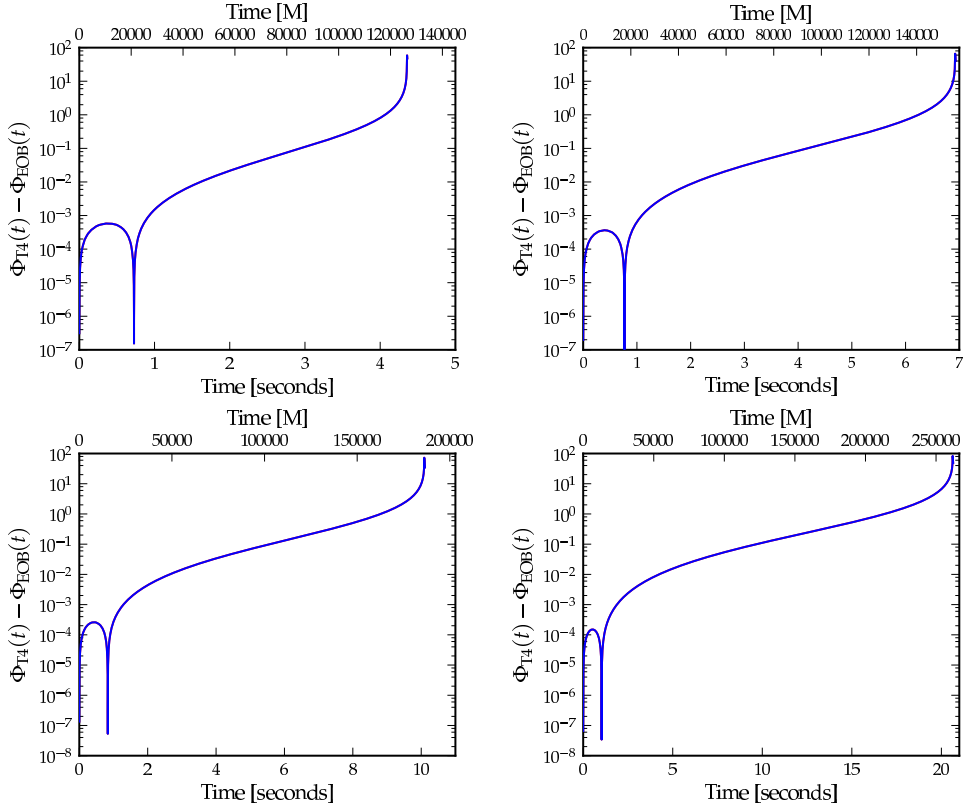


Figure 37: The phase discrepancy in radians between the PN approximant TaylorT4, and the Effective One Body model, shown as a function of time from $r = 30M$ to the point when the TaylorT4 model reaches the ISCO. The systems have mass-ratio, q , total mass, M_{tot} , and final phase discrepancy, $\Delta\Phi$:
 $(q, M_{\text{tot}}, \Delta\Phi) = (1/6, 7M_{\odot}, 21.5 \text{ rads})$ (top-left),
 $(1/8, 9M_{\odot}, 30.2 \text{ rads})$ (top-right),
 $(1/10, 11M_{\odot}, 70.1 \text{ rads})$ (bottom-left) and
 $(1/15, 16M_{\odot}, 83.2 \text{ rads})$ (bottom-right)
respectively.

the IRS model, and show their equivalence. Section 8.3 presents a summary of our findings and future directions of work.

8.2 Modeling

8.2.1 Nomenclature

Throughout this chapter we will use units with $G = c = 1$, unless otherwise stated. We will consider BH binaries on circular orbits with component masses m_1, m_2 , such that $m_1 < m_2$. We assume that the binary components are non spinning. We will use several combinations of the masses $m_{1,2}$ in the following Sections, which are

summarized in Table 11.

Binary masses	
m_1	mass of inspiralling compact object
m_2	mass of central compact object
$M = m_1 + m_2$	total mass of binary system
$q = \frac{m_1}{m_2}$	mass–ratio
$\mu = \frac{m_1 m_2}{m_1 + m_2}$	reduced mass
$\eta = \frac{\mu}{M}$	symmetric mass–ratio

Table 11: The table summarizes the nomenclature we will use throughout our analysis.

Having defined the variables to be used in the subsequent sections, we shall now describe the construction of the self-forced waveform model. The model consists of four building blocks — the inspiral, the transition, the plunge and the ringdown phases. The next section describes the inspiral evolution.

8.2.2 Inspiral evolution

We model the inspiral phase evolution in the context of the Effective One Body (EOB) formalism [311], i.e., we consider the scenario in which the dynamics of a binary system is mapped onto the motion of a test particle in a time-independent and spherically symmetric Schwarzschild space-time with total mass M :

$$ds_{\text{EOB}}^2 = -A(r)dt^2 + B(r)dr^2 + r^2d\Omega^2, \quad (8.2)$$

where the potentials A , B are known to 3PN order [312, 313]. In the test-mass particle limit $\eta \rightarrow 0$, these potentials recover the Schwarzschild results, namely:

$$A(u, \eta \rightarrow 0) = B^{-1}(u, \eta \rightarrow 0) = 1 - 2u, \quad \text{with} \quad u = \frac{M}{r}. \quad (8.3)$$

In the EOB formalism, the orbital frequency evolution can be derived from a Hamiltonian, H_{EOB} [311], given by:

$$H_{\text{EOB}} = M\sqrt{1 + 2\eta(H_{\text{eff}} - 1)}, \quad (8.4)$$

using the general Hamiltonian equation:

$$\frac{d\phi}{dt} = M\Omega = \frac{\partial H_{\text{EOB}}}{\partial L} = \frac{u^2 L(x) A(u)}{H(u) H_{\text{eff}}(u)}, \quad (8.5)$$

where

$$\begin{aligned} H_{\text{eff}}(u) &= \frac{A(u)}{\sqrt{\tilde{A}(u)}}, \quad \tilde{A}(u) = A(u) + \frac{1}{2} u A'(u), \\ \text{and} \quad H(u) &= \sqrt{1 + 2\eta(H_{\text{eff}} - 1)}. \end{aligned} \quad (8.6)$$

Recent work in the self-force formalism has enabled the derivation of gravitational self-force corrections to the EOB potential $A(u) \rightarrow 1 - 2u + \eta a(u) + \mathcal{O}(\eta^2)$ [234]. Deriving this gravitational self-force contribution, $a(u)$, is equivalent to including all PN corrections to the EOB potential $A(u)$ at linear order in η . We shall now briefly describe the construction of the gravitational self-force contribution $a(u)$, emphasizing the fact that this contribution encodes information about the strong-field regime of the gravitational field.

As shown by Detweiler and Whiting [314], the gravitational self-force corrected worldline can be interpreted as a geodesic in a smooth perturbed spacetime with metric

$$g_{\alpha\beta} = g_{\alpha\beta}^0(m_2) + h_{\alpha\beta}^R, \quad (8.7)$$

where the regularized R field is a smooth perturbation associated with m_1 . Detweiler proposed a gauge invariant relation to handle the conservative effect of the gravitational self-force in circular motion [315, 316]:

$$z_1(\Omega) = \sqrt{1 - 3x} \left(1 - \frac{1}{2} h_{uu}^{R,F} + q \frac{x}{1 - 3x} \right), \quad (8.8)$$

where x is the gauge-invariant dimensionless frequency parameter given by $x = (M\Omega)^{2/3}$, $h_{uu}^{R,G}$ is a double contraction of the regularised metric perturbation with the four-velocity, u^μ , $h_{uu}^{R,G} = h_{\mu\nu}^{R,G} u^\mu u^\nu$, the label G indicates the gauge used to evaluate the metric perturbation and the label F indicates that this expression is valid within the class of asymptotically flat gauges. In [307], $z_1(\Omega)$ was calculated in Lorenz

gauge and the following gauge transformation can be used to link the asymptotically flat $h_{uu}^{R,F}$ metric perturbation to its Lorenz-gauge counterpart $h_{uu}^{R,L}$:

$$h_{uu}^{R,F} = h_{uu}^{R,L} + 2q \frac{x(1-2x)}{(1-3x)^{3/2}}. \quad (8.9)$$

Hence, inserting Eq. (8.9) into Eq. (8.8) leads to

$$z_1(\Omega) = \sqrt{1-3x} \left(1 - \frac{1}{2} h_{uu}^{R,L} - 2q \frac{x(1-2x)}{(1-3x)^{3/2}} + q \frac{x}{1-3x} \right). \quad (8.10)$$

The numerical data obtained in [307] for $h_{uu}^{R,L}$ from $x > 1/5$ was new and the numerical accuracy for $x < 1/5$ was also much improved compared to previous results [315, 231]. The EoB potential $a(x)$ can be constructed from $h_{uu}^{R,L}$ via

$$a(x) = -\frac{1}{2} (1-3x) \tilde{h}_{uu}^{R,L} - 2x\sqrt{1-3x}, \quad (8.11)$$

with $\tilde{h}_{uu}^{R,L} = q^{-1} h_{uu}^{R,L}$. In [307], a global fit formula for $a(x)$ was given a dense sample of numerical values over the entire range $0 < x < \frac{1}{3}$. The numerical fit for $a(x)$ that we use in this study is taken from Eq.(54) of [307]. This global analytic fit for $a(x)$ can be recast using the relation

$$a(x) = 2x^3 \frac{(1-2x)}{\sqrt{1-3x}} a_E(x). \quad (8.12)$$

Using the above dictionary, the model for $a(x)$ in this chapter reproduces the numerical data points for the function $a_E(x)$ to within a maximal absolute difference of 1.2×10^{-5} over the domain $0 < x < \frac{1}{3}$. The corresponding self-force corrected energy and angular momentum are given by [307, 234]

$$\begin{aligned} E(u(x)) &= E_0(x) + \eta \left(-\frac{1}{3} \frac{x}{\sqrt{1-3x}} a'(x) + \frac{1}{2} \frac{1-4x}{(1-3x)^{3/2}} a(x) - E_0(x) \left(\frac{1}{2} E_0(x) + \frac{x}{3} \frac{1-6x}{(1-3x)^{3/2}} \right) \right), \\ L_z(u(x)) &= L_0(x) + \eta \left(-\frac{1}{3} \frac{x}{\sqrt{x(1-3x)}} a'(x) - \frac{1}{2} \frac{1}{\sqrt{x}(1-3x)^{3/2}} a(x) - \frac{1}{3} \frac{1-6x}{\sqrt{x}(1-3x)^{3/2}} (E_0(x) - E(u(x))) \right), \end{aligned}$$

with $u(x) = x \left(1 + \eta \left[\frac{1}{6} a'(x) + \frac{2}{3} \left(\frac{1-2x}{\sqrt{1-3x}} - 1 \right) \right] \right),$

where $E_0(x)$ and $L_0(x)$ are given by

$$E_0(x) = \frac{1 - 2x}{\sqrt{1 - 3x}} - 1, \quad (8.16)$$

$$L_0(x) = \frac{1}{\sqrt{x(1 - 3x)}}. \quad (8.17)$$

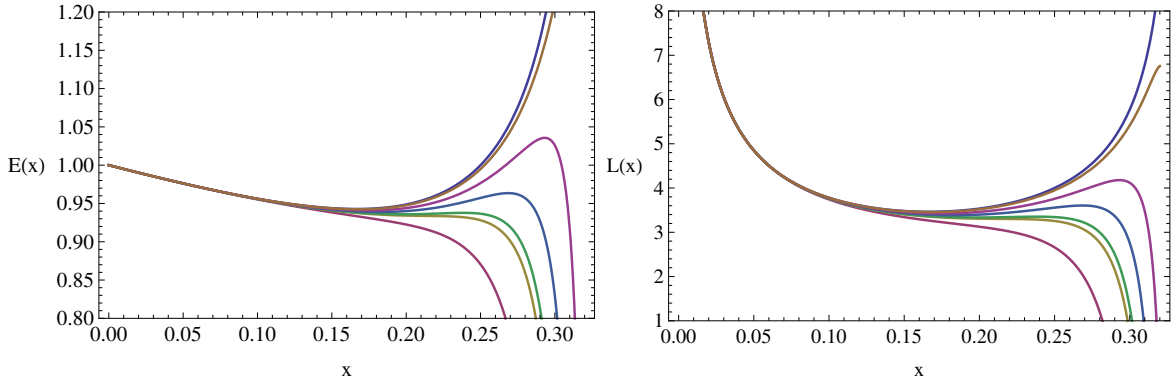


Figure 38: The panels show the energy and angular momentum given by Eqs. (8.13)-(8.14), respectively. We show the functional form of these parameters for binary systems with mass-ratio values, from top to bottom, $q \in [0, 1/100, 1/20, 1/10, 1/6, 1/5, 1]$.

In Figure 38, we show the effect of these conservative corrections on the orbital parameters.

As discussed in [234], if one makes use of the self-force expression for the energy given by Eq. (8.13), and minimize it with respect to the orbital frequency, then one finds that binary systems with mass-ratios $q \in [1, 1/2, 1/3]$ do not have an ISCO in this model. It was argued in [234] that deriving self-force results in the strong field regime may alleviate this problem. We have explored this issue, and have found that using linear self-force corrections that are valid all the way to the light ring (last unstable circular orbit for massless particles) does not fix this problem for comparable mass-ratio systems. In Figure 39, we show that the existence of an ISCO is guaranteed for BH binaries with symmetric mass-ratio $\eta \lesssim 6/49$ (or $q \lesssim 1/6$), and its location may be approximated by

$$x_{\text{ISCO}} = \frac{1}{6} (1 + 0.83401\eta + 4.59483\eta^2). \quad (8.18)$$

It remains to be seen whether the inclusion of second-order conservative corrections gives an ISCO for binaries with mass-ratios $q \gtrsim 1/6$.

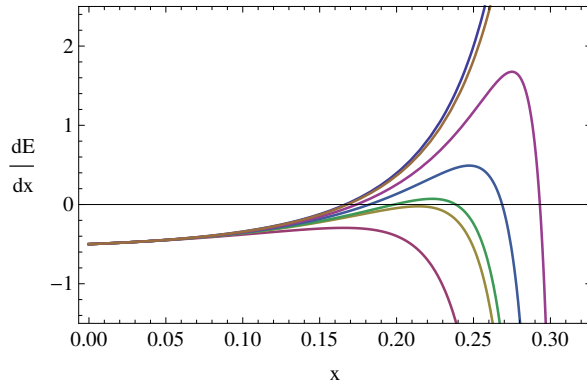


Figure 39: The location of the innermost stable circular orbit is determined by the condition $dE/dx = 0$. The panel shows dE/dx as a function of the gauge invariant quantity $x = (M \Omega)^{2/3}$. The various curves represent binary systems with mass-ratios, from top to bottom, $q \in [0, 1/100, 1/20, 1/10, 1/6, 1/5, 1]$. Note that binaries with mass-ratios $q \gtrsim 1/6$ do not have an ISCO in this model.

In summary, the building blocks we use to construct the conservative dynamics are

- The orbital frequency evolution is computed using Eq. (8.5) with the gravitational self-force contribution included in the potential $A(u) = 1 - 2u + \eta a(u)$.
- Eq. (8.5) is evaluated using the self-force-corrected expression for the angular momentum, $L(x)$, given by Eq. (8.14). The self-force-corrected expression for the energy, given in Eq. (8.13) is only used to determine the point at which the inspiral ends and the transition region begins.

Eq. (8.5) provides a very accurate modeling of the orbital frequency from early inspiral through the ISCO. However, the post-ISCO time evolution of this prescription does not render an accurate representation of the orbital frequency as compared to numerical relativity simulations. This is a problem that has been addressed in the EOB formalism by introducing a phenomenological approach —the so-called non-quasi-circular coefficients— that enabled them to reproduce the orbital evolution extracted from numerical simulations [38]. The approach we will follow to circumvent

this problem is described in detail in Section 8.2.4, and consists of embedding the self-force formalism in the context of the implicit rotating source model [317] after the ISCO.

This completes the description of the conservative part of the self-force. We now describe how to couple this with the radiative part of the self-force to model the inspiral evolution.

8.2.3 Dissipative dynamics

A consistent self-force evolution model that incorporates first-order in mass-ratio conservative corrections should also include second-order radiative corrections. The model we described in the previous section was constructed including first order conservative corrections. However, second-order self-force radiative corrections are not known at present. Several studies have demonstrated the importance of including the missing second order corrections to the radiative part of the self-force, both for source detection and for parameter estimation [318, 319, 303, 301, 300].

We use a new prescription for the energy flux that uses the first-order in mass ratio terms derived in [320], including PN corrections up to 22nd PN order

$$\begin{aligned} \left(\dot{E}\right)_{\text{PN}} = & -\frac{32}{5} \frac{\mu^2}{M} x^{7/2} \left[1 - \frac{1247}{336} x + 4\pi x^{3/2} - \frac{44711}{9072} x^2 - \frac{8191}{672} \pi x^{5/2} \right. \\ & + x^3 \left\{ \frac{6643739519}{69854400} + \frac{16}{3} \pi^2 - \frac{1712}{105} \gamma_E - \frac{856}{105} \ln(16x) \right\} - \frac{16285}{504} \pi x^{7/2} \\ & + x^4 \left\{ -\frac{323105549467}{3178375200} + \frac{232597}{4410} \gamma_E - \frac{1369}{126} \pi + \frac{39931}{294} \ln(2) - \frac{47385}{1568} \ln(3) + \frac{232597}{4410} \ln(x) \right. \\ & + x^{9/2} \left\{ \frac{265978667519}{745113600} \pi - \frac{6848}{105} \gamma_E \pi - \frac{13696}{105} \pi \ln(2) - \frac{6848}{105} \pi \ln(x) \right\} \\ & \left. + \text{higher order corrections up to 22PN order} \right]. \end{aligned} \quad (8.19)$$

We include higher-order in mass-ratio terms using the exponential resummation approach described in [318]. In this approach, the energy flux is

$$\left(\frac{dE}{dt}\right)_{\text{hybrid}} = \mathcal{L}_0 \exp(\mathcal{L}_\eta), \quad (8.20)$$

where \mathcal{L}_0 denotes the leading-order in mass-ratio PN energy flux given in Eq. (8.19), and \mathcal{L}_η incorporates mass-ratio corrections to the highest PN order available [321, 322, 318], and additional corrections characterised by a set of unknown coefficients, b_i

$$\begin{aligned}\mathcal{L}_\eta = & \left[x \left[-\frac{35}{12} \eta + b_1 \eta^2 \right] + 4\pi x^{3/2} \left[b_2 \eta + b_3 \eta^2 \right] + x^2 \left[\frac{9271}{504} \eta + \frac{65}{18} \eta^2 \right] + \pi x^{5/2} \left[-\frac{583}{24} \eta + b_4 \eta^2 \right] \right. \\ & \left. + x^3 \left[\eta \left(-\frac{134543}{7776} + \frac{41}{48} \pi^2 \right) - \frac{94403}{3024} \eta^2 - \frac{775}{324} \eta^3 \right] + \pi x^{7/2} \left[\frac{214745}{1728} \eta + \frac{193385}{3024} \eta^2 \right] \right].\end{aligned}\quad (8.21)$$

The coefficients b_i were taken to be constant in [318], but we found that a better match to the EOB phase evolution could be obtained by allowing an additional dependence on mass-ratio in these terms (see Eqs. (8.23)-(8.25) below). We constrain the b_i coefficients by ensuring that the phase evolution of this model reproduces the phase evolution predicted by the EOB model introduced in [38, 305], which was calibrated to the phase evolution of compact binaries observed in numerical relativity simulations. To do so, we implemented the EOB model [38] and performed a Monte Carlo simulation to optimize the values of the b_i coefficients (see Figure 40). The optimization was done in two stages. We started by considering the three coefficients b_1 , b_2 and b_4 , sampling a wide range of parameter space, namely $b_i \in [-200, 200]$. We constrained the duration of the waveform from early inspiral to the light-ring to be similar to its EOB counterpart. Waveforms that differed from their EOB counterparts by more than 10^{-4} seconds were discarded. Once the region under consideration had been sparsely sampled, we focused on regions of parameter space where the orbital phase evolution was closest to the EOB evolution, and finely sampled these to obtain the optimal values for the coefficients. We found that this approach enabled us to reproduce the EOB phase evolution with a phase discrepancy of the order ~ 1 rad. After constraining b_1 , b_2 and b_4 , we explored whether including additional corrections could further improve the phase evolution, by adding η corrections beyond 3PN order. Such corrections were found to have a negligible impact on the actual phase evolution. This is not difficult to understand, since such corrections are of order $(\mathcal{O}(\eta^4), \mathcal{O}(\eta^3))$, at (3PN, 3.5PN) respectively. We found a similar behavior when we added leading order mass-ratios corrections beyond 4PN order. Thus, we took a different approach:

having derived the optimal value for b_1 , b_2 and b_4 , we took these results as initial seeds for an additional MC simulation in which b_3 was also included in Eq. (8.21), and repeated the optimization procedure. The results of these simulations are shown in Figure 40.

We carried out several different Monte Carlo runs to find the ‘optimal’ optimization interval, meaning the range of radial separations over which we tried to best match the phase evolution relative to the EOB model. We found that starting the optimization at $r = 30M$ gave results that performed moderately well at early inspiral, but that underperformed at late inspiral, leading to phase discrepancies of order ~ 3 rads. Starting the optimization at $r = 20M$ instead decreased the phase discrepancy with respect to the former case by a factor of 10 during early inspiral, and enabled us to reproduce the phase evolution in the EOB model for all the mass-ratios considered to within the accuracy of the numerical waveforms used to calibrate the EOB model in [38, 305]. Implementing these numerically optimized higher-order η corrections in Eq. (8.21) leads to:

$$\begin{aligned} \mathcal{L}_\eta &= \left[x \left[-\frac{35}{12}\eta + B_1 \right] + 4\pi x^{3/2} B_2 + x^2 \left[\frac{9271}{504}\eta + \frac{65}{18}\eta^2 \right] + \pi x^{5/2} \left[-\frac{583}{24}\eta + B_3 \right] \right. \\ &\quad \left. + x^3 \left[\eta \left(-\frac{134543}{7776} + \frac{41}{48}\pi^2 \right) - \frac{94403}{3024}\eta^2 - \frac{775}{324}\eta^3 \right] + \pi x^{7/2} \left[\frac{214745}{1728}\eta + \frac{193385}{3024}\eta^2 \right] \right]. \end{aligned} \quad (8.22)$$

where:

$$B_1 = \frac{1583.650 - 11760.507\eta}{1 + 142.389\eta - 981.723\eta^2} \eta^2, \quad (8.23)$$

$$B_2 = \frac{-12.081 + 35.482\eta}{1 - 4.678\eta + 13.280\eta^2} \eta + \frac{19.045 - 240.031\eta}{1 - 18.461\eta + 74.142\eta^2} \eta^2, \quad (8.24)$$

$$B_3 = \frac{51.814 - 980.100\eta}{1 - 13.912\eta + 88.797\eta^2} \eta^2. \quad (8.25)$$

This improved prescription for the energy flux, which incorporates second-order mass-ratio corrections to the PN expansion up to 3.5PN order, is sufficient to generate a model whose phase evolution reproduces with excellent accuracy the phase evolution predicted by EOB throughout inspiral and merger (see Figure 41).

Given the energy flux defined by Eqs (8.19)–(8.21), we generate the inspiral trajectory using the simple prescription

$$\frac{dx}{dt} = \frac{dE}{dt} \frac{dx}{dE}, \quad (8.26)$$

where we have used the mass-ratio corrected energy —Eq. (8.13)— to compute dE/dx . Figure 41 shows that for binaries with mass-ratio $q = 1/6$, the phase discrepancy between our self-force model and EOB is $\lesssim 0.5$ rads at the light-ring, which is within the numerical accuracy of the simulations used to calibrate EOB. It has been shown recently that EOB remains accurate for mass-ratios up to $q = 1/8$ [323]. In that regime the phase discrepancy between this model and EOB at the light-ring is less than 1 rad, as shown in Figure 41. For binaries with $q = 1/10$, the phase discrepancy at the light-ring is $\lesssim 1.2$ rads, which is still within the numerical accuracy of available simulations [252, 253].

It must be emphasized that even if we only use the inspiral evolution to model binaries with mass-ratios that typically describe NSBH binaries, our self-force evolution model performs better than TaylorT4, since we can reduce the phase discrepancy between TaylorT4 and EOB at the last stable circular orbit by a factor of (~ 40 , ~ 70) for binaries with $q = (1/6, 1/10)$ and total mass $M_{\text{tot}} \in (7M_{\odot}, 11M_{\odot})$ (see Figure 37).

Figure 41 conveys an important message — deriving the second order corrections to the radiative part of the self-force may well provide a robust framework to describe in a single model not only events that are naturally described by BHPT, such as the mergers of stellar mass compact objects with supermassive BHs in galactic nuclei [303, 301, 223, 245, 246, 243, 324], but also events that are more naturally described by PN or numerical methods, in particular the coalescences of compact object binaries with comparable or intermediate mass-ratios [303, 227, 287, 288, 226].

To finish this Section, we describe the approach followed to construct the gravitational waveform from the inspiral trajectory. At leading post-Newtonian order, a general inspiral waveform can be written as

$$h(t) = -(h_+ - i h_{\times}) = \sum_{\ell=2}^{\infty} \sum_{m=-\ell}^{\ell} h^{\ell m} {}_{-2}Y_{\ell m}(\iota, \Phi). \quad (8.27)$$

If only the leading-order modes $(\ell, m) = (2, \pm 2)$ are included, the inspiral waveform

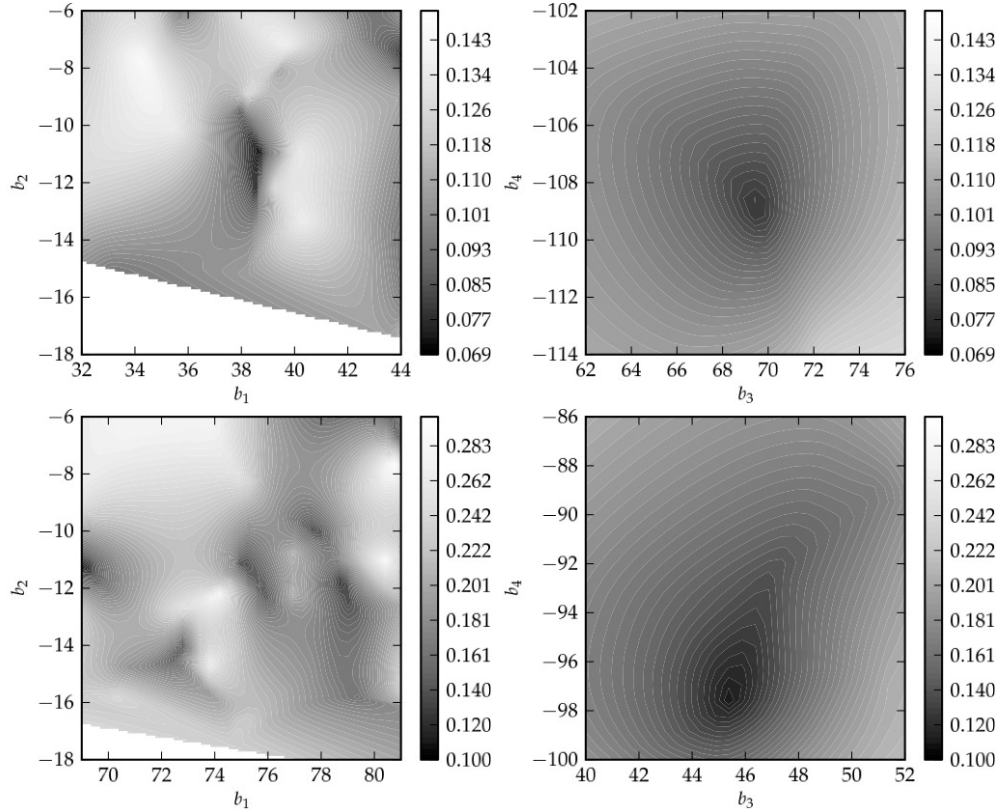


Figure 40: The (top, bottom) panels show the results of the optimization runs that were used to constrain the values of the b_i coefficients given in Eq. (8.21). The panels show the results for binaries of mass-ratio $q \in [1/6, 1/8]$, and total mass $M_{\text{tot}} = [7M_\odot, 9M_\odot]$. The ‘optimal’ value for the coefficients has been chosen by ensuring that the flux prescription minimizes the phase discrepancy between the EOB model and our self-force model. The color bar shows the phase difference squared between both models, which is integrated from $r = 20M$ all the way to the light-ring.

components are given by

$$h_+(t) = \frac{4\mu r^2 \dot{\phi}^2}{D} \left(\frac{1 + \cos^2 \iota}{2} \right) \cos [2(\phi(t) + \Phi)], \quad (8.28)$$

$$h_\times(t) = \frac{4\mu r^2 \dot{\phi}^2}{D} \cos \iota \sin [2(\phi(t) + \Phi)], \quad (8.29)$$

where D is the distance to the source. Since the orbital evolution will deviate from a circular trajectory during late inspiral ($\dot{r} \neq 0$), we must consider more general orbits in which both \dot{r} and $\dot{r}\dot{\phi}$ are non-negligible. For such orbits, the Newtonian GW

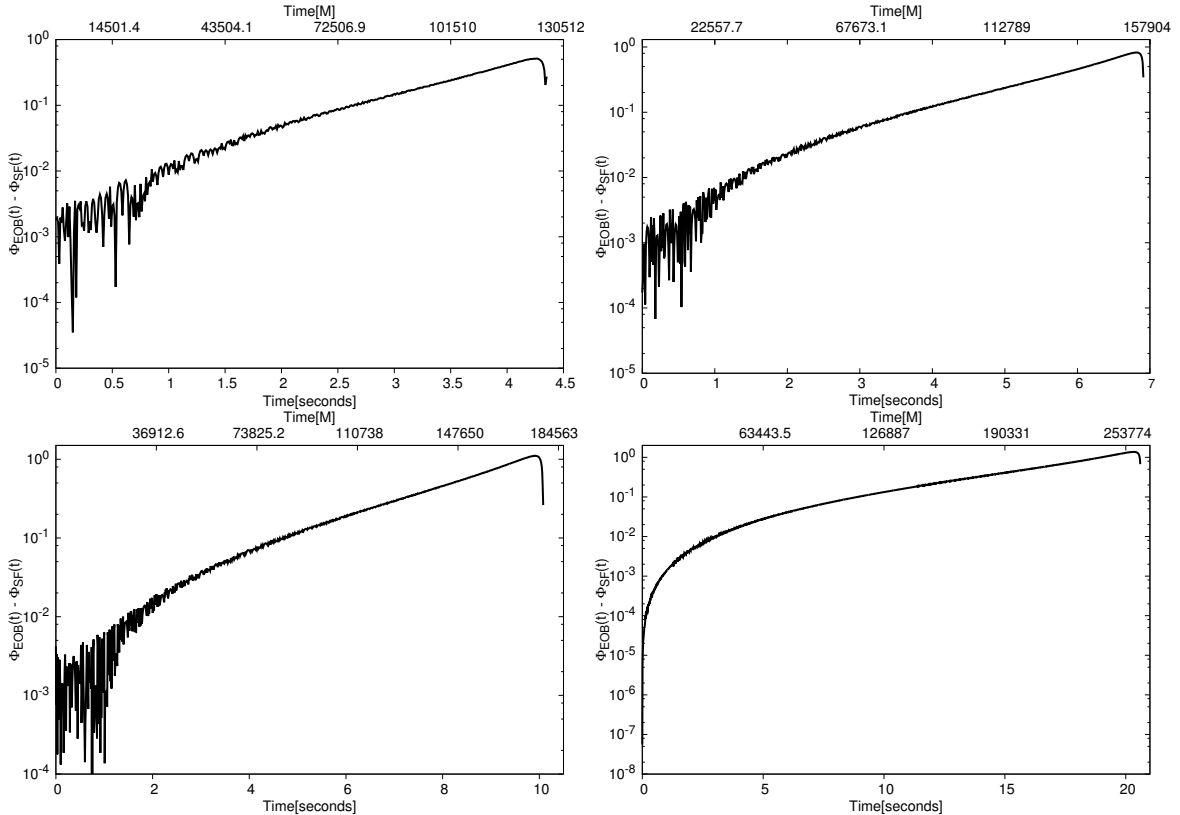


Figure 41: The panels show the orbital phase evolution of a self-force model making use of optimized PN energy flux given by Eq. (8.20) and the phase evolution as predicted by the EOB model. The [top/bottom] panels exhibit this evolution for a compact binary with mass–ratio $q = [(1/6, 1/8), (1/10, 1/15)]$, and total mass $M_{\text{tot}} = [(7M_{\odot}, 9M_{\odot}), (11M_{\odot}, 16M_{\odot})]$, respectively.

polarizations are given by [325]:

$$\begin{aligned} h_+(t) &= \frac{2\mu}{D} \left\{ (1 + \cos^2 \iota) \left[\cos [2(\phi(t) + \Phi)] \left(-\dot{r}^2 + r^2 \dot{\phi}^2 + \frac{1}{r} \right) \right. \right. \\ &\quad \left. \left. + 2r \dot{r} \dot{\phi} \sin [2(\phi(t) + \Phi)] \right] + \left(-\dot{r}^2 - r^2 \dot{\phi}^2 + \frac{1}{r} \right) \sin^2 \iota \right\}, \end{aligned} \quad (8.30)$$

$$\begin{aligned} h_\times(t) &= \frac{4\mu}{D} \cos \iota \left\{ \sin [2(\phi(t) + \Phi)] \left(-\dot{r}^2 + r^2 \dot{\phi}^2 + \frac{1}{r} \right) \right. \\ &\quad \left. - 2r \dot{r} \dot{\phi} \cos [2(\phi(t) + \Phi)] \right\}, \end{aligned} \quad (8.31)$$

where \dot{r} can be computed using

$$\frac{dr}{dt} = -\frac{1}{u^2} \frac{du}{dx} \frac{dx}{dt}.$$

Having described the construction of the inspiral evolution, we shall now describe the approach followed to smoothly connect the late inspiral evolution onto the plunge phase. The adiabatic prescription given by Eq. (8.26) breaks down when $dE/dx \rightarrow 0$. Hence, we need a scheme that enables us to match the late inspiral phase onto the plunge phase. We will do this by modifying the “transition” phase developed by Ori and Thorne [244] by including finite mass–ratio corrections.

8.2.4 Transition and plunge phases

In this Section we describe an extension of the transition phase model introduced by Ori and Thorne [244]. The basic idea behind this approach can be understood by studying the motion of an inspiralling object in terms of the effective potential, $V(r, L)$, which takes the following simple form for a Schwarzschild BH [42]:

$$V(r, L) = \left(1 - \frac{2}{r}\right) \left(1 + \frac{L^2}{r^2}\right). \quad (8.32)$$

Throughout the inspiral, the body moves along a nearly circular orbit, and hence the ratio of the energy flux to the angular momentum flux is given by:

$$\frac{dE}{d\tau} = \Omega \frac{dL}{d\tau}. \quad (8.33)$$

Hence, near the ISCO, the energy and angular momentum of the body satisfy the following relations:

$$E \rightarrow E_{\text{ISCO}} + \Omega_{\text{ISCO}} \xi, \quad (8.34)$$

$$L \rightarrow L_{\text{ISCO}} + \xi. \quad (8.35)$$

Re-writing the effective potential, Eq. (8.32), in terms of $\xi = L - L_{\text{ISCO}}$, one notices that during early inspiral, $\xi \gg 0$, the motion of the object is adiabatic, and the object sits at the minimum of the potential—as shown in the left panel of Figure 42. However, as the object nears the ISCO, the minimum of the potential moves inward

due to radiation reaction. At some point, the body's inertia prevents the body from staying at the minimum of the potential, and adiabatic inspiral breaks down [244] — illustrated in the right-hand panel of Figure 42.

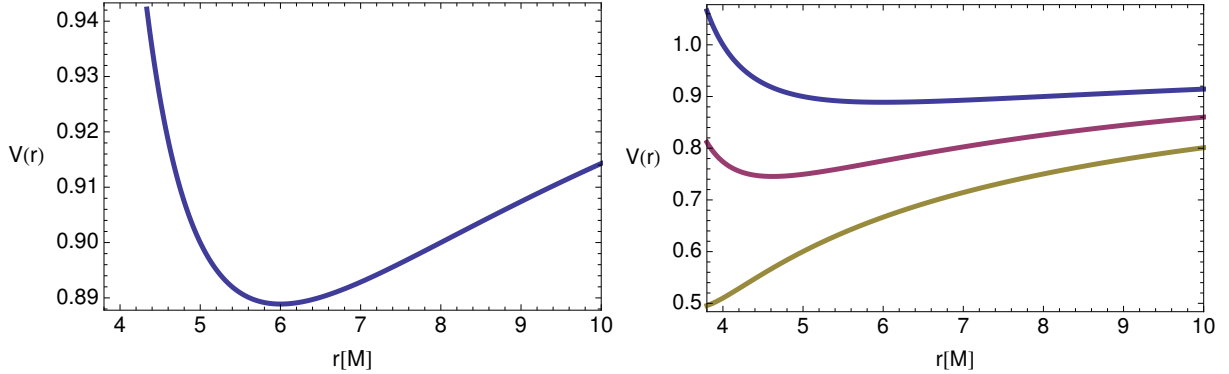


Figure 42: Left panel: The object sits at the minimum of the effective potential, Eq. (8.32), which corresponds to the case $\xi = L - L_{\text{ISCO}} \gg 0$. Right panel. Blue (top) curve: radial geodesic motion, which corresponds to $\xi = L - L_{\text{ISCO}} \gg 0$; Red (middle) curve: the object nears the ISCO and the orbit shrinks due to radiation reaction. Note that the minimum of the potential has moved inwards ($\xi = 0.35$). Yellow (bottom) curve: body's inertia prevents it from staying at the minimum of the potential, and adiabatic inspiral breaks down ($\xi = 0$). At this point the transition regime takes over the late inspiral evolution [244]. Note: this plot is based on Figure 1 of [244].

The equation that governs the radial motion during the transition regime is found by linearising the equation

$$\left(\frac{dr}{d\tau} \right)^2 = E(r)^2 - V(r, L), \quad (8.36)$$

using Eqs. (8.34), (8.35), and

$$\frac{d\xi}{d\tau} = \kappa \eta, \quad \text{with} \quad \kappa = \left[\frac{32}{5} \Omega^{7/3} \frac{\dot{\mathcal{E}}}{\sqrt{1-3u}} \right]_{\text{ISCO}}, \quad (8.37)$$

where $\dot{\mathcal{E}}$ is the general relativistic correction to the Newtonian, quadrupole-moment formula [254]. We now extend these Eqs. by including finite mass-ratio corrections. Eq. (8.36) can be replaced by

$$\frac{dx}{dt} = \frac{u^2(1-2u)}{E(x)} \left(\frac{du}{dx} \right)^{-1} \left[E(x)^2 - V(u(x), L(x)) \right]^{1/2}, \quad (8.38)$$

where we have used

$$\frac{d\tau}{dt} = \frac{1 - 2u(x)}{E(x)}, \quad (8.39)$$

and the expressions for the energy and angular momentum are given by Eqs. (8.13), (8.14). In order to linearize Eq. (8.38) we replace $E(x)$ and $L(x)$ by Eqs (8.34) and (8.35) respectively.

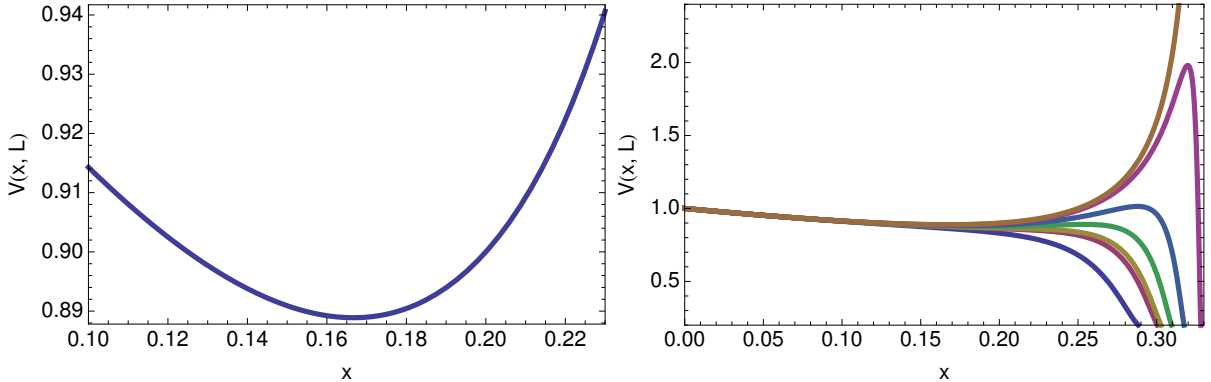


Figure 43: The left panel shows the effective potential for a Schwarzschild BH without including finite mass–ratio corrections. Note that the minimum of the potential takes place at the ISCO, which can be determined using Eq. (8.18). The right panel exhibits the influence of finite mass-ratio corrections on the effective potential used to modify Ori and Thorne transition regime [244]. The curves represent binaries, from top to bottom, with mass-ratios $q \in [0, 1/100, 1/20, 1/10, 1/6, 1/5, 1]$.

As discussed in [244], since these equations use the η -corrected values for $E(x_{\text{ISCO}})$, $L(x_{\text{ISCO}})$ and Ω_{ISCO} , then they remain valid even for finite mass-ratio η [244]. In Figure 43 we show the effect that these finite mass-ratio η corrections have on the effective potential $V(x, L(x))$. We determine the point at which the transition regime starts by carrying out a stability analysis near the ISCO using dE/dx . As shown in Figure 39, the ISCO is determined by the relation $dE/dx = 0$. We have found that the relation

$$\left(\frac{dE}{dx} \right) \Big|_{\text{transition}} = -0.054 + \frac{1.757 \times 10^{-4}}{\eta}, \quad (8.40)$$

provides a robust criterion to mark the start of the transition regime for binaries with mass-ratios $1/100 < q < 1/6$.

In [254], the authors only kept terms linear in ξ , but we have explored which higher order terms had a noticeable impact on the evolution by examining their impact on

the length and phasing of the waveform. We found that terms $\propto \xi$ and $\propto (u - u_{\text{ISCO}})\xi$ were important, but corrections at order $\mathcal{O}(\xi^2)$ could be ignored even for comparable mass-ratio systems.

We model the evolution of the orbital frequency during the transition regime and thereafter in a different manner to that proposed by Ori and Thorne [244]. In order to ensure that the late-time evolution of the orbital frequency of our self-force model is as close as possible to the orbital evolution extracted from numerical relativity simulations, we incorporate the late-time frequency evolution that was derived by Baker et al [317] in their implicit rotating source (IRS) model, namely:

$$\frac{d\phi}{dt} = \Omega_i + (\Omega_f - \Omega_i) \left(\frac{1 + \tanh(\ln \sqrt{\varkappa} + (t - t_0)/b)}{2} \right)^{\varkappa}, \quad (8.41)$$

where Ω_i is the value of the orbital frequency when the transition regime begins, and Ω_f is the value of the frequency at the light ring, which corresponds to $\omega_{\ell mn}/m$, where $\omega_{\ell mn}$ is the fundamental quasi-normal ringing frequency ($n = 0$) for the fundamental mode $(\ell, m) = (2, 2)$ of the post-merger black hole (see Eq. (8.45) below). The constant mass-dependent coefficient t_0 is computed by ensuring that $d\Omega/dt$ peaks at a time $t = t_0$. The parameter \varkappa is computed by enforcing continuity between the first order time derivative of the orbital frequency as predicted by the self-force evolution —Eq. (8.5)— and that given by the first order time derivative of Eq. (8.41).

At the end of the plunge phase, we match the plunge waveforms, which are generated using Eqs. (8.30), (8.31), onto the $l = m = 2, n = 0$ ringdown mode since this dominates the ringdown radiation. In the following Section we will describe in detail the procedure followed to attach the ringdown waveform.

After the transition regime, the equations of motion we use to model the plunge phase are: the second order time derivative of Eq. (8.38) which gives the radial evolution, and Eq. (8.41) which describes the orbital frequency evolution. We determine the point at which to attach the plunge phase by integrating Eq. (8.38) backwards in time, and finding the point at which the transition and plunge equations of motion smoothly match.

In Figures 44 and 45 we show the evolution obtained by combining Ori and Thorne's [244] transition approach for the radial motion with the frequency evolution proposed by Baker et al [317]. In all the cases shown in Figures 44 and 45, the orbital

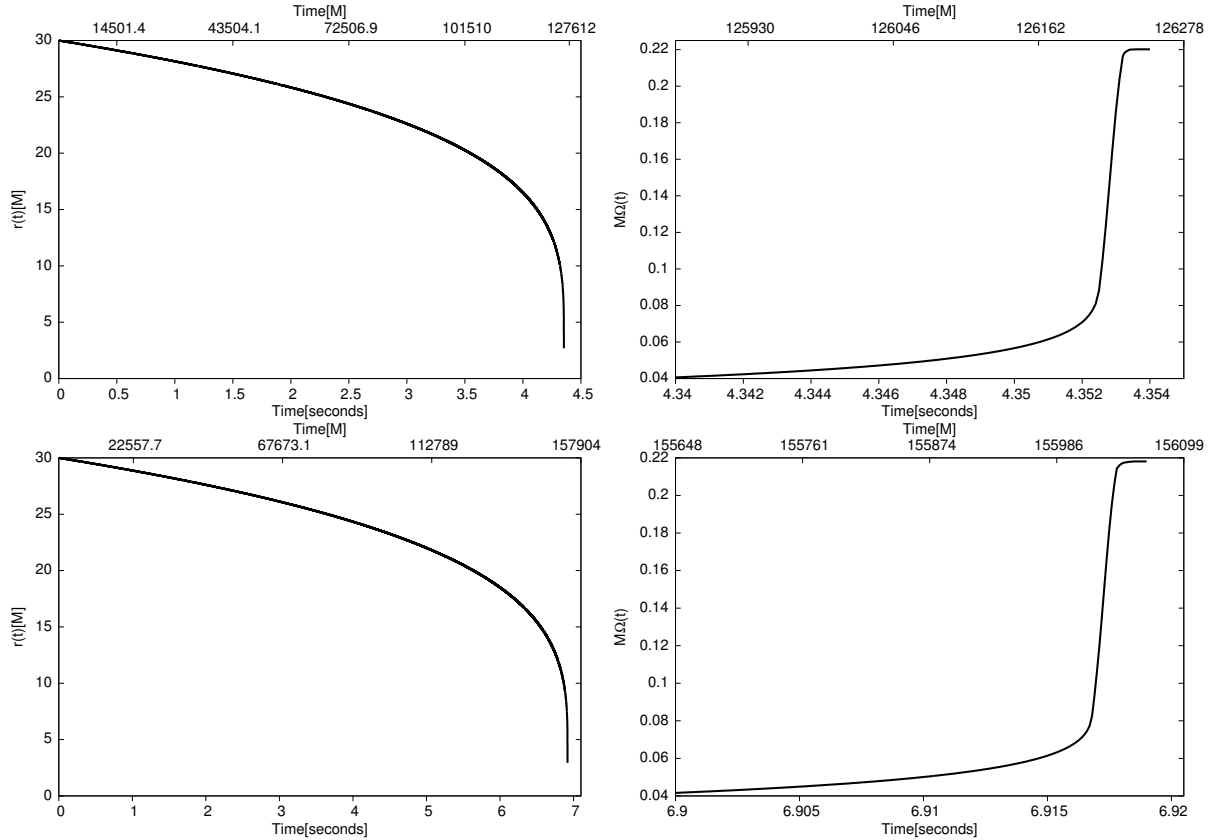


Figure 44: (Top, bottom) panels: the left panel shows the inspiral, transition and plunge radial evolution for a BH binary of mass-ratio $q = (1/6, 1/8)$ — and total mass $M_{\text{tot}} \in (7M_{\odot}, 9M_{\odot})$ — using the coordinate transformation given by Eq. (8.15). The right panel shows the orbital frequency $M\Omega$ from late inspiral all the way to the light ring. The evolution starts from an initial radial value $r = 30M$.

frequency peaks and saturates at a value given by $\omega_{\ell mn}/m$. This can be understood if we analyze the asymptotic behavior of Eq. (8.41) near the light-ring, i.e.,

$$\frac{d\phi}{dt} \approx \Omega_f - (\Omega_f - \Omega_i) e^{-2(t-t_0)/b}. \quad (8.42)$$

Recasting Eq. (8.41) in this form, enables us to identify the constant coefficient b with the e-folding rate for the decay of the fundamental quasinormal mode (QNM). As discussed previously, Eq. (8.41) predicts the expected orbital evolution during late inspiral and onward. To provide a unified description from late inspiral through to ringdown, we have decided to adopt the IRS approach, since this framework allows us to smoothly transition from late inspiral onto the plunge phase, and finally describe

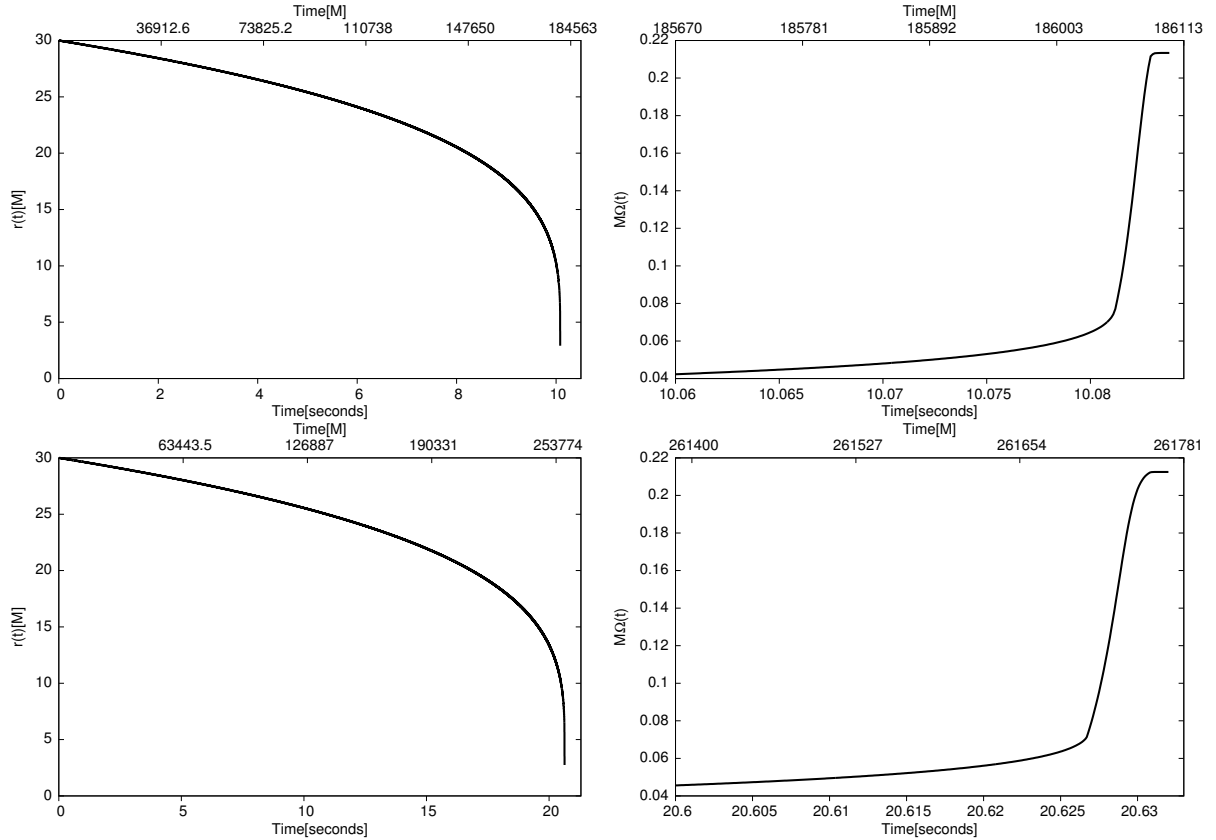


Figure 45: As in Figure 44, but with the (top, bottom) panels showing the radial and orbital frequency evolution for binaries with mass–ratios $q = (1/10, 1/15)$, and total mass $M_{\text{tot}} \in (11M_{\odot}, 16M_{\odot})$, respectively. As before, the evolution starts from an initial radial value $r = 30M$.

the ringdown waveform as a natural consequence of the IRS strain-rate amplitude decay relation $A^2(t) \propto \Omega \dot{\Omega}$ [317]. In other words, since Eq. (8.42) has the correct behavior near the light-ring as predicted by BHPT, the IRS model provides a natural framework to attach the ringdownm waveform at the end of the plunge phase. We will discuss this feature in further detail in the following Section.

8.2.5 Ringdown Waveform

Numerical relativity simulations have shown that coalescing binary BHs in general relativity lead to the formation of a distorted rotating remnant, which radiates GWs while it settles down into a stationary Kerr BH [326, 327]. The GWs emitted during this intermediate phase resemble a ringing bell. Hence, this type of radiation is

commonly known in the literature as ringdown radiation, and consists of a superposition of QNMs — first discovered in numerical studies of the scattering of GWs in the Schwarzschild spacetime by Vishveshwara [328]. QNMs are damped oscillations whose frequencies and damping times are uniquely determined by the mass and spin of the post-merger Kerr BH. The frequency $\hat{\omega}$ of each QNM has two components: the real part represents the oscillation frequency, and the imaginary part corresponds to the inverse of the damping time:

$$\hat{\omega} = \omega_{\ell mn} - i/\tau_{\ell mn}. \quad (8.43)$$

As discussed above, the observables $\omega_{\ell mn}, \tau_{\ell mn}$ are uniquely determined by the final mass, M_f , and final spin, q_f , of the post-merger Kerr BH. To determine M_f , we use the analytic phenomenological expression for the final mass of the BH remnant that results from the merger of generic binary BHs on circular quasi-orbits introduced in [329], namely,

$$\frac{M_f}{M} = 1 - \left(1 - \frac{2\sqrt{2}}{3}\right) \eta - 0.543763 \eta^2. \quad (8.44)$$

This expression reproduces the expected result in the test mass particle limit, and also reproduces results from currently available numerical relativity simulations [329, 330]. We determine the final spin of the BH remnant q_f using the fit proposed in [331]:

$$q_f = \sqrt{12} \eta + s_1 \eta^2 + s_2 \eta^3, \quad (8.45)$$

with:

$$s_1 = -3.454 \pm 0.132, \quad s_2 = 2.353 \pm 0.548. \quad (8.46)$$

This prescription is consistent with the numerical relativity simulations described in [331, 330], and reproduces test mass limit predictions. This compact formula is also consistent with the prescriptions introduced in [332, 333]. The largest discrepancy between Eq. (8.45) and those derived in [332, 333] is $\lesssim 2.5\%$ for binaries with $q \lesssim 1/6$.

The ringdown waveform is given by [327, 317]

$$h(t) = -(h_+ - i h_\times) = \frac{M_f}{D} \sum_{\ell mn} \mathcal{A}_{\ell mn} e^{-i(\omega_{\ell mn} t + \phi_{\ell mn})} e^{-t/\tau_{\ell mn}}, \quad (8.47)$$

where $\mathcal{A}_{\ell mn}$ and $\phi_{\ell mn}$ are constants to be determined by smoothly matching the plunge waveform onto the subsequent ringdown. The ringdown portion of the self-force waveform model constructed in this chapter includes the mode $\ell = m = 2$ and the tones $n = 0, 1, 2$. The approach we follow to attach the leading mode and overtones is the following:

- In order to ensure continuity between the plunge and ringdown waveforms, we use the end of the plunge waveform — Eqs. (8.30), (8.31) — to construct an interpolation function $F(t)$. The interpolation method used to construct $F(t)$ is a cubic spline.
- We match the plunge waveform onto the leading mode $\ell = m = 2, n = 0$ of the ringdown waveform, Eq. (8.47), at the point where the amplitude of the plunge waveform peaks, t_{\max} . Attaching the mode requires $F(t = t_{\max})$ and $F'(t = t_{\max})$ which are computed from the interpolation function. These conditions fix two constants per polarisation.
- To attach the first overtone, $\ell = m = 2, n = 1$, we insert into Eq. (8.47) the constants determined by attaching the leading mode as seeds to compute the amplitude and phase coefficients for the first overtone by enforcing continuity at $t_{\max} + dt$.
- Finally, we insert into Eq. (8.47) the value of the amplitude and phase coefficients previously determined for the leading mode and first overtone, and determine the four remaining constants by enforcing continuity at $t_{\max} + 2dt$.

Having described the methodology followed to construct complete waveforms for comparable and intermediate mass-ratio systems, we finish this Section by putting together all these various pieces to construct sample waveforms for a few systems with mass-ratio $q \in [1/6, 1/8, 1/10, 1/15]$, and total mass $M_{\text{tot}} \in (7M_\odot, 9M_\odot, 11M_\odot, 16M_\odot)$ in Figure 46.

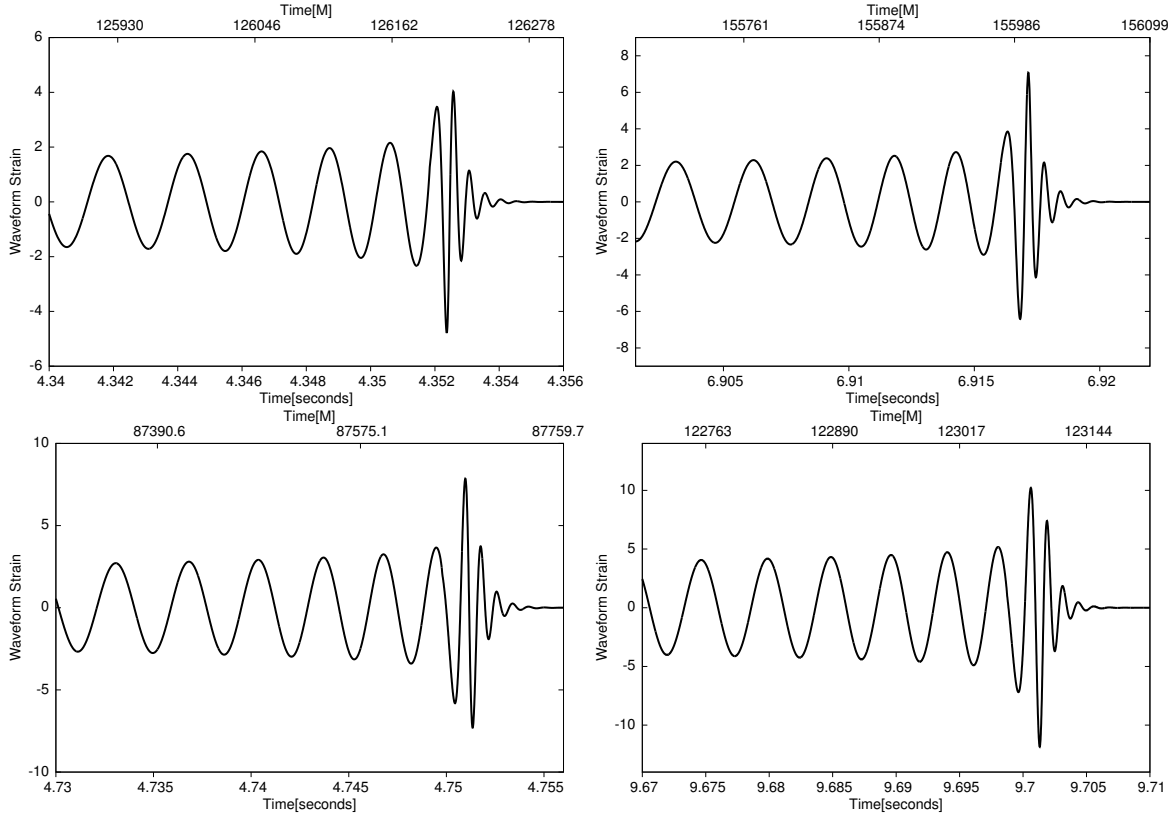


Figure 46: The panels show sample waveforms from inspiral to ringdown for systems with mass-ratios $q \in [1/6, 1/8]$ —and total mass $M_{\text{tot}} \in (7M_{\odot}, 9M_{\odot})$ — (top panels—from left to right) and $q \in [1/10, 1/15]$ —and total mass $M_{\text{tot}} \in (11M_{\odot}, 16M_{\odot})$ — (bottom panels —from left to right). The inspiral evolution for the [top, bottom] panels starts from $r = [30M, 25M]$.

8.2.6 Ringdown waveform construction in the context of an Implicit Rotating Source

Having described the ringdown waveform construction as a sum of quasinormal modes, we finish this Section by exhibiting the power of the IRS model to describe the ringdown evolution. In the IRS model, the strain-rate amplitude decay is given by [317]:

$$A^2(t) = 16 \pi \dot{E} \approx 16 \pi \xi \Omega \dot{\Omega}. \quad (8.48)$$

Using Eq. (8.42), in the limit $\Omega \rightarrow \Omega_f$, the amplitude decay is given by

$$A_0^2 e^{-2t/\tau} \approx \frac{32 \pi \xi \Omega_f}{b} (\Omega_f - \Omega_i) e^{-2(t-t_0)/\tau}. \quad (8.49)$$

Hence, the late-time amplitude in the IRS model is given by

$$A_{\ell m}^2 \approx 16 \pi \xi_{\ell m} \omega_{\ell m} \dot{\omega}_{\ell m}, \quad (8.50)$$

where the value of $\xi_{\ell m}$ is set by ensuring amplitude continuity at the light-ring. In Figure 47 we explicitly show the equivalence of the ringdown waveform construction both in the IRS approach and using the sum of QNMs utilized in the previous Section. This detailed analysis shows that the IRS is a powerful tool to model the late time portions of the waveforms in a unified way.

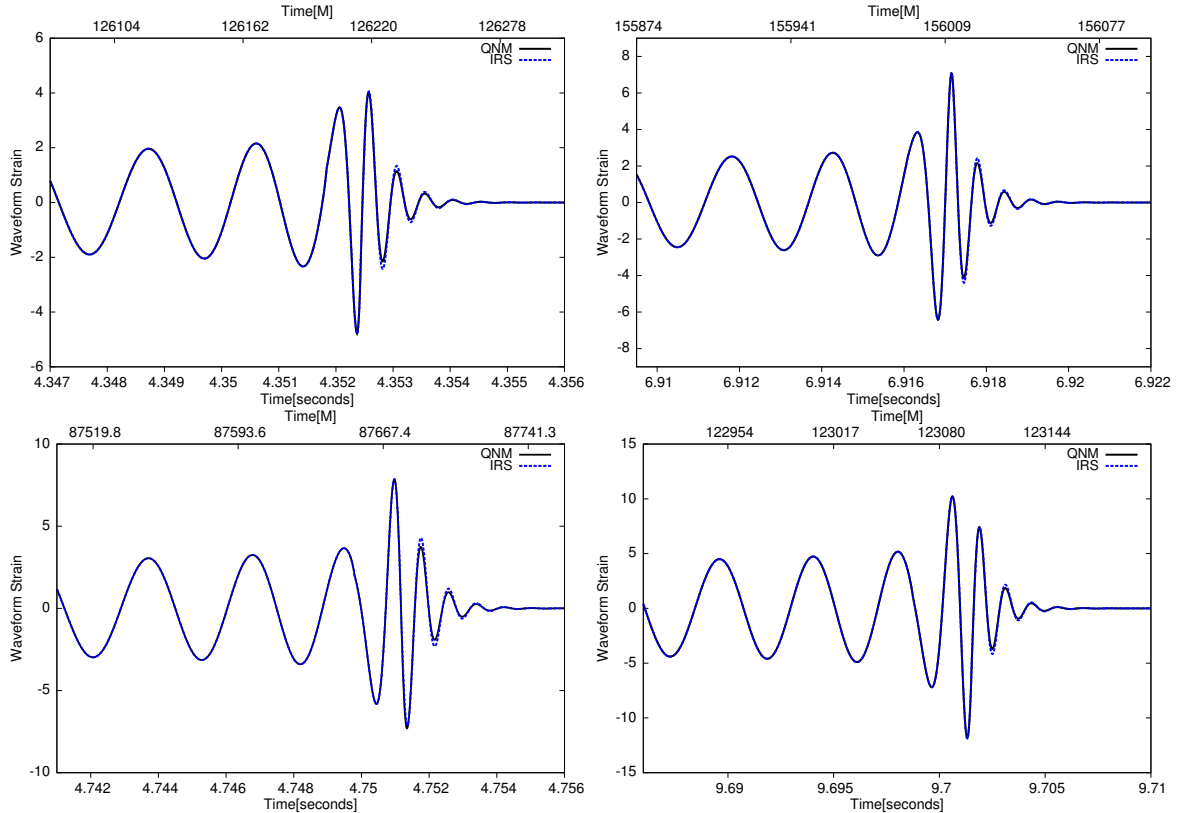


Figure 47: The panels show sample the late-time evolution of waveforms whose ringdown phase is modeled using the implicit rotating source (IRS) model and a sum of quasinormal modes (QNMs). The systems shown correspond to binaries with mass-ratios $q \in [1/6, 1/8]$ —and total mass $M_{\text{tot}} \in (7M_{\odot}, 9M_{\odot})$ — (top panels—from left to right) and $q \in [1/10, 1/15]$ —and total mass $M_{\text{tot}} \in (11M_{\odot}, 16M_{\odot})$ — (bottom panels —from left to right). The inspiral evolution for the [top, bottom] panels starts from $r = [30M, 25M]$.

8.2.7 Summary

In this Section we briefly summarize the key ingredients that were used to develop the waveform model described in this chapter:

- Inspiral evolution
 - The building blocks of the inspiral evolution are the expressions for the energy, E , and angular momentum, L , — Eqs. (8.13) and (8.14) — that include gravitational self-force corrections and are valid over the domain $0 < x < \frac{1}{3}$ [307].
 - The orbital frequency is modeled using Eq. (8.5). This prescription encapsulates gravitational self-force corrections that render a better phase evolution when calibrated against EOB.
 - The inspiral trajectory is modeled using the simple prescription (8.26). This scheme is no longer valid near ISCO, where $dE/dx = 0$ for binaries with $q \leq 6$.
 - We construct the inspiral waveform using Eqs. (8.30), (8.31).

When the inspiralling object nears the ISCO, we need to invoke the ‘transition scheme’ introduced by Ori and Thorne [244], which enables us to smoothly attach the late inspiral evolution onto the plunge phase.

- Transition phase
 - The transition regime starts at a point when dE/dx satisfies Eq. (8.40).
 - The equations of motion that govern the transition phase are (8.34), (8.35). These relations are valid, since the motion near the ISCO is nearly-circular.
 - Using Eqs. (8.34), (8.35), we linearize the second order time derivative of Eq. (8.38).

- In order to reproduce the orbital phase evolution predicted by numerical simulations from the ISCO to the light-ring, we modify the original transition phase by smoothly matching the inspiral orbital phase evolution, Eq. (8.5), onto the IRS model, Eq. (8.41) at the start of the transition phase.

- Plunge phase

- The equations of motion that govern the plunge phase are given by the second order time derivative of Eq. (8.38), and Eq. (8.41).
- We integrate these relations backwards in time to find the point at which both the transition and plunge equations of motion smoothly match. The transition phase ends at this point.
- Near the light-ring Eq. (8.41) has the behavior predicted by BHPT, which enables us to smoothly match the plunge phase onto the ringdown.
- Both the transition and plunge waveforms are constructed using Eqs. (8.30) and (8.31).

Having constructed the waveform from inspiral to ringdown, we derived second-order radiative corrections to improve the radiative evolution of the waveform model. This was necessary in order to construct a waveform model that is internally consistent, i.e., since the orbital elements include first-order conservative corrections, then radiative corrections should enter the fluxes at second order. We have derived these corrections by enforcing a close agreement between our self-force model and EOB, and have shown that our model can reproduce the orbital phase evolution predicted by EOB within the numerical error of the simulations used to calibrate this model for a variety of mass-ratios.

- Ringdown phase

- The ringdown waveform is constructed using Eq. (8.47).

- We use the plunge waveform to construct an interpolation function $F(t)$, and then use this function to attach the leading mode $\ell = m = 2, n = 0$ at the point where the amplitude of the plunge waveform peaks, t_{\max} . We enforce continuity by ensuring that $F(t_{\max}) = h_{\text{RD}}^{n=0}$ and $F'(t_{\max}) = h'_{\text{RD}}^{n=0}$.
- We include the first and second overtone $n = 1, n = 2$ in the ringdown waveform.
- Using the IRS model, we have shown that having knowledge of the time evolution of the orbital frequency provides sufficient information to construct the amplitude decay during ringdown. Hence, we can construct an alternative ringdown waveform using only Eq. (8.50), and ensuring smooth continuity with the plunge waveform.
- Finally, we have explicitly shown that the implicit rotating source approach provides a natural transition from late-time radiation to ringdown that is equivalent to ringdown waveform modeling based on a sum of QNMs.

Throughout the chapter we have emphasized the fact that our model provides a more reliable framework to model binaries whose components are non-spinning, and with mass-ratios $q \leq 1/6$, as compared to available PN approximants. It is worth emphasizing that our model is also computationally inexpensive. All the waveforms we generated to constrain the higher-order η corrections in the energy flux—Eq. (8.22)—can be generated in fractions of a second. A direct comparison between our code and EOB shows that, averaged over 500 realizations, our code is $\sim 20\%$ faster than the optimized version of the EOB code currently available in the LIGO Scientific Collaboration LAL library. It should be emphasized, though, that our code at present has not been optimized, and hence, compared to EOB our model is expected to significantly reduce the cost of waveform generation, making it relatively more viable for parameter estimation efforts. This is a key feature in our model that enabled us to sample a wide region of parameter space to constrain the B_i coefficients in Eq. (8.22). Furthermore, these self-forced waveforms do not need to be highly sampled near the light-ring, hence decreasing the speed with which they can be generated, because the prescription we have used to model the late-time orbital frequency evolution provides

the correct evolution near the light-ring. This particular feature also enables us to match the plunge waveform onto its ringdown counterpart without having to interpolate the orbital frequency evolution using a phenomenological approach. The model is internally consistent and the only phenomenology invoked during its construction is related to currently unknown physics, i.e., higher order radiative corrections to the energy flux. Once these corrections are formally derived in the near future, the flexibility of our model will enable us to replace the radiative corrections that we have currently computed by numerical optimization. At that stage, we will be able to describe in a single unified model the dynamical evolution of binaries whose mass-ratios range from the extreme to the comparable regime.

8.3 Conclusions

In this chapter we have developed a self-force waveform model that is capable of reproducing with good accuracy the inspiral, merger and ringdown of binaries with mass-ratios $q \leq 1/6$. This work suggests that a model that incorporates first order conservative self-force corrections in the orbital elements, and second-order radiative corrections in the dissipative piece of the self-force may suffice to describe in a unified manner the coalescence of binaries with mass-ratios that range from the comparable to the extreme. Our model includes conservative self-force corrections that have been derived in the strong-field regime [307]. Using these results, we find that binaries with mass-ratios $q \gtrsim 1/6$ do not have an ISCO. For systems with $q \leq 1/6$, we have derived a simple relation that provides the location of the ISCO in terms of the symmetric mass-ratio (see Eq. (8.18)). To describe the inspiral evolution, we have derived second-order corrections to the energy flux by minimizing the phase discrepancy between our self-force model and the EOB model [38, 305] for a variety of mass-ratios. We have shown that our model reproduces the phase evolution of the EOB model within the accuracy of available numerical simulations for a variety of mass-ratios.

This chapter also presents an extension of the “transition regime” developed by Ori and Thorne [244] to smoothly match the late inspiral evolution onto the plunge phase. We have found that using the inspiral phase expression for the orbital frequency during the plunge phase does not render an accurate description of the actual orbital evolution as predicted by numerical simulations. Hence, we have embedded

the self-force framework in the IRS model proposed by Baker et al [317] to ensure that our model is as close as possible to the orbital evolution predicted by numerical relativity simulations. The implementation of this prescription ensures that the orbital frequency saturates near the light-ring, which facilitates matching onto the ringdown phase. We have shown that the IRS model provides a natural transition onto the ringdown phase that is equivalent to a ringdown waveform construction based on a sum of QNMs.

The motivation for constructing this model is two-fold: to exhibit the versatility of the self-force formalism to accurately describe the evolution of binaries beyond the extreme mass-ratio limit; and to provide a tool that can be used to explore the information that could be extracted by GW detectors that target binaries with comparable and intermediate mass-ratios. Current studies have only explored the use of PN approximants to model the merger of NSBH binaries, despite their inadequacy to capture the evolution of these systems [334, 309, 51] (see Figure 37). Comparing Figures 37 and 41, we conclude that even if second generation GW detectors were only capable of capturing the inspiral evolution of NSBH mergers, our self-force model would be better equipped to describe these events. The construction of this IRS self-force model constitutes an important step towards the construction of more reliable waveforms to describe IMRCs. In citeSmith:2013, it was shown that Huerta–Gair (HG) waveforms — which are closely related to the model developed in this chapter, and which were also based on a consistent combination of BHPT and self-force corrections — work in the relevant mass range for advanced detectors. The new model introduced in this article, improves upon these waveforms and should therefore not only work in the regime of interest to advanced detectors but over a wider parameter space that could be applicable to third generation detectors or later observations.

Having developed a strong foundation to model binaries on circular orbits whose components are not rotating, it is necessary to incorporate more ingredients to the waveform model to capture GW signals from binaries whose components have significant spin [335, 38, 336, 337, 226, 338, 339, 310], or systems that form in core-collapsed globular clusters, and hence are expected to have non-negligible eccentricity at merger [340, 341]. In order to do so, we require input both from the self-force program — which is making substantial progress towards the computation of the self-force in a Kerr background [342, 343, 344]— and from numerical simulations [37],

in particular from binaries with typical mass-ratios $1/20 < q < 1/10$ to explore the performance of our self-force model in this currently unconstrained regime. Undoubtedly, the development and implementation of improved numerical algorithms [345] to carry out these simulations will facilitate the realization of these studies in the near future.

Recent observational discoveries [256] suggest that NSBH mergers may also occur in globular clusters. Hence, in these dense stellar environments we may expect that multiple n -body interactions and binary exchange processes may lead to the formation of binaries on eccentric orbits. Detectors such as the Einstein Telescope, operating at low frequencies $\sim 1\text{Hz}$, may be capable of detecting the signature of eccentricity during the early inspiral. In order to assess these effects, we aim to extend the model introduced in this chapter by including eccentricity, making use of self-force corrections for generic orbits in a Schwarzschild background [223].

Chapter 9

Conclusions

Appendix A

Post-Newtonian Waveforms

The basic ingredients for building post-Newtonian waveforms are the orbital energy and energy flux. From these, we can obtain the phase and amplitude evolution of the gravitational waveform emitted by a binary of black holes. In this section, we collect results from PN theoretic calculations for non-precessing binaries, i.e. those for which the orbital plane remains fixed all through the inspiral and merger phases (referred to as *aligned*-spin binaries).

A.1 Phasing

In the PN approximation, the orbit related quantities are computed as expansions in the velocity parameter,

$$v := \left(M \frac{d\phi}{dt} \right)^{1/3} = (\pi M f)^{1/3}, \quad (\text{A.1})$$

The energy loss from the system is compensated by the energy carried by the outgoing gravitational radiation F , as well as the flow of energy into each black holes due to the tides raised on its horizon by the other hole. The latter is given as a rate of change in the mass of the black holes $\dot{M}(v)$. Using this, we modify the energy balance equation, Eq. 2.52, as

$$\frac{dE}{dt} = -F - \dot{M} \quad (\text{A.2})$$

Using the chain rule, $dE/dt = \partial E/\partial v dv/dt$, the same for $d\phi/dt$, and Eq. A.1, we can write the equation for the phase of the emitted gravitational radiation as the integral

equation

$$\phi = \phi(v_0) + \int_{v_0}^v \frac{v^3}{M} \frac{\partial E(v)/\partial v}{F(v) + \dot{M}(v)}. \quad (\text{A.3})$$

We can also solve

$$\frac{dv}{dt} = -\frac{F(v) + \dot{M}(v)}{\partial E(v)/\partial v}, \quad (\text{A.4})$$

to obtain the characteristic velocity v as a function of time t , and combine with Eq. A.3 to get the phase as a function of time. Therefore, the phasing can be obtained in both time and frequency domains.

We will now collect formulae for the energy flux, mass loss due to tidal deformation of black hole horizons, and the orbital energy from past work in the field. Given the masses m_1 and m_2 and spin vectors \mathbf{S}_1 and \mathbf{S}_2 , we define the following parameters:

$$\begin{aligned} M &:= m_1 + m_2 , \\ \eta &:= m_1 m_2 / M^2 , \\ \delta &:= (m_1 - m_2) / M , \\ \boldsymbol{\chi}_i &:= \mathbf{S}_i / M_i^2 , \\ \boldsymbol{\chi}_s &:= (\boldsymbol{\chi}_1 + \boldsymbol{\chi}_2) / 2 , \\ \boldsymbol{\chi}_a &:= (\boldsymbol{\chi}_1 - \boldsymbol{\chi}_2) / 2 . \end{aligned} \quad (\text{A.5})$$

We also define the quantities χ_s and χ_a to be the components of the spin vectors perpendicular to the orbital plane, namely $\chi_s := \boldsymbol{\chi}_s \cdot \mathbf{l}_N$ and $\chi_a := \boldsymbol{\chi}_a \cdot \mathbf{l}_N$, where \mathbf{l}_N is the unit vector along the Newtonian angular momentum $\mathbf{L}_N := \vec{r} \times \vec{p}$.

The orbital energy can be written in terms of the PN expansion parameter v defined above as [346, 347, 348, 349, 350, 351, 352, 353, 354, 202, 355, 356, 357, 358,

[359, 360, 361, 362]

$$\begin{aligned}
E(v) = & -\frac{M\eta v^2}{2} \left\{ 1 + v^2 \left(-\frac{3}{4} - \frac{\eta}{12} \right) + v^3 \left[\frac{8\delta\chi_a}{3} + \left(\frac{8}{3} - \frac{4\eta}{3} \right) \chi_s \right] \right. \\
& + v^4 \left[-2\delta\chi_a\chi_s - \frac{\eta^2}{24} + (4\eta - 1)\chi_a^2 + \frac{19\eta}{8} - \chi_s^2 - \frac{27}{8} \right] \\
& + v^5 \left[\chi_a \left(8\delta - \frac{31\delta\eta}{9} \right) + \left(\frac{2\eta^2}{9} - \frac{121\eta}{9} + 8 \right) \chi_s \right] \\
& + v^6 \left[-\frac{35\eta^3}{5184} - \frac{155\eta^2}{96} + \left(\frac{34445}{576} - \frac{205\pi^2}{96} \right) \eta - \frac{675}{64} \right] \\
& \left. v^7 \sum_{i=1}^2 \left[\left(27 - \frac{211}{4}\eta + \frac{7}{6}\eta^2 \right) \left(\frac{m_i}{M} \right)^2 + \eta \left(\frac{27}{4} - 39\eta + \frac{5}{4}\eta^2 \right) \right] (\boldsymbol{\chi}_i \cdot \boldsymbol{l}_N) \right\}. \tag{A.6}
\end{aligned}$$

We take the derivative of this formula with respect to v to find the energy function appearing in Eq. A.3:

$$\begin{aligned}
\frac{\partial E(v)}{\partial v} = & -M\eta v \left\{ 1 + v^2 \left(-\frac{3}{2} - \frac{\eta}{6} \right) + v^3 \left[\frac{20\delta\chi_a}{3} + \left(\frac{20}{3} - \frac{10\eta}{3} \right) \chi_s \right] \right. \\
& + v^4 \left[-6\delta\chi_a\chi_s - \frac{\eta^2}{8} + (12\eta - 3)\chi_a^2 + \frac{57\eta}{8} - 3\chi_s^2 - \frac{81}{8} \right] \\
& + v^5 \left[\chi_a \left(28\delta - \frac{217\delta\eta}{18} \right) + \left(\frac{7\eta^2}{9} - \frac{847\eta}{18} + 28 \right) \chi_s \right] \\
& \left. + v^6 \left[-\frac{35\eta^3}{1296} - \frac{155\eta^2}{24} + \left(\frac{34445}{144} - \frac{205\pi^2}{24} \right) \eta - \frac{675}{16} \right] \right\}. \tag{A.7}
\end{aligned}$$

Similarly, the energy flux can be written as [346, 347, 348, 349, 350, 351, 352, 353,

[354, 202, 355, 356, 357, 358, 359, 360, 361, 362]

$$\begin{aligned}
F(v) = & \frac{32}{5} v^{10} \eta^2 \left\{ 1 + v^2 \left(-\frac{1247}{336} - \frac{35}{12} \eta \right) + v^3 \left[-\frac{11\delta\chi_a}{4} + \left(3\eta - \frac{11}{4} \right) \chi_s + 4\pi \right] \right. \\
& + v^4 \left[\frac{33\delta\chi_a\chi_s}{8} + \frac{65\eta^2}{18} + \left(\frac{33}{16} - 8\eta \right) \chi_a^2 + \left(\frac{33}{16} - \frac{\eta}{4} \right) \chi_s^2 + \frac{9271\eta}{504} - \frac{44711}{9072} \right] \\
& + v^5 \left[\left(\frac{701\delta\eta}{36} - \frac{59\delta}{16} \right) \chi_a + \left(-\frac{157\eta^2}{9} + \frac{227\eta}{9} - \frac{59}{16} \right) \chi_s - \frac{583\pi\eta}{24} - \frac{8191\pi}{672} \right] \\
& + v^6 \left[-\frac{1712}{105} \ln(4v) - \frac{1712\gamma}{105} - \frac{775\eta^3}{324} - \frac{94403\eta^2}{3024} + \left(\frac{41\pi^2}{48} - \frac{134543}{7776} \right) \eta + \frac{16\pi^2}{3} + \frac{6643739519}{69854400} \right] \\
& + v^7 \left[\frac{193385\pi\eta^2}{3024} + \frac{214745\pi\eta}{1728} - \frac{16285\pi}{504} \right] \\
& \left. + v^7 \sum_{i=1}^2 \left[\left(\frac{162305}{3888} + \frac{971}{54} \eta - \frac{6737}{108} \eta^2 \right) \left(\frac{m_i}{M} \right)^2 + \eta \left(\frac{9535}{336} + \frac{1849}{126} \eta - \frac{1501}{36} \eta^2 \right) \right] (\boldsymbol{\chi}_i \cdot \boldsymbol{l}_N) \right\}, \tag{A.8}
\end{aligned}$$

where γ is the Euler constant.

In [363], Alvi computed the energy flowing in and out of the inspiraling black holes, leading to the change in their mass, spin and area of the horizon. The calculation involved calculating the effect of the Newtonian field of each black hole on the horizon of the other hole, and using the horizon deformation to obtain the energy absorption. By combining the rates of mass change for both black holes, we obtain the rate of change of the total mass as

$$\dot{M}(v) = \frac{32}{5} v^{10} \eta^2 \left\{ -\frac{v^5}{4} \left[(1 - 3\eta) \chi_s (1 + 3\chi_s^2 + 9\chi_a^2) + (1 - \eta) \delta \chi_a (1 + 3\chi_a^2 + 9\chi_s^2) \right] \right\}. \tag{A.9}$$

This formula was derived for comparable mass-ratio binaries. A similar calculation has been done in the extreme-mass-ratio limit [364], and agrees with this formula in that limit. The effect of the total $\dot{M}(v)$ term in energy balance is to change the orbital phase of the emitted gravitational waves by less than a radian in the duration in which the waveform is in the frequency range of terrestrial detectors [363]. Therefore:

- Except for its explicit presence in Eq. (A.4), we always treat the mass as a constant.
- We also ignore the higher-order spin terms calculated in [363].

Below we describe the formulae for the different post-Newtonian variants that are

used in the context of terrestrial gravitational wave detectors. The naming convention, which is colloquially used, follows from [365]. First, we define the leading order spin-orbit correction β at 1.5PN, leading order spin-spin correction σ at 2PN, next-to-leading order spin-orbit corrections γ at 2.5PN, tail-induced spin orbit corrections ξ at 3PN and third order spin-orbit corrections ζ appearing at 3.5PN, as follows:

$$\beta = \sum_{i=1}^2 \left[\frac{113}{12} \left(\frac{m_i}{M} \right)^2 + \frac{25}{4} \eta \right] (\chi_i \cdot \hat{L}_N), \quad (\text{A.10})$$

$$\begin{aligned} \sigma = \eta & \left[\frac{721}{48} (\chi_1 \cdot \hat{L}_N) (\chi_2 \cdot \hat{L}_N) - \frac{247}{48} \chi_1 \cdot \chi_2 \right] \\ & + \frac{5}{2} \sum_{i=1}^2 q_i \left(\frac{m_i}{M} \right)^2 \left[3 (\chi_i \cdot \hat{L}_N)^2 - \chi_i^2 \right] \\ & + \frac{1}{96} \sum_{i=1}^2 \left(\frac{m_i}{M} \right)^2 \left[7 \chi_i^2 - (\chi_i \cdot \hat{L}_N)^2 \right], \end{aligned} \quad (\text{A.11})$$

$$\gamma = \sum_{i=1}^2 \left[\left(\frac{732\,985}{2268} + \frac{140}{9} \eta \right) \left(\frac{m_i}{M} \right)^2 + \eta \left(\frac{13\,915}{84} - \frac{10}{3} \eta \right) \right] (\chi_i \cdot \hat{L}_N), \quad (\text{A.12})$$

$$\xi = \pi \sum_{i=1}^2 \left[\frac{75}{2} \left(\frac{m_i}{M} \right)^2 + \frac{151}{6} \eta \right] (\chi_i \cdot \hat{L}_N), \quad (\text{A.13})$$

$$\zeta = \sum_{i=1}^2 \left[\left(\frac{130\,325}{756} - \frac{796\,069}{2016} \eta + \frac{100\,019}{864} \eta^2 \right) \left(\frac{m_i}{M} \right)^2 + \eta \left(\frac{1\,195\,759}{18\,144} - \frac{257\,023}{1008} \eta + \frac{2903}{32} \eta^2 \right) \right] (\chi_i \cdot \hat{L}_N). \quad (\text{A.14})$$

A.1.1 TaylorT1 phasing

The TaylorT1 approximant is computed by numerically integrating the ordinary differential equation for $v(t)$ in Eq. (A.4), using the expressions for orbital energy, flux, and mass change given in Eqs. (A.7), (A.8), and (A.9). The phase is then computed

by substituting this result for $v(t)$ in $\phi(v(t))$ obtained by integrating Eq. (A.3).

A.1.2 TaylorT4 phasing

The TaylorT4 approximant is similar to the TaylorT1 approximant, except that the ratio of the polynomials on the right-hand side of Eq. (A.4) is first expanded as a Taylor series, and truncated at consistent PN order. Explicitly, dv/dt becomes

$$\begin{aligned} \frac{dv}{dt} = \frac{32\eta}{5M} v^9 & \left\{ 1 + \left(-\frac{743}{336} - \frac{11}{4}\eta \right) v^2 + (4\pi - \beta)v^3 + \left(\frac{34\,103}{18\,144} + \frac{13\,661}{2016}\eta + \frac{59}{18}\eta^2 + \sigma \right) v^4 \right. \\ & + \left(-\frac{4159\pi}{672} - \frac{189\pi}{8}\eta - \frac{9}{40}\gamma + \left(\frac{743}{168} + \frac{11}{2}\eta \right)\beta \right) v^5 \\ & + \left[\frac{16\,447\,322\,263}{139\,708\,800} - \frac{1712\gamma_E}{105} + \frac{16\pi^2}{3} - \frac{1712}{105} \log(4v) \right. \\ & \quad \left. + \left(-\frac{56\,198\,689}{217\,728} + \frac{451\pi^2}{48} \right)\eta + \frac{541}{896}\eta^2 - \frac{5605}{2592}\eta^3 - \xi \right] v^6 \\ & + \left. \pi \left(-\frac{4415}{4032} + \frac{358\,675}{6048}\eta + \frac{91\,495}{1512}\eta^2 - \zeta \right) v^7 \right\} \end{aligned} \quad (\text{A.15})$$

A.1.3 TaylorT2 phasing

Instead of integrating Eq. (A.4) to obtain $v(t)$, we can also invert the same equation and solve for $t(v)$. This leads to the TaylorT2 approximant. The expression for $t(v)$ so obtained is:

$$\begin{aligned} \frac{dt}{dv} = \frac{5M}{32\eta} v^{-9} & \left\{ 1 + \left(\frac{743}{336} + \frac{11}{4}\eta \right) v^2 + (-4\pi + \beta)v^3 + \left(\frac{3\,058\,673}{1\,016\,064} + \frac{5429}{1008}\eta + \frac{617}{144}\eta^2 - \sigma \right) v^4 \right. \\ & + \left(-\frac{7729\pi}{672} + \frac{13\pi}{8}\eta + \frac{9}{40}\gamma \right) v^5 \\ & + \left[-\frac{10\,817\,850\,546\,611}{93\,884\,313\,600} + \frac{32\pi^2}{3} + \frac{1712\gamma_E}{105} + \frac{1712}{105} \log(4v) \right. \\ & \quad \left. + \left(\frac{3\,147\,553\,127}{12\,192\,768} - \frac{451\pi^2}{48} \right)\eta - \frac{15\,211}{6912}\eta^2 + \frac{25\,565}{5184}\eta^3 - 8\pi\beta + \xi \right] v^6 \\ & + \pi \left(-\frac{15\,419\,335}{1\,016\,064} - \frac{75\,703}{6048}\eta + \frac{14\,809}{3024}\eta^2 - \beta \left(\frac{8\,787\,977}{1\,016\,064} + \frac{51\,841}{2016}\eta + \frac{2033}{144}\eta^2 \right) \right. \\ & \quad \left. + \gamma \left(\frac{2229}{2240} + \frac{99}{80}\eta \right) + \zeta \right) v^7 \right\} \end{aligned} \quad (\text{A.16})$$

Integrating Eq. A.3 by first expanding the right hand side gives the phase as a function of velocity, $\phi(v)$. This completes the construction of TaylorT2 waveforms.

A.1.4 TaylorF2 phasing

Starting from the explicit expressions for time and orbital phase in the TaylorT2 approximant, it is possible to analytically construct the Fourier transform of the gravitational waveform using the stationary phase approximation [365, 366, 367]. This was described in the discussion preceding Eq. 2.61. We can decompose the Fourier transform of $\tilde{h}(f) := \tilde{A}_{lm}(f) e^{i\Psi_{lm}(f)}$, and contemporary gravitational wave searches use the ($l = 2, m = \pm 2$) multipoles in searches. The form of the Taylor series of Ψ_{22} is given as:

$$\begin{aligned} \Psi_{22}(f) = & 2\pi f t_c - \phi_c + \frac{3}{128\eta} v^{-5} \left\{ 1 + \left(\frac{3715}{756} + \frac{55}{9}\eta \right) v^2 + (4\beta - 16\pi)v^3 \right. \\ & + \left(\frac{15\,293\,365}{508\,032} + \frac{27\,145}{504}\eta + \frac{3085}{72}\eta^2 - 10\sigma \right) v^4 + \left(\frac{38\,645}{756}\pi - \frac{65}{9}\pi\eta - \gamma \right) (1 + 3\log(v)) v^5 \\ & + \left[\frac{11\,583\,231\,236\,531}{4\,694\,215\,680} - \frac{640}{3}\pi^2 - \frac{6848\gamma_E}{21} - \frac{6848}{21}\log(4v) + \left(-\frac{15\,737\,765\,635}{3\,048\,192} + \frac{2255\pi^2}{12} \right) \eta \right. \\ & + \left. \frac{76\,055}{1728}\eta^2 - \frac{127\,825}{1296}\eta^3 + 160\pi\beta - 20\xi \right] v^6 + \pi \left(\frac{77\,096\,675}{254\,016} + \frac{378\,515}{1512}\eta - \frac{74\,045}{756}\eta^2 \right. \\ & \left. + \beta \left(\frac{43\,939\,885}{254\,016} + \frac{259\,205}{504}\eta + \frac{10\,165}{36}\eta^2 \right) - \gamma \left(\frac{2229}{112} - \frac{99}{4}\eta \right) - 20\zeta \right) v^7 \end{aligned} \quad (\text{A.17})$$

Substituting $v = (\pi M f)^{1/3}$, we obtain the TaylorF2 phasing as a function of the gravitational wave frequency.

A.1.5 Waveform amplitudes

The currently available expressions for the nonspinning parts of the waveform are found in [368]. Due to space consideration, we refer the reader to Eqs. (9.3) and (9.4) of that reference for the amplitude of different multipoles resulting from the decomposition of $h_+ - i h_\times$ into harmonics. To these, we must add the spin terms given

in [369], which can be decomposed into harmonics and written as [370]

$$H_{2,2} = -\frac{16}{3}\sqrt{\frac{\pi}{5}}v^5\eta[2\delta\chi_a + 2(1-\eta)\chi_s + 3v\eta(\chi_a^2 - \chi_s^2)]e^{-2i\Phi}, \quad (\text{A.18})$$

$$H_{2,1} = 4i\sqrt{\frac{\pi}{5}}v^4\eta(\delta\chi_s + \chi_a)e^{-i\Phi}, \quad (\text{A.19})$$

$$H_{3,2} = \frac{32}{3}\sqrt{\frac{\pi}{7}}v^5\eta^2\chi_se^{-2i\Phi}. \quad (\text{A.20})$$

Waveform multipoles with negative values of m can be obtained from

$$H_{\ell,-m} = (-1)^\ell \bar{H}_{\ell,m}. \quad (\text{A.21})$$

The frequency domain TaylorF2 amplitudes in Fourier space can be deduced from their time-domain description $A_{\ell m}$ by

$$\tilde{A}_{\ell m} = A_{\ell m}\sqrt{\frac{2\pi}{m\ddot{\phi}}} = A_{\ell m}\sqrt{\frac{2\pi M}{3mv^2\dot{v}}}, \quad (\text{A.22})$$

where \dot{v} can be calculated from Eq. (A.15) and replacing v with $(\pi Mf)^{1/3}$.

Bibliography

- [1] R. A. Hulse and J. H. Taylor. *Discovery of a pulsar in a binary system.* *ApJL*, 195:L51–L53, January 1975.
- [2] J.M. Weisberg, J.H. Taylor, and L.A. Fowler. GRAVITATIONAL WAVES FROM AN ORBITING PULSAR. *Sci.Am.*, 245:66–74, 1981.
- [3] J. H. Taylor and J. M. Weisberg. Further experimental tests of relativistic gravity using the binary pulsar PSR 1913 + 16. *Astrophys. J.*, 345:434–450, October 1989.
- [4] Marta Burgay, N. D’Amico, A. Possenti, R.N. Manchester, A.G. Lyne, et al. An Increased estimate of the merger rate of double neutron stars from observations of a highly relativistic system. *Nature*, 426:531–533, 2003.
- [5] F. A. E. Pirani. *Acta Physica Polonica*, 15:389, 1956.
- [6] G. F. Moss, L. R. Miller, and Forward R. L. Photon-noise-limited laser transducer for gravitational antenna. *Applied Optics*, 10:2495–2498, 1971.
- [7] R Weiss. Electromagnetically coupled broadband gravitational wave antenna. *Quarterly Progress Report of the Research Laboratory of Electronics of the Massachusetts Institutue of Technology*, 105:54, April 1972.
- [8] R. P. Drever et al. A gravity-wave detector using optical cavity sensing. In E. Schmutzler, editor, *Proceedings of the Ninth International Conference on General Relativity and Gravitation*, pages 265–267. Cambridge University Press, Cambridge, UK, 1983.
- [9] Peter R. Saulson. Fundamentals of interferometric gravitational wave detectors. 1995.

- [10] Eirini Messaritaki. Report on the first binary black hole inspiral search in LIGO data. *Class.Quant.Grav.*, 22:S1119–S1128, 2005.
- [11] J. Abadie et al. All-sky search for gravitational-wave bursts in the first joint LIGO-GEO-Virgo run. *Phys.Rev.*, D81:102001, 2010.
- [12] J. Abadie et al. All-sky search for gravitational-wave bursts in the second joint LIGO-Virgo run. *Phys.Rev.*, D85:122007, 2012.
- [13] B.P. Abbott et al. Search for gravitational wave ringdowns from perturbed black holes in LIGO S4 data. *Phys.Rev.*, D80:062001, 2009.
- [14] J. Abadie et al. Search for Gravitational Waves from Low Mass Compact Binary Coalescence in LIGO’s Sixth Science Run and Virgo’s Science Runs 2 and 3. *Phys.Rev.*, D85:082002, 2012.
- [15] J. Abadie et al. Search for Gravitational Waves from Compact Binary Coalescence in LIGO and Virgo Data from S5 and VSR1. *Phys.Rev.*, D82:102001, 2010.
- [16] B.P. Abbott et al. Search for Gravitational Waves from Low Mass Compact Binary Coalescence in 186 Days of LIGO’s fifth Science Run. *Phys.Rev.*, D80:047101, 2009.
- [17] B.P. Abbott et al. Search for Gravitational Waves from Low Mass Binary Coalescences in the First Year of LIGO’s S5 Data. *Phys.Rev.*, D79:122001, 2009.
- [18] J. Abadie et al. Search for gravitational waves from binary black hole inspiral, merger and ringdown. *Phys.Rev.*, D83:122005, 2011.
- [19] J. Aasi et al. Search for Gravitational Waves from Binary Black Hole Inspiral, Merger and Ringdown in LIGO-Virgo Data from 2009-2010. *Phys.Rev.*, D87:022002, 2013.
- [20] B. Abbott et al. Setting upper limits on the strength of periodic gravitational waves using the first science data from the GEO 600 and LIGO detectors. *Phys.Rev.*, D69:082004, 2004.

- [21] B. Abbott et al. First all-sky upper limits from LIGO on the strength of periodic gravitational waves using the Hough transform. *Phys.Rev.*, D72:102004, 2005.
- [22] Alicia M. Sintes. Recent results on the search for continuous sources with LIGO and GEO 600. *J.Phys.Conf.Ser.*, 39:36–38, 2006.
- [23] J. Abadie et al. Beating the spin-down limit on gravitational wave emission from the Vela pulsar. *Astrophys.J.*, 737:93, 2011.
- [24] C. Palomba. Searches for continuous gravitational wave signals and stochastic backgrounds in LIGO and Virgo data. 2012.
- [25] Gregory M. Harry et al. Advanced LIGO: The next generation of gravitational wave detectors. *Class.Quant.Grav.*, 27:084006, 2010.
- [26] F. Acernese et al. Advanced Virgo Baseline Design, 2009. [Virgo Technical Document VIR-0027A-09].
- [27] J. Aasi et al. Prospects for Localization of Gravitational Wave Transients by the Advanced LIGO and Advanced Virgo Observatories. 2013.
- [28] J. Abadie et al. Predictions for the Rates of Compact Binary Coalescences Observable by Ground-based Gravitational-wave Detectors. *Class.Quant.Grav.*, 27:173001, 2010.
- [29] Luc Blanchet. Gravitational radiation from post-Newtonian sources and inspiralling compact binaries. *Living Rev.Rel.*, 9:4, 2006.
- [30] A. Buonanno and T. Damour. Effective one-body approach to general relativistic two-body dynamics. *Phys.Rev.*, D59:084006, 1999.
- [31] S. E. Gralla and R. M. Wald. A rigorous derivation of gravitational self-force. *Classical and Quantum Gravity*, 25(20):205009, October 2008.
- [32] S. E. Gralla and R. M. Wald. Derivation of Gravitational Self-Force. *ArXiv e-prints*, July 2009.
- [33] Frans Pretorius. Evolution of binary black hole spacetimes. *Phys.Rev.Lett.*, 95:121101, 2005.

- [34] Frans Pretorius. Simulation of binary black hole spacetimes with a harmonic evolution scheme. *Class.Quant.Grav.*, 23:S529–S552, 2006.
- [35] Manuela Campanelli, C.O. Lousto, P. Marronetti, and Y. Zlochower. Accurate evolutions of orbiting black-hole binaries without excision. *Phys.Rev.Lett.*, 96:111101, 2006.
- [36] Simulating eXtreme Spacetimes collaboration.
- [37] Abdul H. Mroue et al. A catalog of 174 binary black-hole simulations for gravitational-wave astronomy. *Phys.Rev.Lett.*, 111:241104, 2013.
- [38] Yi Pan, Alessandra Buonanno, Michael Boyle, Luisa T. Buchman, Lawrence E. Kidder, et al. Inspiral-merger-ringdown multipolar waveforms of nonspinning black-hole binaries using the effective-one-body formalism. *Phys.Rev.*, D84:124052, 2011. 26 pages, 25 figures.
- [39] L. Santamaria, F. Ohme, P. Ajith, B. Bruegmann, N. Dorband, et al. Matching post-Newtonian and numerical relativity waveforms: systematic errors and a new phenomenological model for non-precessing black hole binaries. *Phys.Rev.*, D82:064016, 2010.
- [40] M. Brett Deaton, Matthew D. Duez, Francois Foucart, Evan O'Connor, Christian D. Ott, et al. Black Hole-Neutron Star Mergers with a Hot Nuclear Equation of State: Outflow and Neutrino-Cooled Disk for a Low-Mass, High-Spin Case. *Astrophys.J.*, 776:47, 2013.
- [41] Philipp Msta, Sherwood Richers, Christian D. Ott, Roland Haas, Anthony L. Piro, et al. Magnetorotational Core-Collapse Supernovae in Three Dimensions. *Astrophys.J.*, 785:L29, 2014.
- [42] C. W. Misner, K. S. Thorne, and J. A. Wheeler. *Gravitation*. San Francisco: W.H. Freeman and Co., 1973, 1973.
- [43] Bernard Schutz. *A First Course in General Relativity*. Cambridge University Press, 1985.
- [44] Robert M. Wald. *General Relativity*. University of Chicago Press, 1984.

- [45] Joseph Weber and John A. Wheeler. Reality of the cylindrical gravitational waves of einstein and rosen. *Rev. Mod. Phys.*, 29(3):509–515, Jul 1957.
- [46] P.A.R. Ade et al. BICEP2 I: Detection Of B-mode Polarization at Degree Angular Scales. 2014.
- [47] Duncan A. Brown. Searching for gravitational radiation from binary black hole MACHOs in the galactic halo. 2004.
- [48] Jon Mathews and Robert L. Walker. *Mathematical Methods of Physics*. W.A. Benjamin; 2nd edition, 1970.
- [49] Alessandra Buonanno, Bala Iyer, Evan Ochsner, Yi Pan, and B.S. Sathyaprakash. Comparison of post-Newtonian templates for compact binary inspiral signals in gravitational-wave detectors. *Phys.Rev.*, D80:084043, 2009.
- [50] Michael Boyle, Duncan A. Brown, Lawrence E. Kidder, Abdul H. Mroue, Harald P. Pfeiffer, et al. High-accuracy comparison of numerical relativity simulations with post-Newtonian expansions. *Phys.Rev.*, D76:124038, 2007.
- [51] A. H. Nitz, A. Lundgren, D. A. Brown, E. Ochsner, et al. Accuracy of gravitational waveform models for observing neutron-star–black-hole binaries in Advanced LIGO. *ArXiv e-prints*, July 2013.
- [52] Ian Hinder. The Current Status of Binary Black Hole Simulations in Numerical Relativity. *Class.Quant.Grav.*, 27:114004, 2010.
- [53] Harald P. Pfeiffer. Numerical simulations of compact object binaries. *Class.Quant.Grav.*, 29:124004, 2012.
- [54] P. Ajith, Michael Boyle, Duncan A. Brown, Bernd Brugmann, Luisa T. Buchman, et al. The NINJA-2 catalog of hybrid post-Newtonian/numerical-relativity waveforms for non-precessing black-hole binaries. *Class.Quant.Grav.*, 29:124001, 2012.
- [55] Thibault Damour, Alessandro Nagar, Mark Hannam, Sascha Husa, and Bernd Bruegmann. Accurate Effective-One-Body waveforms of inspiralling and coalescing black-hole binaries. *Phys.Rev.*, D78:044039, 2008.

- [56] Alessandra Buonanno, Yi Pan, Harald P. Pfeiffer, Mark A. Scheel, Luisa T. Buchman, et al. Effective-one-body waveforms calibrated to numerical relativity simulations: Coalescence of non-spinning, equal-mass black holes. *Phys.Rev.*, D79:124028, 2009.
- [57] Thibault Damour and Alessandro Nagar. An Improved analytical description of inspiralling and coalescing black-hole binaries. *Phys.Rev.*, D79:081503, 2009.
- [58] Thibault Damour and Alessandro Nagar. Comparing Effective-One-Body gravitational waveforms to accurate numerical data. *Phys.Rev.*, D77:024043, 2008.
- [59] Thibault Damour, Alessandro Nagar, Ernst Nils Dorband, Denis Pollney, and Luciano Rezzolla. Faithful Effective-One-Body waveforms of equal-mass coalescing black-hole binaries. *Phys.Rev.*, D77:084017, 2008.
- [60] Alessandra Buonanno and Thibault Damour. Transition from inspiral to plunge in binary black hole coalescences. *Phys.Rev.*, D62:064015, 2000. 52 pages, 21 figures, ReVTex, epsfig; few misprints corrected.
- [61] Thibault Damour, Bala R. Iyer, Piotr Jaranowski, and B.S. Sathyaprakash. Gravitational waves from black hole binary inspiral and merger: The Span of third postNewtonian effective one-body templates. *Phys.Rev.*, D67:064028, 2003.
- [62] Thibault Damour, Piotr Jaranowski, and Gerhard Schaefer. On the determination of the last stable orbit for circular general relativistic binaries at the third postNewtonian approximation. *Phys.Rev.*, D62:084011, 2000.
- [63] Thibault Damour, Bala R. Iyer, and Alessandro Nagar. Improved resummation of post-Newtonian multipolar waveforms from circularized compact binaries. *Phys.Rev.*, D79:064004, 2009.
- [64] A. Buonanno and T. Damour. Effective one-body approach to general relativistic two-body dynamics. *Phys.Rev.*, D59:084006, 1999.
- [65] Alessandra Buonanno, Yanbei Chen, and Thibault Damour. Transition from inspiral to plunge in precessing binaries of spinning black holes. *Phys.Rev.*, D74:104005, 2006.

- [66] Emanuele Berti, Vitor Cardoso, and Clifford M. Will. On gravitational-wave spectroscopy of massive black holes with the space interferometer LISA. *Phys.Rev.*, D73:064030, 2006.
- [67] LSC Algorithm Library. <https://www.lsc-group.phys.uwm.edu/daswg/projects/lalsuite.html>.
- [68] Matthew Pitkin, Stuart Reid, Sheila Rowan, and James Hough. Gravitational wave detection by interferometry (ground and space). *Living Reviews in Relativity*, 14(5), 2011.
- [69] B.S. Sathyaprakash and B.F. Schutz. Physics, Astrophysics and Cosmology with Gravitational Waves. *Living Rev.Rel.*, 12:2, 2009.
- [70] Kentaro Somiya. Detector configuration of KAGRA: The Japanese cryogenic gravitational-wave detector. *Class.Quant.Grav.*, 29:124007, 2012.
- [71] A. Tutukov and L. Yungelson. Evolution of close binary with relativistic component. *Nauchnye Informatsii*, 27:86, 1973.
- [72] A. Tutukov and L. Yungelson. Evolution of massive close binaries. *Nauchnye Informatsii*, 27:70, 1973.
- [73] R.F. Webbink. Double white dwarfs as progenitors of R Coronae Borealis stars and Type I supernovae. *Astrophys.J.*, 277:355–360, 1984.
- [74] I. Kowalska, T. Regimbau, T. Bulik, M. Dominik, and K. Belczynski. Effect of metallicity on the gravitational-wave signal from the cosmological population of compact binary coalescences. 2012.
- [75] Chris L. Fryer, Krzysztof Belczynski, Grzegorz Wiktorowicz, Michal Dominik, Vicky Kalogera, et al. Compact Remnant Mass Function: Dependence on the Explosion Mechanism and Metallicity. *Astrophys.J.*, 749:91, 2012.
- [76] Michal Dominik, Krzysztof Belczynski, Christopher Fryer, Daniel Holz, Emanuele Berti, et al. Double Compact Objects I: The Significance of the Common Envelope on Merger Rates. *Astrophys.J.*, 759:52, 2012.

- [77] Krzysztof Belczynski and Michal Dominik. A test of black hole natal kick mechanism by the first gravitational radiation detections. 2012.
- [78] L A Wainstein and V D Zubakov. *Extraction of signals from noise*. Prentice-Hall, Englewood Cliffs, NJ, 1962.
- [79] Bruce Allen, Warren G. Anderson, Patrick R. Brady, Duncan A. Brown, and Jolien D.E. Creighton. FINDCHIRP: An Algorithm for detection of gravitational waves from inspiraling compact binaries. *Phys.Rev.*, D85:122006, 2012.
- [80] Feryal Ozel, Dimitrios Psaltis, Ramesh Narayan, and Jeffrey E. McClintock. The Black Hole Mass Distribution in the Galaxy. *Astrophys.J.*, 725:1918–1927, 2010.
- [81] B.S. Sathyaprakash and S.V. Dhurandhar. Choice of filters for the detection of gravitational waves from coalescing binaries. *Phys.Rev.*, D44:3819–3834, 1991.
- [82] R. Balasubramanian, B.S. Sathyaprakash, and S.V. Dhurandhar. Gravitational waves from coalescing binaries: Detection strategies and Monte Carlo estimation of parameters. *Phys.Rev.*, D53:3033–3055, 1996.
- [83] T.A. Apostolatos. Search templates for gravitational waves from precessing, inspiraling binaries. *Phys.Rev.*, D52:605–620, 1995.
- [84] Kipp Cannon et al. Singular value decomposition applied to compact binary coalescence gravitational-wave signals. *Phys.Rev.*, D82:044025, 2010.
- [85] Benjamin J. Owen. Search templates for gravitational waves from inspiraling binaries: Choice of template spacing. *Phys.Rev.*, D53:6749–6761, 1996.
- [86] B.S. Sathyaprakash. Filtering postNewtonian gravitational waves from coalescing binaries. *Phys.Rev.*, D50:7111–7115, 1994.
- [87] S. Babak, R. Balasubramanian, D. Churches, T. Cokelaer, and B.S. Sathyaprakash. A Template bank to search for gravitational waves from inspiralling compact binaries. I. Physical models. *Class.Quant.Grav.*, 23:5477–5504, 2006.

- [88] Benjamin J. Owen and B.S. Sathyaprakash. Matched filtering of gravitational waves from inspiraling compact binaries: Computational cost and template placement. *Phys.Rev.*, D60:022002, 1999.
- [89] Thomas Cokelaer. Gravitational waves from inspiralling compact binaries: Hexagonal template placement and its efficiency in detecting physical signals. *Phys.Rev.*, D76:102004, 2007.
- [90] LIGO (David Shoemaker). Advanced LIGO anticipated sensitivity curves. Technical report, LIGO Document T0900288-v3, 2009.
- [91] Curt Cutler and Eanna E. Flanagan. Gravitational waves from merging compact binaries: How accurately can one extract the binary's parameters from the inspiral wave form? *Phys.Rev.*, D49:2658–2697, 1994.
- [92] Serge Droz, Daniel J. Knapp, Eric Poisson, and Benjamin J. Owen. Gravitational waves from inspiraling compact binaries: Validity of the stationary phase approximation to the Fourier transform. *Phys.Rev.*, D59:124016, 1999.
- [93] Luc Blanchet, Thibault Damour, Gilles Esposito-Farese, and Bala R. Iyer. Gravitational radiation from inspiralling compact binaries completed at the third post-Newtonian order. *Phys.Rev.Lett.*, 93:091101, 2004.
- [94] Luc Blanchet and Bala R. Iyer. Hadamard regularization of the third post-Newtonian gravitational wave generation of two point masses. *Phys.Rev.*, D71:024004, 2005.
- [95] Piotr Jaranowski and Gerhard Schaefer. The Binary black hole dynamics at the third postNewtonian order in the orbital motion. *Annalen Phys.*, 9:378–383, 2000.
- [96] Piotr Jaranowski and Gerhard Schaefer. The Binary black hole problem at the third postNewtonian approximation in the orbital motion: Static part. *Phys.Rev.*, D60:124003, 1999.
- [97] Thibault Damour, Piotr Jaranowski, and Gerhard Schaefer. Dimensional regularization of the gravitational interaction of point masses. *Phys.Lett.*, B513:147–155, 2001.

- [98] Lawrence E. Kidder. Using full information when computing modes of post-Newtonian waveforms from inspiralling compact binaries in circular orbit. *Phys.Rev.*, D77:044016, 2008.
- [99] Luc Blanchet, Guillaume Faye, Bala R. Iyer, and Siddhartha Sinha. The Third post-Newtonian gravitational wave polarisations and associated spherical harmonic modes for inspiralling compact binaries in quasi-circular orbits. *Class.Quant.Grav.*, 25:165003, 2008. 57 pages, no figures.
- [100] Alessandra Buonanno, Bala Iyer, Evan Ochsner, Yi Pan, and B.S. Sathyaprakash. Comparison of post-Newtonian templates for compact binary inspiral signals in gravitational-wave detectors. *Phys.Rev.*, D80:084043, 2009.
- [101] D.J.A. McKechnie. On the use of higher order waveforms in the search for gravitational waves emitted by compact binary coalescences. 2011. Ph.D. thesis.
- [102] Larne Pekowsky, James Healy, Deirdre Shoemaker, and Pablo Laguna. Impact of Higher-order Modes on the Detection of Binary Black Hole Coalescences. 2012.
- [103] Lee Lindblom, Benjamin J. Owen, and Duncan A. Brown. Model Waveform Accuracy Standards for Gravitational Wave Data Analysis. *Phys.Rev.*, D78:124020, 2008.
- [104] Lee Lindblom, John G. Baker, and Benjamin J. Owen. Improved Time-Domain Accuracy Standards for Model Gravitational Waveforms. *Phys.Rev.*, D82:084020, 2010.
- [105] Lee Samuel Finn and David F. Chernoff. Observing binary inspiral in gravitational radiation: One interferometer. *Phys.Rev.*, D47:2198–2219, 1993.
- [106] Alessandra Buonanno, Yi Pan, John G. Baker, Joan Centrella, Bernard J. Kelly, et al. Toward faithful templates for non-spinning binary black holes using the effective-one-body approach. *Phys.Rev.*, D76:104049, 2007.
- [107] B.S. Sathyaprakash and B.F. Schutz. Physics, Astrophysics and Cosmology with Gravitational Waves. *Living Rev.Rel.*, 12:2, 2009.

- [108] J. Abadie et al. Search for Gravitational Wave Bursts from Six Magnetars. *Astrophys.J.*, 734:L35, 2011.
- [109] G.L. Turin. An introduction to matched filters. *Information Theory, IRE Transactions on*, 6(3):311–329, 1960.
- [110] John G. Baker, Joan Centrella, Dae-Il Choi, Michael Koppitz, and James van Meter. Gravitational wave extraction from an inspiraling configuration of merging black holes. *Phys.Rev.Lett.*, 96:111102, 2006.
- [111] Lee Lindblom, Mark A. Scheel, Lawrence E. Kidder, Robert Owen, and Oliver Rinne. A New generalized harmonic evolution system. *Class.Quant.Grav.*, 23:S447–S462, 2006.
- [112] Frans Pretorius. Binary Black Hole Coalescence. 2007.
- [113] Mark Hannam. Status of black-hole-binary simulations for gravitational-wave detection. *Class.Quant.Grav.*, 26:114001, 2009.
- [114] <http://www.black-holes.org/SpEC.html>.
- [115] Luisa T. Buchman, Harald P. Pfeiffer, Mark A. Scheel, and Bela Szilagyi. Simulations of non-equal mass black hole binaries with spectral methods. *Phys.Rev.*, D86:084033, 2012.
- [116] Abdul H. Mroue and Harald P. Pfeiffer. Precessing Binary Black Holes Simulations: Quasicircular Initial Data. 2012.
- [117] Andrea Taracchini, Yi Pan, Alessandra Buonanno, Enrico Barausse, Michael Boyle, et al. Prototype effective-one-body model for nonprecessing spinning inspiral-merger-ringdown waveforms. *Phys.Rev.*, D86:024011, 2012.
- [118] Michael Boyle. Uncertainty in hybrid gravitational waveforms: Optimizing initial orbital frequencies for binary black-hole simulations. *Phys.Rev.*, D84:064013, 2011.
- [119] Ilana MacDonald, Samaya Nissanke, Harald P. Pfeiffer, and Harald P. Pfeiffer. Suitability of post-Newtonian/numerical-relativity hybrid waveforms for gravitational wave detectors. *Class.Quant.Grav.*, 28:134002, 2011.

- [120] Ilana MacDonald, Abdul H. Mroue, Harald P. Pfeiffer, Michael Boyle, Lawrence E. Kidder, et al. Suitability of hybrid gravitational waveforms for unequal-mass binaries. *Phys.Rev.*, D87:024009, 2013.
- [121] Frank Ohme, Mark Hannam, and Sascha Husa. Reliability of complete gravitational waveform models for compact binary coalescences. *Phys.Rev.*, D84:064029, 2011.
- [122] Mark Hannam, Sascha Husa, Frank Ohme, and P. Ajith. Length requirements for numerical-relativity waveforms. *Phys.Rev.*, D82:124052, 2010.
- [123] Parameswaran Ajith, S. Babak, Y. Chen, M. Hewitson, B. Krishnan, et al. Phenomenological template family for black-hole coalescence waveforms. *Class.Quant.Grav.*, 24:S689–S700, 2007.
- [124] Benjamin Aylott, John G. Baker, William D. Boggs, Michael Boyle, Patrick R. Brady, et al. Status of NINJA: The Numerical INjection Analysis project. *Class.Quant.Grav.*, 26:114008, 2009.
- [125] Lucia Santamaría, Badri Krishnan, and John T. Whelan. Searching for numerically-simulated signals of black hole binaries with a phenomenological template family. *Class.Quant.Grav.*, 26:114010, 2009.
- [126] Benjamin Aylott, John G. Baker, William D. Boggs, Michael Boyle, Patrick R. Brady, et al. Testing gravitational-wave searches with numerical relativity waveforms: Results from the first Numerical INjection Analysis (NINJA) project. *Class.Quant.Grav.*, 26:165008, 2009.
- [127] Duncan A. Brown, Prayush Kumar, and Alexander H. Nitz. Template banks to search for low-mass binary black holes in advanced gravitational-wave detectors. *Phys. Rev. D*, 87:082004, Apr 2013.
- [128] Bela Szilagyi. Stretching the limits of NR (NRDA 2013). http://www.grg.uib.es/NRDA13/slides/Szilagyi_StretchingTheLimitsOfNR.pdf.
- [129] J. Abadie et al. Results from the ninja-2 mock data challenge. In Prep.

- [130] Ian W. Harry, Bruce Allen, and B.S. Sathyaprakash. A Stochastic template placement algorithm for gravitational wave data analysis. *Phys.Rev.*, D80:104014, 2009.
- [131] P. Ajith, N. Fotopoulos, S. Privitera, A. Neunzert, and A.J. Weinstein. An effectual template bank for the detection of gravitational waves from inspiralling compact binaries with generic spins. 2012.
- [132] Gian Mario Manca and Michele Vallisneri. Cover art: Issues in the metric-guided and metric-less placement of random and stochastic template banks. *Phys.Rev.*, D81:024004, 2010.
- [133] B.S. Sathyaprakash. Mother templates for gravitational wave chirps. *Class.Quant.Grav.*, 17:L157–162, 2000.
- [134] Mark A. Scheel, Michael Boyle, Tony Chu, Lawrence E. Kidder, Keith D. Matthews, et al. High-accuracy waveforms for binary black hole inspiral, merger, and ringdown. *Phys.Rev.*, D79:024003, 2009.
- [135] Kipp Cannon, J.D. Emberson, Chad Hanna, Drew Keppel, and Harald Pfeiffer. Interpolation in waveform space: enhancing the accuracy of gravitational waveform families using numerical relativity. *Phys.Rev.*, D87(4):044008, 2013.
- [136] Mark A. Scheel, Bela Szilagyi, and Harald P. Pfeiffer. ”Private communication.”.
- [137] S. Babak, R. Biswas, P.R. Brady, D.A. Brown, K. Cannon, et al. Searching for gravitational waves from binary coalescence. *Phys.Rev.*, D87:024033, 2013.
- [138] Numerical Relativity - Analytical Relativity Collaboration (NRAR).
- [139] Eliu A. Huerta, Prayush Kumar, and Duncan A. Brown. Accurate modeling of intermediate-mass-ratio inspirals: exploring the form of the self-force in the intermediate-mass-ratio regime. *Phys.Rev.*, D86:024024, 2012.
- [140] Michael Boyle. Angular velocity of gravitational radiation from precessing binaries and the corotating frame. 2013.

- [141] Patricia Schmidt, Mark Hannam, and Sascha Husa. Towards models of gravitational waveforms from generic binaries: A simple approximate mapping between precessing and non-precessing inspiral signals. *Phys.Rev.*, D86:104063, 2012.
- [142] C. Capano, Y. Pan, and A. Buonanno. Impact of higher harmonics in searching for gravitational waves from non-spinning binary black hole. In Prep.
- [143] Jeffrey E. McClintock et al. Measuring the Spins of Accreting Black Holes. *Class.Quant.Grav.*, 28:114009, 2011.
- [144] Krzysztof Belczynski, Ronald E. Taam, Emmanouela Rantsiou, and Marc van der Sluys. Black Hole Spin Evolution: Implications for Short-hard Gamma Ray Bursts and Gravitational Wave Detection. *Astrophys.J.*, 2007.
- [145] Thibault Damour and Alessandro Nagar. An Improved analytical description of inspiralling and coalescing black-hole binaries. *Phys.Rev.*, D79:081503, 2009.
- [146] Yi Pan et al. Inspiral-merger-ringdown multipolar waveforms of nonspinning black-hole binaries using the effective-one-body formalism. *Phys.Rev.*, D84:124052, 2011.
- [147] P. Ajith et al. Inspiral-merger-ringdown waveforms for black-hole binaries with non-precessing spins. *Phys.Rev.Lett.*, 106:241101, 2011.
- [148] Thibault Damour, Alessandro Nagar, and Sebastiano Bernuzzi. Improved effective-one-body description of coalescing nonspinning black-hole binaries and its numerical-relativity completion. *Phys.Rev.*, D87:084035, 2013.
- [149] Andrea Taracchini et al. Effective-one-body model for black-hole binaries with generic mass ratios and spins. 2013.
- [150] Joan Centrella, John G. Baker, Bernard J. Kelly, and James R. van Meter. Black-hole binaries, gravitational waves, and numerical relativity. *Rev.Mod.Phys.*, 82:3069, 2010.
- [151] Will M. Farr et al. The Mass Distribution of Stellar-Mass Black Holes. *Astrophys.J.*, 741:103, 2011.

- [152] D. Brown et al. Data formats for numerical relativity waves. 2007.
- [153] P. Ajith et al. The NINJA-2 catalog of hybrid post-Newtonian/numerical-relativity waveforms for non-precessing black-hole binaries. *Class.Quant.Grav.*, 29:124001, 2012.
- [154] Ian Hinder et al. Error-analysis and comparison to analytical models of numerical waveforms produced by the NRAR Collaboration. *Class.Quant.Grav.*, 31:025012, 2013.
- [155] Frank Ohme. Analytical meets numerical relativity - status of complete gravitational waveform models for binary black holes. *Class.Quant.Grav.*, 29:124002, 2012.
- [156] Wolfgang Tichy and Pedro Marronetti. A Simple method to set up low eccentricity initial data for moving puncture simulations. *Phys.Rev.*, D83:024012, 2011.
- [157] Bernd Bruegmann et al. Calibration of Moving Puncture Simulations. *Phys.Rev.*, D77:024027, 2008.
- [158] Pedro Marronetti et al. Binary black holes on a budget: Simulations using workstations. *Class.Quant.Grav.*, 24:S43–S58, 2007.
- [159] Bernd Bruegmann, Wolfgang Tichy, and Nina Jansen. Numerical simulation of orbiting black holes. *Phys.Rev.Lett.*, 92:211101, 2004.
- [160] James Healy, Frank Herrmann, Ian Hinder, Deirdre M. Shoemaker, Pablo Laguna, et al. Superkicks in Hyperbolic Encounters of Binary Black Holes. *Phys.Rev.Lett.*, 102:041101, 2009.
- [161] James Healy, Pablo Laguna, Richard A. Matzner, and Deirdre M. Shoemaker. Final Mass and Spin of Merged Black Holes and the Golden Black Hole. *Phys.Rev.*, D81:081501, 2010.
- [162] Tanja Bode, Roland Haas, Tamara Bogdanovic, Pablo Laguna, and Deirdre Shoemaker. Relativistic Mergers of Supermassive Black Holes and their Electromagnetic Signatures. *Astrophys.J.*, 715:1117–1131, 2010.

- [163] Frank Herrmann, Ian Hinder, Deirdre M. Shoemaker, Pablo Laguna, and Richard A. Matzner. Binary Black Holes: Spin Dynamics and Gravitational Recoil. *Phys.Rev.*, D76:084032, 2007.
- [164] James Healy, Janna Levin, and Deirdre Shoemaker. Zoom-Whirl Orbits in Black Hole Binaries. *Phys.Rev.Lett.*, 103:131101, 2009.
- [165] Tanja Bode et al. Mergers of Supermassive Black Holes in Astrophysical Environments. *Astrophys.J.*, 744:45, 2012.
- [166] Ian Hinder, Birjoo Vaishnav, Frank Herrmann, Deirdre Shoemaker, and Pablo Laguna. Universality and final spin in eccentric binary black hole inspirals. *Phys.Rev.*, D77:081502, 2008.
- [167] Sascha Husa, Jose A. Gonzalez, Mark Hannam, Bernd Bruegmann, and Ulrich Sperhake. Reducing phase error in long numerical binary black hole evolutions with sixth order finite differencing. *Class.Quant.Grav.*, 25:105006, 2008.
- [168] Mark Hannam, Sascha Husa, Bernd Bruegmann, and Achamveedu Gopakumar. Comparison between numerical-relativity and post-Newtonian waveforms from spinning binaries: The Orbital hang-up case. *Phys.Rev.*, D78:104007, 2008.
- [169] Mark Hannam, Sascha Husa, Frank Ohme, Doreen Muller, and Bernd Bruegmann. Simulations of black-hole binaries with unequal masses or nonprecessing spins: Accuracy, physical properties, and comparison with post-Newtonian results. *Phys.Rev.*, D82:124008, 2010.
- [170] Mark Hannam, Sascha Husa, Ulrich Sperhake, Bernd Bruegmann, and Jose A. Gonzalez. Where post-Newtonian and numerical-relativity waveforms meet. *Phys.Rev.*, D77:044020, 2008.
- [171] Ulrich Sperhake. Binary black-hole evolutions of excision and puncture data. *Phys.Rev.*, D76:104015, 2007.
- [172] Ulrich Sperhake et al. Eccentric binary black-hole mergers: The Transition from inspiral to plunge in general relativity. *Phys.Rev.*, D78:064069, 2008.

- [173] Denis Pollney and Christian Reisswig. Gravitational memory in binary black hole mergers. *Astrophys.J.*, 732:L13, 2011.
- [174] C. Reisswig, N.T. Bishop, D. Pollney, and B. Szilagyi. Characteristic extraction in numerical relativity: binary black hole merger waveforms at null infinity. *Class.Quant.Grav.*, 27:075014, 2010.
- [175] Denis Pollney, Christian Reisswig, Erik Schnetter, Nils Dorband, and Peter Diener. High accuracy binary black hole simulations with an extended wave zone. *Phys.Rev.*, D83:044045, 2011.
- [176] Carlos O. Lousto, Hiroyuki Nakano, Yosef Zlochower, and Manuela Campanelli. Intermediate Mass Ratio Black Hole Binaries: Numerical Relativity meets Perturbation Theory. *Phys.Rev.Lett.*, 104:211101, 2010.
- [177] Carlos O. Lousto, Hiroyuki Nakano, Yosef Zlochower, and Manuela Campanelli. Intermediate-mass-ratio black hole binaries: Intertwining numerical and perturbative techniques. *Phys.Rev.*, D82:104057, 2010.
- [178] Hiroyuki Nakano, Yosef Zlochower, Carlos O. Lousto, and Manuela Campanelli. Intermediate-mass-ratio black hole binaries II: Modeling Trajectories and Gravitational Waveforms. *Phys.Rev.*, D84:124006, 2011.
- [179] Harald P. Pfeiffer, Lawrence E. Kidder, Mark A. Scheel, and Saul A. Teukolsky. A Multidomain spectral method for solving elliptic equations. *Comput.Phys.Commun.*, 152:253–273, 2003.
- [180] Mark A. Scheel et al. Solving Einstein’s equations with dual coordinate frames. *Phys.Rev.*, D74:104006, 2006.
- [181] Geoffrey Lovelace, Michael Boyle, Mark A. Scheel, and Bela Szilagyi. Accurate gravitational waveforms for binary-black-hole mergers with nearly extremal spins. *Class.Quant.Grav.*, 29:045003, 2012.
- [182] Bela Szilagyi, Lee Lindblom, and Mark A. Scheel. Simulations of Binary Black Hole Mergers Using Spectral Methods. *Phys.Rev.*, D80:124010, 2009.

- [183] Geoffrey Lovelace, Mark.A. Scheel, and Bela Szilagyi. Simulating merging binary black holes with nearly extremal spins. *Phys.Rev.*, D83:024010, 2011.
- [184] Spectral Einstein Code.
- [185] Michael Boyle et al. High-accuracy comparison of numerical relativity simulations with post-Newtonian expansions. *Phys.Rev.*, D76:124038, 2007.
- [186] Michael Boyle and Abdul H. Mroue. Extrapolating gravitational-wave data from numerical simulations. *Phys.Rev.*, D80:124045, 2009.
- [187] Zachariah B. Etienne, Yuk Tung Liu, Stuart L. Shapiro, and Thomas W. Baumgarte. General relativistic simulations of black-hole-neutron-star mergers: Effects of black-hole spin. *Phys.Rev.*, D79:044024, 2009.
- [188] Manuela Campanelli, Carlos O. Lousto, Hiroyuki Nakano, and Yosef Zlochower. Comparison of Numerical and Post-Newtonian Waveforms for Generic Precessing Black-Hole Binaries. *Phys.Rev.*, D79:084010, 2009.
- [189] J Aasi et al. *Possible scenarios for Commissioning and Early observing with the Second Generation Detectors*, LIGO Tech. Rep. LIGO-G1000176, 2010.
- [190] LSC Algorithm Library for GStreamer.
- [191] J. Aasi et al. The characterization of Virgo data and its impact on gravitational-wave searches. *Class.Quant.Grav.*, 29:155002, 2012.
- [192] J. Aasi et al. *Characterizing the LIGO instruments in their sixth science run*, in preparation, 2014.
- [193] J. Abadie et al. Search for Gravitational Waves from Low Mass Compact Binary Coalescence in LIGO’s Sixth Science Run and Virgo’s Science Runs 2 and 3. *Phys.Rev.*, D85:082002, 2012.
- [194] B. Abbott et al. Search for gravitational-wave bursts in LIGO data from the fourth science run. *Class.Quant.Grav.*, 24:5343–5370, 2007.
- [195] J. Abadie et al. Search for Gravitational Waves from Intermediate Mass Binary Black Holes. *Phys.Rev.*, D85:102004, 2012.

- [196] B. Abbott et al. Search for gravitational waves from binary inspirals in S3 and S4 LIGO data. *Phys.Rev.*, D77:062002, 2008.
- [197] Stanislav Babak et al. The Mock LISA Data Challenges: From Challenge 1B to Challenge 3. *Class.Quant.Grav.*, 25:184026, 2008.
- [198] S. Babak, R. Balasubramanian, D. Churches, T. Cokelaer, and B.S. Sathyaprakash. A Template bank to search for gravitational waves from inspiralling compact binaries. I. Physical models. *Class.Quant.Grav.*, 23:5477–5504, 2006.
- [199] C.A.K. Robinson, B.S. Sathyaprakash, and Anand S. Sengupta. A Geometric algorithm for efficient coincident detection of gravitational waves. *Phys.Rev.*, D78:062002, 2008.
- [200] Bruce Allen. A chi**2 time-frequency discriminator for gravitational wave detection. *Phys.Rev.*, D71:062001, 2005.
- [201] Luc Blanchet, Guillaume Faye, Bala R. Iyer, and Benoit Joguet. Gravitational wave inspiral of compact binary systems to 7/2 postNewtonian order. *Phys.Rev.*, D65:061501, 2002.
- [202] Luc Blanchet, Bala R. Iyer, and Benoit Joguet. Gravitational waves from inspiralling compact binaries: Energy flux to third postNewtonian order. *Phys.Rev.*, D65:064005, 2002.
- [203] Drew Keppel. *Signatures and dynamics of compact binary coalescences and a search in LIGO’s S5 data*. PhD thesis, California Institute of Technology, 2009.
- [204] J. Aasi et al. The NINJA-2 project: Detecting and characterizing gravitational waveforms modelled using numerical binary black hole simulations. *Class.Quant.Grav.*, 31:115004, 2014.
- [205] Wolfgang Tichy and Pedro Marronetti. Binary black hole mergers: Large kicks for generic spin orientations. *Phys.Rev.*, D76:061502, 2007.
- [206] Wolfgang Tichy and Pedro Marronetti. The Final mass and spin of black hole mergers. *Phys.Rev.*, D78:081501, 2008.

- [207] Patricia Schmidt, Mark Hannam, Sascha Husa, and P. Ajith. Tracking the precession of compact binaries from their gravitational-wave signal. *Phys.Rev.*, D84:024046, 2011.
- [208] R. O'Shaughnessy, B. Vaishnav, J. Healy, Z. Meeks, and D. Shoemaker. Efficient asymptotic frame selection for binary black hole spacetimes using asymptotic radiation. *Phys.Rev.*, D84:124002, 2011.
- [209] R. O'Shaughnessy, J. Healy, L. London, Z. Meeks, and D. Shoemaker. Is J enough? Comparison of gravitational waves emitted along the total angular momentum direction with other preferred orientations. *Phys.Rev.*, D85(6):084003, 2012.
- [210] R. O'Shaughnessy, L. London, J. Healy, and D. Shoemaker. Precession during merger: Strong polarization changes are observationally accessible features of strong-field gravity during binary black hole merger. *Phys.Rev.*, D87(4):044038, 2013.
- [211] James Healy, Pablo Laguna, Larne Pekowsky, and Deirdre Shoemaker. Template Mode Hierarchies for Binary Black Hole Mergers. *Phys.Rev.*, D88:024034, 2013.
- [212] Sean T. McWilliams, Bernard J. Kelly, and John G. Baker. Observing mergers of non-spinning black-hole binaries. *Phys.Rev.*, D82:024014, 2010.
- [213] Yi Pan et al. Inspiral-merger-ringdown waveforms of spinning, precessing black-hole binaries in the effective-one-body formalism. 2013.
- [214] Mark Hannam et al. Twist and shout: A simple model of complete precessing black-hole-binary gravitational waveforms. 2013.
- [215] Duncan A. Brown, Ian Harry, Andrew Lundgren, and Alexander H. Nitz. Detecting binary neutron star systems with spin in advanced gravitational-wave detectors. *Phys.Rev.*, D86:084017, 2012.
- [216] I.W. Harry et al. Investigating the effect of precession on searches for neutron-star-black-hole binaries with Advanced LIGO. 2013.

- [217] Tyson B. Littenberg, Michael Coughlin, Benjamin Farr, and Will M. Farr. Fortifying the characterization of binary mergers in LIGO data. 2013.
- [218] P. A. M. Dirac. Classical Theory of Radiating Electrons. *Royal Society of London Proceedings Series A*, 167:148–169, August 1938.
- [219] B. S. DeWitt and R. W. Brehme. Radiation damping in a gravitational field. *Annals of Physics*, 9:220–259, February 1960.
- [220] T. C. Quinn and R. M. Wald. Axiomatic approach to electromagnetic and gravitational radiation reaction of particles in curved spacetime. *Phys. Rev. D*, 56:3381–3394, September 1997.
- [221] Y. Mino, M. Sasaki, and T. Tanaka. *Gravitational radiation reaction to a particle motion*. *Phys. Rev. D*, 55:3457–3476, March 1997.
- [222] P. Canizares and C. F. Sopuerta. Tuning time-domain pseudospectral computations of the self-force on a charged scalar particle. *Classical and Quantum Gravity*, 28(13):134011, July 2011.
- [223] Niels Warburton, Sarp Akcay, Leor Barack, Jonathan R. Gair, and Norichika Sago. Evolution of inspiral orbits around a Schwarzschild black hole. *Phys. Rev.*, D85:061501, 2012.
- [224] N. Warburton and L. Barack. Self force on a scalar charge in Kerr spacetime: eccentric equatorial orbits. *ArXiv e-prints*, March 2011.
- [225] N. Warburton and L. Barack. Self-force on a scalar charge in Kerr spacetime: Circular equatorial orbits. *Phys. Rev. D*, 81(8):084039–+, April 2010.
- [226] E.A. Huerta and Jonathan R Gair. Importance of including small body spin effects in the modelling of extreme and intermediate mass-ratio inspirals. *Phys. Rev.*, D84:064023, 2011.
- [227] E.A. Huerta, Jonathan R. Gair, and Duncan A. Brown. Importance of including small body spin effects in the modelling of intermediate mass-ratio inspirals. II Accurate parameter extraction of strong sources using higher-order spin effects. *Phys. Rev.*, D85:064023, 2012.

- [228] D. A. Brown, J. Brink, H. Fang, J. R. Gair, C. Li, G. Lovelace, I. Mandel, and K. S. Thorne. Prospects for Detection of Gravitational Waves from Intermediate-Mass-Ratio Inspirals. *Physical Review Letters*, 99(20):201102–+, November 2007.
- [229] M. C. Miller and E. J. M. Colbert. Intermediate-Mass Black Holes. *International Journal of Modern Physics D*, 13:1–64, January 2004.
- [230] L. Barack and N. Sago. Gravitational Self-Force Correction to the Innermost Stable Circular Orbit of a Schwarzschild Black Hole. *Phys. Rev. Lett.*, 102(19):191101–+, May 2009.
- [231] N. Sago, L. Barack, and S. Detweiler. Two approaches for the gravitational self-force in black hole spacetime: Comparison of numerical results. *Phys. Rev. D*, 78(12):124024–+, December 2008.
- [232] L. Barack and N. Sago. *Gravitational self-force on a particle in circular orbit around a Schwarzschild black hole*. *Phys. Rev. D*, 75(6):064021–+, March 2007.
- [233] Thibault Damour. Gravitational Self Force in a Schwarzschild Background and the Effective One Body Formalism. *Phys. Rev.*, D81:024017, 2010.
- [234] Enrico Barausse, Alessandra Buonanno, and Alexandre Le Tiec. The complete non-spinning effective-one-body metric at linear order in the mass ratio. *Phys. Rev.*, D85:064010, 2012.
- [235] T. Damour and A. Nagar. The Effective One Body description of the Two-Body problem. *ArXiv e-prints*, June 2009.
- [236] Sebastiano Bernuzzi and Alessandro Nagar. Binary black hole merger in the extreme-mass-ratio limit: a multipolar analysis. *Phys. Rev.*, D81:084056, 2010.
- [237] J. R. Gair and K. Glampedakis. *Improved approximate inspirals of test bodies into Kerr black holes*. *Phys. Rev. D*, 73(6):064037–+, March 2006.
- [238] T. Damour, B. R. Iyer, and A. Nagar. Improved resummation of post-Newtonian multipolar waveforms from circularized compact binaries. *Phys. Rev. D*, 79(6):064004–+, March 2009.

- [239] Yi Pan, Alessandra Buonanno, Ryuichi Fujita, Etienne Racine, and Hideyuki Tagoshi. Post-Newtonian factorized multipolar waveforms for spinning, non-precessing black-hole binaries. *Phys. Rev.*, D83:064003, 2011.
- [240] N. Yunes, A. Buonanno, S. A. Hughes, Y. Pan, E. Barausse, M. C. Miller, and W. Throwe. Extreme Mass-Ratio Inspirals in the Effective-One-Body Approach: Quasi-Circular, Equatorial Orbits around a Spinning Black Hole. *ArXiv e-prints*, September 2010.
- [241] Nicolas Yunes, Alessandra Buonanno, Scott A. Hughes, Yi Pan, Enrico Barausse, et al. Extreme Mass-Ratio Inspirals in the Effective-One-Body Approach: Quasi-Circular, Equatorial Orbits around a Spinning Black Hole. *Phys. Rev.*, D83:044044, 2011.
- [242] C. O. Lousto and Y. Zlochower. Orbital Evolution of Extreme-Mass-Ratio Black-Hole Binaries with Numerical Relativity. *Physical Review Letters*, 106(4):041101, January 2011.
- [243] L. Barack. TOPICAL REVIEW: Gravitational self-force in extreme mass-ratio inspirals. *Class. Quantum Grav.*, 26(21):213001–+, November 2009.
- [244] A. Ori and K. S. Thorne. Transition from inspiral to plunge for a compact body in a circular equatorial orbit around a massive, spinning black hole. *Phys. Rev. D*, 62(12):124022–+, December 2000.
- [245] L. Barack and C. Cutler. *LISA capture sources: Approximate waveforms, signal-to-noise ratios, and parameter estimation accuracy*. *Phys. Rev. D*, 69(8):082005–+, April 2004.
- [246] J. R. Gair, L. Barack, T. Creighton, C. Cutler, S. L. Larson, E. S. Phinney, and M. Vallisneri. *Event rate estimates for LISA extreme mass ratio capture sources*. *Class. Quantum Grav.*, 21:1595–+, October 2004.
- [247] S. Babak, H. Fang, J. R. Gair, K. Glampedakis, and S. A. Hughes. ‘‘Kludge’’ gravitational waveforms for a test-body orbiting a Kerr black hole. *Phys. Rev. D*, 75(2):024005–+, January 2007.

- [248] L. Barack and C. Cutler. Confusion noise from LISA capture sources. *Phys. Rev. D*, 70(12):122002–+, December 2004.
- [249] P. Amaro-Seoane, J. R. Gair, M. Freitag, M. C. Miller, I. Mandel, C. J. Cutler, and S. Babak. *TOPICAL REVIEW: Intermediate and extreme mass-ratio inspirals—astrophysics, science applications and detection using LISA*. *Class. Quantum Grav.*, 24:113–+, September 2007.
- [250] M. Favata. Conservative self-force correction to the innermost stable circular orbit: Comparison with multiple post-Newtonian-based methods. *Phys. Rev. D*, 83(2):024027–+, January 2011.
- [251] Ulrich Sperhake, Vitor Cardoso, Christian D. Ott, Erik Schnetter, and Helvi Witek. Extreme black hole simulations: collisions of unequal mass black holes and the point particle limit. *Phys. Rev.*, D84:084038, 2011.
- [252] Carlos O. Lousto, Hiroyuki Nakano, Yosef Zlochower, and Manuela Campanelli. Intermediate-mass-ratio black hole binaries: Intertwining numerical and perturbative techniques. *Phys. Rev.*, D82:104057, 2010.
- [253] Hiroyuki Nakano, Yosef Zlochower, Carlos O. Lousto, and Manuela Campanelli. Intermediate-mass-ratio black hole binaries II: Modeling Trajectories and Gravitational Waveforms. *Phys. Rev.*, D84:124006, 2011.
- [254] D. Kennefick and A. Ori. *Radiation-reaction-induced evolution of circular orbits of particles around Kerr black holes*. *Phys. Rev. D*, 53:4319–4326, April 1996.
- [255] J. E. McClintock and R. A. Remillard. *Black hole binaries*, pages 157–213. April 2006.
- [256] M. Morscher, S. Umbreit, W. M. Farr, and F. A. Rasio. Retention of Stellar-mass Black Holes in Globular Clusters. *Astrophys. J. Lett.*, 763:L15, January 2013.
- [257] A. Merloni and S. Heinz. A synthesis model for AGN evolution: supermassive black holes growth and feedback modes. *MNRAS*, 388:1011–1030, August 2008.

- [258] M. Fukugita and P. J. E. Peebles. The Cosmic Energy Inventory. *Astrophys. J.*, 616:643–668, December 2004.
- [259] J. M. Miller, A. Zezas, G. Fabbiano, and F. Schweizer. XMM-Newton Spectroscopy of Four Bright Ultraluminous X-Ray Sources in the Antennae Galaxies (NGC 4038/4039). *Astrophys. J.*, 609:728–734, July 2004.
- [260] J. M. Miller, A. C. Fabian, and M. C. Miller. Revealing a Cool Accretion Disk in the Ultraluminous X-Ray Source M81 X-9 (Holmberg IX X-1): Evidence for an Intermediate-Mass Black Hole. *Astrophys. J.*, 607:931–938, June 2004.
- [261] J. M. Miller. *Present evidence for intermediate mass black holes in ULXs and future prospects*, pages 227–238. January 2005.
- [262] D. A. Swartz, R. Soria, A. F. Tenant, and M. Yukita. A Complete Sample of Ultraluminous X-ray Source Host Galaxies. *Astrophys. J.*, 741:49, November 2011.
- [263] L. Zampieri and T. P. Roberts. Low-metallicity natal environments and black hole masses in ultraluminous X-ray sources. *MNRAS*, 400:677–686, December 2009.
- [264] K. Belczynski, T. Bulik, C. L. Fryer, A. Ruiter, F. Valsecchi, J. S. Vink, and J. R. Hurley. On the Maximum Mass of Stellar Black Holes. *Astrophys. J.*, 714:1217–1226, May 2010.
- [265] K. Ohsuga and S. Mineshige. Global Structure of Three Distinct Accretion Flows and Outflows around Black Holes from Two-dimensional Radiation-magnetohydrodynamic Simulations. *Astrophys. J.*, 736:2, July 2011.
- [266] H. Matsumoto, T. G. Tsuru, K. Koyama, H. Awaki, C. R. Canizares, N. Kawai, S. Matsushita, and R. Kawabe. Discovery of a Luminous, Variable, Off-Center Source in the Nucleus of M82 with the Chandra High-Resolution Camera. *Astrophys. J. Lett.*, 547:L25–L28, January 2001.
- [267] Sean Farrell, Natalie Webb, Didier Barret, Olivier Godet, and Joana Rodrigues. An Intermediate-mass Black Hole of Over 500 Solar Masses in the Galaxy ESO 243-49. *Nature*, 460:73–75, 2009.

- [268] F. P. A. Wolter Ginevra Trinchieri. Chandra observations of the ULX N10 in the Cartwheel galaxy. *ArXiv e-prints*, March 2010.
- [269] P. G. Jonker, M. A. P. Torres, A. C. Fabian, M. Heida, G. Miniutti, and D. Pooley. A bright off-nuclear X-ray source: a type IIn supernova, a bright ULX or a recoiling supermassive black hole in CXOJ122518.6+144545. *MNRAS*, 407:645–650, September 2010.
- [270] Simon F. Portegies Zwart, Holger Baumgardt, Piet Hut, Junichiro Makino, and Stephen L.W. McMillan. The Formation of massive black holes through collision runaway in dense young star clusters. *Nature*, 428:724, 2004.
- [271] T. E. Strohmayer and R. F. Mushotzky. Discovery of X-Ray Quasi-periodic Oscillations from an Ultraluminous X-Ray Source in M82: Evidence against Beaming. *Astrophys. J. Lett* , 586:L61–L64, March 2003.
- [272] P. Kaaret and H. Feng. Confirmation of the 62 Day X-Ray Periodicity from M82. *Astrophys. J.*, 669:106–108, November 2007.
- [273] H. Feng and P. Kaaret. Identification of the X-ray Thermal Dominant State in an Ultraluminous X-ray Source in M82. *Astrophys. J. Lett* , 712:L169–L173, April 2010.
- [274] A. D. Sutton, T. P. Roberts, D. J. Walton, J. C. Gladstone, and A. E. Scott. The most extreme ultraluminous X-ray sources: evidence for intermediate-mass black holes? *MNRAS*, 423:1154–1177, June 2012.
- [275] M. Trenti. Dynamical evidence for intermediate mass black holes in old globular clusters. *ArXiv Astrophysics e-prints*, December 2006.
- [276] M. Coleman Miller and E. J. M. Colbert. Intermediate-Mass Black Holes. *International Journal of Modern Physics D*, 13:1–64, 2004.
- [277] M. Volonteri. Formation of supermassive black holes. *A&ARv*, 18:279–315, July 2010.
- [278] R. Schneider, A. Ferrara, P. Natarajan, and K. Omukai. First Stars, Very Massive Black Holes, and Metals. *Astrophys. J.*, 571:30–39, May 2002.

- [279] Q. Yu and S. Tremaine. Observational constraints on growth of massive black holes. *MNRAS*, 335:965–976, October 2002.
- [280] I. Mandel. Spin distribution following minor mergers and the effect of spin on the detection range for low-mass-ratio inspirals. *ArXiv e-prints*, July 2007.
- [281] G. M. Harry and LIGO Scientific Collaboration. Advanced LIGO: the next generation of gravitational wave detectors. *Class. Quantum Grav.*, 27(8):084006, April 2010.
- [282] F. Acernese et al. Virgo status. *Class. Quantum Grav.*, 25(18):184001–+, September 2008.
- [283] K. Somiya and the KAGRA Collaboration. Detector configuration of KAGRA—the Japanese cryogenic gravitational-wave detector. *Class. Quantum Grav.*, 29(12):124007, June 2012.
- [284] David Shoemaker. Advanced LIGO anticipated sensitivity curves, 2010. <https://dcc.ligo.org/cgi-bin/DocDB>ShowDocument?docid=2974>.
- [285] A. Freise, S. Chelkowski, S. Hild, W. Del Pozzo, A. Perreca, and A. Vecchio. Triple Michelson interferometer for a third-generation gravitational wave detector. *Class. Quantum Grav.*, 26(8):085012–+, April 2009.
- [286] J. R. Gair, I. Mandel, M. C. Miller, and M. Volonteri. Exploring intermediate and massive black-hole binaries with the Einstein Telescope. *General Relativity and Gravitation*, 43:485–518, February 2011.
- [287] E. A. Huerta and J. R. Gair. Intermediate-mass-ratio inspirals in the Einstein Telescope. I. Signal-to-noise ratio calculations. *Phys. Rev. D*, 83(4):044020–+, February 2011.
- [288] E. A. Huerta and J. R. Gair. Intermediate-mass-ratio inspirals in the Einstein Telescope. II. Parameter estimation errors. *Phys. Rev. D*, 83(4):044021–+, February 2011.
- [289] Y. Taniguchi, Y. Shioya, T. G. Tsuru, and S. Ikeuchi. Formation of Intermediate-Mass Black Holes in Circumnuclear Regions of Galaxies. *PASJ*, 52:533–537, June 2000.

- [290] M. C. Miller and D. P. Hamilton. Four-Body Effects in Globular Cluster Black Hole Coalescence. *Astrophys. J.*, 576:894–898, September 2002.
- [291] H. Mouri and Y. Taniguchi. Runaway Merging of Black Holes: Analytical Constraint on the Timescale. *Astrophys. J. Lett* , 566:L17–L20, February 2002.
- [292] H. Mouri and Y. Taniguchi. Mass Segregation in Star Clusters: Analytic Estimation of the Timescale. *Astrophys. J.*, 580:844–849, December 2002.
- [293] K. Gultekin, M. C. Miller, and D. P. Hamilton. Growth of Intermediate-Mass Black Holes in Globular Clusters. *Astrophys. J.*, 616:221–230, November 2004.
- [294] K. Gultekin, M. C. Miller, and D. P. Hamilton. Three-Body Dynamics with Gravitational Wave Emission. *Astrophys. J.*, 640:156–166, March 2006.
- [295] R. M. O’Leary, F. A. Rasio, J. M. Fregeau, N. Ivanova, and R. O’Shaughnessy. Binary Mergers and Growth of Black Holes in Dense Star Clusters. *Astrophys. J.*, 637:937–951, February 2006.
- [296] R. M. O’Leary, R. O’Shaughnessy, and F. A. Rasio. Dynamical interactions and the black-hole merger rate of the Universe. *Phys. Rev. D* , 76(6):061504, September 2007.
- [297] I. Mandel, D. A. Brown, J. R. Gair, and M. C. Miller. Rates and Characteristics of Intermediate Mass Ratio Inspirals Detectable by Advanced LIGO. *Astrophys. J.*, 681:1431–1447, July 2008.
- [298] J. Abadie, B. P. Abbott, R. Abbott, M. Abernathy, T. Accadia, F. Acernese, C. Adams, R. Adhikari, P. Ajith, B. Allen, et al. TOPICAL REVIEW: Predictions for the rates of compact binary coalescences observable by ground-based gravitational-wave detectors. *Class. Quantum Grav.*, 27(17):173001, September 2010.
- [299] R. J. E. Smith, I. Mandel, and A. Vecchio. Studies of waveform requirements for intermediate mass-ratio coalescence searches with advanced gravitational-wave detectors. *Phys. Rev. D* , 88(4):044010, August 2013.

- [300] E. A. Huerta and J. R. Gair. Influence of conservative corrections on parameter estimation for extreme-mass-ratio inspirals. *Phys. Rev. D*, 79(8):084021–+, April 2009.
- [301] E. A. Huerta and J. R Gair. On the relevance of gravitational self-force corrections on parameter estimation errors for extreme-mass-ratio inspirals. *ArXiv e-prints*, September 2010.
- [302] E. A. Huerta and J. R. Gair. Erratum: Influence of conservative corrections on parameter estimation for extreme-mass-ratio inspirals [Phys. Rev. D 79, 084021 (2009)]. *Phys. Rev. D*, 84(4):049903, August 2011.
- [303] E. A. Huerta, P. Kumar, and D. A. Brown. Accurate modeling of intermediate-mass-ratio inspirals: Exploring the form of the self-force in the intermediate-mass-ratio regime. *Phys. Rev. D*, 86(2):024024, July 2012.
- [304] E. Poisson, A. Pound, and I. Vega. The Motion of Point Particles in Curved Spacetime. *Living Reviews in Relativity*, 14:7, September 2011.
- [305] T. Damour, A. Nagar, and S. Bernuzzi. Improved effective-one-body description of coalescing nonspinning black-hole binaries and its numerical-relativity completion. *Phys. Rev. D*, 87(8):084035, April 2013.
- [306] A. Le Tiec, E. Barausse, and A. Buonanno. Gravitational Self-Force Correction to the Binding Energy of Compact Binary Systems. *Phys. Rev. Lett.*, 108(13):131103, March 2012.
- [307] S. Akcay, L. Barack, T. Damour, and N. Sago. Gravitational self-force and the effective-one-body formalism between the innermost stable circular orbit and the light ring. *Phys. Rev. D*, 86(10):104041, November 2012.
- [308] LIGO Scientific Collaboration, Virgo Collaboration, J. Aasi, J. Abadie, B. P. Abbott, R. Abbott, T. D. Abbott, M. Abernathy, T. Accadia, F. Acernese, et al. Prospects for Localization of Gravitational Wave Transients by the Advanced LIGO and Advanced Virgo Observatories. *ArXiv e-prints*, April 2013.

- [309] A. Buonanno, B. R. Iyer, E. Ochsner, Y. Pan, and B. S. Sathyaprakash. Comparison of post-Newtonian templates for compact binary inspiral signals in gravitational-wave detectors. *Phys. Rev. D*, 80(8):084043, October 2009.
- [310] Alessandra Buonanno, Yan-bei Chen, and Michele Vallisneri. Detecting gravitational waves from precessing binaries of spinning compact objects: Adiabatic limit. *Phys. Rev.*, D67:104025, 2003.
- [311] Thibault Damour. Coalescence of two spinning black holes: An effective one-body approach. *Phys. Rev. D*, 64(12):124013, Nov 2001.
- [312] A. Buonanno and T. Damour. Effective one-body approach to general relativistic two-body dynamics. *Phys. Rev. D*, 59(8):084006, April 1999.
- [313] T. Damour, P. Jaranowski, and G. Schäfer. Determination of the last stable orbit for circular general relativistic binaries at the third post-Newtonian approximation. *Phys. Rev. D*, 62(8):084011, October 2000.
- [314] S. Detweiler and B. F. Whiting. Self-force via a Green's function decomposition. *Phys. Rev. D*, 67(2):024025, January 2003.
- [315] S. Detweiler. Consequence of the gravitational self-force for circular orbits of the Schwarzschild geometry. *Phys. Rev. D*, 77(12):124026, June 2008.
- [316] S. Detweiler. Elementary development of the gravitational self-force. *ArXiv e-prints*, August 2009.
- [317] J. G. Baker, W. D. Boggs, J. Centrella, B. J. Kelly, S. T. McWilliams, and J. R. van Meter. Mergers of nonspinning black-hole binaries: Gravitational radiation characteristics. *Phys. Rev. D*, 78(4):044046, August 2008.
- [318] S. Isoyama, R. Fujita, N. Sago, H. Tagoshi, and T. Tanaka. Impact of the second-order self-forces on the dephasing of the gravitational waves from quasicircular extreme mass-ratio inspirals. *Phys. Rev. D*, 87(2):024010, January 2013.
- [319] L. M. Burko and G. Khanna. Self-force gravitational waveforms for extreme and intermediate mass ratio inspirals. II. Importance of the second-order dissipative effect. *Phys. Rev. D*, 88(2):024002, July 2013.

- [320] R. Fujita. Gravitational Waves from a Particle in Circular Orbits around a Schwarzschild Black Hole to the 22nd Post-Newtonian Order. *Progress of Theoretical Physics*, 128:971–992, November 2012.
- [321] L. Blanchet, G. Faye, B. R. Iyer, and B. Joguet. Gravitational-wave inspiral of compact binary systems to $7/2$ post-Newtonian order. *Phys. Rev. D*, 65(6):061501, March 2002.
- [322] L. Blanchet, A. Buonanno, and G. Faye. Tail-induced spin-orbit effect in the gravitational radiation of compact binaries. *Phys. Rev. D*, 84(6):064041, September 2011.
- [323] Y. Pan, A. Buonanno, A. Taracchini, M. Boyle, L. E. Kidder, A. H. Mroue, H. P. Pfeiffer, M. A. Scheel, B. Szilagyi, and A. Zenginoglu. Stability of non-spinning effective-one-body model in approximating two-body dynamics and gravitational-wave emission. *ArXiv e-prints*, November 2013.
- [324] J. R. Gair, M. Vallisneri, S. L. Larson, and J. G. Baker. Testing General Relativity with Low-Frequency, Space-Based Gravitational-Wave Detectors. *Living Reviews in Relativity*, 16:7, September 2013.
- [325] A. Gopakumar and B. R. Iyer. Second post-Newtonian gravitational wave polarizations for compact binaries in elliptical orbits. *Phys. Rev. D*, 65(8):084011, April 2002.
- [326] E. Berti, V. Cardoso, and M. Casals. Eigenvalues and eigenfunctions of spin-weighted spheroidal harmonics in four and higher dimensions. *Phys. Rev. D*, 73(2):024013, January 2006.
- [327] E. Berti, V. Cardoso, and C. M. Will. Gravitational-wave spectroscopy of massive black holes with the space interferometer LISA. *Phys. Rev. D*, 73(6):064030–+, March 2006.
- [328] C.V. Vishveshwara. Scattering of Gravitational Radiation by a Schwarzschild Black-hole. *Nature*, 227:936–938, 1970.
- [329] E. Barausse, V. Morozova, and L. Rezzolla. On the Mass Radiated by Coalescing Black Hole Binaries. *Astrophys. J.*, 758:63, October 2012.

- [330] L. Rezzolla, P. Diener, E. N. Dorband, D. Pollney, C. Reisswig, E. Schnetter, and J. Seiler. The Final Spin from the Coalescence of Aligned-Spin Black Hole Binaries. *Astrophys. J. Lett.*, 674:L29–L32, February 2008.
- [331] A. Buonanno, Y. Pan, J. G. Baker, J. Centrella, B. J. Kelly, S. T. McWilliams, and J. R. van Meter. Approaching faithful templates for nonspinning binary black holes using the effective-one-body approach. *Phys. Rev. D*, 76(10):104049, November 2007.
- [332] E. Barausse and L. Rezzolla. Predicting the Direction of the Final Spin from the Coalescence of Two Black Holes. *Astrophys. J. Lett.*, 704:L40–L44, October 2009.
- [333] L. Rezzolla, E. Barausse, E. N. Dorband, D. Pollney, C. Reisswig, J. Seiler, and S. Husa. Final spin from the coalescence of two black holes. *Phys. Rev. D*, 78(4):044002, August 2008.
- [334] D. A. Brown, P. Kumar, and A. H. Nitz. Template banks to search for low-mass binary black holes in advanced gravitational-wave detectors. *Phys. Rev. D*, 87(8):082004, April 2013.
- [335] F. Foucart, M. B. Deaton, M. D. Duez, L. E. Kidder, I. MacDonald, C. D. Ott, H. P. Pfeiffer, M. A. Scheel, B. Szilagyi, and S. A. Teukolsky. Black-hole-neutron-star mergers at realistic mass ratios: Equation of state and spin orientation effects. *Phys. Rev. D*, 87(8):084006, April 2013.
- [336] M. Saijo, K.-I. Maeda, M. Shibata, and Y. Mino. Gravitational waves from a spinning particle plunging into a Kerr black hole. *Phys. Rev. D*, 58(6):064005–+, September 1998.
- [337] L. M. Burko. Orbital evolution of a test particle around a black hole. II. Comparison of contributions of spin-orbit coupling and the self-force. *Phys. Rev. D*, 69(4):044011–+, February 2004.
- [338] Luc Blanchet, Alessandra Buonanno, and Guillaume Faye. Erratum: Higher-order spin effects in the dynamics of compact binaries. ii. radiation field [phys. rev. d 74, 104034 (2006)]. *Phys. Rev. D*, 75:049903, Feb 2007.

- [339] L. Blanchet, A. Buonanno, and G. Faye. Higher-order spin effects in the dynamics of compact binaries. II. Radiation field. *Phys. Rev. D*, 74(10):104034–+, November 2006.
- [340] R. M. O’Leary, B. Kocsis, and A. Loeb. Gravitational waves from scattering of stellar-mass black holes in galactic nuclei. *MNRAS*, 395:2127–2146, June 2009.
- [341] E. A. Huerta and D. A. Brown. Effect of eccentricity on binary neutron star searches in advanced LIGO. *Phys. Rev. D*, 87(12):127501, June 2013.
- [342] H. Yang, F. Zhang, A. Zimmerman, and Y. Chen. The scalar Green function of the Kerr spacetime. *ArXiv e-prints*, November 2013.
- [343] S. R. Dolan, L. Barack, and B. Wardell. Self-force via m-mode regularization and 2+1D evolution. II. Scalar-field implementation on Kerr spacetime. *Phys. Rev. D*, 84(8):084001, October 2011.
- [344] A. Pound, C. Merlin, and L. Barack. Gravitational self-force from radiation-gauge metric perturbations. *ArXiv e-prints*, October 2013.
- [345] F. Zhang and B. Szilágyi. Joint approach for reducing eccentricity and spurious gravitational radiation in binary black hole initial data construction. *Phys. Rev. D*, 88(8):084033, October 2013.
- [346] Luc Blanchet, Guillaume Faye, Bala R. Iyer, and Benoit Joguet. Gravitational-wave inspiral of compact binary systems to 7/2 post-Newtonian order. *Phys. Rev. D*, 65(6):061501, Feb 2002.
- [347] Luc Blanchet, Guillaume Faye, Bala R. Iyer, and Benoit Joguet. Erratum: Gravitational-wave inspiral of compact binary systems to 7/2 post-Newtonian order [Phys. Rev. D 65, 061501(R) (2002)]. *Phys. Rev. D*, 71(12):129902, Jun 2005.
- [348] Luc Blanchet, Bala R. Iyer, and Benoit Joguet. Erratum: Gravitational waves from inspiraling compact binaries: Energy flux to third post-Newtonian order [Phys. Rev. D 65, 064005 (2002)]. *Phys. Rev. D*, 71(12):129903, Jun 2005.

- [349] K. G. Arun, Alessandra Buonanno, Guillaume Faye, and Evan Ochsner. Higher-order spin effects in the amplitude and phase of gravitational waveforms emitted by inspiraling compact binaries: Ready-to-use gravitational waveforms. *Phys. Rev. D*, 79(10):104023, May 2009. Note that the 1.5 and 2.5pN spin terms in the flux and energy expressions do not account for an erratum from 2010.
- [350] Luc Blanchet, Alessandra Buonanno, and Guillaume Faye. Higher-order spin effects in the dynamics of compact binaries. II. Radiation field. *Phys. Rev. D*, 74(10):104034, November 2006. Note the two associated errata; the arXiv version has been corrected.
- [351] Luc Blanchet, Alessandra Buonanno, and Guillaume Faye. Erratum: Higher-order spin effects in the dynamics of compact binaries. II. Radiation field [Phys. Rev. D 74, 104034 (2006)]. *Phys. Rev. D*, 75(4):049903, February 2007.
- [352] Luc Blanchet, Alessandra Buonanno, and Guillaume Faye. Erratum: Higher-order spin effects in the dynamics of compact binaries. II. Radiation field [Phys. Rev. D 74, 104034 (2006)]. *Phys. Rev. D*, 81(8):089901, April 2010.
- [353] Thibault Damour, Piotr Jaranowski, and Gerhard Schaefer. Dynamical invariants for general relativistic two-body systems at the third postNewtonian approximation. *Phys. Rev.*, D62:044024, 2000.
- [354] Luc Blanchet and Guillaume Faye. Equations of motion of point particle binaries at the third postNewtonian order. *Phys. Lett.*, A271:58, 2000.
- [355] Lawrence E. Kidder. Coalescing binary systems of compact objects to post-Newtonian 5/2 order. 5. Spin effects. *Phys. Rev.*, D52:821–847, 1995.
- [356] Guillaume Faye, Luc Blanchet, and Alessandra Buonanno. Higher-order spin effects in the dynamics of compact binaries. I. Equations of motion. *Phys. Rev.*, D74:104033, 2006.
- [357] Eric Poisson. Gravitational waves from inspiraling compact binaries: The Quadrupole moment term. *Phys. Rev.*, D57:5287–5290, 1998.
- [358] Balazs Mikoczi, Matyas Vasuth, and Laszlo A. Gergely. Self-interaction spin effects in inspiralling compact binaries. *Phys. Rev.*, D71:124043, 2005.

- [359] K.G. Arun, Alessandra Buonanno, Guillaume Faye, and Evan Ochsner. Higher-order spin effects in the amplitude and phase of gravitational waveforms emitted by inspiraling compact binaries: Ready-to-use gravitational waveforms. *Phys.Rev.*, D79:104023, 2009.
- [360] Sylvain Marsat, Alejandro Bohe, Guillaume Faye, and Luc Blanchet. Next-to-next-to-leading order spin-orbit effects in the equations of motion of compact binary systems. *Class.Quant.Grav.*, 30:055007, 2013.
- [361] Alejandro Bohe, Sylvain Marsat, Guillaume Faye, and Luc Blanchet. Next-to-next-to-leading order spin-orbit effects in the near-zone metric and precession equations of compact binaries. *Class.Quant.Grav.*, 30:075017, 2013.
- [362] Alejandro Boh, Sylvain Marsat, and Luc Blanchet. Next-to-next-to-leading order spinorbit effects in the gravitational wave flux and orbital phasing of compact binaries. *Class.Quant.Grav.*, 30:135009, 2013.
- [363] Kashif Alvi. Energy and angular momentum flow into a black hole in a binary. *Phys. Rev. D* , 64(10):104020, Oct 2001.
- [364] Hideyuki Tagoshi, Shuhei Mano, and Eiichi Takasugi. Post-Newtonian expansion of gravitational waves from a particle in circular orbits around a rotating black hole :Effects of black hole absorption. *gr-qc/9711072*, November 1997.
- [365] Thibault Damour, Bala R. Iyer, and B. S. Sathyaprakash. Comparison of search templates for gravitational waves from binary inspiral. *Phys. Rev. D* , 63(4):044023, 2001.
- [366] Thibault Damour, Bala R. Iyer, and B. S. Sathyaprakash. Comparison of search templates for gravitational waves from binary inspiral: 3.5PN update. *Phys. Rev. D* , 66(2):027502, 2002.
- [367] K. G. Arun, Bala R. Iyer, B. S. Sathyaprakash, and Pranesh A. Sundararajan. Parameter estimation of inspiralling compact binaries using 3.5 post-Newtonian gravitational wave phasing: The non-spinning case. *Phys. Rev.*, D71:084008, 2005.

- [368] Luc Blanchet, Guillaume Faye, Bala R. Iyer, and Siddhartha Sinha. The third post-Newtonian gravitational wave polarizations and associated spherical harmonic modes for inspiralling compact binaries in quasi-circular orbits. *Class. Quant. Grav.*, 25(16):165003, 2008.
- [369] Clifford M. Will and Alan G. Wiseman. Gravitational radiation from compact binary systems: Gravitational waveforms and energy loss to second post-Newtonian order. *Phys. Rev. D*, 54:4813–4848, 1996.
- [370] Larne Pekowsky. *Characterization of Enhanced Interferometric Gravitational Wave Detectors and Studies of Numeric Simulations for Compact-Binary Coalescences*. PhD thesis, Syracuse University, 2009.